Bioelectrocatalytic oxidation and reduction of different substrates using carbon nanostructured electrodes

Xiaohong Chen

Communauté
UNIVERSITÉ Grenoble Alpes

THÈSE

Pour obtenir le grade de

DOCTEUR DE LA COMMUNAUTÉ UNIVERSITÉ GRENOBLE ALPES

Spécialité : **Chimie inorganique et Bio inorganique**

Arrêté ministériel : 25 mai 2016

Présentée par

Xiaohong CHEN

Thèse dirigée par **Serge COSNIER,** Directeur de Recherche
et co-encadrée par **Fabien GIROUD,** Université Grenoble Alpes

préparée au sein du **Laboratoire Département de Chimie Moléculaire**
dans **l'École Doctorale Chimie et Sciences du Vivant**

Oxydation et réduction bioélectrocatalytique de différents substrats à l'aide d'électrodes en carbone nanostructurées

Bioelectrocatalytic oxidation and reduction of different substrates using carbon nanostructured electrodes

Thèse soutenue publiquement le **9 décembre 2019**,
devant le jury composé de :

Monsieur Guy ROYAL
Professeur des Universités, Université Grenoble Alpes, Président
Madame Sophie TINGRY
Directeur de Recherche, Institut Européen des Membranes, Rapporteur
Madame Carole CHAIX
Directeur de Recherche, Institut des Sciences Analytiques, Rapporteur
Monsieur Laurent BOUFFIER
Chargé de Recherche, Institut des Sciences Moléculaires, Université de Bordeaux, Examinateur
Monsieur Serge COSNIER
Directeur de Recherche, Université Grenoble Alpes, Directeur de thèse

Table of Contents

List of Figures

List of Tables

General Introduction

Introduction générale

Les biopiles sont un sujet de recherche brûlant depuis des décennies dans le but d'établir des sources d'énergie de remplacement pour atténuer les problèmes environnementaux causés par les combustibles fossiles classiques. Une sous-catégorie des biopiles, les biopiles enzymatiques (EFC) ont beaucoup attiré l'attention ces derniers temps, alors que les scientifiques tentaient de récupérer de l'énergie directement du corps humain. L'intérêt des enzymes comme catalyseurs réside dans le fait qu'ils peuvent fonctionner dans des conditions physiologiques complexes et utiliser diverses sources de carburant durables, notamment le sucre contenu dans les fluides corporels, qui sont très intéressantes pour alimenter de futurs dispositifs électroniques implantables et portables dans le corps ou à la surface du corps. Dans cette configuration, au moins deux enzymes rédox sont nécessaires; un à l'anode pour oxyder le combustible et un à la cathode pour réduire un oxydant.

Les nanotubes de carbone (CNTs) sont utilisés comme matériaux d'électrode en raison de leur surface spécifique élevée et de leurs propriétés électroniques exceptionnelles. Par ailleurs, le faible diamètre des CNTs permet d'approcher de plus près le site actif des enzymes, ce qui pourrait théoriquement améliorer le câblage électrique des protéines rédox. Buckypaper (BP) est un matériau ressemblant à du papier formé par un réseau de CNTs enchevêtrés et est maintenu par les forces de Van der Waals. Les BPs peuvent être facilement préparés en laboratoire par filtration de suspensions de nanotubes de carbone pour former des films uniformes. Ils sont minces, légers, hautement conducteurs et faciles à fonctionnaliser, ce qui en fait d'excellents candidats comme matériau d'électrode pour les applications de piles à combustible.

Le but de cette thèse est d'explorer les formulations, les caractérisations et les applications pratiques des buckypapers dans les biopiles enzymatiques.

Le premier chapitre est une revue de littérature sur les connaissances générales et les derniers rapports scientifiques permettant de bien comprendre la bioélectrochimie et en particulier les EFCs. Il est structuré en quatre sections. La première section présente le contexte général des piles à combustible et des biopiles. Une description plus détaillée du principe de fonctionnement et des caractéristiques des EFCs est donnée. La deuxième section présente les méthodes d'immobilisation d'enzymes et les mécanismes de transfert d'électrons des enzymes. Une introduction détaillée de

certaines enzymes communément utilisées dans les EFCs est également présentée. La troisième section concerne la structure et les propriétés du papier mâché en nanotube de carbone en tant que matériau d'électrode. Ce chapitre se termine par la présentation de différentes applications des EFCs et des résultats les plus récents dans ces domaines de recherche.

Dans le chapitre 2, les buckypapers commerciaux obtenus auprès d'un fournisseur et de buckypapers fabriqués en laboratoire ont été comparés afin d'établir leurs propriétés pour une utilisation future en tant que bioélectrodes avancées. Les propriétés physiques des films de nanotubes de carbone ressemblant à du papier ont été caractérisées par différentes techniques. Les propriétés électrochimiques ont été étudiées par voltamétrie en l'absence et en présence de sondes redox. La réduction bio-électrocatalytique de l'oxygène a été évaluée avec des neutrophages modifiés au fer-protoporphyrine après immobilisation de la bilirubine oxydase (BOx).

Le chapitre 3 explore l'utilisation de l'hydrogel d'alginate comme couche protectrice afin d'améliorer la stabilité de la bioanode pour l'oxydation du glucose. La bioanode oxydante du glucose a été préparée en immobilisant la glucose déshydrogénase (GDH) dépendante de la flavine adénine dinucléotide (FAD) sur un papier gabarit de laboratoire fonctionnalisé avec la 1,10-phénanthroline-5,6-dione en tant que médiateur. De l'hydrogel préparé à partir de différents paramètres de fabrication a été déposé sur la surface de l'électrode en buckypaper. L'effet du revêtement d'hydrogel sur le stockage et la stabilité opérationnelle de la bioanode a été évalué par voie électrochimique.

Au chapitre 4, une biopile à combustible lactate/O_2, extensible et flexible, a été réalisée en utilisant un papier mâché pour électrode. La BP flexible a été fabriquée en tant que matrice d'immobilisation pour la lactate oxydase (LOx) à l'anode et BOx à la cathode. Pour répondre aux exigences des composants électroniques portables, les électrodes BP fonctionnalisées ont été assemblées sur un collecteur de courant sérigraphié extensible avec une configuration «îlot-pont», qui confère au EFC une excellente stabilité de performance en étirement. La stabilité mécanique et les performances énergétiques de l'appareil ont été examinées.

Le cinquième chapitre présente brièvement une autre configuration d'électrodes pour la réaction bioélectrocatalytique dans laquelle les deux médiateurs et les enzymes sont en solution. Des glyconanoparticules nouvellement synthétisées permettent la solubilisation d'un médiateur redox non soluble dans l'eau pour donner

des nanoparticules à activité rédox. Dans ce chapitre, la préparation et la caractérisation détaillée de nanoparticules ont été présentées et leur utilisation comme navettes électroniques pour les oxydoréductases a été étudiée.

Enfin, la thèse se termine par une conclusion de ce travail et une discussion sur les perspectives futures.

General Introduction

Biofuel cells have been a hot research topic for decades aiming to establish alternative energy options to alleviate the environmental problems caused by conventional fossil fuels. A subcategory of biofuel cells, enzymatic biofuel cells (EFCs) have drawn a lot of attention lately as scientists are trying to harvest energy directly from the human body. The beauty of using enzymes as catalysts is that they can operate at complex physiological conditions and utilize various sustainable fuel sources, especially sugar in body fluids, which are very interesting for powering future implantable and wearable electronic devices inside the body or on the surface of the skin. In such configuration, at least two redox enzymes are required; one at the anode to oxidize the fuel and one at the cathode to reduce an oxidant.

Carbon nanotubes (CNTs) are used as electrode materials due to their high specific surface area and exceptional electronic properties. Besides, the thin diameter of CNTs makes it possible to approach more closely the active site of enzymes, which could theoretically enhance the electrical wiring of redox proteins. Buckypaper (BP) is a paper-like material formed by entangled CNTs network and is held together by Van der Waals forces. BPs can be easily prepared in labs by filtration of carbon nanotubes suspensions to form uniform films. They are thin, lightweight, highly conductive and easy to functionalize, which makes them great candidates as electrode material for fuel cell applications.

The aim of this thesis is to explore the formulations, characterizations and practical applications of buckypapers in enzymatic biofuel cells.

The first chapter is a literature survey on general knowledge and latest scientific reports to get a good grasp on bioelectrochemistry and especially on EFCs. It is structured in four sections. The first section introduces the general context of fuel cells and biofuel cells. A more detailed description of the working principle and characteristics of EFCs are given. The second section presents enzyme immobilization methods and electron transfer mechanisms of enzymes. A detailed introduction of some commonly used enzymes in EFCs is also given. The third section concerns the structure and properties of carbon nanotube buckypaper as electrode material. This chapter ends with the presentation of different applications of EFCs and state-of-the-art results in these research fields.

In chapter 2, commercial buckypapers obtained from a supplier and

laboratory-made buckypapers have been compared to establish their properties for future use as advanced bioelectrodes. The physical properties of the paper-like carbon nanotube films were characterized with different techniques. The electrochemical properties were investigated by voltammetry in the absence and presence of redox probes. Bioelectrocatalytic oxygen reduction was evaluated with iron-protoporphyrin modified buckypapers after immobilization of bilirubin oxidase (BOx).

Chapter 3 explores the use of alginate hydrogel as a protective layer to improve stability of bioanode for glucose oxidation. The glucose oxidizing bioanode was prepared by immobilizing flavin adenine dinucleotide (FAD) dependent glucose dehydrogenase (GDH) onto lab-made buckykpaper functionalized with 1,10-phenanthroline-5,6-dione as the mediator. Hydrogel prepared from different fabrication parameters was deposited onto buckypaper electrode surface. The effect of hydrogel coating on the storage and operational stability of the bioanode was evaluated electrochemically.

In chapter 4, a stretchable and flexible lactate/O_2 biofuel cell was realized using buckypaper as the electrode material. Flexible BP was fabricated as the immobilization matrix for lactate oxidase (LOx) at the anode and BOx at the cathode. To fulfill the strain-enduring requirement of wearable electronics, the functionalized BP electrodes were assembled onto a stretchable screen-printed current collector with an “island–bridge” configuration, which endows the EFC with excellent performance stability under stretching condition. The mechanical stability and power performance of the device were examined.

The fifth chapter briefly introduces an alternative electrode configuration for bioelectrocatalytic reaction where both mediators and enzymes are in solution. Newly synthesized glyconanoparticles enable the solubilization of non-water soluble redox mediator to give redox-active nanoparticles. In this chapter, the preparation and detailed characterization of nanoparticles were presented and their use as electron shuttles for oxidoreductases was investigated.

Finally, the thesis ends with a conclusion of this work and a discussion of future perspectives.

Chapter 1:

Introduction

Chapter 1 Introduction

1.1 Background

1.1.1 Fuel cells

In modern society, the majority of world energy comes from fossil fuels, which contains petroleum, natural gas and coal. Despite their relatively large availability on earth, their stocks are limited. Their extraction requires large infrastructures and can eventually lead to the contamination of the area. Furthermore, greenhouse gases are released from the combustion of these non-renewable fuels. This leads to huge environmental impacts and without a doubt contributes to the current climate change. With the continuously growing energy demand and decreasing reserve of fossil fuels, there has been much interest in developing environmentally friendly and renewable energy sources without greenhouse gas emission. Compared with combustion of fossil fuels, fuel cells represent a more efficient and more environmentally friendly power generation system that transforms chemical energy stored in various sustainable fuels (H_2, natural gas, sugar, *etc*…) into electricity without intermediate steps.

1.1.1.1 Principle of a fuel cell

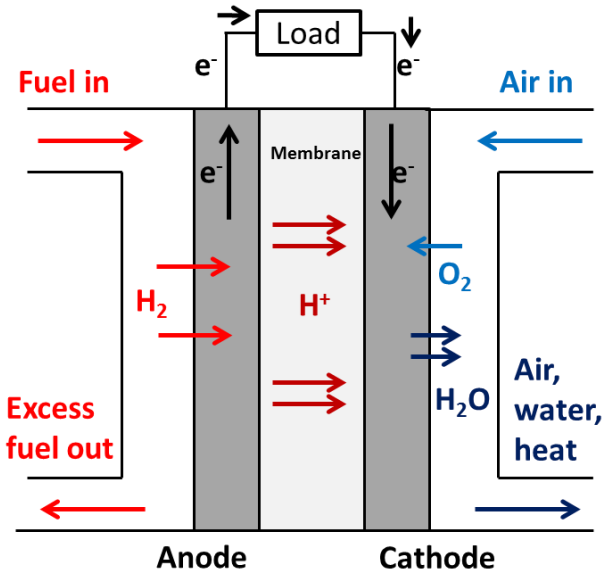

Figure 1.1 Schematic representation of an H_2/O_2 fuel cell

Figure 1.1 depicts the general scheme of a H_2/O_2 fuel cell, exploiting H_2 as fuel and O_2 as oxidant, which is one of the most studied systems in fuel cells. In general, fuel cells are electrochemical devices comprised of anodes, cathodes and electrolytes that

can convert chemical energy into electrical current *via* redox reactions. In this case, H_2 is oxidized by the electrocatalyst at the anode. The released electrons then flow in the external circuit and the generated protons diffuse through the electrolyte toward the cathode, where oxidants (O_2, H_2O_2) are reduced with the combination of electrons and protons. The generated electricity can then be used to do work. The only product in this process is water, making it exceptionally attractive for the development of clean power sources.

1.1.1.2 Applications and limitations

Based on the types of electrolytes, fuel cells can be divided into five main categories. Characteristics of the different fuel cells are summarized in **Table 1.1**. These fuel cells have been used in different applications. For example, vehicles powered by PEMFCs have been developed by several companies (Toyota, Honda and Hyundai) and AFCs were used by NASA in the Apollo-series missions and space shuttles. However, energy conversion in fuel cells usually relies on the use of noble metal platinum (Pt) as the electrocatalyst or high temperature conditions. Thus, efforts have been dedicated to developing platinum group metal (PGM)-free catalyst and lowering operating temperature of high temperature fuel cell.[1–3]

Table 1.1 Comparison of different fuel cells.

Classification	**Operation temperature / °C**	**Electrolyte**	**Catalyst**	**Applications**	**Drawbacks**
Polymer electrolyte membrane fuel cell (PEMFC)	70-110	Nafion membrane	Pt	Transportation, portable electronics, stationary	Expensive catalyst, highly pure fuel
Alkaline fuel cell (AFC)	<100	Alkaline solution	Non-noble metal	Space, Stationary power, military,	CO_2 poisoning, electrolyte management
Phosphoric acid fuel cell (PAFC)	150-200	Phosphoric acid	Pt	Stationary power, transportation	Expensive catalyst, long start up time
Molten carbonate fuel cell (MCFC)	550-650	Molten carbonate	Non-noble metal	Distributed power generation	High temperature, corrosion of the cell components, long start up time

Solid oxide fuel cell (SOFC)	500-800	Ceramic oxide	Cathode: perovskite Anode: cermet	Distributed power generation	High temperature, corrosion of the cell components, long start up time

A subcategory of fuel cells, biofuel cells (BFCs), have attracted considerable attention as they use biological entities as electrocatalysts instead of traditional expensive and nonrenewable noble metal-based catalysts. Compared with conventional fuel cells, BFCs are capable to operate at mild conditions, neutral pH, and in complex media. Biological catalysts are renewable resources, which makes BFC ideal candidate to replace commercial lithium battery for low power portable applications. The concept of BFCs will be further elaborated in the following part.

1.1.2 Biofuel cells

Depending on the nature of biocatalysts, biofuel cells can be categorized into microbial fuel cells,[4,5] mitochondrial biofuel cells[6] and enzymatic biofuel cells.[7] The different characteristics of the biocatalysts therefore determine the different operational conditions and applications of these BFCs.

1.1.2.1 Microbial fuel cells

Microbial fuel cells (MFCs) utilize whole microorganisms as electrocatalysts. These microorganisms (bacteria, yeast or archaea) contain enzyme cascades that can oxidize carbohydrates completely to carbon dioxide, which endows microbial fuel cells with high energy density. Since enzymes can be regenerated by the living organism, the life time of MFCs can be up to order of years.[8] However, the mass transfer and electron transfer processes of MFCs involve crossing the cell membrane, resulting in low power density, which remains the major roadblock for commercialization.[9] Besides, given the living nature of biocatalysts, it is necessary to separate the cathodic and anodic compartments to avoid cross-reaction. In 2005, Bergel *et al.* developed a microbial-based biocathode for oxygen reduction by growing a marine biofilm on a stainless steel electrode.[10] Later, Rabaey *et al.* reported a complete MFC with both microbial-based biocathode and bioanode, the MFC produced a maximum power density of 30.3 $\mu W\ cm^{-2}$.[11]

As a result of the underlying challenges, microbial fuel cell is not economically competitive as a power source.[12] Given the large size and long lifetime of MFCs, a

promising application is wastewater treatment combined with electricity generation.[13,14] Ieropoulos *et al.* demonstrated the first example of electricity generation from urine using MFCs.[15] The same group later conducted field trials on campus and a music festival, where they demonstrated the feasibility of MFCs for stable power generation and urine treatment simultaneously.[16]

1.1.2.2 Enzymatic fuel cells

Enzymatic fuel cells and microbial fuel cells are the two most studied groups of BFCs. The former group employs oxidoreductases as the catalysts, which are a group of redox active enzymes that can catalyze the electron transfer process that occurs during the substrate cleavage. Oxidoreductases are important in biotechnology as they can be explored in practical applications such as biosensors and biofuel cells. Compared with microorganisms, their small size and the absence of cell membranes facilitate both mass and electron transfer. The specificity of enzymes towards their substrates usually eliminates the need for membrane for compartmentalization, which greatly simplifies the design and miniaturization of devices. The first EFC was developed by Yahiro *et al.* in 1964, where glucose oxidase (GOx) was used for glucose oxidation at the anode and platinum was used as catalyst for oxygen reduction at the cathode.[17] Tremendous improvements have been made ever since then with the power density increases to the order of mW cm^{-2}.[7,18]

The biggest challenge of EFCs is their limited stability, ranging from days to weeks,[18,19] which can be ascribed to the fragile nature of purified enzymes. Another challenge lies in the low power density. In contrast to MFCs, enzymes usually perform one-step oxidation of the biofuel, leading to low energy efficiency. On the other hand, the power performance is greatly influenced by the operating environment conditions (pH, temperature and inhibitors). One of the contributing factors is the limited substrate availability. In addition, many reported EFCs are tested in buffer solutions, where oxygen reduction currents are small due to the slow diffusion and low concentrations of dissolved O_2 (~0.25 mmol L^{-1} at 25 °C) in aqueous solutions.[20]

1.1.2.3 Mitochondria fuel cell

Mitochondrial fuel cell has been exploited in recent years as an alternative solution to overcome the limitations of MFCs and EFCs. Mitochondria, regarded as the powerhouse of the cell, are organelles present in eukaryotic cells. As part of the living

cells, mitochondria contain readily multiple enzymes that can deeply oxidize some organic substrates (pyruvate,[21] fatty acids,[22] and amino acids[6]), providing similar energy efficiency as MFCs. Mitochondria are considered as a compromise between microorganisms and enzymes. Fuel cells utilizing these species exhibit higher power density than MFCs due to more facile mass transfer. Mitochondrial fuel cells also possess longer lifetime than EFCs due to the presence of mitochondria membranes. In 2008, Arechederra and Minteer demonstrated the first mitochondria-based bioanode that can completely oxidize pyruvate into carbon dioxide.[21] By coupling with a Pt cathode, the biofuel cell achieved a power density of 203 μW cm^{-2} and a lifetime of 60 days.[21] However, power densities obtained in the reported literatures are still lower than the theoretical values.[6,21,22] The following works mostly done by Minteer's group have been more driven in using mitochondria for self-powered explosive sensing.[23–25]

1.1.3 Enzymatic fuel cell

1.1.3.1 Principle of enzymatic biofuel cells

Regardless of the type of biocatalysts, BFCs share similar operation principle as conventional fuel cells (see chapter 1.1.1.1). One big distinction between FC and BFC is the different electron exchange properties. The difference of the electrode reaction mechanism between FC and BFC is illustrated in **Figure 1.2**. Compared with conventional metal catalysts used in FCs, enzymes are macromolecules with their redox centers buried in non-conductive protein shell. The low active sites density and long electron tunneling distance therefore hinders the electrical coupling between enzymes and electrode surfaces.[26]

In general, the reaction at an enzyme-modified electrode can be separated into three regions (**Figure 1.2**): 1) mass transfer between bulk electrolyte and catalyst active sites; 2) enzyme-catalyzed reaction; 3) electron transfer between active sites and the electrode. To increase the overall current output of the reaction, researchers are focusing on lowering the energy barrier of the rate limiting step. Thorough investigation of the reaction mechanism is needed to identify the rate limiting step, followed by optimization of the parameters involved in the reaction. The improvement in the current density of the bioelectrode can be implemented in different research areas. For example, catalytic current can be increased by utilization of nanomaterial-based electrodes (directly linked to the increase in surface area) for

higher enzyme loading on the electrode. To improve the overall current and fuel cell efficiency, engineering aspects also need to be considered such as optimization of the electrode spacing, matching of the cathode and anode performance, *etc*.

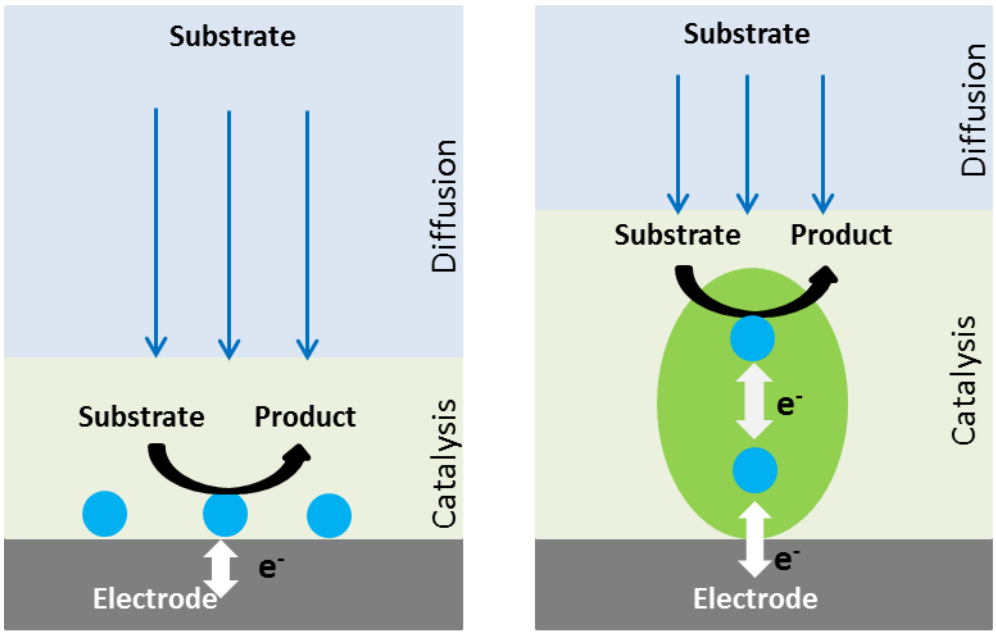

Figure 1.2 Schematic representations of the mechanism of a catalytic reaction at an electrode of (left) a fuel cell and (right) a biofuel cell (blue sphere: active site)

1.1.3.2 Substrates and enzymes used in EFCs

Although the power density of EFCs are not comparable to conventional PGM-based fuel cells, a big advantage of EFCs is that it opens up the possibility to harvest chemical energy from various and abundant organic compounds using biosourced and renewable electrocatalysts. The choice of fuel and oxidant determines the corresponding enzymes used in the system. Although there is a wide range of fuels that can be used for EFCs, factors such as energy density, cost, storage and safety of fuels have limited the option for actual applications. The fuels used in EFCs are mostly saccharides, H_2, alcohol and some intermediates present in metabolism. A list of representative fuels and enzymes is shown in **Table 1.2**.

Table 1.2 List of fuels found in EFCs, their product, the enzymes responsible for their oxidation and the cofactors of the enzyme

Fuels	Half-Reactions	Enzymes	Cofactors	Reference
Aldehyde	Aldehyde→Acid	Aldehyde dehydrogenase (AlDH)	Nicotinamide adenine dinucleotide	Marchitti *et al.*[27]

			(NAD^+)	
Cellobiose	Cellobiose→ Cellobionolactone	Cellobiose DH (CDH)	Flavin adenine dinucleotide (FAD)/Heme	Ludwig *et al.*[28]
Ethanol Methanol	Alcohol→Aldehyde	Alcohol DH (ADH)	NAD^+	Theorell and McKinley-McKee[29]
Formic acid	HCOOH→CO_2	Formate DH	NAD^+	Ferry *et al.*[30]
Fructose	$_D$-fructose→ 5-Keto-$_D$-fructose	Fructose DH (FDH)	FAD/Heme	Adachi *et al.*[31]
Glucose	$_D$-Glucose→ $_D$-glconolactone	Glucose oxidase (GOx)	FAD	Ferri *et al.*[32]
		Glucose DH (GDH)	FAD or NAD^+ or Pyrroloquinoline quinone (PQQ)	
Lactate	Lactate→Pyruvate	Lactate oxidase (LOx)	Flavin mononucleotide (FMN)	Maeda-Yorita *et al.*[33]
		Lactate DH (LDH)	NAD^+	Holbrook *et al.*[34]
Hydrogen	H_2 →$2H^+$+$2e^-$	Hydrogenase (H_2ase)	[NiFe] or [FeFe]	Adams *et al.*[35]

As a clean fuel with high energy density, hydrogen has also been widely studied in EFCs.[36,37] Hydrogenases (H_2ase) are metalloenzymes with active sites composed of Ni-Fe or Fe-Fe that can catalyze the oxidation of H_2 at low overpotential.[38] Compared with platinum, H_2ase has high efficiency, can operate at mild conditions and is not susceptible to carbon monoxide poisoning.[39] However, H_2ase can be (strongly) deactivated in the presence of oxygen.[40] Researchers have been working on the isolation and characterization of O_2-tolerant H_2ase from *Ralstonia eutropha* to overcome the limitations.[41,42] Another strategy is to integrate the O_2-sensitive H_2ase into a protective layer composed of viologen-based redox polymer for shielding the enzyme from O_2.[43]

The most commonly used fuels in EFCs are saccharides due to their low costs, availability, renewability and safety. Many sugars including fructose, lactose and polysaccharides can be used as fuels. Among these sugars, glucose is the most widely used fuel due to its presence in human body fluids at moderate concentration,[44] which makes it an ideal candidate as the power source for implantable electronic devices.

Glucose oxidation can be catalyzed by several enzymes such as glucose oxidase or glucose dehydrogenase. Since the first glucose/O_2 EFC developed in 1964,[17] GOx has been the most used enzyme for glucose oxidation due to its high stability and low cost.[45–47] However, GOx is an oxygen-sensitive enzyme that uses oxygen as a natural electron acceptor and can produce hydrogen peroxide in the electrocatalytic process.[48] The as-produced H_2O_2 has been shown to be detrimental to cathodic enzyme activity.[48] Furthermore, the competitive reaction with O_2 implies that a fraction of the electrons produced during the catalytic oxidation of glucose will deviate from flowing to the cathode via interconnects, instead going to O_2 and resulting in a decrease of the cell performance.

Glucose dehydrogenases (GDH), on the other hand, are oxygen insensitive enzymes. Three specific GDH have been discovered so far and are classified based on their redox active center and each of them has its own specificity. NAD-dependent GDH (NAD-GDH) utilizes NAD^+ as the cofactor. Although the low apparent redox potential of this cofactor ($E^{\circ}_{NAD+/NADH}$ = -0.56 V *vs.* SCE at pH 7.0)[49] can be seen as an appealing trait for an anodic enzyme, the use of such enzyme has some limitations. First, NAD is not bound to the protein. Hence it has to be added to the electrolyte which increases the cost of the device and the possibility for crossover reaction at the cathodic side. Additionally, despite its low redox potential, the regeneration of NAD^+ requires high overpotential at unmodified electrodes.[50] There have been more and more interests in using PQQ-dependent GDH (PQQ-GDH) and FAD-dependent GDH (FAD-GDH) with bound cofactors. It should be noted that PQQ-GDH displays broad substrate specificity and therefore is not suitable for sensing applications.[32]

As for the reduction reaction at the cathode, oxygen is the most commonly used oxidant. Laccase (Lac)[51] and bilirubin oxidase (BOx)[52] are the two most used enzymes for bioelectrocatalytic four-electron reduction of oxygen. Both of them belong to the group of multi-copper oxidases (MCOs), which contains at least four copper atoms acting as redox active centers and can reduce oxygen with small overpotential.[53] There are other enzymes such as copper efflux oxidase (CueO),[54] polyphenol oxidase[55] (PPO) and cytochrome oxidase[56] (CytOx) that can reduce oxygen. Nevertheless, they are rarely used to construct biocathode due to high overpotential.[54,55,57] In certain cases, hydrogen peroxide has been explored as oxidant at the cathode, which involves a two-electron reduction reaction catalyzed by peroxidase.[58] Oxidants and enzymes used for biocathode are

summarized in **Table 1.3**.

Table 1.3 List of oxidants used in EFCs, their product, the enzymes responsible for their reduction and the cofactors of the enzyme

Oxidants	Half-Reactions	Enzymes	Cofactors	Reference
O_2	O_2+ $4H^+$+$4e^-$ →$2H_2O$	Lac	Cu	Tarasevich *et al.*[59]
		BOx		Tsujimura *et al.*[60]
		CueO		Miura *et al.*[54]
		PPO		Reuillard *et al.*[55]
		Cyt Ox	Cu/Fe/Heme	Katz *et al.*[56]
H_2O_2	H_2O_2 + $2H^+$+$2e^-$ →$2H_2O$	Horseradish peroxidase (HRP)	Fe/Heme	Elouarzaki *et al.*[58]

A more detailed introduction on each redox enzymes used during the course of this thesis is given in section 1.2.4.

1.1.3.3 Characteristics of the biofuel cell

Open circuit voltage (OCV) and power density are two key parameters for evaluation of the fuel cell performance. OCV describes the potential difference between the cathode and the anode at zero current, which is the maximum voltage of the fuel cell. OCV corresponds to the cell voltage at equilibrium (E_{eq}), which can be calculated from the change in Gibbs free energy of reaction (ΔG_{eq}) in the galvanic cell by[61]

$$E_{eq} = -\Delta G_{eq}/nF \qquad (1.1)$$

where n is the number of electrons, and F is the Faradaic constant. In H_2/O_2 fuel cell, the overall chemical reaction is:

$$H_{2(g)} + \frac{1}{2}O_{2(g)} \rightarrow H_2O_{(l)} \qquad (1.2)$$

According to **Equation 1.1**, OCV is calculated to be 1.23 V in the standard condition.[19] In electrochemistry, OCV is measured by open circuit potentiometry. This is similar to connecting the fuel cell to an infinite load resistance. The actual OCV is usually lower than the theoretical E_{eq} due to the nature of the redox centers of the enzymes or the redox potential of the mediators. When current starts to flow in the cell, the measured cell potential ($E_{measured}$) will depart from its equilibrium value. The

term that describes the potential loss is called overpotential (η). There are three types of overpotential:[62] the activation overpotential (η_{act}), the ohmic overpotential (η_{iR}) and the mass transfer overpotential (η_{mt}). The relation between $E_{measured}$ and E_{eq} can be expressed as:

$$E_{measured} = E_{eq} - \eta_{act} - \eta_{iR} - \eta_{mt} \qquad (1.3)$$

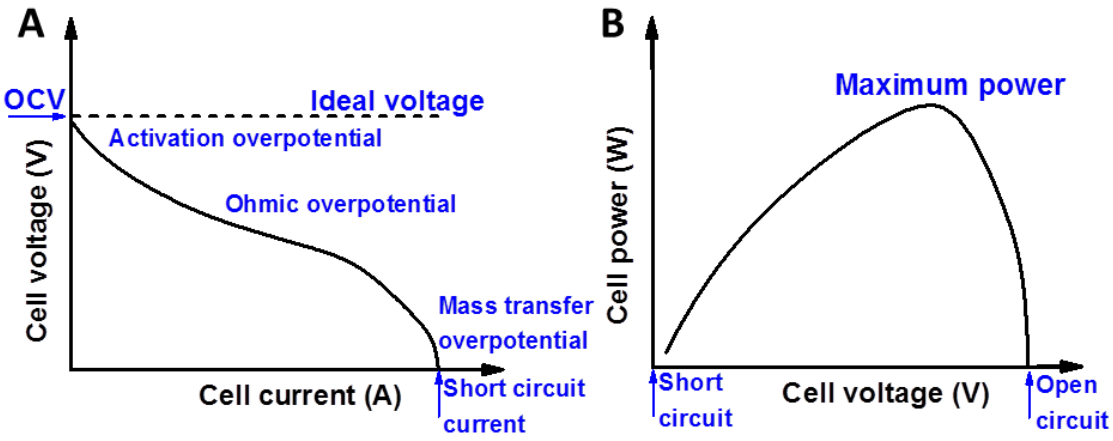

Figure 1.3 (A) Voltage-Current profile and (B) power-voltage profile of a fuel cell

The contribution of each type of overpotential to the shape of voltage-current curve is shown in **Figure 1.3**. η_{act} describes the activation energy required to overcome the energy barrier of the electrode-electrolyte interface. η_{iR} is related to the overall resistance of the fuel cell including electrodes, electrolyte and electrical connections. η_{mt} origins from the mass transfer limitation of the reaction at limiting currents. For a fuel cell with a defined E_{eq}, **Equation 1.3** suggests the strategy to maximize cell voltage through minimization of all three types of potential. For example, ohmic overpotential can be improved by using high conductivity material. Mass transfer overpotential can be improved by incorporating porous electrode materials to facilitate substrate diffusion.

The power (or power density) is another key parameter to evaluate fuel cell performances. Power profile of EBFC is often described by power-voltage curve (**Figure 1.3**), which is obtained from fuel cell polarization curve, based on the equation:

$$P = E \times I \qquad (1.4)$$

Polarization curve is often obtained by performing linear sweep voltammetry (LSV). In order to limit the non-faradaic current contribution originated from the electrode capacitance, slow scan rates (≤ 1 mV s^{-1}) are required for the LSV method. Another

option is to use the backward scan of a cyclic voltammetry (CV) performed at a slow scan rate. A decent experiment to measure power should show a small difference between the forward and the backward of CV scan. This provides crucial information on diffusion limitation that could arise during experiments. Finally, to exclude the power from capacitive current contribution and verify no diffusion limitation is encountered, power profile can also be obtained by connecting to a variable load or applying a series of constant potential. The value of the potential/current will be recorded after stabilization of the system (depending on the time scale needed during fuel cell operation).

Power-voltage curve reveals the maximum power delivered by the fuel cell and the optimum operation voltage for maximizing power density. However, such representation often hides useful information such as diffusion limitation and does not display short circuit currents. As a summary, an ideal fuel cell characterization profile should include both its polarization and its power curve.

1.1.3.4 Electroanalytical techniques for fuel cell characterization

Different electroanalytical methods can be used to study the bioelectrochemical reactions taking place at the bioelectrode in the fuel cell. Electrochemical measurement cells can be arranged in two-electrode or three-electrode configuration. Cathode and anode are usually characterized separately as working electrode in three-electrode configuration to obtain the individual characteristics of the half-cells constituting the whole device. When the fuel cell is assembled, it is usually studied in two-electrode configuration with cathode as the working electrode and anode as the combined reference/counter electrode to ensure a positive readout of the OCV. Hence, the monitored reaction being the reduction reaction, negative currents will be recorded in this configuration. The behavior of the fuel cell in two-electrode configuration can then be explained by combining the characteristics of the two electrodes. Commonly used techniques for characterization of EFCs are potential sweep, amperometry and potentiometry techniques.

For potential sweep techniques, the potential of the working electrode is modified linearly from potential E_1 to E_2 with a constant scan rate (mV s^{-1}). When the potential reaches E_2, the scan stops for linear sweep voltammetry while for cyclic voltammetry, a reverse scan is performed typically back to the initial potential E_1. The resulting current between the counter electrode and the working electrode is recorded to

produce the current-voltage curve called linear sweep voltammogram or cyclic voltammogram. **Figure 1.4** shows linear sweep voltammograms of a bioanode and a biocathode, which are usually used to demonstrate the enzyme catalyzed oxidation and reduction reaction. The polarization curves allow for the determination of the onset redox potential for electrocatalysis, the anodic or cathodic overpotentials and the identification of the limiting electrode in the system (electrode showing the lowest current value).

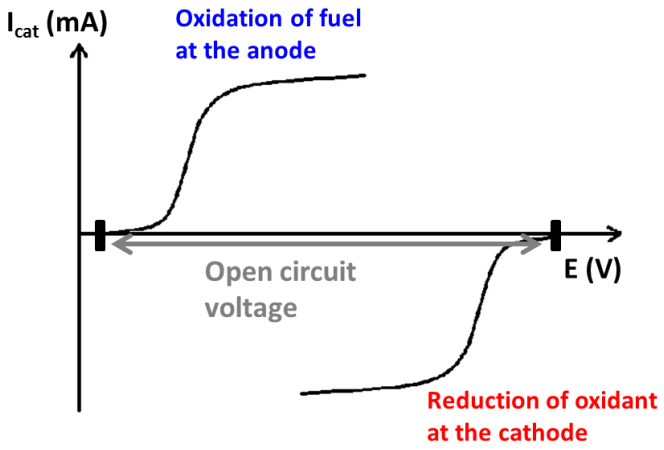

Figure 1.4 Polarization curves and characteristics of a biocathode and a bioanode tested separately in a three-electrode setup

Cyclic voltammetry can be used to examine the electron transfer kinetics of redox processes. For example, for immobilized redox mediators, the electron transfer rate constant can be evaluated by analysis of the peak potential separation and scan rate dependence using the Laviron method.[63]

The current curves recorded using potential sweep techniques contain faradaic current and non-faradaic current as the potential is shifted continuously. Amperometry is often used to eliminate the capacitive current contribution by applying a constant potential and record the current as a function of time. The current-time curve, also named as chronoamperograms, can be used to examine the operational stability of the electrode.

High surface area nanomaterials are often used to construct bioelectrodes, which possess high electrostatic double-layer capacitance. Therefore, the EFC displays charge storing capability. The capacitance of the device can be characterized using galvanostatic charge-discharge measurements. A constant current is applied to charge and discharge the EFCs and the capacitance can be calculated based on the following

equation:

$$C = I\Delta t/\Delta U \qquad (1.5)$$

where ΔU is the voltage drop during the interval Δt in **Equation 1.5** when current I is applied.

1.2 Enzymes immobilization and wiring

1.2.1 Immobilization methods

In the bioelectrochemistry research field, enzyme immobilization is an essential step in studying electron transfer processes of biological entities. By immobilizing enzymes on the designed electrode support, enzyme stability and electron transfer efficiency can be improved. More specifically, to increase the overall power performance of enzymatic fuel cells, the amount of enzyme immobilized on the electrode support plays a crucial role. For bioelectronics applications, enzyme immobilization is often required to build miniaturized devices. Different types of immobilization techniques have been studied and are summarized in the following section (**Figure 1.5**).[64]

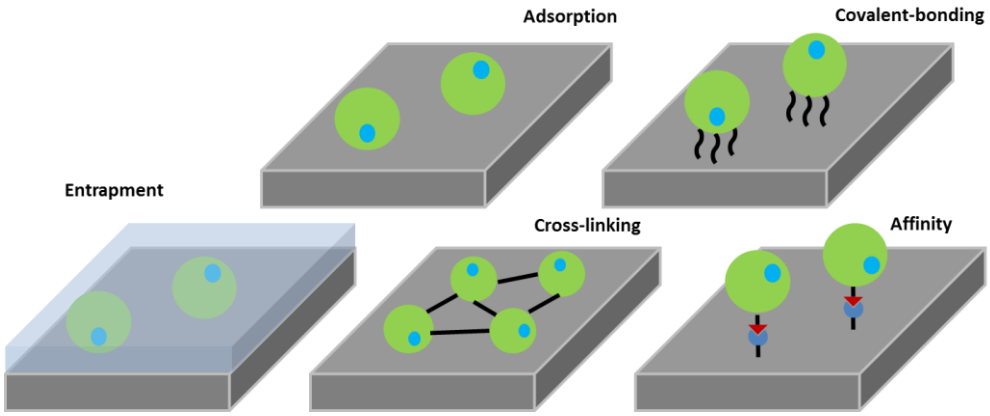

Figure 1.5 Schematic representations of different enzymes immobilization methods

1.2.2.1 Adsorption

An easy and widely used method is simple adsorption of enzymes on electrode surface. It can be done by directly drop-casting enzyme solution on electrode surface or by incubating the electrode in enzyme solution.[65] Enzymes are immobilized on the electrode *via* the non-specific interactions involving hydrophobic, electrostatic or Van der Waal's forces between the biomolecule and the electrode. This method is simple and most of the enzyme activity is preserved due to low change of the

three-dimensional structure of the protein. However, it suffers from poor stability with enzyme desorption from the surface due to the weak interaction forces.

1.2.2.2 Covalent bonding

Enzymes can also be immobilized through covalent coupling to the electrode surface *via* chemical reaction to form stable covalent bond. This method can prevent enzyme detachment from the surface but it also irreversibly decrease enzyme activity due to chemical modification or conformational change of the biomolecule.[66]

To form covalent bonds between the enzyme and the electrode surface, prior modification of the electrode support is necessary to introduce functional groups such as diazonium,[67] carboxylic,[68] thiol,[69] epoxy[70] and maleimide[71] groups. These functional groups can be coupled to the primary amine groups of lysine residues or thiol groups of cysteine residues. Recently, site-specific modifications of enzymes have been developed in order to immobilize the redox proteins with favored orientation.[72]

1.2.2.3 Encapsulation

Encapsulation involves the immobilization of enzymes in a three-dimensional matrix. Conducting polymers have been widely used for enzyme encapsulation.[73] By mixing enzymes and the monomers together, followed by chemical or electrochemical oxidation, enzymes can be retained in the three-dimensional environment. **Figure 1.6** shows examples of commonly used conducting polymers. Other encapsulation matrices consist of non-conductive polymers (chitosan,[74] alginate,[73] Nafion,[75]…) and inorganic sol-gel composite.[76] Encapsulation is able to retain large amount of enzymes and preserve enzyme activity in the matrix, however, the thickness of the film needs to be well-tuned to reduce diffusion barrier. In addition, enzyme leakage and detachment of the matrix can also happen and therefore limit electrode stability.

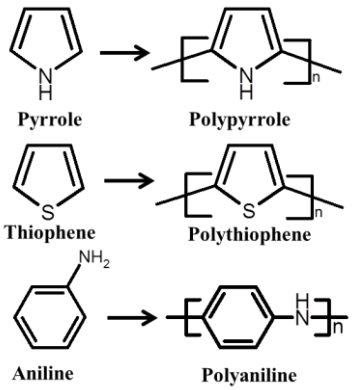

Figure 1.6 Structures of polymerizable monomers to form conductive polymer through chemical or electrochemical oxidation

1.2.2.4 Cross-linking

Enzyme cross-linking is done through the assistance of a cross-linker to form aggregates on the electrode surface. Commonly used cross-linkers such as glutaraldehyde, poly(ethylene glycol) diglycidyl ether (PEGDGE) and activated ester can cross-link enzymes by reacting with the amine groups of enzymes (**Figure 1.7**). Recently, there are growing interests in using redox polymer hydrogel as enzyme immobilization and wiring matrix.[77,78] PEGDGE is able to cross-link with the amine groups of enzymes and imidazole groups of redox polymers. This method has the similar drawback as covalent bonding, both of which can denature enzymes leading to lower enzyme activity.

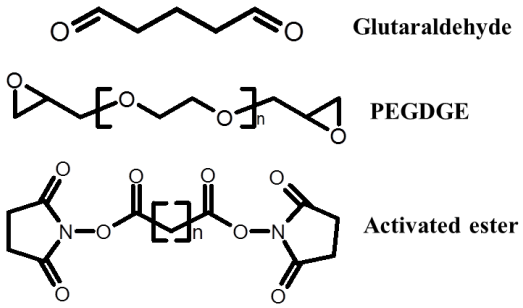

Figure 1.7 Structures of coupling agents commonly used for protein cross-linking

1.2.2.5 Affinity

Another method to immobilize enzymes exploits affinity interactions between specific functional groups on the electrode surface and affinity tags on proteins to form supramolecular assemblies. Affinity interactions rely on affinity partners that can bind selectively together. Commonly affinity partners include lectin-carbohydrate,[79] avidin-biotin,[80] cyclodextin-adamantane[81] and metal cation-chelator.[82] One of the biggest advantages of this method is its selectivity, which allows controlled enzyme immobilization. Besides, the non-covalent nature of affinity bonding can minimize conformational change of enzymes. However, this method involves relative complex procedures for the introduction of specific tags for affinity interactions.

1.2.2 Electron transfer mechanism

One of the key parameters to construct high-power enzymatic biofuel cells is to

achieve efficient electron transfer or "electrical wiring" between enzymes and electrodes. Electron transfer between the redox centers of the enzymes and the electrodes can be realized *via* direct electron transfer (DET) and mediated electron transfer (MET), as illustrated in **Figure 1.8**. According to Marcus's theory, DET rate decreases exponentially as the electron donor-acceptor distance increases.[83] To realize DET between enzyme and the electrode, the electron transfer path should be as short as possible. Page *et al.* demonstrated that electron tunneling is unlikely to happen for redox centers spacing beyond 14 Å in the proteins.[84] In many cases, the redox centers of enzymes are deeply buried in the protein structure and therefore electron transfer *via* DET is not always possible.[85]

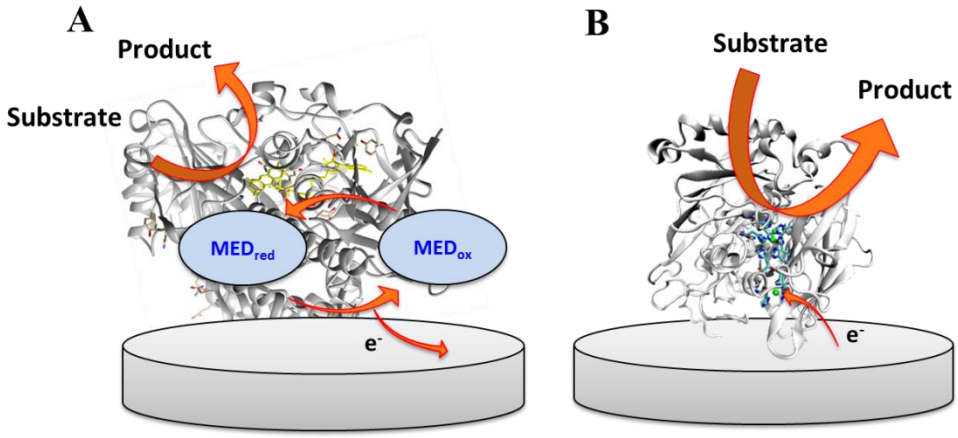

Figure 1.8 Schematic representations of different electron transfer mechanisms: (A) mediated electron transfer and (B) direct electron transfer

Figure 1.8A shows the mechanism for MET. Small redox molecules are used to shuttle electrons between the enzyme active site and the electrode. For anodic reaction, the enzyme first reacts with the substrate (the fuel) and is re-oxidized to its active form by the mediator. Hence at the end of a single catalytic cycle, the redox mediator is in its reduced state. Then, the mediator re-oxidizes to its oxidized state by transferring electrons to the electrode. If the potential is chosen correctly, the mediator is continuously cycling between its reduced and its oxidized forms, producing anodic current for the substrate oxidation. Dioxygen, a natural electron acceptor for many oxidases, has been used as mediator in the first generation biosensors.[86,87] To avoid the oxygen competition with cathode reduction reaction, artificial molecules are explored as mediators. Common mediators include ferrocene derivatives, ferricyanide, transition metal complexes, organic dyes, quinone compounds and conducting salts.[88] When choosing redox mediators for the enzymes, the following criteria should be

fulfilled:[88]

1. The redox mediator must have a suitable redox potential close to the redox potential of the enzyme active site. The redox potential should have an optimized compromise between electromotive driving force and onset potential of the reaction. In addition, if the redox potential is too positive (negative for cathode), it may lead to unwanted catalysis with other species in the electrolyte.
2. The reaction of the mediator should be reversible.
3. The mediator should be stable in both reduced and oxidized forms.
4. The mediator should exhibit fast electron exchange rate with both the enzyme and the electrode.

The most important group of redox mediators in EFC and biosensors are probably osmium-based complexes, which are introduced by Heller *et al.* in his pioneer works and are still fast developing.[89,90] Based on the ligand used for complexation of osmium, they can be anchored on the polymer backbone to form redox polymer. Osmium-based redox polymers are the most widely used redox polymers and their redox potential can be finely tuned through modification of the ligand around the coordination sphere.[91,92] The polymer backbones can be modified to introduce additional functionalities such as cross-linking capability with enzymes. Besides electron transfer, redox polymers also serve as immobilization matrix, where enzymes are immobilized through entrapment, chemical cross-linking or electrostatic interactions depending on the nature of the polymer. Other redox polymers bearing ferrocene,[93] cobaltocene,[94] viologen,[95] phenothiazine[96] and quinone[97] have also been reported and used for fabrication of bioelectrodes.

Mediators can operate in solution or immobilized on the electrode surface. To eliminate the need for compartmentalization, both mediators and enzymes are usually immobilized on the electrode surface. Although MET can provide high current by increasing the number of enzymes electrically connected to the electrode, the utilization of mediator inevitably reduces the cell voltage as the reaction takes place at potentials where the redox mediator can undergo to its own oxidation or reduction for the oxidation of the fuel or the reduction of the oxidant, respectively. The use of these mediators also introduces concerns such as mediator stability and toxicity.

Another electron transfer mechanism is the direct electron transfer (DET, **Figure 1.8B**), for which the electrode works as the electron acceptor/donor without the need of an additional redox mediator. This means the reactions start at the standard

apparent potential of the redox proteins, which can maximize the cell voltage. DET is regarded as a more elegant way for electron transfer as it eliminates the issues with mediator listed before. This mechanism was first discovered in 1977, when DET with cytochrome c on different electrodes were reported.[98,99] Later, more enzymes were discovered to be able to undergo DET (e.g. laccase,[59] fructose dehydrogenase,[100] cellobiose dehydrogenase[101]). In general, DET is more likely to be realized on enzymes with redox active metallocenters (iron-sulfur cluster,[102] copper center,[103] heme[104]) located near their surface due to a shorter distance for electron tunneling.[104] To realize DET on electrode surface, the material and modification of the conductive material also play a crucial role. Although DET method is reasonably simple, only a maximum of monolayer enzymes can be connected. If the immobilized enzymes are not well oriented with their active sites facing electrode surface, some of the enzymes will not be involved in the bioelectrocatalytic reaction, therefore reducing the catalytic current. Hence, the electrode surface has to be tailored in order to improve the specific orientation of the enzyme. DET between bilirubin oxidase and the tailored electrode surface is described in section 1.2.4.4.

1.2.3 Solubilized mediator and enzymes

In most biosensors and enzymatic biofuel cells, both mediators and enzymes are immobilized on electrode surface to achieve high power densities. However, with this configuration, it is difficult to restore the bioelectrode activity when either mediators or enzymes gradually lose their activity.[105] As previously described, enzymes desorption and leaching can be an issue for the non-covalent immobilization methods while covalent attachment of enzymes can reduce enzyme activity. High surface coverage of mediators and enzymes are also necessary to increase power densities, but it can be hard to achieve on limited electrode surface area, and also expensive for commercial concern.

An alternative solution is to use solubilized mediators and enzymes, which opens up a new strategy to prolong EFC lifetime through exchange of the fuel cell compartment with fresh active materials. The main advantage of this approach is that a solution-based biofuel cells can be envisioned where nanostructured electrodes, mediators and enzymes solution will be introduced inside a chamber permeable to substrates. Previously, Bourourou *et al.* developed a buckypaper electrode modified

with a bis-pyrene derivative redox mediator, the electrode showed high catalytic current density and stability up to two weeks with laccase in solution.[106] Zhu and Zhang reported a high power density closed biobattery with non-immobilized enzymes and mediators.[107]

In this thesis, a polymeric nanoparticle based system is developed by using redox-active glyconanoparticles as supramolecular vehicles for introduction of a wide range of insoluble catalyst-mediators into fuel cells. The use of redox active glyconanoparticles also avoids the issue of cross-reaction between cathodic and anodic compartment due to their large size. The development and characterization of the redox active glyconanoparticels and their use as electron shuttles for biocatalytic reaction are detailed in Chapter 5.

1.2.4 Common enzymes used in EFCs

Enzymes are biological macromolecules that work as catalysts in metabolic processes in living organisms. Most enzymes are proteins, only a few are RNA molecules. The enzyme activity and specificity rely on their three-dimensional structures, with an active site surrounded by a protein backbone. In bioelectrochemistry, oxidoreductases are a group of enzymes that are particularly interesting as they catalyze redox reactions. These enzymes usually require the use of either inorganic ions or organic molecules as their cofactors. The different enzymes used for the design of EFCs during this PhD program will be introduced in the following section.

1.2.4.1 Glucose oxidase

Glucose oxidase (GOx, EC 1.1.3.4) has been one of the most studied oxidoreductases due to its application for glucose oxidation since the development of the first glucose biosensor[108] and the first glucose based EFC.[17] GOx is a flavoprotein consisting of two identical subunits with a flavin adenine dinucleotide (FAD) cofactor (**Figure 1.9**). GOx can be naturally produced by some fungi and insects, among which the most commonly used one is GOx from *Aspergillus Niger* (*An*).[109] Crystal structure of *An*GOx revealed a three dimensional size of 7×5.5×8 nm and a molecular weight of 160 kDa.[110] This enzyme catalyzes the two-electron oxidation of β-D-glucose to $_D$-glucono-δ-lactone (which then hydrolyzes to gluconic acid) with the FAD reduced to $FADH_2$. Molecular oxygen is a natural electron acceptor utilized by GOx to

re-oxidize $FADH_2$ back to FAD with the generation of hydrogen peroxide. The reaction is written as below:

$$\beta\text{-D-glucose} + FAD(GOx) \rightarrow \text{D-glucono-}\delta\text{-lactone} + FADH_2(GOx)$$

$$FADH_2(GOx) + O_2 \rightarrow FAD(GOx) + H_2O_2 \qquad (1.6)$$

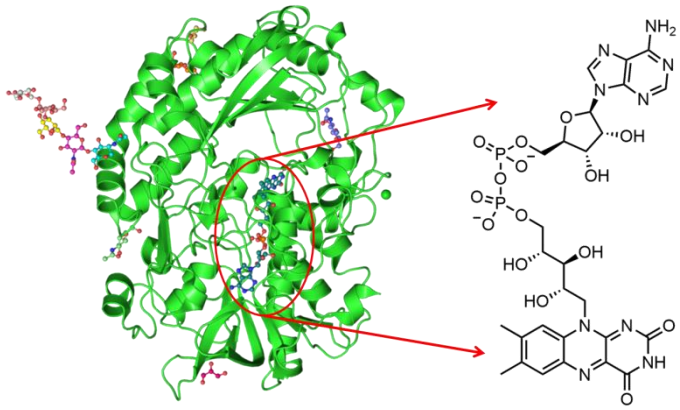

Figure 1.9 Structure of (left) a subunit of the dimeric *An*GOx (PDB: 3QVP) and (right) the FAD cofactor

For electron transfer between GOx and the electrode, many researchers have claimed to establish DET on various electrode materials (e.g. carbon nanotube,[111] graphene[112]) based on the observed redox peaks of FAD/$FADH_2$ near -0.47 V *vs.* SCE at pH 7.0. However, structural studies suggest that DET is difficult to achieve due to the fact that GOx is highly glycosylated (16% to 25%)[113] and there is a long electron transfer distance between FAD and the periphery of GOx (13 to 18 Å).[114] The redox peaks observed probably belong to free FAD disassociated from GOx, which are no longer enzymatically active.[115] Nevertheless, there are some convincing reports on realizing DET on GOx. Liu *et al.* achieved DET by modifying the electrode with molecular wire.[116] In 2009, Courjean *et al.* deglycosylated *An*GOx and observed glucose oxidation at a low potential of -0.49 V *vs.* Ag/AgCl at pH 7.4.[117] Given the difficulty of achieving DET, most glucose based bioelectrodes utilize MET for electrical connection with the electrode. In 1993, Ohara *et al.* demonstrated the use of osmium-based redox polymer $[Os(2,2'\text{-bipyridine})_2(PVI)_{10}Cl]^{+/2+}$ for electrical wiring of GOx.[77] Since then, osmium based redox polymers have been widely used as mediators for GOx to construct glucose biosensor and glucose biofuel cell.[118–120]

1.2.4.2 Flavin adenine dinucleotide-dependent glucose dehydrogenase

Although GOx has been the gold standard for glucose biosensing, its oxygen sensitivity can cause measurement errors due to oxygen level fluctuations in sample

solutions (saliva, plasma, blood, *etc*…). There has been growing interest in developing glucose biosensors using FAD-dependent glucose dehydrogenase (FAD-GDH, EC 1.1.99.10) for the two electron oxidation of glucose.[121–123] This enzyme contains the same cofactor as GOx, but it does not use O_2 as electron acceptor, which makes it an ideal candidate for all type of self-monitoring glucose biosensors or glucose biofuel cell. FAD-GDH can be expressed in bacteria, fungi and some insects. Among them, fungi-derived FAD-GDH has received the most attention due to its substrate specificity toward glucose.[32] Fungal FAD-GDHs have been identified in *Aspergillus* subspecies with structures ranging from monomeric to homooligomeric.[121,124] Despite broad interest in FAD-GDH, structural information and their availability remain scarce.

A recent study by Yoshida *et al.* reveals that the overall structure and active site structure of fungal FAD-GDH are similar to GOx, with the FAD cofactor deeply buried below the protein surface (~1.4 nm).[125] Therefore, it is difficult to achieve DET between FAD-GDH and the electrode. Muguruma *et al.* reported DET signal of FAD-GDH on gold electrode by using de-bundled single walled carbon nanotube.[126] It is worth noting that in this work the oxidation current in the presence of glucose starts at a relatively high potential of 0.1 V *vs.* Ag/AgCl at pH 7.4.

Unlike the fungal enzyme, bacteria-derived FAD-GDH is possible to undergo DET as it contains a cytochrome-complex electron-transfer subunit.[32] However, bacterial-derived FAD-GDH has broad substrate specificity and requires protein engineering to improve its substrate specificity towards glucose.[32] Yamashita *et al.* developed a DET-type amperometric glucose biosensor disposable strip, where a FAD-GDH mutant produced by site-directed mutagenesis was immobilized on screen-printed carbon electrode.[127]

For MET between FAD-GDH and the electrode, various mediators can be used such as those used for GOx bioelectrodes,[118] but may display different catalytic rate constant. In the work of Tsuruoka *et al.*, bimolecular oxidation rate of different mediators (quinones and phenothiazines) in solution were studied and the results showed that the rate constant for FAD-GDH are higher than that for GOx.[128] Redox polymers are also used as mediators for FAD-GDH. For example, a high current FAD-GDH based bioelectrode was constructed using osmium-based redox polymers.[78] Milton *et al.* designed a new redox polymer hydrogel by immobilizing naphthoquinone (NQ) onto linear polyethyleneimine.[97] The NQ-based redox polymer

was used as mediators for FAD-GDH and produced a catalytic current of 1.95 mA cm^{-2} with an onset potential of -0.25 V *vs.* SCE at pH 6.5. Interestingly, GOx did not show catalytic current with the same redox polymer.

1.2.4.3 Lactate oxidase

Lactate oxidase (LOx, EC 1.1.3.2) has been used predominantly to construct biosensors for the detection of lactate and recently has also been used in enzymatic biofuel cell applications.[129,130] LOx is a flavoprotein with a cofactor of flavin mononucleotide (FMN). Similar to GOx, it catalyzes the oxidation of its natural substrate $_L$-lactate to pyruvate using oxygen as electron acceptor.[33] The enzyme catalyzed reaction is written as below:

$$_L\text{-lactate} + \text{FMN(LOx)} \rightarrow \text{Pyruvate} + \text{FMNH}_2\text{(LOx)}$$
$$\text{FMNH}_2\text{(LOx)} + \text{O}_2 \rightarrow \text{FMN(LOx)} + \text{H}_2\text{O}_2 \qquad (1.7)$$

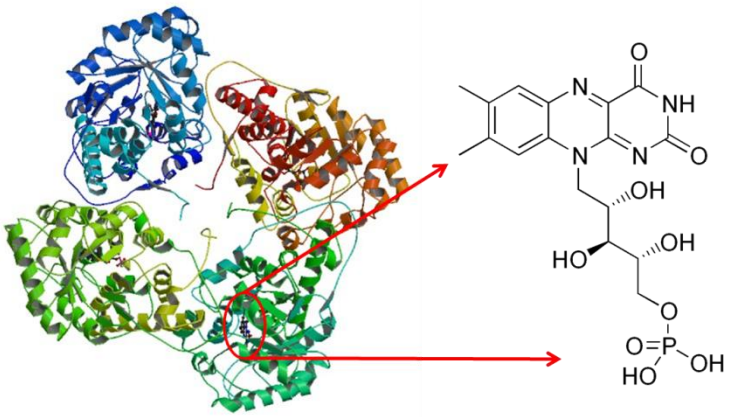

Figure 1.10 Structure of (left) LOx from *Aerococcus viridans* (PDB ID: 2DU2)[131] and (right) the FMN cofactor

This enzyme has been identified in bacterial sources and the most studied one is derived from *Aerococcus viridans*.[132] The crystal structure of LOx reveals that the enzyme is a tetramer made of four monomers with almost identical structure (**Figure 1.10**).[131] For electron transfer between LOx and the electrode, artificial electron mediators are preferred to avoid the generation of hydrogen peroxide. Different mediators have been reported to construct lactate biosensors and biofuel cells, such as ferrocene derivatives,[133] phenoxazine derivatives,[134] tetrathiafulvalene,[135] osmium complexes,[136] *etc.*

1.2.4.4 Bilirubin oxidase

Bilirubin oxidase (BOx, EC 1.3.3.5) is able to oxidize its natural substrate bilirubin using oxygen as electron acceptor.[137] In the construction of biocathode, electrode acts as substrate feeding BOx with electrons for the concomitant bioelectrocatatlytic reduction of dioxygen to water. This enzyme has been identified in *Myrothecium verrucaria* (*Mv*BOx),[138] *Trachyderma tsunodae* (*Tt*BOx),[139] *Magnaporthae orizae* (*Mo*BOx)[140] and *Bacillus pumilus* (*Bp*BOx),[141] among which *Mv*BOx is the most commercialized and studied one. Structural analysis revealed that BOx contains two distinct active sites made of four copper ions, which are classified into type 1, type 2 and a pair of type 3 coppers based on optical and magnetic properties (**Figure 1.11**).[137] It is widely accepted that electrons from substrates or electrodes are first transferred to the mononuclear site (T1), and then are transferred to the trinuclear site (T2/T3) where the four-electron four-proton oxygen reduction takes place.

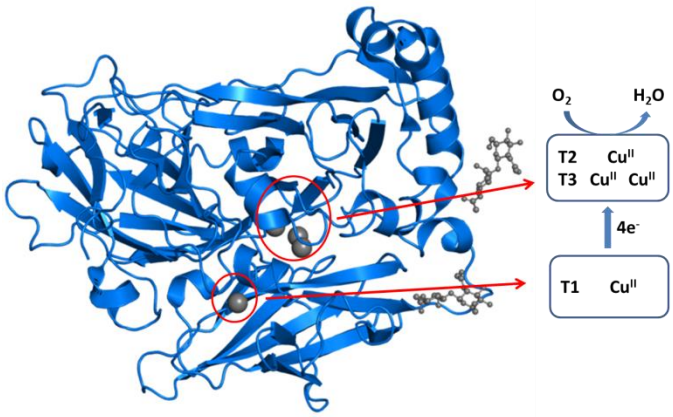

Figure 1.11 Structure of (left) BOx from *Myrothecium verrucaria* (PDB ID: 2xll) and (right) the T1 and T2/T3 active sites

BOx was first reported for oxygen reduction by Tsujimura *et al.* and has now been widely used for biocathode in BFC due to its high activity at mild pH and its tolerance towards chloride.[60] The benefit of using BOx compared to Pt-based catalyst is their ability to reduce oxygen with low overpotential. The redox potential of the T1 center at neutral pH is around 0.67 V *vs.* NHE,[142] which is close to the thermodynamic value of the O_2/H_2O couple (0.82 V *vs.* NHE at 25 °C, pH 7).[143] Electron transfer between BOx and the electrode was first realized using ABTS (2,2'-azino-bis(3-ethylbenzothiazoline-6-sulphonic acid)) as the soluble redox mediator.[60] Redox mediators used for BOx are still mainly osmium based redox

polymers due to their success use with glucose oxidase.[144–147] Conducting polymer doped with redox mediators, protein, and inorganic/organic compounds can also be used as mediator for BOx for the oxygen reduction.[148–150]

BOx, as a MCO, is well known for its relative ease to establish direct electron transfer connection. BOx is a relatively small enzyme with a molecular weight of about 60 kDa and its T1 site is close to the protein surface. Hence, DET is possible.[142] DET for BOx was first reported in 2004 with adsorbed BOx on carbon electrodes.[151] In the early stage of research, current densities were small as enzymes were randomly oriented, leading to dispersion of the intermolecular electron transfer rate constant.[152] Later, nanomaterials with high surface area were exploited to increase the amount of enzymes immobilized on electrode surface, including CNT, graphene and gold nanostructures.[112,153,154] To further improve the electron transfer efficiency, it is necessary to optimize the orientation of the enzyme to minimize the distance between the T1 site and the electrode surface and to increase the amount of oriented species. Strategies to control and optimize the orientation are developed by taking advantage of the hydrophilic substrate binding site of *Mv*BOx near its T1 center, which exhibits positive charge at acidic and neutral pH.[155] Negatively charged electrode surface has shown to be beneficial for DET of BOx due to electrostatic interaction.[156] Substrates of BOx such as bilirubin,[155,157,158] syringaldazine[159] and porphyrins also promoted the favorable orientation of the enzyme.[160] Several studies show that for efficient orientation of *Mv*BOx, the anchoring molecules on electrode surface should possess both aromatic structures and negative charges.[160,161] The DET of BOx on carbon nanostructured electrodes is more detailed in Chapter 2.

1.3 Carbon nanotube buckypaper electrode

As previously described, the key challenge in enzymatic biofuel cells is to achieve effective electron transfer between enzymes and the electrode, therefore the design of the electrodes for immobilization of biocatalysts is of significant importance. The amount of active enzyme immobilized on the electrode surface plays a crucial role in determining the overall performance of EFCs. The basic requirements for electrode material are high conductivity, chemical stability, ease of modification, availability, *etc*. For immobilization of enzymes, properties including: 1-high surface area, 2-mechanical stability, 3-high porosity and 4-biocompatibility are also expected. The development of carbon nanostructured electrodes has greatly inspired the enzymatic

biofuel cells research field as they possess high conductivity, high surface area, wide electrochemical window and can be (easily) functionalized.[162,163] Examples of carbon nanomaterials include carbon nanotubes (CNTs), graphene and carbon nanoparticles, among which CNTs are the most widely used materials to date for bioelectrode fabrication.[164]

1.3.1 Structures and properties of carbon nanotube

Carbon nanotubes are allotropes of carbon materials, which can be envisaged as sheets of graphene rolled up into cylinders. CNTs were first discovered by Radushkevich and Lukyanovich in 1952, who presented an image of hollow graphitic fibers with diameters of 50 nm.[165] In 1991, Iijima discovered multi-walled CNTs (MWCNTs) in the electric arc burned rods.[166] The predictions of the excellent electronic properties of single-walled CNTs (SWCNTs) by Mintmire, Dunlap and White,[167] finally brought awareness of CNTs into the scientific community.

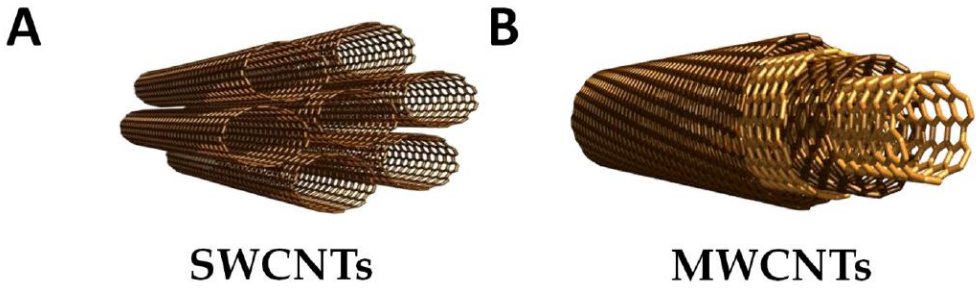

Figure 1.12 Schematic representations of molecular structure of (A) SWCNTs and (B) MWCNTs

According to the number of graphene layers, CNTs can be categorized into single-walled and multi-walled CNTs (**Figure 1.12**). For SWCNTs, the structure can be described by the tube chirality, which is defined by the indices (*n* and *m*) of their chiral vector, C_h, defined as:

$$C_h = na_1 + ma_2 \qquad (1.8)$$

where *n* and *m* are integers, a_1 and a_1 are unit vectors of the hexagonal lattice. SWCNTs can be further divided into “arm-chair” type ((n, n), m = n), “zig-zag” type ((n, 0), m = 0), and chiral type ((n, m), n ≠ m) based on their chirality. The definition of the chiral vector and the three types of SWCNTs are depicted in **Figure 1.13**. The chirality of SWCNTs also determines the electronic property, which can be semiconducting or metallic according to electronic band structure calculations.[168] When (2n+m)/3 is an integer, the tube is considered as metallic, otherwise it is seen as

semiconducting.[168] This suggests that around two thirds of SWCNTs are semiconductor-type and others are metallic type. MWCNTs composed of multiple concentric graphene layers are generally considered as metallic if at least one CNT sheet is metallic.

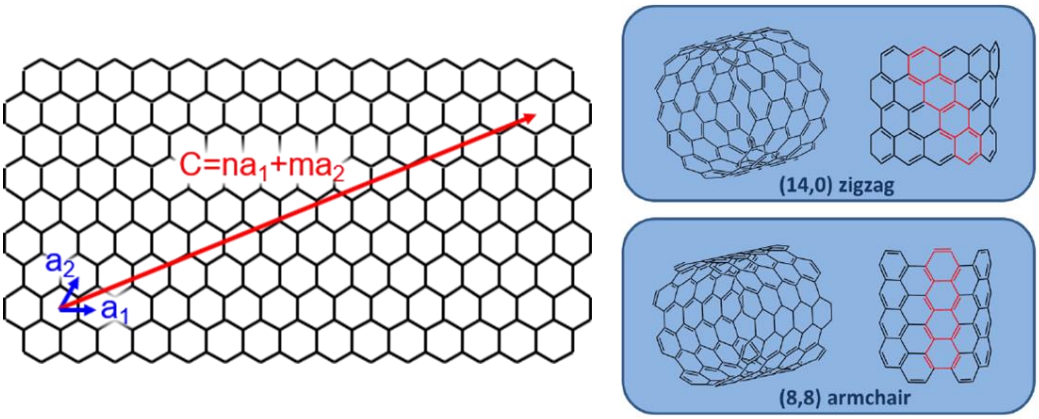

Figure 1.13 Schematic representations of rolling directions of graphene layer to form "arm-chair", "zig-zag" and chiral types of CNTs

The ideal structure of CNT consists of only sp^2 carbon atoms, while the synthesis process will introduce different levels of structural defects and impurities and, therefore, affects properties of the produced tubes.[169] CNTs can be fabricated in large quantities by arc discharge,[170] laser ablation,[171] high-pressure carbon monoxide (HiPco) method[172] and chemical vapor deposition (CVD).[173] Among them, CVD is the most widely used method due to its low cost, ease of scale-up and high yield.[174] This method utilizes metal catalysts (*i.e.* iron) and carbon-containing source (*i.e.* methane) in the high temperature chambers, where the decomposition of hydrocarbon takes place and nanotubes grow at the metal catalysts sites.[173] CNTs produced using CVD method can contain impurities including metal catalyst residues, nanographite and amorphous carbon.[175]

Given the excellent electrical conductivity, thermal conductivity and mechanical strength of CNTs, they have been widely evaluated for various applications, especially for electronic and energy devices. CNTs have been used in lithium ion batteries as additives in anode composites to improve capacity and cycling efficiency due to their high conductivity and their high surface-to-volume ratio.[176] By using CNTs as the backbone in anodes, the structural degradation caused by volume change in the charging and discharging process can be alleviated.[177] CNTs are excellent

electrode materials for electrochemical supercapacitor due to their high surface area, resulting in high electrostatic double-layer capacitance.[178] CNTs also find wide applications in proton exchange membrane fuel cells mainly to reduce platinum loading while maintaining the fuel cell efficiency.[179]

The unique features of CNTs are also beneficial for applications in bioelectrochemistry. The entangled CNTs can form three-dimensional network with high porosity to immobilize enzymes. More importantly, the thin diameter of CNTs makes it possible to approach the active site of enzymes, therefore promoting direct electron transfer.[180] However, the hydrophobic nature of CNTs makes them insoluble and they tend to aggregate in most solvents, resulting in more difficulty in handling. Organic solvents or surfactants are required to make stable dispersion of CNTs for practical applications.[181]

1.3.2 Modification and functionalization of carbon nanotubes

As previously described for enzyme immobilization, modifications of the electrode surface are often required to introduce different functionalities to favor orientation and immobilization of enzymes for applications, *e.g.* in bioelectrochemical devices. Functionalization of CNTs has been intensively studied for the development of EFCs in recent years.[182,183] The functionalization methods of CNTs are divided into covalent and non-covalent methods.

1.3.2.1 Covalent method

Covalent method is based on introduction of functional groups by creating stable covalent bonds on the CNT surface, which simultaneously changes the hybridization of carbon atoms from sp^2 to sp^3. The generated functionalities can improve solubility of CNTs and enable further coupling reactions. However, covalent method will inevitably damage their π-conjugated system, which impacts the electronic and mechanical properties of CNTs. In general, there are two approaches to covalently modify CNTs: esterification or amidation of oxidized CNTs and addition chemistry of CNTs.[184]

Oxidation treatment is a widely used method to generate oxygen-containing groups such as carboxylic, carbonyl and hydroxyl groups along the sidewall or at the pre-existing defect sites at the open ends of CNTs (**Figure 1.14**).[185] Chemical oxidation involves placing CNTs in oxidative mediums under reflux conditions with

acidic (sulfuric acid and nitric acid) or basic (ammonium hydroxide/hydrogen peroxide) agents.[186] There are many studies on investigating the effect of oxidation conditions on the structure of CNTs.[185–187] In brief, the degradation of the CNT structure increases with the duration and hardness of the oxidation treatment.[187] The as-generated carboxylic groups can undergo further modification through esterification or amidation (**Figure 1.14**).

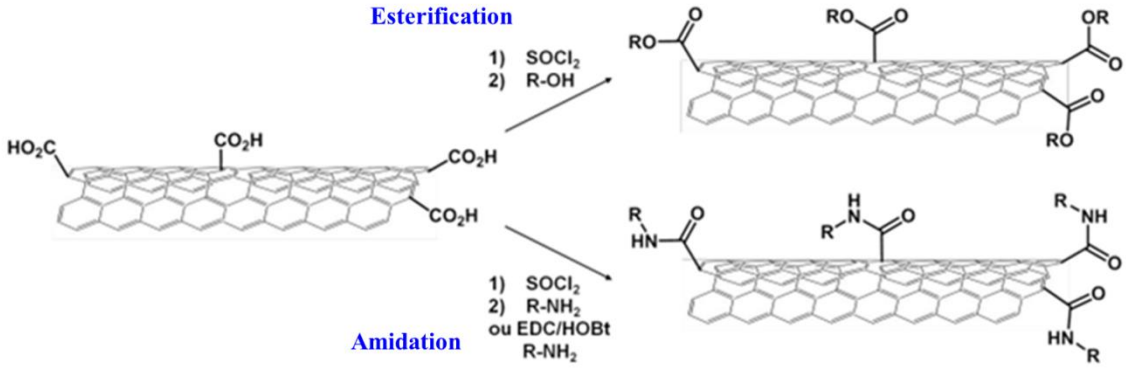

Figure 1.14 Scheme of esterification or amidation (peptide coupling if R is an enzyme) of oxidized CNTs

Another covalent method for functionalization of this carbon material is the use of addition chemistry to attach organic moieties to the sidewall of CNTs. This method contains diverse reactions such as cycloaddition,[188] addition of carbenes[189] and nitrenes,[190,191] radical additions,[190,192] *etc*... Among them, the most investigated reaction is the radical addition of phenyldiazonium (**Figure 1.15)**. The popularity of this reaction is related to its versatility and high functionalization degree.[193] The grafted phenyl groups can then be used to react with other molecules.

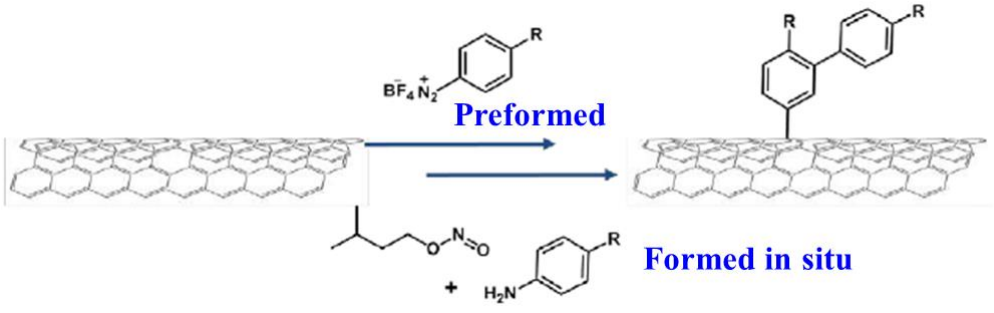

Figure 1.15 Modification of CNTs by radical addition of a diazonium salt preformed or formed in situ

1.3.2.2 Non-covalent method

Compared with covalent method, non-covalent method takes advantage of the sp^2 carbon atoms on the sidewall of CNTs, which can facilitate strong interaction between

CNTs and delocalized electron rich-systems (aromatic compounds, polymers) through π-π stacking and hydrophobic interactions.[194–196] This method is very attractive as it preserves the sp^2 structure of CNTs, therefore maintaining high electronic properties. Aromatic compounds such as pyrene, anthracene, porphyrins and their derivatives have been used to functionalize CNT sidewalls in a simple and effective way (**Figure 1.16**). Chen *et al.* reported the first non-covalent functionalization of CNT sidewall using 1-pyrenebutanoic acid-*N*-hydroxysuccinimidyl ester (PBSE).[197] The activated ester group of this bi-functional agent was utilized to react with amine groups of proteins in order to immobilize them at the surface of the CNTs. This strategy is still widely used for protein immobilization in various applications.[198–200] Non-covalent functionalization allows facile immobilization of redox mediators with aromatic rings on CNT surface *via* π-π stacking interaction,[201,202] which can be used to construct bioelectrode by immobilizing redox enzymes on the electrode.

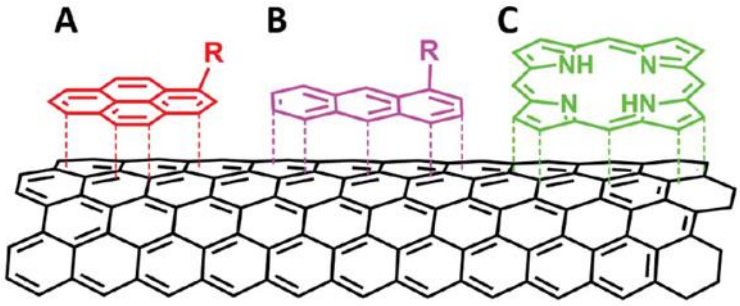

Figure 1.16 "π- π stacking" interaction between aromatic compounds and the CNT sidewall: A) pyrene derivative; B) anthracene derivative and C) porphyrin derivative

The second method to non-covalently functionalize CNTs regards the use of polymers, which can introduce new properties to the CNT/polymer composite depending on their structural features. This method has been used to form polymer-wrapped CNTs to improve the dispersion of CNT in different solvents.[194] The composite material can be obtained by simply mixing the CNT and the polymer together. Polymer film can also be electrogenerated onto the CNT surface through electropolymerization. A well-studied example is polypyrrole as the resulting composite can improve conductivity and can serve as immobilization matrix for biosensor and biofuel cell applications.[73,203–205]

1.3.3 Carbon nanotube buckypaper

Although the use of CNT has greatly improved biofuel cell performance in terms of

power density, the difficulty of manipulating CNT has impeded the industrialization and commercialization of CNT-based bioelectronics devices. In most studies, bioelectrodes have been constructed by depositing CNTs on supporting substrates such as glassy carbon electrode to form thin films of several μm. For practical applications, efforts have been made to improve the manipulation of CNTs by shaping them into different forms of self-supporting electrodes, such as yarns,[206,207] pellets[46] and papers.[208]

CNT pellet electrodes are obtained by mechanical compression of CNTs-based slurry. Often, the CNTs are readily compressed in the presence of enzymes and other components such as electron mediators to ensure efficient distribution/homogenization of the redox species in the whole electrode volume.[46] Most high power EFC reported to date are based on CNT pellet bioelectrodes.[46,47,209] Although the three-dimensional pellet can host high number of enzymes and mediators, the deeper volume of the pellet (as opposed to the interfacial layer with the electrolyte) is hard to access due to inherent hydrophobicity of the tubes. Furthermore, slow mass transfer across the volume (substrate consumption during electrocatalysis) can lead to low volumetric power density.

In this thesis, a paper-like material called buckypaper is chosen as the material to construct bioelectrodes. Buckypaper (BP) is a thin sheet made from entangled CNTs held together by π-π interactions.[210,211] For free-standing BP without the need of a supporting material, the thickness should be at least over 80 μm.[210] In 1998, Rinzler *et al.* demonstrated the first so-called "buckypaper" made by vacuum filtration method.[208] BP was first fabricated as a way to manipulate SWCNTs, but has now been used as promising materials in different applications such as supercapacitors,[212] fuel cells,[213] sensors and biosensors,[214,215] *etc*... BP is thin, lightweight, highly conductive and easy to manipulate, which makes it a great candidate as the electrode material for body interfaced bioelectronic devices. More importantly, BP is self-supporting, therefore differentiates from other carbon nanostructured materials.

1.3.3.1 Fabrication of buckypaper

Given the attractive capabilities of BP, different methods have been developed for the fabrication of BP. For example, CNT drawing, membrane filtration and casting techniques are frequently found in literature reports.[216,217] Buckypaper sheets are also now commercially available from several manufacturers. Commercial buckypapers

from Buckeye Composite have been widely reported for the construction of bioelectrodes.[218–220] Buckypapers can also be obtained from US Research Nanomaterials Inc.,[221] NanoLab Inc.[222] and Nanocomp Technologies Inc..[223,224] However, the fabrication method of commercial buckypaper remains undisclosed and these materials can display very different physical properties depending on the manufacturers.

In laboratories, buckypapers are mostly fabricated using membrane filtration technique, which is straightforward and can be easily set up. CNTs are first dispersed in non-aqueous solvents such as *N*,*N*-dimethylformamide (DMF) and *N*-methyl-2-pyrrolidinone (NMP), followed by sonication to form stable and homogeneous suspension.[225] Subsequently, the suspension is filtered through a microporous membrane under negative pressure. After removal of the residual solvent by a drying process, a self-supporting buckypaper can be obtained by carefully peeling the CNTs film from the membrane. Although this method is simple and widely used in research, there are challenges in the quality and reproducibility of buckypapers. There are many factors that can affect the formation of buckypaper including the suspension homogeneity, sonication procedure, type and length of CNT, functionality and purity of the CNTs and the following treatments after filtration.[216,226]

An advantage of using membrane filtration method is the possibility to include a wide range of molecules to the suspension to prepare functionalized buckypaper. For example, buckypaper made from pristine CNTs is fragile and typically requires reinforcement, which can be realized through the addition of a polymer[227,228] or pyrene-derivatives.[106] The pyrene moieties of the modifiers can form strong interaction with the CNTs and therefore improve cross-linking of CNTs.

1.3.4 Buckypaper-based biofuel cell

In 2011, Hussein *et al.* demonstrated the first results of buckypaper as electrode material for enzymatic fuel cells.[180,210,229] A buckypaper biocathode was fabricated by immobilizing *Mv*BOx and ABTS onto BP films, achieving a current density of 0.235 mA cm^{-2} in air-saturated buffer solution.[210] The authors compared the oxygen reduction performance of BP electrodes prepared from as-received CNTs and acid-treated CNTs. In contrast, the BP electrode made from acid-treated CNTs showed a 1.5-fold higher electrocatalytic current, which were attributed to more hydrophilic

electrode surface.[210] The same group later developed a laccase-modified biocathode with a catalytic current of 0.422 mA cm^{-2}, indicating the feasibility of using BP as favorable electrode material for enzyme immobilization.[180]

Narváez Villarrubia *et al.* demonstrated the first buckypaper bioanode for $_L$-malate oxidation using a porcine NAD-dependent malate dehydrogenase (NAD-MDH).[230] The BP was fabricated *via* filtration method with SWCNTs and was then modified with poly methylene green (PMG) by electropolymerization. With the enzyme and the cofactor NAD^+ in solution, the bioanode shows a current density of 22 μA cm^{-2} in the presence of 160 mmol L^{-1} $_L$-malate.

Buckypaper based enzymatic fuel cell was first reported by Halámková *et al.* in 2012.[218] The described glucose/O_2 EFC consisted of a PQQ-GDH bioanode and a *Trametes versicolor* laccase (*Tv*Lac) biocathode. Both electrodes were fabricated using commercial buckypaper (Buckeye Composites). The EFCs was implanted in a living snail.[218] An OCV of 0.53 V and a power density of 30 μW cm^{-2} were obtained. This is the first demonstration of BP-based fuel cell implanted in a living creature. Later the same group reported implantable EFCs operating in clams,[231] rats,[232] lobsters[233] and oranges.[234]

Reid *et al.* prepared a lactate biofuel cell integrated on contact lens using commercial buckypaper, demonstrating the flexibility of this material.[235] The biofuel cell with a NAD-dependent lactate dehydrogenase (NAD-LDH) bioanode and a *Mv*BOx biocathode was tested in synthetic tear solution (~ 3 mmol L^{-1} lactate) and delivered an OCV of 0.41 V and a power density of 8 μW cm^{-2}. The state-of-art characteristics and performances of buckypaper based enzymatic fuel cells are summarized in **Table 1.4**.

Nowadays the development of EFCs is progressing towards flexible, stretchable and miniaturized electrodes for practical applications.[19] The representative applications of EFCs are described in the following section.

Table 1.4 Characteristics and performances of buckypaper-based enzymatic biofuel cell

Year	Buckypapeper	Anodic enzyme	Cathodic enzyme	Substrate	OCV / V	Power / μW cm^{-2}	Reference
2012	Commercial BP	PQQ-GDH (DET)	*Tv*Lac (DET)	Glucose, O_2 (snail)	0.53	30	Halámková *et al.*[218]

2013	Commercial BP	PQQ-GDH (DET)	*Tv*Lac (DET)	Glucose, O_2 (lobster)	0.54	640	MacVittie *et al.*[233]
2014	Lab-made BP	GOx (MET)	*Mv*BOx (DET)	5 mmol L^{-1} glucose, O_2 (air-saturated)	0.55	26	Bunte *et al.*[236]
2014	Commercial BP	PQQ-GDH (DET)	*Mv*BOx (DET)	10 mmol L^{-1} glucose, O_2 (air-saturated)	0.7	107	Scherbahn *et al.*[237]
2014	Commercial BP	NAD-GDH (MET)	*Mv*BOx (DET)	Mono/disaccharides O_2	1.8 (3 in series)	0.18 (mW mg^{-1} GDH)	Narváez Villarrubia *et al.*[238]
2015	Commercial BP	NAD-LDH (MET)	*Mv*BOx (DET)	3 mmol L^{-1} lactate, O_2 (tear)	0.41	8	Reid *et al.*[235]
2016	Commercial BP	PQQ-GDH (DET)	*Mv*BOx (DET)	Glucose, O_2 (urine)	0.4	13	Göbel *et al.*[220]
				Glucose, O_2 (saliva)	0.67	19	
2016	Commercial BP	NAD-GDH (MET)	*Mv*BOx (DET)	100 mmol L^{-1} glucose, O_2	0.59	1070	Narváez Villarrubia *et al.*[239]
2017	Lab-made BP	FAD-GDH (MET)	*Tv*Lac (DET)	30 mmol L^{-1} glucose, O_2-saturated	1.4 (2 in series)	326	Hou and Liu[240]
2019	Commercial BP	PQQ-GDH (DET)	*Mv*BOx (DET)	Glucose, O_2 (slug)	0.31	200 μW cm^{-3}	Bollella *et al.*[241]

1.4 Applications of enzymatic fuel cells

1.4.1 Implantable glucose/O_2 biofuel cells

Since the development of enzymatic biofuel cells, one of the most promising applications of EFCs is to replace lithium batteries as power sources for implantable electronic devices. These lithium batteries pose safety concerns to human body and requires complex surgery for replacement.[242,243] Glucose/O_2 EFCs instead are energy conversion devices that can harvest energy directly from the human body due to the constant occurrence of "fuels" in body fluids. However, the power performance of EFCs is limited by the low concentration of glucose (~ 5.5 mmol L^{-1} in blood[44]) and oxygen (~ 90 μmol L^{-1} in plasma,[244] ~ 50 μmol L^{-1} in cerebrospinal fluid[245]) in human

physiological fluids.

The first successful *in vivo* demonstration of implantable enzymatic biofuel cell was operated in a grape, which was developed by Mano and Heller.[246] In this work, both bioanode and biocathode were electrically wired by osmium redox polymer. Miyake[247] and Yoshino[248] also reported several implantable biofuel cells operated in grapes and showed improved power density by using ketjen black and CNTs as electrode materials, respectively.

A major breakthrough in this field is the successful implantation of EFCs in rats.[249] Compared with previous work in living plants, implantation in animals are much more difficult. On one hand, the electrical connection needs to be robust enough to withstand the strain caused by the movement of the animals. On the other hand, biocompatible packaging of the device is required to avoid inflammatory responses. The collaborative work of Cosnier and Cinquin demonstrated the first implantable EFC operated in a living mammal. The device composed of a GOx bioanode and a polyphenol oxidase (PPO) biocathode was placed in the retroperitoneal space of the rat.[249] Followed by this pioneer work, various implanted devices have been reported (**Table 1.5**). It is worth noting that to date most EFCs are developed based on CNT nanostructured materials to improve power performance.

With the emerging of ultra-lower power consumption electronic devices and nanomaterial-based EFCs, glucose/O_2 EFCs remain attractive as energy harvesters. Another challenge in this field is the device lifetime, which should be longer than current commercial batteries used for implantable medical devices (IMDs). For example, the lithium iodide cells used for pacemaker usually lasts 7-8 years.[250] The state-of-art power and lifetime of the reported implantable glucose/O_2 EFCs are summarized in **Table 1.5**. The current lifetime is still far below the requirement for IMD application. For successful implantation of EFCs, intensive studies are also required to understand and improve the biocompatibility of bioelectrodes. This includes factors such as cytotoxicity, carcinogenicity, genotoxicity, irritation and sensitization, *etc*.[251]

Table 1.5 Characteristics and performances of implantable glucose/O_2 enzymatic biofuel cells

Year	Organism	Electrode material	Anodic enzyme	Cathodic enzyme	Power / μW cm^{-2}	Stability	Reference

2003	Grape	Carbon fiber	GOx (MET)	BOx (MET)	430	1 week (in buffer)[119]	Mano *et al.*[246]
2010	Rat	Graphite	GOx (MET)	PPO (MET)	1.5	11 days	Cinquin *et al.*[249]
2011	Rabbit ear	Ketjen black	GDH (MET)	BOx (DET)	1310	/	Miyake *et al.*[247]
2012	Cockroach	Carbon rod	TOx[a]|GOx (MET)	BOx (MET)	55	2.5 hours	Rasmussen *et al.*[252]
2013	Grape	CNT forest	GOx (MET)	BOx (DET)	1750	/	Yoshino *et al.*[248]
2013	Rat	CNT Pellet	GOx (DET)	Lac (DET)	193	9 days	Zebda *et al.*[253]
2013	Rat	Commercial BP	PQQ-GDH (DET)	Lac (DET)	0.17	/	Castorena-Gonzalez *et al.*[232]
2013	Lobster	Commercial BP	PQQ-GDH (DET)	Lac (DET)	640	/	MacVittie *et al.*[233]
2013	Rat	Au microwire	CDH (DET)	BOx (DET)	2	Several hours	Andoralov *et al.*[254]
2018	Rabbit	CNT Pellet	GOx (MET)	Lac (DET)	16 $\mu W\ cm^{-3}$	2 months	El Ichi-Ribault *et al.*[255]
2019	Slug	Commercial BP	PQQ-GDH (DET)	BOx (DET)	200 $\mu W\ cm^{-3}$	/	Bollella *et al.*[241]

[a] Trehalase oxidase

1.4.2 Wearable lactate/O_2 biofuel cells

Wearable electronics has recently drawn significant attention especially wearable biomedical devices for health and fitness monitoring.[256] Since most wearable devices are skin-worn, the device should be small, flexible, robust and do not pose any burden to the wearer. One of the key challenges in this field is to develop a power source that is equally flexible and robust to meet the requirements of wearable devices. Epidermal lactate/O_2 EFCs are attractive candidates as they can harvest energy

directly from sweat. Human sweat contains several metabolites such as glucose, alcohol, lactate and cortisol.[257] Among them, lactate is exploited as the biofuel due to its high concentration in sweat, with an average level of 14 mmol L^{-1} in sweat.[257]

The first successful demonstration of wearable sweat-based enzymatic biofuel cell was developed by Jia *et al.* in 2013.[135] In this work, screen printing technology was used to fabricate electrode on the tattoo paper using CNT ink. The anode and cathode were modified with lactate oxidase and platinum black, respectively. This work demonstrates the first prototype device that can harvest energy from on-body experiments. Later, the same group developed a textile-based biofuel cell by screen-printing the biofuel cell onto detachable care label.[258] Obviously, textile-based biofuel cells enable large area of device integration and different combinations to increase voltage and power. Besides sweat, lactate in tears has also been exploited as fuels by integration of a biofuel cell onto contact lens.[235]

Although lactate based biofuel cells show promise as power sources for wearable electronics, multiple issues need to be addressed for further development. The biggest challenge is the limited power density due to the low catalytic performance of the bioanode. Intensive studies are necessary to develop a more efficient mediator for lactate oxidase. Secondly, current devices are not able to deliver stable power output due to factors such as fluctuations of lactate level and inhibitors present in sweat. Similar to implantable EFCs, lifetime and biocompatibility are also major challenges that limit the use of wearable lactate enzymatic fuel cell.

1.4.3 Biosupercapacitor

Enzymatic fuel cell is an attractive energy conversion device with an inherent issue of low power density. In contrast, supercapacitor is an energy storage device that can deliver high power pulses. A new hybrid device called “self-charging electrochemical biocapacitor” has been proposed by Pankratov *et al.* to construct hybrid device that contains an enzymatic fuel cell and an electrochemical capacitor.[259] The principle is to release power by high-current pulse discharge while the capacitor self-charges through enzymatic conversion of the substrate. The device developed by Pankratov *et al.* in 2014 was based on dual-feature electrodes. One side of the graphite electrode was modified with polyaniline for pseudocapacitance while the other side was immobilized with enzyme for biocatalytic reaction. Upon pulse discharge, the device

reached a power density of 1.2 mW cm^{-2} at 0.38 V. In principle, most EFCs can also work as self-charging electrochemical biocapacitor without modification. Agnès *et al.* reported the first supercapacitor/biofuel cell hybrid device based on double layer capacitance.[260] This new concept shows promises to overcome the low power density issues in traditional enzymatic biofuel cells.

References

1. Jaouen, F., Lefèvre, M., Dodelet, J.-P. & Cai, M. Heat-Treated Fe/N/C Catalysts for O2 Electroreduction: Are Active Sites Hosted in Micropores? *J. Phys. Chem. B* **110**, 5553–5558 (2006).
2. Stariha, S. *et al.* PGM-free Fe-N-C catalysts for oxygen reduction reaction: Catalyst layer design. *Journal of Power Sources* **326**, 43–49 (2016).
3. Wachsman, E. D. & Lee, K. T. Lowering the Temperature of Solid Oxide Fuel Cells. *Science* **334**, 935–939 (2011).
4. Logan, B. E. *et al.* Microbial Fuel Cells: Methodology and Technology. *Environ. Sci. Technol.* **40**, 5181–5192 (2006).
5. Logan, B. E. & Regan, J. M. Microbial Fuel Cells—Challenges and Applications. *Environ. Sci. Technol.* **40**, 5172–5180 (2006).
6. Bhatnagar, D., Xu, S., Fischer, C., L. Arechederra, R. & D. Minteer, S. Mitochondrial biofuel cells : expanding fuel diversity to amino acids. *Physical Chemistry Chemical Physics* **13**, 86–92 (2011).
7. Rasmussen, M., Abdellaoui, S. & Minteer, S. D. Enzymatic biofuel cells: 30 years of critical advancements. *Biosensors and Bioelectronics* **76**, 91–102 (2016).
8. Gil, G.-C. *et al.* Operational parameters affecting the performannce of a mediator-less microbial fuel cell. *Biosensors and Bioelectronics* **18**, 327–334 (2003).
9. Heijne, A. T. *et al.* Identifying charge and mass transfer resistances of an oxygen reducing biocathode. *Energy & Environmental Science* **4**, 5035–5043 (2011).
10. Bergel, A., Féron, D. & Mollica, A. Catalysis of oxygen reduction in PEM fuel cell by seawater biofilm. *Electrochemistry Communications* **7**, 900–904 (2005).
11. Rabaey, K. *et al.* Cathodic oxygen reduction catalyzed by bacteria in microbial fuel cells. *ISME J* **2**, 519–527 (2008).
12. Pant, D. *et al.* An introduction to the life cycle assessment (LCA) of bioelectrochemical systems (BES) for sustainable energy and product generation: Relevance and key aspects. *Renewable and Sustainable Energy Reviews* **15**, 1305–1313 (2011).
13. Logan, B. E. & Rabaey, K. Conversion of Wastes into Bioelectricity and Chemicals by Using Microbial Electrochemical Technologies. *Science* **337**, 686–690 (2012).
14. Rozendal, R. A., Hamelers, H. V. M., Rabaey, K., Keller, J. & Buisman, C. J. N. Towards practical implementation of bioelectrochemical wastewater treatment. *Trends in Biotechnology* **26**, 450–459 (2008).
15. Ieropoulos, I., Greenman, J. & Melhuish, C. Urine utilisation by microbial fuel cells; energy fuel for the future. *Physical Chemistry Chemical Physics* **14**, 94–98 (2012).
16. Andrea Ieropoulos, I. *et al.* Pee power urinal – microbial fuel cell technology field trials in the context of sanitation. *Environmental Science: Water Research & Technology* **2**, 336–343 (2016).
17. Yahiro, A. T., Lee, S. M. & Kimble, D. O. Bioelectrochemistry: I. Enzyme utilizing bio-fuel cell studies. *Biochimica et Biophysica Acta (BBA) - Specialized Section on Biophysical Subjects* **88**, 375–383 (1964).

18. Xiao, X. *et al.* Tackling the Challenges of Enzymatic (Bio)Fuel Cells. *Chem. Rev.* (2019) doi:10.1021/acs.chemrev.9b00115.
19. Luz, R. A. S., Pereira, A. R., de Souza, J. C. P., Sales, F. C. P. F. & Crespilho, F. N. Enzyme Biofuel Cells: Thermodynamics, Kinetics and Challenges in Applicability. *CHEMELECTROCHEM* **1**, 1751–1777 (2014).
20. Truesdale, G. A. & Downing, A. L. Solubility of Oxygen in Water. *Nature* **173**, 1236–1236 (1954).
21. Arechederra, R. & Minteer, S. D. Organelle-based biofuel cells: Immobilized mitochondria on carbon paper electrodes. *Electrochimica Acta* **53**, 6698–6703 (2008).
22. Arechederra, R. L., Boehm, K. & Minteer, S. D. Mitochondrial bioelectrocatalysis for biofuel cell applications. *Electrochimica Acta* **54**, 7268–7273 (2009).
23. Germain, M. N., Arechederra, R. L. & Minteer, S. D. Nitroaromatic Actuation of Mitochondrial Bioelectrocatalysis for Self-Powered Explosive Sensors. *J. Am. Chem. Soc.* **130**, 15272–15273 (2008).
24. L. Maltzman, S. & D. Minteer, S. Mitochondrial-based voltammetric sensor for pesticides. *Analytical Methods* **4**, 1202–1206 (2012).
25. De Michele, R., Carimi, F. & Frommer, W. B. Mitochondrial biosensors. *The International Journal of Biochemistry & Cell Biology* **48**, 39–44 (2014).
26. Masa, J. & Schuhmann, W. Electrocatalysis and bioelectrocatalysis – Distinction without a difference. *Nano Energy* **29**, 466–475 (2016).
27. Marchitti, S. A., Brocker, C., Stagos, D. & Vasiliou, V. Non-P450 aldehyde oxidizing enzymes: the aldehyde dehydrogenase superfamily. *Expert Opinion on Drug Metabolism & Toxicology* **4**, 697–720 (2008).
28. Ludwig, R., Harreither, W., Tasca, F. & Gorton, L. Cellobiose Dehydrogenase: A Versatile Catalyst for Electrochemical Applications. *ChemPhysChem* **11**, 2674–2697 (2010).
29. Theorell, H. & McKEE, J. S. M. Mechanism of Action of Liver Alcohol Dehydrogenase. *Nature* **192**, 47–50 (1961).
30. Ferry, J. G. Formate dehydrogenase. *FEMS Microbiol Rev* **7**, 377–382 (1990).
31. Adachi, T., Kaida, Y., Kitazumi, Y., Shirai, O. & Kano, K. Bioelectrocatalytic performance of d-fructose dehydrogenase. *Bioelectrochemistry* **129**, 1–9 (2019).
32. Ferri, S., Kojima, K. & Sode, K. Review of Glucose Oxidases and Glucose Dehydrogenases: A Bird's Eye View of Glucose Sensing Enzymes. *J Diabetes Sci Technol* **5**, 1068–1076 (2011).
33. Maeda-Yorita, K., Aki, K., Sagai, H., Misaki, H. & Massey, V. L-lactate oxidase and L-lactate monooxygenase: Mechanistic variations on a common structural theme. *Biochimie* **77**, 631–642 (1995).
34. Holbrook, J. J., Liljas, A., Steindel, S. J. & Rossmann, M. G. 4 Lactate Dehydrogenase. in *The Enzymes* (ed. Boyer, P. D.) vol. 11 191–292 (Academic Press, 1975).
35. Adams, M. W. W., Mortenson, L. E. & Chen, J.-S. Hydrogenase. *Biochimica et Biophysica Acta (BBA) - Reviews on Bioenergetics* **594**, 105–176 (1980).
36. Cosnier, S., J. Gross, A., Le Goff, A. & Holzinger, M. Recent advances on enzymatic glucose/oxygen and hydrogen/oxygen biofuel cells: Achievements and limitations. *Journal of*

Power Sources **325**, 252–263 (2016).

37. de Poulpiquet, A., Ranava, D., Monsalve, K., Giudici-Orticoni, M.-T. & Lojou, E. Biohydrogen for a New Generation of H2/O2 Biofuel Cells: A Sustainable Energy Perspective. *ChemElectroChem* **1**, 1724–1750 (2014).
38. Frey, M. Hydrogenases: Hydrogen-Activating Enzymes. *ChemBioChem* **3**, 153–160 (2002).
39. K. Jones, A., Sillery, E., J. Albracht, S. P. & A. Armstrong, F. Direct comparison of the electrocatalytic oxidation of hydrogen by an enzyme and a platinum catalyst. *Chemical Communications* **0**, 866–867 (2002).
40. De Lacey, A. L., Fernández, V. M., Rousset, M. & Cammack, R. Activation and Inactivation of Hydrogenase Function and the Catalytic Cycle: Spectroelectrochemical Studies. *Chem. Rev.* **107**, 4304–4330 (2007).
41. Wait, A. F., Parkin, A., Morley, G. M., dos Santos, L. & Armstrong, F. A. Characteristics of Enzyme-Based Hydrogen Fuel Cells Using an Oxygen-Tolerant Hydrogenase as the Anodic Catalyst. *J. Phys. Chem. C* **114**, 12003–12009 (2010).
42. Cracknell, J. A., Wait, A. F., Lenz, O., Friedrich, B. & Armstrong, F. A. A kinetic and thermodynamic understanding of O2 tolerance in [NiFe]-hydrogenases. *PNAS* **106**, 20681–20686 (2009).
43. Plumeré, N. *et al.* A redox hydrogel protects hydrogenase from high-potential deactivation and oxygen damage. *Nature Chemistry* **6**, 822–827 (2014).
44. Danaei, G. *et al.* National, regional, and global trends in fasting plasma glucose and diabetes prevalence since 1980: systematic analysis of health examination surveys and epidemiological studies with 370 country-years and 2·7 million participants. *The Lancet* **378**, 31–40 (2011).
45. Gregg, B. A. & Heller, Adam. Cross-linked redox gels containing glucose oxidase for amperometric biosensor applications. *Analytical Chemistry* **62**, 258–263 (1990).
46. Zebda, A. *et al.* Mediatorless high-power glucose biofuel cells based on compressed carbon nanotube-enzyme electrodes. *Nature Communications* **2**, 370 (2011).
47. Reuillard, B. *et al.* High power enzymatic biofuel cell based on naphthoquinone-mediated oxidation of glucose by glucose oxidase in a carbon nanotube 3D matrix. *Physical Chemistry Chemical Physics* **15**, 4892 (2013).
48. D. Milton, R., Giroud, F., E. Thumser, A., D. Minteer, S. & T. Slade, R. C. Hydrogen peroxide produced by glucose oxidase affects the performance of laccase cathodes in glucose/oxygen fuel cells: FAD-dependent glucose dehydrogenase as a replacement. *Physical Chemistry Chemical Physics* **15**, 19371–19379 (2013).
49. Clark, W. M. (William M. & 1884-1964. Oxidation-reduction potentials of organic systems. (1960).
50. Karyakin, A. A., Karyakina, E. E. & Schmidt, H.-L. Electropolymerized Azines: A New Group of Electroactive Polymers. *Electroanalysis* **11**, 149–155 (1999).
51. Le Goff, A., Holzinger, M. & Cosnier, S. Recent progress in oxygen-reducing laccase biocathodes for enzymatic biofuel cells. *Cellular and Molecular Life Sciences* **72**, 941–952 (2015).
52. Mano, N. & Edembe, L. Bilirubin oxidases in bioelectrochemistry: Features and recent findings.

Biosensors and Bioelectronics **50**, 478–485 (2013).

53. Solomon, E. I. *et al.* Copper Active Sites in Biology. *Chem. Rev.* **114**, 3659–3853 (2014).
54. Miura, Y. *et al.* Direct Electrochemistry of CueO and Its Mutants at Residues to and Near Type I Cu for Oxygen-Reducing Biocathode. *Fuel Cells* **9**, 70–78 (2009).
55. Reuillard, B. *et al.* Direct electron transfer between tyrosinase and multi-walled carbon nanotubes for bioelectrocatalytic oxygen reduction. *Electrochemistry Communications* **20**, 19–22 (2012).
56. Katz, E., Lioubashevski, O. & Willner, I. Magnetic Field Effects on Bioelectrocatalytic Reactions of Surface-Confined Enzyme Systems: Enhanced Performance of Biofuel Cells. *J. Am. Chem. Soc.* **127**, 3979–3988 (2005).
57. Heering, H. A. Analysis of protein film voltammograms as Michaelis–Menten saturation curves yield the electron cooperativity number for deconvolution. *Bioelectrochemistry* **87**, 58–64 (2012).
58. Elouarzaki, K. *et al.* Freestanding HRP–GOx redox buckypaper as an oxygen-reducing biocathode for biofuel cell applications. *Energy Environ. Sci.* **8**, 2069–2074 (2015).
59. Tarasevich, M. R., Yaropolov, A. I., Bogdanovskaya, V. A. & Varfolomeev, S. D. 293 - Electrocatalysis of a cathodic oxygen reduction by laccase. *Bioelectrochemistry and Bioenergetics* **6**, 393–403 (1979).
60. Tsujimura, S. *et al.* Bioelectrocatalytic reduction of dioxygen to water at neutral pH using bilirubin oxidase as an enzyme and 2,2′-azinobis (3-ethylbenzothiazolin-6-sulfonate) as an electron transfer mediator. *Journal of Electroanalytical Chemistry* **496**, 69–75 (2001).
61. Palmore, G. T. R. Biofuel Cells. in *Bioelectrochemistry* 359–375 (John Wiley & Sons, Ltd, 2008). doi:10.1002/9780470753842.ch10.
62. Bard, A. J. & Faulkner, L. R. *Electrochemical methods: fundamentals and applications*. (Wiley, 2001).
63. LAVIRON, E. GENERAL EXPRESSION OF THE LINEAR POTENTIAL SWEEP VOLTAMMOGRAM IN THE CASE OF DIFFUSIONLESS ELECTROCHEMICAL SYSTEMS. 10.
64. *Enzyme Stabilization and Immobilization*. vol. 1504 (Springer New York, 2017).
65. Armstrong, F. A. & Wilson, G. S. Recent developments in faradaic bioelectrochemistry. *Electrochimica Acta* **45**, 2623–2645 (2000).
66. Kowalewska, B. & Jakubow, K. The impact of immobilization process on the electrochemical performance, bioactivity and conformation of glucose oxidase enzyme. *Sensors and Actuators B: Chemical* **238**, 852–861 (2017).
67. Alonso-Lomillo, M. A., Yardimci, C., Domínguez-Renedo, O. & Arcos-Martínez, M. J. CYP450 2B4 covalently attached to carbon and gold screen printed electrodes by diazonium salt and thiols monolayers. *Analytica Chimica Acta* **633**, 51–56 (2009).
68. Gao, Y. & Kyratzis, I. Covalent Immobilization of Proteins on Carbon Nanotubes Using the Cross-Linker 1-Ethyl-3-(3-dimethylaminopropyl)carbodiimide—a Critical Assessment. *Bioconjugate Chem.* **19**, 1945–1950 (2008).
69. Rusmini, F., Zhong, Z. & Feijen, J. Protein Immobilization Strategies for Protein Biochips.

Biomacromolecules **8**, 1775–1789 (2007).

70. Mateo, C., Fernández-Lorente, G., Abian, O., Fernández-Lafuente, R. & Guisán, J. M. Multifunctional Epoxy Supports: A New Tool To Improve the Covalent Immobilization of Proteins. The Promotion of Physical Adsorptions of Proteins on the Supports before Their Covalent Linkage. *Biomacromolecules* **1**, 739–745 (2000).
71. Al-Lolage, F. A., Meneghello, M., Ma, S., Ludwig, R. & Bartlett, P. N. A Flexible Method for the Stable, Covalent Immobilization of Enzymes at Electrode Surfaces. *ChemElectroChem* **4**, 1528–1534 (2017).
72. Soellner, M. B., Dickson, K. A., Nilsson, B. L. & Raines, R. T. Site-Specific Protein Immobilization by Staudinger Ligation. *J. Am. Chem. Soc.* **125**, 11790–11791 (2003).
73. Ionescu, R. E., Abu-Rabeah, K., Cosnier, S. & Marks, R. S. Improved enzyme retention from an electropolymerized polypyrrole-alginate matrix in the development of biosensors. *Electrochemistry Communications* **7**, 1277–1282 (2005).
74. Ichi, S. E. *et al.* Chitosan improves stability of carbon nanotube biocathodes for glucose biofuel cells. *Chem. Commun.* **50**, 14535–14538 (2014).
75. Moore, C. M., Akers, N. L., Hill, A. D., Johnson, Z. C. & Minteer, S. D. Improving the Environment for Immobilized Dehydrogenase Enzymes by Modifying Nafion with Tetraalkylammonium Bromides. *Biomacromolecules* **5**, 1241–1247 (2004).
76. Li, J., Tan, S. N. & Ge, H. Silica sol-gel immobilized amperometric biosensor for hydrogen peroxide. *Analytica Chimica Acta* **335**, 137–145 (1996).
77. Ohara, T. J., Rajagopalan, Ravi. & Heller, Adam. Glucose electrodes based on cross-linked bis(2,2'-bipyridine)chloroosmium(+/2+) complexed poly(1-vinylimidazole) films. *Analytical Chemistry* **65**, 3512–3517 (1993).
78. Tsujimura, S., Murata, K. & Akatsuka, W. Exceptionally High Glucose Current on a Hierarchically Structured Porous Carbon Electrode with 'Wired' Flavin Adenine Dinucleotide-Dependent Glucose Dehydrogenase. *J. Am. Chem. Soc.* **136**, 14432–14437 (2014).
79. Bucur, B., Danet, A. F. & Marty, J.-L. Versatile method of cholinesterase immobilisation via affinity bonds using Concanavalin A applied to the construction of a screen-printed biosensor. *Biosensors and Bioelectronics* **20**, 217–225 (2004).
80. Esseghaier, C. *et al.* Impedance spectroscopy on immobilized streptavidin horseradish peroxidase layer for biosensing. *Sensors and Actuators B: Chemical* **134**, 112–116 (2008).
81. Holzinger, M., Bouffier, L., Villalonga, R. & Cosnier, S. Adamantane/β-cyclodextrin affinity biosensors based on single-walled carbon nanotubes. *Biosensors and Bioelectronics* **24**, 1128–1134 (2009).
82. Halliwell, C. M., Simon, E., Toh, C.-S., Bartlett, P. N. & Cass, A. E. G. Immobilisation of lactate dehydrogenase on poly(aniline)–poly(acrylate) and poly(aniline)–poly(vinyl sulphonate) films for use in a lactate biosensor. *Analytica Chimica Acta* **453**, 191–200 (2002).
83. Marcus, R. A. & Sutin, N. Electron transfers in chemistry and biology. *Biochimica et Biophysica Acta (BBA) - Reviews on Bioenergetics* **811**, 265–322 (1985).
84. Page, C. C., Moser, C. C., Chen, X. & Dutton, P. L. Natural engineering principles of electron tunnelling in biological oxidation–reduction. *Nature* **402**, 47–52 (1999).

85. Turner, A., Karube, I. & Wilson, G. S. *Biosensors : Fundamentals and Applications*. (Oxford University Press, 1987).
86. Updike, S. J. & Hicks, G. P. The Enzyme Electrode. *Nature* **214**, 986–988 (1967).
87. Guilbault, G. G. & Lubrano, G. J. An enzyme electrode for the amperometric determination of glucose. *Analytica Chimica Acta* **64**, 439–455 (1973).
88. Chaubey, A. & Malhotra, B. D. Mediated biosensors. *Biosensors and Bioelectronics* **17**, 441–456 (2002).
89. Heller, A. Electrical wiring of redox enzymes. *Acc. Chem. Res.* **23**, 128–134 (1990).
90. Heller, A. Electrical connection of enzyme redox centers to electrodes. *J. Phys. Chem.* **96**, 3579–3587 (1992).
91. Guschin, D. A., Castillo, J., Dimcheva, N. & Schuhmann, W. Redox electrodeposition polymers: adaptation of the redox potential of polymer-bound Os complexes for bioanalytical applications. *Anal Bioanal Chem* **398**, 1661–1673 (2010).
92. Pinyou, P. *et al.* Design of an Os Complex-Modified Hydrogel with Optimized Redox Potential for Biosensors and Biofuel Cells. *Chemistry – A European Journal* **22**, 5319–5326 (2016).
93. Knoche, K. L., Hickey, D. P., Milton, R. D., Curchoe, C. L. & Minteer, S. D. Hybrid Glucose/O_2 Biobattery and Supercapacitor Utilizing a Pseudocapacitive Dimethylferrocene Redox Polymer at the Bioanode. *ACS Energy Letters* **1**, 380–385 (2016).
94. Tapia, C. *et al.* Wiring of Photosystem I and Hydrogenase on an Electrode for Photoelectrochemical H2 Production by using Redox Polymers for Relatively Positive Onset Potential. *ChemElectroChem* **4**, 90–95 (2017).
95. Eng, L. H. *et al.* Viologen-Based Redox Polymer for Contacting the Low-Potential Redox Enzyme Hydrogenase at an Electrode Surface. *J. Phys. Chem.* **98**, 7068–7072 (1994).
96. Sokol, K. P. *et al.* Rational wiring of photosystem II to hierarchical indium tin oxide electrodes using redox polymers. *Energy Environ. Sci.* **9**, 3698–3709 (2016).
97. Milton, R. D. *et al.* Rational design of quinones for high power density biofuel cells. *Chem. Sci.* **6**, 4867–4875 (2015).
98. J. Eddowes, M. & O. Hill, H. A. Novel method for the investigation of the electrochemistry of metalloproteins: cytochrome c. *Journal of the Chemical Society, Chemical Communications* **0**, 771b–7772 (1977).
99. Yeh, P. & Kuwana, T. Reversible electrode reaction of cytochrome c. *Chem. Lett.* **6**, 1145–1148 (1977).
100. Murata, K., Suzuki, M., Kajiya, K., Nakamura, N. & Ohno, H. High performance bioanode based on direct electron transfer of fructose dehydrogenase at gold nanoparticle-modified electrodes. *Electrochemistry Communications* **11**, 668–671 (2009).
101. Tasca, F., Harreither, W., Ludwig, R., Gooding, J. J. & Gorton, L. Cellobiose Dehydrogenase Aryl Diazonium Modified Single Walled Carbon Nanotubes: Enhanced Direct Electron Transfer through a Positively Charged Surface. *Anal. Chem.* **83**, 3042–3049 (2011).
102. Kizling, M. & Bilewicz, R. Fructose Dehydrogenase Electron Transfer Pathway in Bioelectrocatalytic Reactions. *ChemElectroChem* **5**, 166–174 (2018).
103. Blanford, C. F., Heath, R. S. & Armstrong, F. A. A stable electrode for high-potential,

electrocatalytic O2 reduction based on rational attachment of a blue copper oxidase to a graphite surface. *Chem. Commun.* 1710–1712 (2007) doi:10.1039/B703114A.

104. Gorton, L. *et al.* Direct electron transfer between heme-containing enzymes and electrodes as basis for third generation biosensors. *Analytica Chimica Acta* **400**, 91–108 (1999).
105. Rubenwolf, S., Kerzenmacher, S., Zengerle, R. & von Stetten, F. Strategies to extend the lifetime of bioelectrochemical enzyme electrodes for biosensing and biofuel cell applications. *Appl Microbiol Biotechnol* **89**, 1315–1322 (2011).
106. Bourourou, M. *et al.* Freestanding redox buckypaper electrodes from multi-wall carbon nanotubes for bioelectrocatalytic oxygen reduction via mediated electron transfer. *Chemical Science* **5**, 2885 (2014).
107. Zhu, Z. & Zhang, Y.-H. P. Use of nonimmobilized enzymes and mediators achieved high power densities in closed biobatteries. *Energy Science & Engineering* **3**, 490–497 (2015).
108. Clark, L. C. & Lyons, C. Electrode Systems for Continuous Monitoring in Cardiovascular Surgery. *Annals of the New York Academy of Sciences* **102**, 29–45 (1962).
109. Wong, C. M., Wong, K. H. & Chen, X. D. Glucose oxidase: natural occurrence, function, properties and industrial applications. *Appl. Microbiol. Biotechnol.* **78**, 927–938 (2008).
110. Wohlfahrt, G. *et al.* 1.8 and 1.9 Å resolution structures of the -Penicillium amagasakiense and Aspergillus niger glucose oxidases as a basis for modelling substrate complexes. *Acta Cryst D* **55**, 969–977 (1999).
111. Cai, C. & Chen, J. Direct electron transfer of glucose oxidase promoted by carbon nanotubes. *Analytical Biochemistry* **332**, 75–83 (2004).
112. Shan, C. *et al.* Direct Electrochemistry of Glucose Oxidase and Biosensing for Glucose Based on Graphene. *Anal. Chem.* **81**, 2378–2382 (2009).
113. Prévoteau, A., Courjean, O. & Mano, N. Deglycosylation of glucose oxidase to improve biosensors and biofuel cells. *Electrochemistry Communications* **12**, 213–215 (2010).
114. Hecht, H. J., Schomburg, D., Kalisz, H. & Schmid, R. D. The 3D structure of glucose oxidase from Aspergillus niger. Implications for the use of GOD as a biosensor enzyme. *Biosensors and Bioelectronics* **8**, 197–203 (1993).
115. Wooten, M., Karra, S., Zhang, M. & Gorski, W. On the Direct Electron Transfer, Sensing, and Enzyme Activity in the Glucose Oxidase/Carbon Nanotubes System. *Anal. Chem.* **86**, 752–757 (2014).
116. Liu, G., Paddon-Row, M. N. & Justin Gooding, J. A molecular wire modified glassy carbon electrode for achieving direct electron transfer to native glucose oxidase. *Electrochemistry Communications* **9**, 2218–2223 (2007).
117. Courjean, O., Gao, F. & Mano, N. Deglycosylation of Glucose Oxidase for Direct and Efficient Glucose Electrooxidation on a Glassy Carbon Electrode. *Angewandte Chemie International Edition* **48**, 5897–5899 (2009).
118. Kavanagh, P. & Leech, D. Mediated electron transfer in glucose oxidising enzyme electrodes for application to biofuel cells: recent progress and perspectives. *Physical Chemistry Chemical Physics* **15**, 4859 (2013).
119. Mano, N., Mao, F. & Heller, A. A Miniature Biofuel Cell Operating in A Physiological Buffer. *J.*

Am. Chem. Soc. **124**, 12962–12963 (2002).

120. Barrière, F., Kavanagh, P. & Leech, D. A laccase–glucose oxidase biofuel cell prototype operating in a physiological buffer. *Electrochimica Acta* **51**, 5187–5192 (2006).
121. Tsujimura, S. *et al.* Novel FAD-Dependent Glucose Dehydrogenase for a Dioxygen-Insensitive Glucose Biosensor. *Bioscience, Biotechnology, and Biochemistry* **70**, 654–659 (2006).
122. Heller, A. & Feldman, B. Electrochemistry in Diabetes Management. *Acc. Chem. Res.* **43**, 963–973 (2010).
123. Zafar, M. N. *et al.* Characterization of different FAD-dependent glucose dehydrogenases for possible use in glucose-based biosensors and biofuel cells. *Anal Bioanal Chem* **402**, 2069–2077 (2012).
124. OGURA, Y. STUDIES ON THE GLUCOSE DEHYDROGENASE OF ASPERGILLUS ORYZAE. *The Journal of Biochemistry* **38**, 75–84 (1951).
125. Yoshida, H. *et al.* Structural analysis of fungus-derived FAD glucose dehydrogenase. *Scientific Reports* **5**, 13498 (2015).
126. Muguruma, H., Iwasa, H., Hidaka, H., Hiratsuka, A. & Uzawa, H. Mediatorless Direct Electron Transfer between Flavin Adenine Dinucleotide-Dependent Glucose Dehydrogenase and Single-Walled Carbon Nanotubes. *ACS Catalysis* **7**, 725–734 (2017).
127. Yamashita, Y. *et al.* Direct electron transfer type disposable sensor strip for glucose sensing employing an engineered FAD glucose dehydrogenase. *Enzyme and Microbial Technology* **52**, 123–128 (2013).
128. Tsuruoka, N., Sadakane, T., Hayashi, R. & Tsujimura, S. Bimolecular Rate Constants for FAD-Dependent Glucose Dehydrogenase from Aspergillus terreus and Organic Electron Acceptors. *International Journal of Molecular Sciences* **18**, 604 (2017).
129. Wang, J. Amperometric biosensors for clinical and therapeutic drug monitoring: a review. *Journal of Pharmaceutical and Biomedical Analysis* **19**, 47–53 (1999).
130. Bandodkar, A. J. & Wang, J. Wearable Biofuel Cells: A Review. *Electroanalysis* **28**, 1188–1200 (2016).
131. Umena, Y. *et al.* The crystal structure of l-lactate oxidase from Aerococcus viridans at 2.1Å resolution reveals the mechanism of strict substrate recognition. *Biochemical and Biophysical Research Communications* **350**, 249–256 (2006).
132. Rathee, K., Dhull, V., Dhull, R. & Singh, S. Biosensors based on electrochemical lactate detection: A comprehensive review. *Biochemistry and Biophysics Reports* **5**, 35–54 (2016).
133. Boujtita, M., Chapleau, M. & Murr, N. E. Enzymatic electrode for the determination of L-lactate. *Electroanalysis* **8**, 485–488 (1996).
134. Kulys, J., Schuhmann, W. & Schmidt, H.-L. Carbon-Paste Electrodes with Incorporated Lactate Oxidase and Mediators. *Analytical Letters* **25**, 1011–1024 (1992).
135. Jia, W., Valdés-Ramírez, G., Bandodkar, A. J., Windmiller, J. R. & Wang, J. Epidermal Biofuel Cells: Energy Harvesting from Human Perspiration. *Angewandte Chemie International Edition* **52**, 7233–7236 (2013).
136. Nieh, C.-H., Tsujimura, S., Shirai, O. & Kano, K. Electrostatic and steric interaction between redox polymers and some flavoenzymes in mediated bioelectrocatalysis. *Journal of*

Electroanalytical Chemistry **689**, 26–30 (2013).

137. Sakurai, T. & Kataoka, K. Basic and applied features of multicopper oxidases, CueO, bilirubin oxidase, and laccase. *The Chemical Record* **7**, 220–229 (2007).
138. Murao, S. & Tanaka, N. A New Enzyme "Bilirubin Oxidase" Produced by Myrothecium verrucaria MT-1. *Agricultural and Biological Chemistry* **45**, 2383–2384 (1981).
139. Mano, N., Kim, H.-H. & Heller, A. On the Relationship between the Characteristics of Bilirubin Oxidases and O2 Cathodes Based on Their "Wiring". *J. Phys. Chem. B* **106**, 8842–8848 (2002).
140. Durand, F., Gounel, S., Kjaergaard, C. H., Solomon, E. I. & Mano, N. Bilirubin oxidase from Magnaporthe oryzae: an attractive new enzyme for biotechnological applications. *Appl. Microbiol. Biotechnol.* **96**, 1489–1498 (2012).
141. Durand, F. *et al.* Bilirubin oxidase from Bacillus pumilus: A promising enzyme for the elaboration of efficient cathodes in biofuel cells. *Biosensors and Bioelectronics* **35**, 140–146 (2012).
142. Christenson, A., Shleev, S., Mano, N., Heller, A. & Gorton, L. Redox potentials of the blue copper sites of bilirubin oxidases. *Biochimica et Biophysica Acta (BBA) - Bioenergetics* **1757**, 1634–1641 (2006).
143. Shleev, S. *et al.* Oxygen Electroreduction versus Bioelectroreduction: Direct Electron Transfer Approach. *Electroanalysis* **28**, 2270–2287 (2016).
144. Jenkins, P. A., Boland, S., Kavanagh, P. & Leech, D. Evaluation of performance and stability of biocatalytic redox films constructed with different copper oxygenases and osmium-based redox polymers. *Bioelectrochemistry* **76**, 162–168 (2009).
145. Mano, N. *et al.* Oxygen Is Electroreduced to Water on a "Wired" Enzyme Electrode at a Lesser Overpotential than on Platinum. *J. Am. Chem. Soc.* **125**, 15290–15291 (2003).
146. Suraniti, E., Studer, V., Sojic, N. & Mano, N. Fast and Easy Enzyme Immobilization by Photoinitiated Polymerization for Efficient Bioelectrochemical Devices. *Anal. Chem.* **83**, 2824–2828 (2011).
147. Lalaoui, N. *et al.* Osmium(II) Complexes Bearing Chelating N-Heterocyclic Carbene and Pyrene-Modified Ligands: Surface Electrochemistry and Electron Transfer Mediation of Oxygen Reduction by Multicopper Enzymes. *Organometallics* **35**, 2987–2992 (2016).
148. Tsujimura, S., Kawaharada, M., Nakagawa, T., Kano, K. & Ikeda, T. Mediated bioelectrocatalytic O2 reduction to water at highly positive electrode potentials near neutral pH. *Electrochemistry Communications* **5**, 138–141 (2003).
149. Cardoso, F. P. *et al.* Biocathodes for Enzymatic Biofuel Cells Using Laccase and Different Redox Mediators Entrapped in Polypyrrole Matrix. *J. Electrochem. Soc.* **161**, F445–F450 (2014).
150. Dronov, R., Kurth, D. G., Möhwald, H., Scheller, F. W. & Lisdat, F. Communication in a Protein Stack: Electron Transfer between Cytochrome c and Bilirubin Oxidase within a Polyelectrolyte Multilayer. *Angewandte Chemie International Edition* **47**, 3000–3003 (2008).
151. Tsujimura, S., Nakagawa, T., Kano, K. & Ikeda, T. Kinetic Study of Direct Bioelectrocatalysis of Dioxygen Reduction with Bilirubin Oxidase at Carbon Electrodes. *Electrochemistry* **72**, 437–439 (2004).
152. Gutiérrez-Sánchez, C., Pita, M., Vaz-Domínguez, C., Shleev, S. & De Lacey, A. L. Gold

Nanoparticles as Electronic Bridges for Laccase-Based Biocathodes. *Journal of the American Chemical Society* **134**, 17212–17220 (2012).

153. Ciaccafava, A. *et al.* An innovative powerful and mediatorless H2/O2 biofuel cell based on an outstanding bioanode. *Electrochemistry Communications* **23**, 25–28 (2012).
154. Murata, K., Kajiya, K., Nakamura, N. & Ohno, H. Direct electrochemistry of bilirubin oxidase on three-dimensional gold nanoparticle electrodes and its application in a biofuel cell. *Energy & Environmental Science* **2**, 1280–1285 (2009).
155. Cracknell, J. A., McNamara, T. P., Lowe, E. D. & Blanford, C. F. Bilirubin oxidase from Myrothecium verrucaria: X-ray determination of the complete crystal structure and a rational surface modification for enhanced electrocatalytic O2 reduction. *Dalton Transactions* **40**, 6668 (2011).
156. Tominaga, M., Ohtani, M. & Taniguchi, I. Gold single-crystal electrode surface modified with self-assembled monolayers for electron tunneling with bilirubin oxidase. *Physical Chemistry Chemical Physics* **10**, 6928–6934 (2008).
157. So, K. *et al.* Improvement of a direct electron transfer-type fructose/dioxygen biofuel cell with a substrate-modified biocathode. *Phys. Chem. Chem. Phys.* **16**, 4823–4829 (2014).
158. Lopez, R. J., Babanova, S., Ulyanova, Y., Singhal, S. & Atanassov, P. Improved Interfacial Electron Transfer in Modified Bilirubin Oxidase Biocathodes. *CHEMELECTROCHEM* **1**, 241–248 (2014).
159. Ulyanova, Y. *et al.* Effect of enzymatic orientation through the use of syringaldazine molecules on multiple multi-copper oxidase enzymes. *Physical Chemistry Chemical Physics* **16**, 13367–13375 (2014).
160. Lalaoui, N., Le Goff, A., Holzinger, M. & Cosnier, S. Fully Oriented Bilirubin Oxidase on Porphyrin-Functionalized Carbon Nanotube Electrodes for Electrocatalytic Oxygen Reduction. *Chemistry - A European Journal* **21**, 16868–16873 (2015).
161. Xia, H., Kitazumi, Y., Shirai, O. & Kano, K. Enhanced direct electron transfer-type bioelectrocatalysis of bilirubin oxidase on negatively charged aromatic compound-modified carbon electrode. *Journal of Electroanalytical Chemistry* **763**, 104–109 (2016).
162. Yan, Y., Zheng, W., Su, L. & Mao, L. Carbon-Nanotube-Based Glucose/O2 Biofuel Cells. *Advanced Materials* **18**, 2639–2643 (2006).
163. Wang, M. *et al.* Direct electrochemistry of microperoxidase 11 using carbon nanotube modified electrodes. *Journal of Electroanalytical Chemistry* **578**, 121–127 (2005).
164. Cosnier, S., Holzinger, M. & Le Goff, A. Recent Advances in Carbon Nanotube-Based Enzymatic Fuel Cells. *Front. Bioeng. Biotechnol.* **2**, (2014).
165. Radushkevich, L. V. & Lukyanovich, V. M. The structure of carbon forming in thermal decomposition of carbon monoxide on an iron catalyst. *Russian Journal of Physical Chemistry* **26**, 88–95 (1952).
166. Iijima, S. Helical microtubules of graphitic carbon. *Nature* **354**, 56–58 (1991).
167. Mintmire, J. W., Dunlap, B. I. & White, C. T. Are fullerene tubules metallic? *Physical Review Letters* **68**, 631–634 (1992).
168. Odom, T. W., Huang, J.-L., Kim, P. & Lieber, C. M. Atomic structure and electronic properties of

single-walled carbon nanotubes. *Nature* **391**, 62–64 (1998).

169. Valcárcel, M., Cárdenas, S. & Simonet, B. M. Role of Carbon Nanotubes in Analytical Science. *Anal. Chem.* **79**, 4788–4797 (2007).
170. Journet, C. *et al.* Large-scale production of single-walled carbon nanotubes by the electric-arc technique. *Nature* **388**, 756–758 (1997).
171. Thess, A. *et al.* Crystalline Ropes of Metallic Carbon Nanotubes. *Science* **273**, 483–487 (1996).
172. Nikolaev, P. *et al.* Gas-phase catalytic growth of single-walled carbon nanotubes from carbon monoxide. *Chemical Physics Letters* **313**, 91–97 (1999).
173. Flahaut, E., Laurent, Ch. & Peigney, A. Catalytic CVD synthesis of double and triple-walled carbon nanotubes by the control of the catalyst preparation. *Carbon* **43**, 375–383 (2005).
174. Kumar, M. & Ando, Y. Chemical Vapor Deposition of Carbon Nanotubes: A Review on Growth Mechanism and Mass Production. *Journal of Nanoscience and Nanotechnology* **10**, 3739–3758 (2010).
175. Pumera, M., Ambrosi, A. & Chng, E. L. K. Impurities in graphenes and carbon nanotubes and their influence on the redox properties. *Chemical Science* **3**, 3347 (2012).
176. de las Casas, C. & Li, W. A review of application of carbon nanotubes for lithium ion battery anode material. *Journal of Power Sources* **208**, 74–85 (2012).
177. Endo, M., Hayashi, T., Kim, Y. A. & Muramatsu, H. Development and Application of Carbon Nanotubes. *Jpn. J. Appl. Phys.* **45**, 4883 (2006).
178. Niu, Z. *et al.* Compact-designed supercapacitors using free-standing single-walled carbon nanotube films. *Energy & Environmental Science* **4**, 1440–1446 (2011).
179. Mukherjee, S., Bates, A., Lee, S. C., Lee, D.-H. & Park, S. A Review of the Application of CNTs in PEM Fuel Cells. *International Journal of Green Energy* **12**, 787–809 (2015).
180. Hussein, L. *et al.* A highly efficient buckypaper-based electrode material for mediatorless laccase-catalyzed dioxygen reduction. *Biosensors and Bioelectronics* **26**, 4133–4138 (2011).
181. Ausman, K. D., Piner, R., Lourie, O., Ruoff, R. S. & Korobov, M. Organic Solvent Dispersions of Single-Walled Carbon Nanotubes: Toward Solutions of Pristine Nanotubes. *J. Phys. Chem. B* **104**, 8911–8915 (2000).
182. Meng, L., Fu, C. & Lu, Q. Advanced technology for functionalization of carbon nanotubes. *Progress in Natural Science* **19**, 801–810 (2009).
183. Zhou, Y., Fang, Y. & Ramasamy, R. P. Non-Covalent Functionalization of Carbon Nanotubes for Electrochemical Biosensor Development. *Sensors (Basel)* **19**, (2019).
184. Singh, P. *et al.* Organic functionalisation and characterisation of single-walled carbon nanotubes. *Chemical Society Reviews* **38**, 2214–2230 (2009).
185. Zhang, J. *et al.* Effect of Chemical Oxidation on the Structure of Single-Walled Carbon Nanotubes. *J. Phys. Chem. B* **107**, 3712–3718 (2003).
186. Datsyuk, V. *et al.* Chemical oxidation of multiwalled carbon nanotubes. *Carbon* **46**, 833–840 (2008).
187. Xing, Y., Li, L., Chusuei, C. C. & Hull, R. V. Sonochemical Oxidation of Multiwalled Carbon Nanotubes. *Langmuir* **21**, 4185–4190 (2005).
188. Tagmatarchis, N. & Prato, M. Functionalization of carbon nanotubes via 1,3-dipolar

cycloadditions. *Journal of Materials Chemistry* **14**, 437–439 (2004).

189. Chen, J. *et al.* Solution Properties of Single-Walled Carbon Nanotubes. *Science* **282**, 95–98 (1998).
190. Holzinger, M. *et al.* Sidewall Functionalization of Carbon Nanotubes. *Angewandte Chemie International Edition* **40**, 4002–4005 (2001).
191. Holzinger, M. *et al.* Functionalization of Single-Walled Carbon Nanotubes with (R-)Oxycarbonyl Nitrenes. *J. Am. Chem. Soc.* **125**, 8566–8580 (2003).
192. Nakamura, T., Ishihara, M., Ohana, T., Tanaka, A. & Koga, Y. Sidewall modification of single-walled carbon nanotubes using photolysis of perfluoroazooctane. *Chem. Commun.* 1336–1337 (2004) doi:10.1039/B402206H.
193. Salice, P. *et al.* An insight into the functionalisation of carbon nanotubes by diazonium chemistry: Towards a controlled decoration. *Carbon* **74**, 73–82 (2014).
194. Fujigaya, T. & Nakashima, N. Non-covalent polymer wrapping of carbon nanotubes and the role of wrapped polymers as functional dispersants. *Sci. Technol. Adv. Mater.* **16**, 024802 (2015).
195. Zhao, Y.-L. & Stoddart, J. F. Noncovalent Functionalization of Single-Walled Carbon Nanotubes. *Acc. Chem. Res.* **42**, 1161–1171 (2009).
196. Zhao, J., Lu, J. P., Han, J. & Yang, C.-K. Noncovalent functionalization of carbon nanotubes by aromatic organic molecules. *Applied Physics Letters* **82**, 3746–3748 (2003).
197. Chen, R. J., Zhang, Y., Wang, D. & Dai, H. Noncovalent Sidewall Functionalization of Single-Walled Carbon Nanotubes for Protein Immobilization. *J. Am. Chem. Soc.* **123**, 3838–3839 (2001).
198. P. Ramasamy, R., R. Luckarift, H., M. Ivnitski, D., B. Atanassov, P. & R. Johnson, G. High electrocatalytic activity of tethered multicopper oxidase– carbon nanotube conjugates. *Chemical Communications* **46**, 6045–6047 (2010).
199. Assali, M. *et al.* Non-covalent functionalization of carbon nanotubes with glycolipids : glyconanomaterials with specific lectin-affinity. *Soft Matter* **5**, 948–950 (2009).
200. Fritea, L. *et al.* A bifunctional triblock polynorbornene/carbon nanotube buckypaper bioelectrode for low-potential/high-current thionine-mediated glucose oxidation by FAD-GDH. *J. Mater. Chem. A* (2019) doi:10.1039/C8TA10644D.
201. Goff, A. L. *et al.* Facile and tunable functionalization of carbon nanotube electrodes with ferrocene by covalent coupling and π-stacking interactions and their relevance to glucose bio-sensing. *Journal of Electroanalytical Chemistry* **641**, 57–63 (2010).
202. Li, Q., Zhang, J., Yan, H., He, M. & Liu, Z. Thionine-mediated chemistry of carbon nanotubes. *Carbon* **42**, 287–291 (2004).
203. Wu, T.-M., Chang, H.-L. & Lin, Y.-W. Synthesis and characterization of conductive polypyrrole/multi-walled carbon nanotubes composites with improved solubility and conductivity. *Composites Science and Technology* **69**, 639–644 (2009).
204. Silveira, C. M. *et al.* Enhanced Direct Electron Transfer of a Multihemic Nitrite Reductase on Single-walled Carbon Nanotube Modified Electrodes. *Electroanalysis* **22**, 2973–2978 (2010).
205. Tam, P. D. & Hieu, N. V. Conducting polymer film-based immunosensors using carbon nanotube/antibodies doped polypyrrole. *Applied Surface Science* **257**, 9817–9824 (2011).

206. Kwon, C. H. *et al.* High-power biofuel cell textiles from woven biscrolled carbon nanotube yarns. *Nature Communications* **5**, (2014).
207. Lima, M. D. *et al.* Biscrolling Nanotube Sheets and Functional Guests into Yarns. *Science* **331**, 51–55 (2011).
208. Rinzler, A. G. *et al.* Large-scale purification of single-wall carbon nanotubes: process, product, and characterization. *Appl Phys A* **67**, 29–37 (1998).
209. Bandodkar, A. J. *et al.* Soft, stretchable, high power density electronic skin-based biofuel cells for scavenging energy from human sweat. *Energy & Environmental Science* **10**, 1581–1589 (2017).
210. Hussein, L., Urban, G. & Krüger, M. Fabrication and characterization of buckypaper-based nanostructured electrodes as a novel material for biofuel cell applications. *Physical Chemistry Chemical Physics* **13**, 5831 (2011).
211. Hennrich, F. *et al.* Preparation, characterization and applications of free-standing single walled carbon nanotube thin films. *Physical Chemistry Chemical Physics* **4**, 2273–2277 (2002).
212. Meng, C., Liu, C. & Fan, S. Flexible carbon nanotube/polyaniline paper-like films and their enhanced electrochemical properties. *Electrochemistry Communications* **11**, 186–189 (2009).
213. Zhu, W. *et al.* Ultra-low platinum loading high-performance PEMFCs using buckypaper-supported electrodes. *Electrochemistry Communications* **12**, 1654–1657 (2010).
214. DeGraff, J. *et al.* Printable low-cost and flexible carbon nanotube buckypaper motion sensors. *Materials & Design* **133**, 47–53 (2017).
215. Papa, H., Gaillard, M., Gonzalez, L. & Chatterjee, J. Fabrication of Functionalized Carbon Nanotube Buckypaper Electrodes for Application in Glucose Biosensors. *Biosensors* **4**, 449–460 (2014).
216. Young, J. P. *Continuous buckypaper manufacturing process: Process investigation and improvement*. (Florida State University, 2009).
217. Susantyoko, R. A. *et al.* A surface-engineered tape-casting fabrication technique toward the commercialisation of freestanding carbon nanotube sheets. *Journal of Materials Chemistry A* **5**, 19255–19266 (2017).
218. Halámková, L. *et al.* Implanted Biofuel Cell Operating in a Living Snail. *J. Am. Chem. Soc.* **134**, 5040–5043 (2012).
219. Villarrubia, C. W. N., Artyushkova, K., Garcia, S. O. & Atanassov, P. NAD+/NADH Tethering on MWNTs-Bucky Papers for Glucose Dehydrogenase-Based Anodes. *J. Electrochem. Soc.* **161**, H3020–H3028 (2014).
220. Göbel, G. *et al.* Operation of a carbon nanotube-based glucose/oxygen biofuel cell in human body liquids—Performance factors and characteristics. *Electrochimica Acta* **218**, 278–284 (2016).
221. Luo, W., Liu, Y. & Saha, M. CNT Bucky Paper Enhanced Sandwich Composites for In-Situ Load Sensing. in *IMECE2017* (2018). doi:10.1115/IMECE2017-71550.
222. Zeni, O. *et al.* Growth inhibition, cell-cycle alteration and apoptosis in stimulated human peripheral blood lymphocytes by multiwalled carbon nanotube buckypaper. *Nanomedicine* **10**, 351–360 (2014).

223. Li, Z. & Liang, Z. Optimization of Buckypaper-enhanced Multifunctional Thermoplastic Composites. *Sci Rep* **7**, (2017).
224. Xiong, G., Hembram, K. P. S. S., Reifenberger, R. G. & Fisher, T. S. MnO2-coated graphitic petals for supercapacitor electrodes. *Journal of Power Sources* **227**, 254–259 (2013).
225. Kharissova, O. V., Kharisov, B. I. & Ortiz, E. G. de C. Dispersion of carbon nanotubes in water and non-aqueous solvents. *RSC Adv.* **3**, 24812–24852 (2013).
226. Gross, A. J., Holzinger, M. & Cosnier, S. Buckypaper bioelectrodes: Emerging materials for implantable and wearable biofuel cells. *Energy Environ. Sci.* (2018) doi:10.1039/C8EE00330K.
227. Cosnier, S., Haddad, R., Moatsou, D. & O'Reilly, R. K. Biofunctionalizable flexible bucky paper by combination of multi-walled carbon nanotubes and polynorbornene-pyrene – Application to the bioelectrocatalytic reduction of oxygen. *Carbon* **93**, 713–718 (2015).
228. Gross, A. J. *et al.* Robust bifunctional buckypapers from carbon nanotubes and polynorbornene copolymers for flexible engineering of enzymatic bioelectrodes. *Carbon* **107**, 542–547 (2016).
229. Hussein, L., Feng, Y. J., Alonso-Vante, N., Urban, G. & Krüger, M. Functionalized-carbon nanotube supported electrocatalysts and buckypaper-based biocathodes for glucose fuel cell applications. *Electrochimica Acta* **56**, 7659–7665 (2011).
230. Narváez Villarrubia, C. W., Rincón, R. A., Radhakrishnan, V. K., Davis, V. & Atanassov, P. Methylene Green Electrodeposited on SWNTs-Based "Bucky" Papers for NADH and l-Malate Oxidation. *ACS Appl. Mater. Interfaces* **3**, 2402–2409 (2011).
231. Szczupak, A. *et al.* Living battery – biofuel cells operating in vivo in clams. *Energy & Environmental Science* **5**, 8891–8895 (2012).
232. Castorena-Gonzalez, J. A. *et al.* Biofuel Cell Operating in Vivo in Rat. *Electroanalysis* **25**, 1579–1584 (2013).
233. MacVittie, K. *et al.* From "cyborg" lobsters to a pacemaker powered by implantable biofuel cells. *Energy & Environmental Science* **6**, 81–86 (2013).
234. MacVittie, K., Conlon, T. & Katz, E. A wireless transmission system powered by an enzyme biofuel cell implanted in an orange. *Bioelectrochemistry* **106**, 28–33 (2015).
235. Reid, R. C., Minteer, S. D. & Gale, B. K. Contact lens biofuel cell tested in a synthetic tear solution. *Biosensors and Bioelectronics* **68**, 142–148 (2015).
236. Bunte, C., Hussein, L. & Urban, G. A. Performance of non-compartmentalized enzymatic biofuel cell based on buckypaper cathode and ferrocene-containing redox polymer anode. *Journal of Power Sources* **247**, 579–586 (2014).
237. Scherbahn, V. *et al.* Biofuel cells based on direct enzyme–electrode contacts using PQQ-dependent glucose dehydrogenase/bilirubin oxidase and modified carbon nanotube materials. *Biosensors and Bioelectronics* **61**, 631–638 (2014).
238. Narváez Villarrubia, C. W. *et al.* Practical electricity generation from a paper based biofuel cell powered by glucose in ubiquitous liquids. *Electrochemistry Communications* **45**, 44–47 (2014).
239. Narvaez Villarrubia, C. W. *et al.* Self-feeding paper based biofuel cell/self-powered hybrid μ-supercapacitor integrated system. *Biosensors and Bioelectronics* **86**, 459–465 (2016).
240. Hou, C. & Liu, A. An integrated device of enzymatic biofuel cells and supercapacitor for both efficient electric energy conversion and storage. *Electrochimica Acta* **245**, 303–308 (2017).

241. Bollella, P., Lee, I., Blaauw, D. & Katz, E. A Microelectronic Sensor Device Powered by a Small Implantable Biofuel Cell. *ChemPhysChem* (2019) doi:10.1002/cphc.201900700.
242. Amar, A. B., Kouki, A. B. & Cao, H. Power Approaches for Implantable Medical Devices. *Sensors* **15**, 28889–28914 (2015).
243. Mallela, V. S., Ilankumaran, V. & Rao, N. S. Trends in Cardiac Pacemaker Batteries. *Indian Pacing Electrophysiol J* **4**, 201–212 (2004).
244. Khonsary, S. A. Guyton and Hall: Textbook of Medical Physiology. *Surg Neurol Int* **8**, (2017).
245. Rapoport, B. I., Kedzierski, J. T. & Sarpeshkar, R. A Glucose Fuel Cell for Implantable Brain–Machine Interfaces. *PLOS ONE* **7**, e38436 (2012).
246. Mano, N., Mao, F. & Heller, A. Characteristics of a Miniature Compartment-less Glucose−O2 Biofuel Cell and Its Operation in a Living Plant. *J. Am. Chem. Soc.* **125**, 6588–6594 (2003).
247. Miyake, T. *et al.* Enzymatic biofuel cells designed for direct power generation from biofluids in living organisms. *Energy Environ. Sci.* **4**, 5008–5012 (2011).
248. Yoshino, S., Miyake, T., Yamada, T., Hata, K. & Nishizawa, M. Molecularly Ordered Bioelectrocatalytic Composite Inside a Film of Aligned Carbon Nanotubes. *Advanced Energy Materials* **3**, 60–64 (2013).
249. Cinquin, P. *et al.* A Glucose BioFuel Cell Implanted in Rats. *PLOS ONE* **5**, e10476 (2010).
250. Morady, F. 66 - Electrophysiologic Interventional Procedures and Surgery. in *Goldman's Cecil Medicine (Twenty Fourth Edition)* (eds. Goldman, L. & Schafer, A. I.) 369–373 (W.B. Saunders, 2012). doi:10.1016/B978-1-4377-1604-7.00066-X.
251. Naahidi, S. *et al.* Biocompatibility of engineered nanoparticles for drug delivery. *Journal of Controlled Release* **166**, 182–194 (2013).
252. Rasmussen, M., Ritzmann, R. E., Lee, I., Pollack, A. J. & Scherson, D. An Implantable Biofuel Cell for a Live Insect. *J. Am. Chem. Soc.* **134**, 1458–1460 (2012).
253. Zebda, A. *et al.* Single Glucose Biofuel Cells Implanted in Rats Power Electronic Devices. *Scientific Reports* **3**, (2013).
254. Andoralov, V. *et al.* Biofuel Cell Based on Microscale Nanostructured Electrodes with Inductive Coupling to Rat Brain Neurons. *Scientific Reports* **3**, 3270 (2013).
255. El Ichi-Ribault, S. *et al.* Remote wireless control of an enzymatic biofuel cell implanted in a rabbit for 2 months. *Electrochimica Acta* **269**, 360–366 (2018).
256. Stoppa, M. & Chiolerio, A. Wearable Electronics and Smart Textiles: A Critical Review. *Sensors* **14**, 11957–11992 (2014).
257. Harvey, C. J., LeBouf, R. F. & Stefaniak, A. B. Formulation and stability of a novel artificial human sweat under conditions of storage and use. *Toxicology in Vitro* **24**, 1790–1796 (2010).
258. Jia, W. *et al.* Wearable textile biofuel cells for powering electronics. *Journal of Materials Chemistry A* **2**, 18184–18189 (2014).
259. Pankratov, D., Blum, Z., Suyatin, D. B., Popov, V. O. & Shleev, S. Self-Charging Electrochemical Biocapacitor. *ChemElectroChem* **1**, 343–346 (2014).
260. Agnès, C. *et al.* Supercapacitor/biofuel cell hybrids based on wired enzymes on carbon nanotube matrices: autonomous reloading after high power pulses in neutral buffered glucose solutions. *Energy & Environmental Science* **7**, 1884 (2014).

Chapter 2:

Comparison of commercial and lab-made MWCNT buckypaper: physicochemical properties and bioelectrocatatlytic O_2 reduction

Chapter 2 Comparison of commercial and lab-made MWCNT buckypaper: physicochemical properties and bioelectrocatalytic O_2 reduction

Résumé

En raison de leur stabilité chimique, de leur conductivité électrique et thermique élevée, de leurs propriétés mécaniques, l'utilisation de nanotubes de carbone (CNTs), en particulier, a suscité un intérêt croissant au sein de la communauté des nanosciences pour l'interfaçage de systèmes biologiques. Leur grande surface spécifique (jusqu'à 850 m^2 g^{-1}) et leur géométrie unique font des CNTs des candidats idéaux pour la construction d'électrodes tridimensionnelles présentant une forte porosité et susceptibles de fixer une large variété de fonctions chimiques ou biologiques. Les électrodes à base de dépôts de CNTs constituent une plate-forme polyvalente pour l'immobilisation et la connexion électrique d'enzymes via des processus de transfert d'électrons directs ou indirects grâce à des médiateurs redox.

Les carbones mésoporeux et les matériaux carbonés nanostructurés basés par exemple sur le graphène ou les nanotubes de carbone, se sont révélés très prometteurs comme électrodes pour l'électroanalyse et l'électrocatalyse et plus particulièrement la bioélectrocatalyse enzymatique dont les applications concernent le développement des biocapteurs électrochimiques et celui des biopiles. Il faut souligner que les électrodes à base de dépôt de CNTs s'avèrent également faciles à modifier par diverses fonctionnalités via des méthodes de greffage chimique ou photochimique ainsi que par des approches non covalentes. La modification de surface non covalente basée des interactions π-πentre des dérivés polyaromatiques et les parois de nanotubes constitue une approche simple et respectueuse de la structure des tubes et par là même de leur conductivité électrique liée à l'intégrité de leur structure électronique délocalisée. Parallèlement à la modification de surface d'électrode par des dépôts de CNTS, une alternative innovante est de créer directement une électrode à partir de CNTS au lieu de les déposer sur une électrode conventionnelle de platine ou de carbone vitreux. Cette stratégie consiste à générer un tissu stable et conducteur composé de CNTS couramment appelé buckypaper (BP).

Les buckypapers sont de minces feuilles macroscopiques composées de nanotubes de carbone enchevêtrés maintenus ensemble par des interactions π-π avec des épaisseurs classiquement comprises entre 5 et 200 μm pouvant s'abaisser jusqu'à 200 nm.

Buckypaper est maintenant une expression classique adoptée pour désigner des feuilles de nanotubes de carbone désordonnées, y compris des matériaux composites, formées par filtration sous vide de dispersions aqueuses ou organiques de nanotubes de carbone à simple paroi, à double paroi et à parois multiples, respectivement SWCNTs, DWCNTs, MWCNTs. Les buckypapers sont typiquement élaborés par filtration d'une dispersion de CNTS préparée par sonication en présence d'un tensioactif pour les milieux aqueux. Des tensioactifs tels que le Triton X-100, le dodécylbenzènesulfonate de sodium (SDBS) et le dodécyl sulfate de sodium (SDS) ont été couramment employés afin d'améliorer la dispersibilité des CNTS dans l'eau. La suspension de CNT est ensuite filtrée à travers une membrane poreuse comme un filtre en téflon ou en polycarbonate conduisant à une feuille de CNTs qui, après lavage et séchage, est décollée du filtre sous-jacent. La fabrication du buckypaper est conceptuellement simple, mais des facteurs tels que l'homogénéité de la suspension, la longueur et la pureté des CNTs, la charge des nanotubes et la nature des fonctionnalités greffées sur les CNTs ainsi que la perméabilité du filtre peuvent générer des problèmes de reproductibilité des matériaux.

L'utilisation de buckypaper pour la construction de bioanodes et de biocathodes catalytiques, est apparue ces dernières années pour l'élaboration de biopiles enzymatiques. En particulier, depuis 2012, des buckypapers commerciaux ont été employés pour développer des biopiles implantées *in vivo* dans des insectes, des mollusques ou des mammifères afin de générer *in vivo* de l'énergie électrique voire pour alimenter des dispositifs électroniques

Les électrodes buckypaper pouvant être fabriquées en laboratoire ou obtenues commercialement, il est apparu que les propriétés électroniques et physicochimiques de ces électrodes pouvaient fortement diverger car liées à des facteurs tels que la diversité des sources de CNTs utilisés (longueur, diamètre, quantité et pureté, par exemple), l'homogénéité de la suspension, la présence d'additifs non répertoriés par les fabricants et les solvants utilisés. Il faut souligner également l'évolution des procédures de fabrication des CNTs vers une chimie plus verte qui théoriquement conduit aux mêmes CNTs mais dans la réalité change drastiquement leurs propriétés de dispersion, d'agglomération ainsi que leurs fonctionnalités de surface et sont à l'origine de problèmes de reproductibilité des buckypapers fabriqués en laboratoire.

Outre les propriétés physiques et électriques de ces électrodes en buckypaper, leur utilisation comme bioélectrodes enzymatiques pour l'élaboration de biopiles, en

particulier comme biocathode, met en exergue l'influence de leur structure sur l'immobilisation de l'enzyme et son orientation et donc sur la possibilité d'établir un transfert direct ou indirect d'électron entre les CNTs et l'enzyme.

Dans ce chapitre, les buckypapers à base de MWCNTs commerciaux ont été comparés physiquement et électrochimiquement afin de déterminer leurs propriétés et donc leurs potentialités en tant qu'électrodes voire comme électrodes enzymatiques pour des applications en bioélectrocatalyse et plus particulièrement dans le domaine des biopiles. Cette étude comparative implique un buckypaper commercial vendu par NanoTechLabs (Buckeye Composites), et un buckypaper issu du laboratoire. Les propriétés physiques des films de nanotubes de carbone ont été caractérisées par des techniques spectrométriques comme la microscopie électronique, la spectroscopie photoélectronique à rayons X et la spectroscopie Raman ainsi que par des mesures de conductivité, un paramètre fondamental pour des applications électrocatalytiques. Un autre paramètre important qui a été examiné, est la surface spécifique de ces buckypapers. Cette dernière a été estimée par des mesures d'adsorption de gaz (BET) et a été comparée à celle déterminée par des mesures électrochimiques mettant en exergue des différences liées à la macro ou microporosité des électrodes.

Les propriétés électrochimiques, quant à elles, ont été étudiées par voltampérométrie en l'absence et la présence de sondes redox exhibant des différences en termes d'encombrement stériques et de charges (hexaammine de ruthénium $Ru(NH_3)_6^{3+/2+}$, ferrocène méthanol $FcMeOH^+$, hexacyanoferrate (III) de potassium $Fe(CN)_6^{3-}$) afin d'étudier la perméation à travers les buckypapers et l'influence de leurs potentielles fonctionnalités de surface. En particulier, l'utilisation de sondes redox non chargées ou exhibant des charges négatives ou positives a confirmé la présence d'espèces chargées négativement à la surface du BP commercial.

Concernant leur utilisation en tant que bioélectrodes, la bilirubine oxydase (BOx) a été immobilisée sur ces buckypapers afin de comparer leur performance vis-à-vis de la réduction bioélectrocatalytique de l'oxygène. Dans cette problématique, nous avons également examiné le rôle d'une protoporphyrine de fer comme promoteur d'orientation de la BOx et donc son impact sur l'établissement d'un transfert direct d'électron (DET) entre la BOx et l'électrode en buckypaper. Cette protoporphyrine exhibe des interactions π-π entre sa structure plane aromatique et les parois de nanotubes et est chargée négativement. Cela induit ainsi des interactions électrostatiques avec une cavité chargée positivement de la BOx (où le substrat naturel

de l’enzyme se fixe) et qui correspond au point d’entrée des électrons dans la protéine au niveau du centre cuivre T1. La présence du fer comme centre métallique permet d’obtenir un signal électrochimique de la protoporphyrine et donc d’estimer son taux de recouvrement sur le film de nanotubes.

Par rapport au buckypaper commercial, il apparait que les buckypapers fabriqués au laboratoire présentent une fenêtre de potentiel plus large combinée à des courants capacitifs nettement plus faibles ainsi qu’un comportement électrochimique plus proche de celui du carbone vitreux.

Concernant l’activité électro-enzymatique, le buckypaper fabriqué au laboratoire présente des courants catalytiques vis-à-vis de la réduction de l’oxygène 10 fois plus élevés que ceux enregistrés pour le buckypaper industriel.

Cet effet résulte d'une combinaison de facteurs comprenant notamment une surface spécifique plus importante (les mesures par BET indiquent une augmentation par un facteur 10), une quantité d’enzyme immobilisée supérieure, une structure plus poreuse avec des nanotubes exhibant des diamètres plus petits. La modification des nanotubes des buckypapers commerciaux et fabriqués au laboratoire a été réalisée par interactions π-π entre les parois des CNTS et des porphyrines de fer en examinant l’effet de la concentration de ces dernières sur leur immobilisation dans le domaine de 0,6, 5 et 10 mmol L^{-1} et donc sur l’activité électroenzymatique des électrodes qui en résultent. Cette modification conduit à une augmentation des densités de courant catalytique tout en diminuant la surtension cathodique relative au potentiel d’initiation de la réduction de l'oxygène passant ainsi de 0,51 V à 0,53 V. Les courants catalytiques maximaux dans une solution saturée en oxygène sont respectivement 0,5 mA cm^{-2} et 1,3 mA cm^{-2} pour les buckypapers commerciaux et les buckypapers « maison » modifiés par les porphyrines.

Chapter 2 Comparison of commercial and lab-made MWCNT buckypaper: physicochemical properties and bioelectrocatalytic O_2 reduction

This chapter is based on the following manuscript-

Xiaohong Chen, Andrew J. Gross, Fabien Giroud, Michael Holzinger, Serge Cosnier

Electroanalysis. **2018**, 30, 1511–1520

2.1 Abstract

The main goal of this thesis is to develop high-power enzymatic biofuel cells (EFCs). Among various carbon nanostructured materials, buckypaper (BP) is one of the most attractive materials to construct bioelectrodes due to its unique properties. Therefore, it is necessary to examine different BPs to understand the bioelectrocatlytic reaction on different electrode materials. In this chapter, a thorough comparison study was conducted on commercial BP and lab-made BP. The former was obtained from Buckeye Composite, while the latter was prepared in the lab using vacuum filtration method. The two types of BPs were characterized using different techniques. The behaviors of enzyme-modified bioelectrodes prepared from these two types of BPs were examined by immobilizing bilirubin oxidase (BOx) for oxygen reduction.

2.2 Introduction

Nanostructured carbon materials such as carbon nanotubes (CNTs) and templated mesoporous carbons have shown great promise as electrodes for enzymatic bioelectrocatalysis for applications including biosensors and biofuel cells.[1–5] CNT-based electrodes are attractive for bioelectrocatalysis owing to their properties such as high conductivity, large specific surface area, exceptional mechanical strength, and the ability to undergo efficient electron transfer with oxidoreductase enzymes.[6,7] CNT electrodes also benefit from being readily modified with surface functionalities *via* covalent and non-covalent methods, for example, to enhance the electrical "wiring" and stabilization of enzymes for bioelectrocatalysis.[8–10] Non-covalent surface modification based on π-π stacking of pyrene derivatives and other polyaromatics on nanotube sidewalls is a convenient strategy which retains the extended π-conjugation of CNT networks and hence their electrical conductivity.[10–14]

Buckypaper is a very attractive type of CNT material which has emerged in recent

years for the construction of bioanodes and biocathodes for use in enzymatic biofuel cells.[13–19] Commercial BP has been used in actual implanted devices since 2012, most notably, for *in vivo* biofuel cells and electronic device powering.[16,18,20,21] BP is a randomly ordered self-supporting film of CNTs which is typically formed by vacuum filtration of aqueous and non-aqueous dispersions of CNTs.[15,22,23] The films are microscale-thin (ca. 5 to 300 μm) and held together by π-π stacking and interweaving interactions.[23,24] Unlike classical CNT electrodes, which are formed by depositing CNT films on conductive glassy carbon and metal substrates, a BP film is the electrode itself. BP electrodes are convenient to fabricate in the lab or can be obtained from commercial sources.[15,18] However, their electronic and physicochemical properties are strongly dependent on factors such as the type of CNTs used (e.g. length, diameter, quantity, defects and purity), dispersion homogeneity, the presence of additives and the solvents used, which create challenges concerning reproducibility and functionality.

For the construction of biocathodes, multi-copper oxidases (MCOs) such as bilirubin oxidase and laccase are typically employed as the biocatalyst for the four-electron reduction of O_2 to H_2O.[25] These enzymes possess four Cu atoms with the T1 Cu center, responsible for substrate oxidation and successive electron transfers, located near the protein surface, and a tri-nuclear cluster of T2/T3 Cu centers which is more deeply buried.[26] Therefore, there is great interest in the development of electrode-enzyme interfaces which permit the efficient orientation and electrical connection of the T1 Cu center.

Hussein and coworkers developed the first buckypaper biocathodes (lab-made) by adsorption of inks containing either BOx or laccase, ABTS (2,2'-azino-bis(3-ethylbenzothiazoline-6-sulphonic acid)) mediator, and Nafion.[23,27,30] In these series of work published in the same year, the best performing biocathode achieved a maximum current density up to 0.7 mA cm^{-2} in oxygen-saturated buffer *via* mediated electron transfer (MET) with BOx.[27] Ciniciato *et al.* developed air-breathing electrodes by fusing commercial BP with Toray paper and a carbon black gas diffusion layer.[28] This approach is attractive for enhancing the mass transport of oxygen from air to the electrode surface, thus helping to address the limited oxygen supply in quiescent aqueous solutions. The best performing biocathode, based on direct electron transfer (DET) with BOx, delivered a current output of ca. 0.7 mA cm^{-2} in buffer solution with capillary flow.[28] Pankratov *et al.*

later reported the simple adsorption of BOx on different lab-made BP samples without the use of Nafion as a binder.[29] DET-type bioelectrocatalysis for oxygen reduction was demonstrated but currents only up to 100 µA cm^{-2} were achieved, implying limited catalytic activity of the nanotubes and a low enzyme loading.

Scherbahn *et al.* demonstrated that pyrroloquinoline quinone (PQQ) can be used as an orientation promoter for DET with BOx on commercial buckypaper.[14] PQQ was effectively adsorbed on the electrode *via* π-π stacking interactions and gave a 5-fold increase in catalytic currents up to 0.97 mA cm^{-2} in buffer solution compared to the simple adsorption of BOx on unmodified electrodes. Minteer and coworkers developed lab-made BPs modified with a pyrene-anthracene for oriented DET with BOx.[19] Although low catalytic currents of ca. 100 µA cm^{-2} were observed, this work demonstrated that BP can be an excellent material for the construction of wearable contact-lens bioelectrodes. Our group has also demonstrated the use of an orientation promoter, protoporphyrin, to enhance DET with BOx on buckypaper.[15] Well-defined voltammetry and high limiting currents up to 1.33 mA cm^{-2} were observed in oxygen-saturated buffer with purging, highlighting the promising electrochemical and catalytic performance of these lab-made buckypapers.

Buckypaper is now an important electrode material for the development of enzymatic biocathodes, yet little attention has been given to establishing their electrochemical and physicochemical properties and how these properties influence DET-type bioelectrocatalysis. The reported studies have until now focused on the development of reliable fabrication methods and enzyme wiring strategies to improve catalytic outputs *in vivo* and *in vitro*.

In this chapter, a comparative study was conducted which establishes a baseline for the electrochemical properties of two prominent types of buckypapers: a commercial buckypaper from an established source, NanoTechLabs Inc. (Buckeye Composites), and a recently reported lab-made buckypaper with promising electrode properties.[15] In addition, this study compares the physicochemical properties and the bioelectrocatalytic oxygen reduction activity of unmodified and iron-protoporphyrin modified buckypapers with immobilized BOx.

2.3 Results and discussion

2.3.1 Physical properties of commercial and lab-made buckypaper

2.3.1.1 Scanning electron microscopy

Figure 2.1 shows top-down and cross-sectional scanning electron microscopy (SEM) images of commercial BP and lab-made BP (defined as c-BP and l-BP in the following context). The c-BP samples display a random, homogeneous and largely macroporous structure (**Figure 2.1A**). The CNTs of the c-BP have large diameters of 75-200 nm. On the other hand, l-BP has a random but homogeneous mesoporous structure of bundled CNTs (**Figure 2.1B**). The CNTs of l-BP have diameters of 10-20 nm. Cross-sectional images revealed that c-BP has a looser structure with wider interlayer separations (**Figure 2.1C**). A denser and more compact structure is observed for l-BP (**Figure 2.1D**).

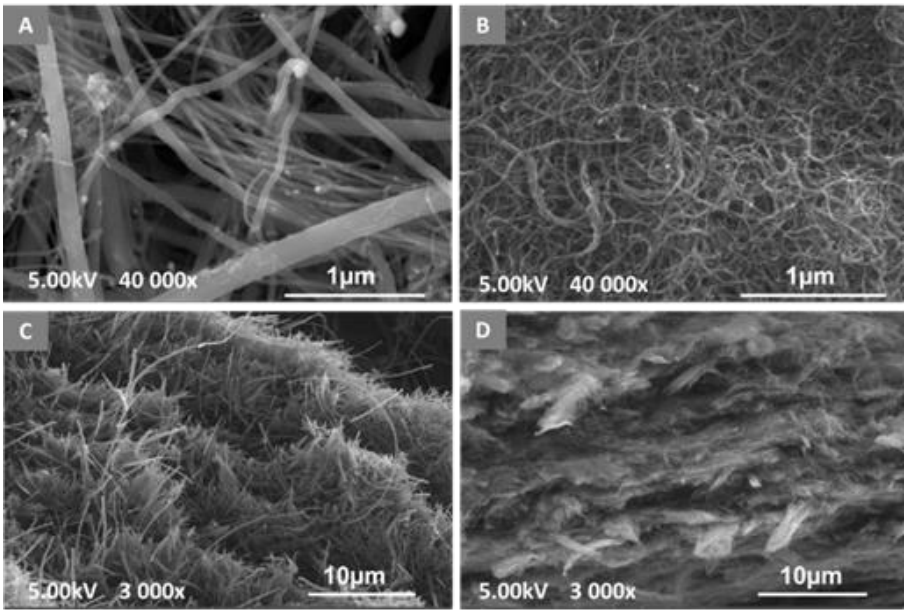

Figure 2.1 SEM images showing (A, B) top-down and (C, D) cross-sectional views of (left) c-BP and (right) l-BP

2.3.1.2 Film thickness, specific surface area and pore size

The average BP thicknesses were estimated to be 227 ± 14 µm (n = 3) and 269 ± 11 µm (n = 5) for the commercial and lab-made BPs, respectively, which is in the range of other BPs obtained from vacuum filtration.[13,15,23] The specific surface area and pore size of the BPs were obtained from nitrogen sorption measurements (**Figure 2.2**), which is a typical method for the characterization of microporous and mesoporous solids.[31] Brunauer-Emmett-Teller (BET) method is then applied to calculate the total specific surface area. Barrett-Joyner-Halenda (BJH) analysis is subsequently

employed to evaluate pore size and volume from nitrogen desorption isotherms.

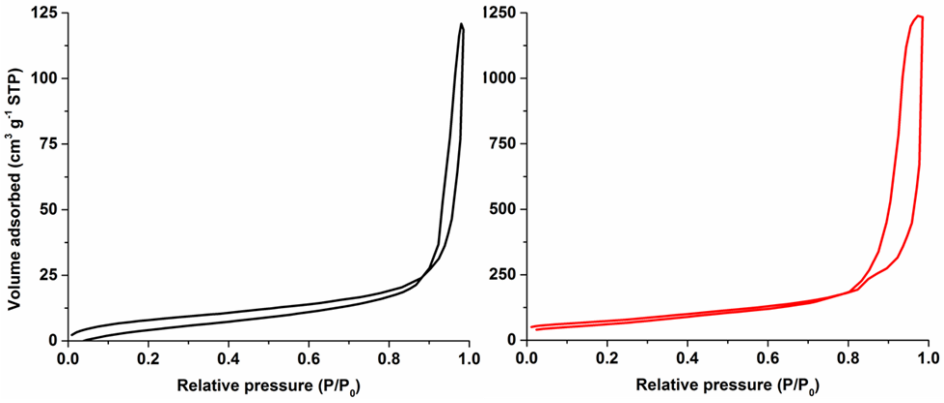

Figure 2.2 Nitrogen adsorption and desorption isotherms of (left) c-BP and (right) l-BP

The BET total specific surface area and BJH mesopore size of the BPs are summarized in **Table 2.1**. The c-BP has a surface area of only 30.2 m^2 g^{-1}. In contrast, l-BP has an estimated surface area of 264 m^2 g^{-1}, which is comparable to previously reported values of 331 m^2g^{-1} and 180 m^2g^{-1} for BP materials.[32,33] The l-BP has an almost 9-fold larger surface area than c-BP. This is consistent with the l-BP having a significantly more mesoporous structure, which is supported by the SEM imaging. The average BJH pore diameter for both materials (noting that the analysis does not account for macropores) was on the same order of magnitude for both BPs with values of 17.0 nm and 14.6 nm for c-BP and l-BP, respectively. The total pore volume, which also accounts for micropores (< 2 nm) and mesopores (2-50 nm), but not macropores (> 50 nm), was negligible for c- BP but significant for l-BP, hence further confirming that c-BPs have a more macroporous structure and that l-BPs are significantly mesoporous.

Table 2.1 Surface area and pore size data from N_2 sorption isotherms for commercial and lab-made BP

Sample	BET surface area /m^2 g^{-1}	BJH mesopores	
		Pore diameter /nm	Pore volume / cm^3 g^{-1}
c-BP	30.2	17.0	4.3×10^{-4}
l-BP	264	14.6	2.0

2.3.1.3 X-ray photoelectron spectroscopy, SEM-Energy dispersive x-ray spectroscopy and Raman spectroscopy

The elemental composition, purity and extent of surface defects at the surface of the

BPs were characterized by XPS and Raman spectroscopy. XPS analysis revealed an elemental composition of only carbon, nitrogen and oxygen at the BPs. The survey spectra are shown in **Figure 2.3**. The quantitative analysis is summarized in **Table 2.2**. The surface of c-BP contains mostly carbon (95.0%), considerable oxygen content (4.4%) and some residual nitrogen (0.6%). The l-BP is also dominated by carbon (98.8%) but possesses significantly less oxygen (1.2%) and no nitrogen. The survey spectra (**Figure 2.3**) for both c-BP and l-BP are largely dominated by the C1s envelope at 284.4 eV, which corresponds to the expected sp^2 structure of the CNTs. Other contributions at 285.3 eV and 289 eV account for hydroxyl and/or sp^3 carbons, and carboxylic acid groups, respectively. Unlike the l-BP spectrum, the c-BP spectrum displays a clear contribution at 286.3 eV, representing surface carbonyl groups.

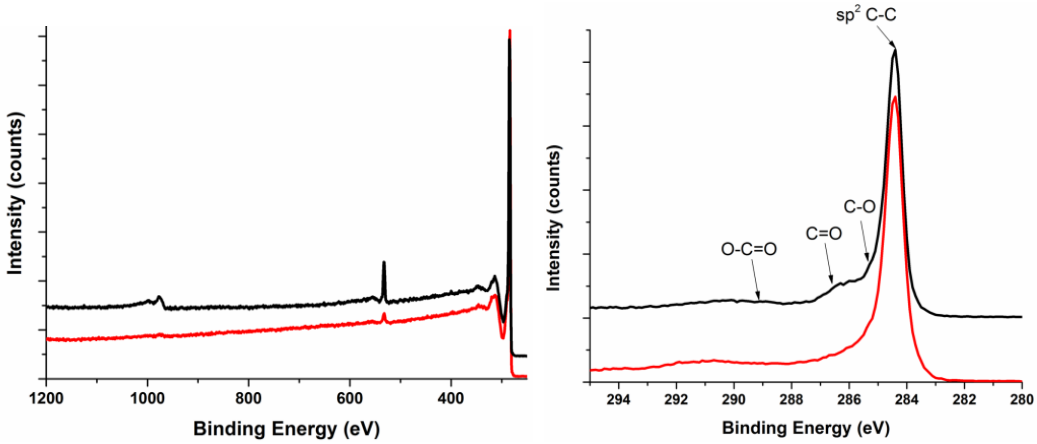

Figure 2.3 (Left) XPS survey spectra and (right) C1s high resolution spectra for (black) c-BP and (red) l-BP substrates

Table 2.2 XPS elemental analysis for c-BP and l-BP surfaces

Sample	Atomic %		
	C	O	N
c-BP	95.0	4.4	0.6
l-BP	98.8	1.2	/

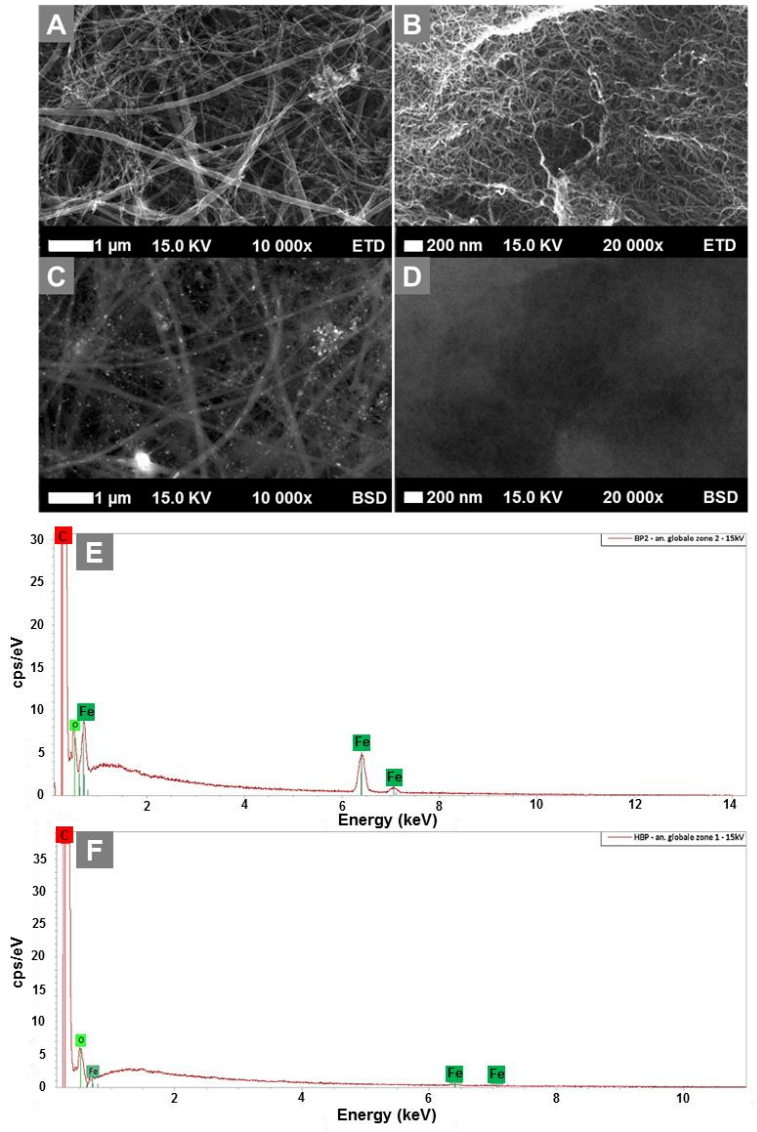

Figure 2.4 SEM-EDS analysis: SEM images showing (A, B) secondary electron detector (Everhart-Thornley; ETD) for topographic visualization and (C, D) backscattered electron detector (BSD) for chemical contrast of the impurities distribution of (left) c-BP and (right) l-BP. Global EDS spectra of the same area as above for (E) c-BP and (F) l-BP

XPS is a surface analysis technique, which normally probes a sampling depth of around 10nm. Therefore, the obtained elemental analysis was limited to the exposed surface of the BP layer to the XPS beam. Given the thick diameter of MWCNTs in c-BP, SEM-energy dispersive x-ray spectroscopy (SEM-EDS) was performed to probe the deeper layer below the surface (**Figure 2.4**). These analyses suggest that CNTs used in the formation of the c-BPs do possess some Fe content (residual catalyst), which are typical impurities of CNTs.[34] In contrast, CNTs used for making l-BPs contains either no Fe content or only trace levels.

Raman spectroscopy was also performed to characterize the surface structure, and in particular, the extent of defect sites in the buckypapers (**Figure 2.5**). Two major bands at approximately 1350 cm^{-1} and 1580 cm^{-1} are present in the Raman spectra, corresponding to the D-band (disordered sp^2 carbon) and G-band (crystalline sp^2 carbon), respectively. The ratio of the D and G band intensities was used to provide a relative but not quantitative comparison of the two BP samples. The c-BP has a comparably more ordered and higher structural purity/crystallinity structure (I_D/I_G = 0.52) while l-BP has a more apparent defective surface (I_D/I_G = 1.74).

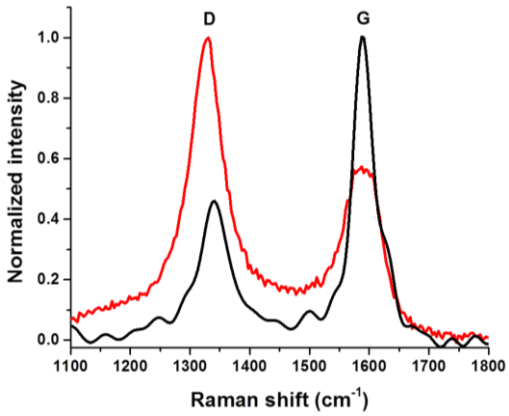

Figure 2.5 Raman spectrums of (black) c-BP and (red) l-BP of the region between 1000 and 2000 cm^{-1}

2.3.1.4. Contact angle, surface profilometry and electrical conductivity

Water contact angle (CA) measurements were performed on c-BP and l-BP. Similar values of 134 ± 8° and 127 ± 18° were obtained for c-BP and l-BP, respectively, which is consistent with both surfaces being hydrophobic (>90°). It was considered that the c-BP, with its high surface oxygen content, might be more hydrophilic than l-BP, but this was not the case. The surface roughness and heterogeneity, rather than the chemical modification, therefore appears to have a more influential effect on the wetting behavior of BP.

Surface profilometry imaging using 3D optical microscopy over large areas of *ca.* 100 μm^2 revealed further insight into the surface structure of the BPs. A larger average roughness value of 4.8 µm root mean square roughness (rms) was estimated for c-BP compared to a value of 1.9 µm rms for l-BP. The profilometry clearly shows that the c-BP has greater surface roughness, which helps to explain its hydrophobicity despite the higher surface oxygen content.[35]

The electrical conductivity of c-BP and l-BP was measured with a four-point probe and revealed average values of 22 ± 3 S cm^{-1} and 13 ± 1 S cm^{-1}, respectively. These

results are similar to conductivity values of around 20-30 S cm^{-1} reported for randomly ordered BP.[23,30,36] The lower electrical conductivity for l-BP, despite the more compact and interconnected structure, can be attributed to the increase of sp^3-type carbon (e.g. higher defect) carbon structure inferred from the Raman spectra.

2.3.2 Electrochemical characterization of commercial and lab-made BPs

Figure 2.6 shows the background voltammetric response recorded at the two BP electrodes in 0.1 mol L^{-1} phosphate buffer (PB) at a scan rate of 20 mV s^{-1}. The two electrodes were scanned between -0.9 V and 1.0 V *vs.* SCE, which is a relevant potential window to observe the electrochemical stability of carbon electrodes in aqueous solution.[37] The c-BP electrode unexpectedly exhibits a pair of redox peaks at E_{pc} = -0.2 V and E_{pa} = 0.5 V. In contrast, the l-BP electrodes exhibited a steady capacitive current response over the same potential range. The redox peaks at c-BP are attributed to electroactive surface-bound oxygen functionalities such as polyaromatic carbonyl, nitroso and phenol groups. The possibility that the redox peaks are due to metal oxides is not entirely ruled out on the basis that Fe impurities were observed by SEM-EDS (**Figure 2.4**). The c-BP electrode showed a 10-fold larger background capacitive current. The larger capacitance observed at c-BP is attributed to the looser packing density of CNT bundles (**Figure 2.1C**), increased surface roughness and the higher concentration of oxygen functionalities.

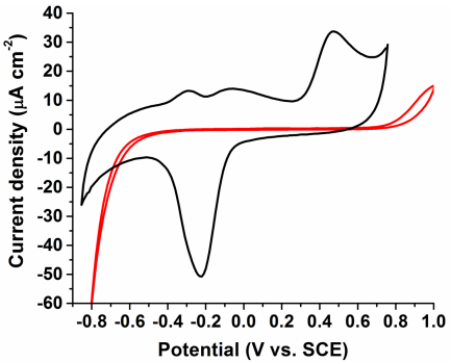

Figure 2.6 Representative cyclic voltammograms recorded at (black) c-BP and (red) l-BP electrodes in 0.1 mol L^{-1} PB (pH 7.0) solution at 20 mV s^{-1}

Next the electron transfer reactivity of c-BP and l-BP electrodes with four different redox probes was evaluated by cyclic voltammetry experiments. The midpoint potential (E_m), peak-to-peak potential separation (ΔE_P), electroactive surface area (ECSA) and heterogeneous rate constant (k°) of the BP electrodes are summarized in

Table 2.3. The ECSA were estimated from cyclic voltammetry performed on BP electrodes (Ø = 10 mm) at varying scan rates according to the Randles-Sevcik equation (**Equation 2.1**):

$$I_p = (2.69 \times 10^5)\, n^{3/2} A D^{1/2} C v^{1/2} \qquad (2.1)$$

where I_p (A) is the peak current, n is the number of electrons transferred in the redox reaction, A (cm^2) is the area of the electrode, C (mol cm^{-3}) is the concentration of the redox species, D ($cm^2\ s^{-1}$) is the diffusion coefficient and v ($V\ s^{-1}$) is the scan rate.

Cyclic voltammetry was first performed using a GCE (Ø = 3 mm) at varying scan rates to determine the diffusion coefficient of the redox probes from linear plots of peak current versus the square root of the scan rate. The diffusion coefficients were estimated from CVs scans recorded on glassy carbon electrode with a known geometric area (0.0707 cm^2) and immersed in 1 mmol L^{-1} redox probes in PB solution. They were found as follow: 5.67×10^{-8} $cm^2\ s^{-1}$ for $Ru(NH_3)_6^{3+/2+}$, 4.42×10^{-6} $cm^2\ s^{-1}$ for $Fc^{+/0}$, and 2.03×10^{-6} $cm^2\ s^{-1}$ for $Fe(CN)_6^{3-/4-}$.

The heterogeneous electron transfer rate constant was calculated based on the Nicholson method.[38] The electron transfer kinetics at carbon electrodes depend on the electronic and surface structure of the electrode and the nature of the redox probe used,[37,39] hence several different redox probes were assessed. Initially, experiments were performed with $Ru(NH_3)_6^{3+/2+}$ and $FcMeOH^{+/0}$, which are outer-sphere redox probes that are relatively "insensitive" to electrode surface chemistry. Cyclic voltammograms (CVs) recorded at BP electrodes revealed well-defined and chemically reversible redox couples for the ruthenium and ferrocenemethanol probes at c-BP and l-BP (**Figure 2.7A** and **Figure 2.7B**). Similar midpoint potential and peak potential separation values to those obtained at GCE are observed (**Table 2.3**).

Table 2.3 Midpoint potential, peak separation, electroactive area and heterogeneous rate constant for $FcMeOH^{0/+}$, $[Ru(NH_3)_6]^{3+/2+}$, $[Fe(CN)_6]^{3-/4-}$, and $Fe^{2+/3+}$ obtained at GCE, l-BP and c-BP electrodes

Electrode	Redox probe	E_m / V	ΔE_p[a] / mV	Active area / cm^2	Rate constant / cm s^{-1}
GCE	$Ru(NH_3)_6^{3+/2+}$	-0.24	70.5	0.07	nd
c-BP		-0.27	70.5	5.39 ± 2.09	nd
l-BP		-0.24	73.0	0.47 ± 0.26	nd
GCE	$FcMeOH^{0/+}$	0.20	70.5	0.07	nd
c-BP		0.20	70.5	1.53 ± 0.13	$(1.25 \pm 0.33) \times 10^{-2}$
l-BP		0.19	80.6	0.50 ± 0.18	$(1.83 \pm 0.09) \times 10^{-2}$
GCE	$Fe(CN)_6^{3-/4-}$	0.20	157.8	0.07	$(5.45 \pm 3.18) \times 10^{-4}$
c-BP		0.19	nd	nd	nd

l-BP		0.20	128.8	0.56 ± 0.36	(1.36 ± 0.72) × 10^{-3}
GCE		0.45	513.6	nd	nd
c-BP	$Fe^{3+/2+}$	0.42	125.9	nd	nd
l-BP		0.50	412.9	nd	nd

[a] Obtained at a scan rate of 20 mV s^{-1}. (nd) not defined.

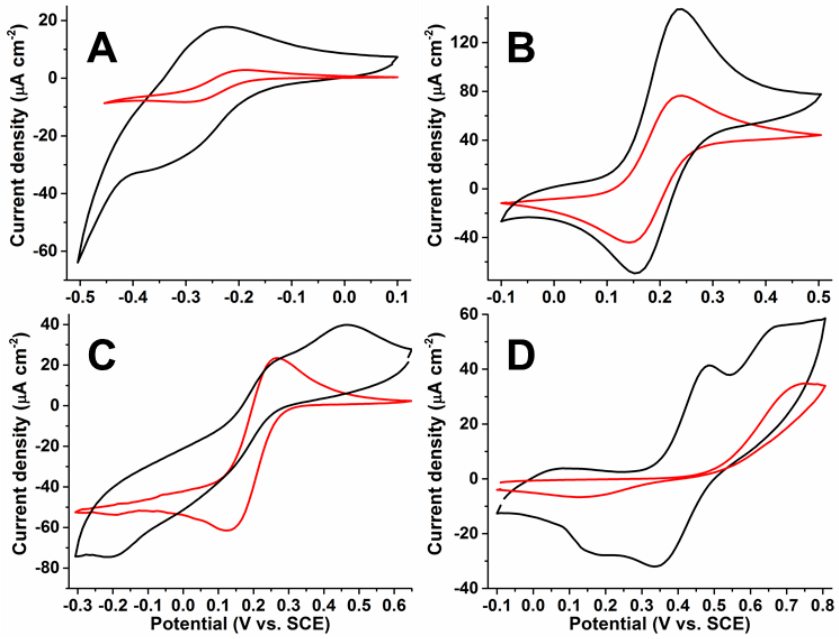

Figure 2.7 Representative cyclic voltammograms recorded at c-BP (black) and l-BP (red) electrodes in 1 mmol L^{-1} redox probe solutions: (A) $Ru(NH_3)_6^{3+/2+}$, (B) $FcMeOH^{+/0}$, and (C) $Fe(CN)_6^{3-/4-}$ in 0.1 mol L^{-1} PB pH 7.0, and (D) $Fe^{3+/2+}$ in 0.5 mol L^{-1} H_2SO_4. Scan rate: 20 mV s^{-1}

A less well-defined cathodic peak was observed for $Ru(NH_3)_6^{3+/2+}$ at c-BP, which suffers from interference due to the reduction of surface oxygen and the presence of the adsorbed complex. Both the ruthenium and ferrocenemethanol redox probes were used to estimate the electroactive surface area (ECSA) of lab-made and commercial buckypapers. ECSA values of *ca.* 0.5 ± 0.3 cm^2 were observed for both probes at l-BP. In contrast, c-BP showed much larger ECSA values of 1.5 ± 0.1 and 5.4 ± 2.1 cm^2 for $FcMeOH^{+/0}$ and $Ru(NH_3)_6^{3+/2+}$, respectively. The ECSA data therefore suggests that c-BP has a larger surface area which could be contrary to the total specific surface area values calculated by gas adsorption, and the SEM images. The smaller ECSA values observed at l-BP suggest that the structure is less permeable to positive and neutral redox species in aqueous solution. As a result, the total volume of the pores in the l-BP structure is not effectively contacted by the redox probe solutions. In contrast, the more loosely packed structure of c-BP (**Figure 2.1**) better facilitates the diffusion of the electrolyte (and hence the redox probes) into the bulk structure. The CVs

obtained at c-BP, but not l-BP, also show evidence for the weak adsorption of both the ferrocene and ruthenium species as larger oxidative peaks than reduction peaks were observed. The adsorbed electroactive species contribute to the peak current and therefore, to some extent, result in an overestimation of the ECSA values at c-BP. The ECSA value at c-BP was 3.5-fold larger using the larger $Ru(NH_3)_6^{3+/2+}$ probe which reflects that this complex adsorbs to a greater extent at c-BP compared to FcMeOH. The adsorption of positively charged $Ru(NH_3)_6^{3+/2+}$ and $FcMeOH^+$ at c-BP can occur *via* electrostatic interactions between surface bound oxygen residues, which would be negatively charged at neutral pH, and the positively charged oxidized species. The possibility that the reduced neutral form of FcMeOH adsorbs at the oxidized graphitic surface is not ruled out.[40]

Electron transfer rates at the buckypapers were estimated based on the $FcMeOH^{+/0}$ probe and revealed slower heterogeneous electron transfer at c-BP compared to l-BP, which is attributed to differences in the physical and electronic structure of the CNTs. For example, Banks *et al.* have shown that catalytic electron transfer on CNTs relies on edge-plane sites and tube ends.[41] It is possible that l-BP, which has shorter and smaller diameter CNT bundles with a more defective structure, benefit from having more exposed edge-plane like sites.

$Fe(CN)_6^{3-/4-}$ is a well-known surface-sensitive redox probe. At c-BP, the redox peaks for this probe are poorly defined. In addition to the weak signal, we observe the redox activity of the oxide groups at -0.2 V and 0.5 V. The ferricyanide redox couple was unfortunately not sufficiently resolved at c-BP to obtain kinetic or surface area data. A well-defined electrochemical response, similar to that observed at GCE, was observed at l-BP. Faster electron transfer by more than 2-fold was observed at l-BP compared to glass carbon electrode (GCE), highlighting the benefits of l-BP as an advanced type of carbon electrode. Both GCE and l-BP exhibited slower electron transfer kinetics towards $Fe(CN)_6^{3-/4-}$ compared to $Ru(NH_3)_6^{3+/2+}$, which is typical for carbon electrodes.[37] The estimated ECSA value for l-BP of 0.56 cm^2 using $Fe(CN)_6^{3-/4-}$ is very similar to the *ca.* 0.5 cm^2 areas estimated using the ferrocene and ruthenium probes at l-BP. The similar ECSA values for all three probes suggests that l-BP is less sensitive to charged species and adsorption effects compared to c-BP.

To further assess the presence and activity of oxygen species on the CNT surface of c-BP, a more specific surface-sensitive redox probe was also investigated. The $Fe^{3+/2+}$ redox probe was chosen as it is known to be highly sensitive to surface oxide.[30] CVs

recorded at the oxygen-rich c-BP showed a reversible couple of the probe with a small peak separation of 126 mV, consistent with "fast" apparent electron transfer kinetics. Additional redox peaks were also present, which appear to be due to the presence of the surface oxide groups which promote a positive shift in potential. In contrast, a much larger peak separation of 413 mV was observed at l-BP, highlighting slower electron transfer behavior at l-BP compared to c-BP. The exact nature of the complex redox behavior is not clear. Nevertheless, the data obtained using the $Fe^{3+/2+}$ probe, which reveals a strong interaction of the iron complex with c-BP but not l-BP, provides supporting evidence for the presence of surface oxygen groups.

2.3.3 Bioelectrocatalytic activity of BOx-modified commercial and lab-made BPs

The buckypapers were investigated for the construction of enzymatic bioelectrodes for bioelectrocatalysis. In this study, the bioelectrocatalytic reduction of O_2 to water was explored. Oxygen reduction reaction (ORR) is currently the most studied reaction for cathodes in enzymatic biofuel cell research. ORR is investigated here, using adsorbed BOx as the biocatalyst, and relies on direct electron transfer between the electrode and the tri-nuclear Cu centre of the immobilized enzymes.

Figure 2.8A shows CVs recorded for bioelectrocatalytic O_2 reduction at BOx modified l-BP and c-BP electrodes. Under O_2-saturated conditions, both BPs displayed onset potentials of 0.51 ± 0.01 V, which is in good agreement with DET mechanism through the T1 Cu center (the theoretical value of the $E_{T1, Cu}$ = 0.43 V *vs.* SCE).[42] For c-BP, the catalytic current density (J_{cat}) is negligible (-23 ± 15 µA cm^{-2}). For l-BP, the catalytic current density was 9-fold larger and reached -214 ± 74 µA cm^{-2} at 0.3 V. This current density is similar to our previous results obtained at unmodified BP with adsorbed BOx (-225 ± 91 µA cm^{-2}) under equivalent conditions.[15] The improvement in DET–type bioelectrocatalysis for unmodified l-BP compared to unmodified c-BP was expected as l-BP has a significantly higher total specific BET surface area and a more defective CNT structure (e.g. more reactive vacancies). Although c-BP electrodes show larger electroactive surface area, the experiments for determination of the ECSA values with different redox probes were performed at a time scale of several minutes. For bioelectrocatalytic studies, enzymes were left to adsorb overnight on the surface, allowing enzymes to diffuse into the BP

matrix.

Enhancements in DET at BOx modified CNT electrodes are also strongly related to the presence of negatively-charged surface groups which orientate the enzyme *via* arginine residues near the T1 Cu center.[43–45] It was therefore postulated that the oxygen-rich c-BP, with negatively-charged surface groups at pH 7.0, would promote a stronger DET response compared to l-BP. This is however not the case. The surface charge and the presence of oxygen groups are therefore relatively insignificant factors for DET bioelectrocatalysis at buckypaper. Hence, the overall charge of the BOx at pH 7.0 (pI = 4.1) is apparently not a crucial factor for its orientation. On the contrary, a large specific surface area and the type and structure of CNTs in the buckypaper (e.g. the π-π network and CNT dimensions[5,43,46,47]) are expected to play a greater role in favoring BOx immobilization. For example, concerning the type of CNTs used, Mugurama *et al.* elegantly reported the importance of the size of CNTs for achieving DET-type bioelectrocatalysis.[46]

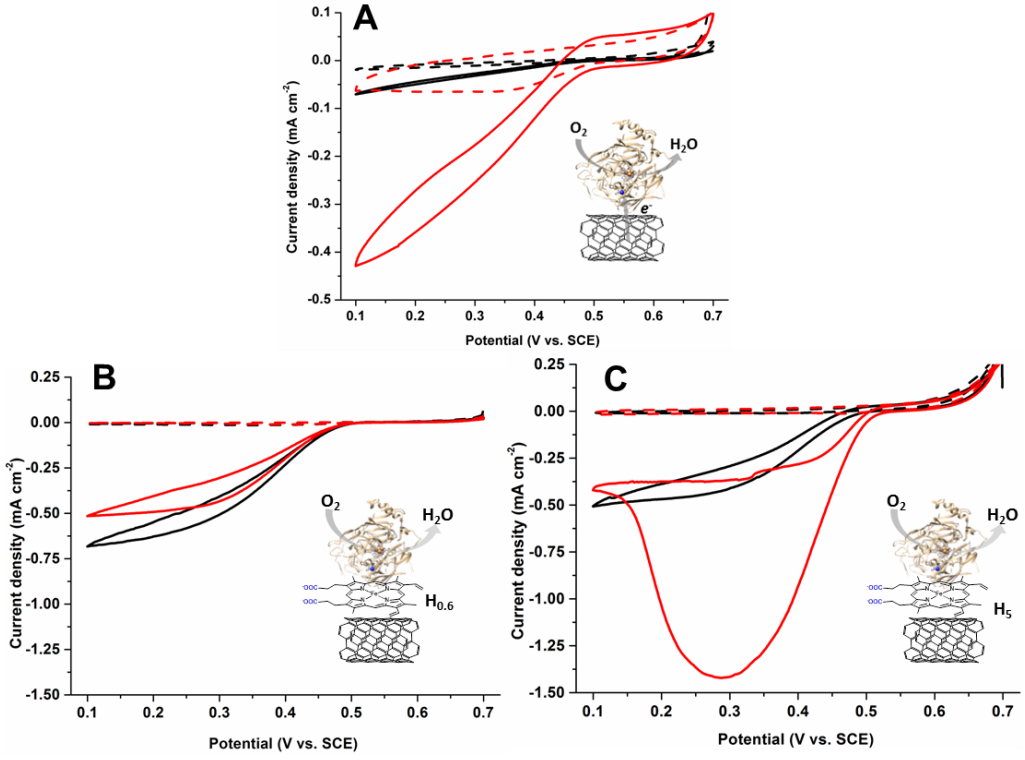

Figure 2.8 Representative cyclic voltammograms for (A) unmodified, (B) $H_{0.6}$ and (C) H_5 modified c-BPs (black) and l-BPs (red) with adsorbed BOx at the electrode surfaces in quiescent (dashes) Ar-saturated or (lines) O_2-saturated in pH 7.0 PB solution (1 mV s^{-1}, 1st scan displayed)

Next, the role of CNT size on the DET bioelectrocatalysis with immobilized BOx was considered. Based on the average outer diameter of the CNTs of c-BP, estimated

from SEM images, the nanotubes of c-BP were postulated to represent a flatter surface upon interaction with the enzyme (assuming the tube as a disk near the pocket). **Figure 2.9** shows a 3D structural view of the enzyme and highlights the hydrophilic substrate pocket, where the active site is located. Based on the distances between each arginine residue, the pocket is estimated to be 1.5 nm in width. To estimate the relative area of an individual tube (represented as a disk) which enters the substrate pocket, the angle describing the arc length of the substrate pocket for the tube was calculated. The larger the angle, the more the individual tube can penetrate inside the pocket. As an example, a hypothetical 1.5 nm diameter tube, which would perfectly fill the entrance of the substrate pocket, would have a 180° arc angle and would represent 50% of the total area of the disk described. On this basis, the arc angle for an average CNT tube of c-BP (ca. 137 nm diameter based on SEM imaging) is only 1.3°. Consequently, the arc segment area of an average CNT in c-BP that could penetrate the pocket would represent only 0.00003% of its total projected disk area. In contrast, the average CNT of l-BP (ca. 15 nm diameter based on SEM imaging) can better penetrate the substrate pocket with an arc angle of 11.5° representing 0.02% of the total projected disk area of the CNT entering the substrate pocket.

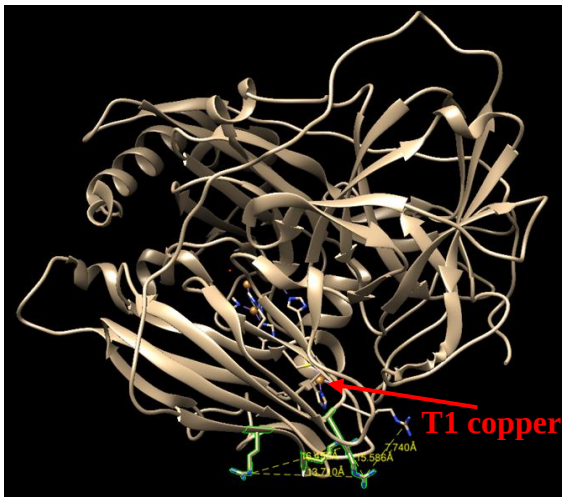

Figure 2.9 Resolved bilirubin oxidase protein structure from *Myrothecium verrucaria* highlighting four arginine residues located near the T1 copper centre of the enzyme. (PDB code: 2XLL)

With the aim to increase the favorable adsorption and orientation of BOx on the electrode, the two different buckypapers were modified with hemin, an iron-protoporphyrin with a substrate-like structure, *via* π-π stacking interactions.[15,44] Hemin-modified BP electrodes (c-BP-H and l-BP-H) were prepared by drop-casting

0.6, 5 or 10 mmol L^{-1} hemin solutions prepared in DMF onto the different BP electrodes. Data from cyclic voltammetry studies performed in PB are summarized in **Table 2.4**. The presence of the $Fe^{2+/3+}$ redox signal from hemin observed at $E_{1/2}$ = -0.330 ± 0.045 V was utilized to evaluate the surface coverage of electroactive porphyrin groups after π-π stacking immobilization on the CNT network of the BP. The surface coverage of hemin molecules was calculated by integration of the anodic peaks of CVs recorded at 20 mV s^{-1}, according to **Equation 2.2**.

$$\Gamma = \frac{Q}{nF\mathrm{A}^*} \qquad (2.2)$$

where Q is the integrated charge, F is the Faraday constant, A^* is the geometric area of the BP electrode, and n is the number of electrons transferred.

Increasing the hemin concentration of the modifier solution resulted in an increase in the porphyrin surface coverage for the buckypaper electrodes for the three concentrations investigated at both l-BP and c-BP. As a result, unambiguous enhancements were observed in the bioelectrocatalytic currents recorded in the presence of saturated O_2 for the hemin-modified BP electrodes. As shown in **Figure 2.8B**, the c-BP-$H_{0.6}$ and l-BP-$H_{0.6}$ electrodes displayed onset potentials of *ca.* 0.53 V compared to *ca.* 0.51 V at the unmodified electrodes (**Figure 2.8A**). The improved onset potentials and more pronounced ORR slope at hemin modified BP is consistent with more efficient direct electron transfer and an improved thermodynamic driving force between the CNTs and the redox site of the enzyme. More specifically, it results from an improved orientation of the T1 redox center oriented towards the CNT walls due to the carboxylic groups of the porphyrin and its π-π conjugated system.[43,44,48]

Table 2.4 Electrochemical characterization data for hemin modified c-BP and l-BP electrodes from 0.6, 5, 10 mmol L^{-1} modifier solutions

Electrode	**$E_{1/2}$ / V**	**ΔE_p [a] / mV**	**Γ_H [b] / 10^{-8} mol cm^{-2}**	
c-BP-$H_{0.6}$	-0.26	75.5	1.7 ± 0.2	(2)
l-BP-$H_{0.6}$	-0.35	17.3	0.07 ± 0.03	(4)
c-BP-H_5	-0.31	161.1	10.8 ± 2.0	(2)
l-BP-H_5	-0.38	141.0	31.8 ± 18.6	(3)
c-BP-H_{10}	-0.32	171.2	20.2 ± 2.1	(2)
l-BP-H_{10}	-0.38	214.8	58.7 ± 20.9	(5)

[a] obtained at a scan rate of 20 mV s^{-1}; [b] calculated using the geometric surface area of BP electrodes (Ø = 10 mm).

The number in brackets corresponds to the number of samples tested

For convenience in the comparison between the two sets of BPs, the performance was compared based on the catalytic current densities measured at 0.3 V during the forward scan in quiescent O_2-saturated PB solution. For c-BP-H samples, J_{cat} were -506 ± 11 µA cm^{-2}, -296 ± 145 µA cm^{-2} and -142 ± 71 µA cm^{-2}, for electrodes modified with 0.6, 5 and 10 mmol L^{-1} hemin modifier solutions, respectively. This result shows that the use of modifier concentrations beyond 0.6 mmol L^{-1}, or surface coverage $\geqslant$ 1.7 ± 0.2 × 10^{-8} mol cm^{-2}, does not improve the adsorption and orientation of BOx at c-BP. In fact, c-BP-H electrodes prepared with 10- to 20-fold higher surface coverage of hemin had a negative impact on DET bioelectrocatalysis. It is considered that all immobilized enzymes were well oriented at low modifier concentration and the further increase of modifier concentration only leads to slower electron transfer kinetics.

At l-BP-H, the catalytic current densities drastically increased with increasing modifier concentration from 0.6 mmol L^{-1} to 5 mmol L^{-1} then remained constant after use of 10 mmol L^{-1} modifier solution. The highest catalytic current density reached was -1336 ± 191 µA cm^{-2} at 0.3 V in O_2-saturated PB solution when the surface coverage of porphyrin groups was 31.8 ± 18.6 × 10^{-8} mol cm^{-2} (**Figure 2.8C**). As was observed for c-BP, the modification of l-BP with hemin groups clearly improved the electrocatalytic efficiency of the oxygen reduction reaction. The results obtained for c-BP-H and l-BP-H highlight limitations for the commercial buckypaper (**Table 2.5**). Under the best conditions, the catalytic current at c-BP-H was more than two-fold smaller than that observed at l-BP-H. Furthermore, the use of high surface coverages of hemin beyond 1.7 ± 0.2 ×10^{-8} mol cm^{-2} enhanced DET bioelectrocatalysis at lab-made buckypaper whereas detrimental effects on catalysis were observed at commercial buckypaper. The different physical structures of the BP samples (e.g. porosity and CNT size) are largely responsible for these results. For example, the BJH pore volume is significantly higher for l-BP compared to c-BP (see **Table 2.1**), and therefore, l-BP benefits from significantly more mesopores which can accommodate higher loadings of BOx. Sugimoto *et al.* have highlighted the importance of mesoporous structures for enhancing DET in a recent paper using Ketjen black electrodes.[5] The beneficial enzyme penetration effect due to the smaller CNTs of lab-made buckypaper is also considered to be an important factor after modification

of the surface with porphyrin molecules.

Table 2.5 Catalytic performance data for unmodified and hemin modified c-BP and l-BP electrodes

Electrode	E_{onset} [a] / mV	J_{cat} [b] / μA cm^{-2}	
c-BP	506 ± 10	-23 ± 15	(3)
l-BP	510 ± 10	-214 ± 74	(3)
c-BP-$H_{0.6}$	526 ± 2	-506 ± 11	(2)
l-BP-$H_{0.6}$	528 ± 6	-330 ± 88	(4)
c-BP-H_5	505 ± 7	-296 ± 145	(2)
l-BP-H_5	542 ± 8	-1336 ± 191	(3)
c-BP-H_{10}	480 ± 4	-142 ± 71	(2)
l-BP-H_{10}	539 ± 6	-1313 ± 61	(5)

[a] for oxygen reduction reaction under oxygen-saturated conditions with no purging or convection; [b] obtained at 0.3 V during the forward scan at 1 mV s^{-1}. Number in brackets represents the number of samples for each configuration.

Another key difference in the electrocatalytic behavior between the lab-made and commercial buckypaper electrodes is that, at the best performing l-BP-H_5 electrode, a large catalytic reduction peak was observed at 0.3 V which reached a pseudo "steady-state" at 0.1 V (J_{cat} = -0.420 mA cm^{-2}) (**Figure 2.8**). It is noted that similar behavior was also observed at l-BP-H_{10} electrode (**Figure 2.10**). This is in sharp contrast to the "resistive slope" observed at unmodified BP (reflecting random enzyme orientation, **Figure 2.8A**) and the well-defined steady state-type voltammograms observed at c-BP-H electrodes. The catalytic peak behavior was only observed during the forward scan and is attributed to a mass transport limitation of dissolved O_2 through the compact 3D mesoporous architecture of the electrode. On the reverse scan, no peak is observed as less oxygen is available in the bulk structure. It is also evident that the slope of the catalytic reduction wave at l-BP-H_5 (**Figure 2.8C**) and l-BP-H_{10} (**Figure 2.10**) is significantly steeper compared to the responses observed at the hemin-modified c-BP electrodes, consistent with a faster rate of oxygen reduction owing not only to the presence of high coverage of hemin but also higher loadings of oriented BOx.

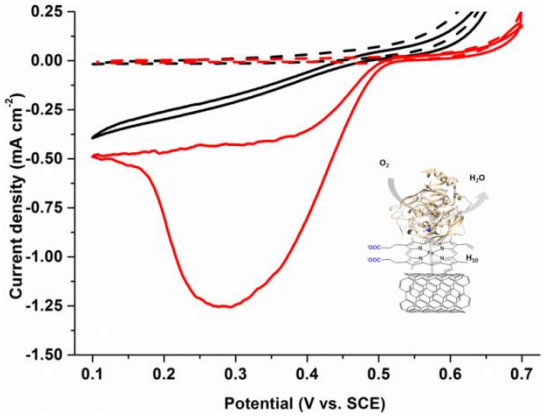

Figure 2.10 Representative cyclic voltammograms for (black) c-BP-H_{10} and (red) l-BP-H_{10} with adsorbed BOx in quiescent (dashes) Ar-saturated and (lines) O_2-saturated 0.1 mol L^{-1} PB solution at pH 7.0 (1 mV s^{-1}, 1st scan displayed)

Experiments performed in the absence of oxygen with the hemin-modified BP electrodes with immobilized BOx revealed the possibility to directly observe the T1 Cu redox couple of the enzyme, but only at the l-BP electrode (**Figure 2.11**). In fact, the redox couple of the Cu site was only observed for electrodes prepared with high surface coverage of $>1.32 \times 10^{-7}$ mol cm^{-2}. This direct redox response of the enzyme was not observed at c-BP electrodes prepared with similarly high surface coverage and hence the superior electrical connection of the enzyme is attributed specifically to the unique mesoporous structure and the size of the CNTs present in the l-BP electrode.

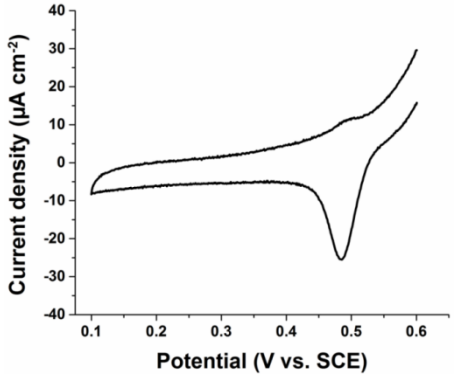

Figure 2.11 Representative cyclic voltammograms for l-BP-H_5 with adsorbed BOx in quiescent Ar-saturated 0.1 mol L^{-1} PB at pH 7 (1 mV s^{-1}, 2nd scan displayed) showing the T1 copper centre at E_p = 0.490 V *vs.* SCE

Similar to hemin, the surface concentration of enzyme can be extracted for the peak height of the CV curves. In order to avoid overestimation of this value if residual O_2 was present in the solution or in the bulk of the electrode, we only took into account

the oxidation peak (non-catalytic) of the T1 Cu center. From this peak of the T1 site (see **Figure 2.11**), the average surface coverage of enzyme on l-BP-H_5 and l-BP-H_{10} was estimated to be 2.73×10^{-10} mol cm^{-2}, which is a significantly higher enzyme loading compared to that previously reported at CNT modified GC electrodes with immobilized BOx (5.0×10^{-12} mol cm^{-2}).[44]

2.4 Conclusion

In this study, the comparison of different grades of buckypaper (commercial and lab-made) was performed in order to assess their physicochemical and catalytic behavior. Very different physicochemical properties were reported, and these were found to greatly influence the bioelectrocatalytic performance. Commercial BP possesses a higher oxygen content but more ordered and looser structure with significantly wider diameter nanotubes compared to our lab-made BP. Electrochemical characterisation experiments revealed complexity for the commercial BP owing to the presence of electroactive oxygen groups which also promoted adsorption of positively-charged redox species and suffered from a short potential window for a carbon electrode. The electrochemical potential window for l-BP was 1.6 V and the redox probe behavior was very classical to quasi-reversible systems compared to other carbon electrodes. The electroactive surface area data contradicted the BET surface area measurements. The lower than expected electroactive surface area at l-BP suggests that the charged redox species did not effectively diffuse into the denser mesoporous structure of l-BP during the time scale of the experiment. Additionally, the electroactive surface area of c-BP is likely overestimated due to adsorption effects *via* the negatively-charged surface oxygen at pH 7.0.

BP electrodes modified with BOx were studied and the best catalytic performance at unmodified and hemin-modified electrodes was obtained at l-BP. At unmodified BP, negligible DET was observed at commercial BP compared to the lab-made counterpart. This suggests that the negatively charged oxygen groups did not promote DET catalysis and that the structure of c-BP was less well suited to effective enzyme adsorption and orientation. At hemin-modified CNT electrodes functionalized with DET promoting porphyrin groups, enhanced currents were observed. The DET enhancement at l-BP was superior and gave a current density of -1.32 mA cm^{-2} and a very pronounced slope for the bioelectrocatalytic wave. Furthermore, the T1 Cu centre was only observed using the l-BP, and only for high surface loadings of

porphyrin. The data points that highly mesoporous surface but also a high coverage of hemin are required for effective DET-type bioelectrocatalysis with BOx at l-BP. This is in contrast to c-BP which requires comparatively lower hemin coverage to obtain optimal catalytic current outputs. This appears to be related to the 9-times smaller BET surface area and likely similar reduction in the enzyme loading. All in all, this report gives the baseline for electrochemical properties of two prominent types of BP and demonstrates that several interdependent physico-chemical "features" play a large role in the efficiency and complexity of bioelectrocatalytic systems.

2.5 Experimental section

2.5.1 Materials and reagents

Potassium phosphate dibasic, potassium phosphate monobasic, *N*,*N*-dimethylformamide (DMF, 99.9%), hexaammineruthenium (III) chloride ($Ru(NH_3)_6$, 98%), hemin (iron-protoporphyrin, ≥97%), potassium hexacyanoferrate(III) ($Fe(CN)_6$, ≥99.0%), sulfuric acid (95-97%) were purchased from Sigma-Aldrich. Ferrocenemethanol (FcMeOH, 97%) was purchased from Acros Organics. Iron (II) sulfate heptahydrate (≥99.0%) was purchased from Prolabo. Bilirubin oxidase (BOx) from *Myrothecium verrucaria* (E.C. 1.3.3.5, estimated activity: 8.36 U mg^{-1})[49] was purchased from Amano Enzyme. Commercial MWCNT proprietary blend buckypaper (c-BP) with reference number NTL-12218 was obtained from NanoTechLabs, Inc. Multi-walled carbon nanotubes (MWCNTs) (Ø = 9.5 nm, purity >95%, 1.5 μm length) were obtained from Nanocyl and used for lab-made buckypaper (l-BP) fabrication. Distilled deionized water (15 MΩ) was obtained from an ELGA PURELAB purification system. Oxygen and argon were purchased from Air Liquide (France). Potassium phosphate buffer (PB) was prepared from potassium phosphate dibasic and potassium phosphate monobasic solutions and adjusted to pH 7.0.

2.5.2 Characterization methods

2.5.2.1 Morphology

High resolution images of BP morphology were obtained using a FEI/Quanta FEG 250 scanning electron microscope (SEM, Hillsboro, OR, USA) with an accelerating voltage of 5 kV. Cross-sectional images of the interlayer structures were snapped after

gently breaking the BP samples.

2.5.2.2 Physical

BP thicknesses were measured using vernier calipers. BP electrical conductivity was measured using a Keithley 2450 SourceMeter with an S-302-4 mounting stand and SP4 four-point probe head. Average values were obtained from 2 conductivity measurements taken on 3 independent samples per BP type.

Surface area and pore size were obtained from nitrogen sorption measurements using a NOVA surface area analyzer (Quantachrome Instruments). BP samples were first outgassed at 40 °C for 15 h. N_2 adsorption/desorption isotherms were obtained at 77 K. Specific surface area and pore sizes were determined from the desorption branch using the BET and BJH methods, respectively.

Water contact angles were obtained at room temperature after delivering a 5 µL droplet of water onto the sample surface using a Dataphysics OCA 35 system. Average values were obtained from at least 5 independent samples.

Surface roughness was investigated by profilometry using a Bruker Contour K 3D Optical Microscope. Root mean square roughness (rms) was estimated from images with a size of 126 × 94 µm.

2.5.2.3 Spectroscopy

X-ray photoelectron spectroscopy (XPS) data was obtained using an ESCALAB 250 from Thermo Scientific with a monochromated Al Kα band (1486.6 eV) as the excitation source. The diameter of the surface spot analyzed was 400 µm. Survey spectra were recorded from 0 to 1200 eV and referenced to the sp^2 carbon energy contribution (C=C) C1s at 284.4 eV.

SEM-Energy dispersive x-ray spectrometry (EDS) analysis was performed using a Zeiss Ultra 55 microscope at 15 kV.

Raman spectra were collected using a WITec alpha300 RA system equipped with a He/Ne laser (λ = 633 nm) and a Zeiss 50× objective. The data was normalized to the highest peak intensity.

2.5.2.4 Electrochemistry

Electrochemical studies were performed on an Eco Chemie Autolab PGSTAT 100 potentiostat with Nova 2.0 software. The three-electrode system consisted of a BP or glassy carbon (GCE) electrode as the working electrode, a saturated calomel electrode

SCE (KCl_{sat}) as the reference electrode, and a platinum wire as the auxiliary electrode. All solutions for voltammetric studies were purged with argon or oxygen gas for 15 min before measurements and a gas flow was maintained on top of the solution during analysis. All experiments were conducted at room temperature. Cyclic voltammograms (CVs) for electrochemical characterization of BP were recorded at a scan rate of 20 mV s^{-1}. CVs for enzyme-catalyzed oxygen reduction were recorded with a relatively slow scan rate of 1 mV s^{-1} to phase out most of the capacitive current contribution. All experiments were performed in a 5 mL volume of 0.1 mol L^{-1} PB (pH 7.0) solution. Catalytic onset potentials were determined from the foot of the electrocatalytic wave.

2.5.3 Procedures

2.5.3.1 Preparation of buckypaper electrodes and bioelectrodes

Lab-made BP was fabricated based on a vacuum filtration method developed in our previous work.[15] A MWCNT dispersion of 1 mg mL^{-1} was first prepared in DMF with 30 min sonication using a Bandelin sonorex RK100 ultrasonic bath. 58 mL of the as-prepared suspension was then filtrated using a diaphragm pump (MZ 2C NT model, Vaccubrand) on a Millipore PTFE filter (JHWP, 0.45 μm pore size). The resulting l-BP was rinsed with water, to facilitate the removal of residual DMF, left under vacuum for 1 h, then left to dry in air overnight. The volume of the suspension was calculated to match the mass density of the commercial buckypaper (60 gsm).

For chemical modification, BP was first cut into individual disk electrodes (Ø = 10 mm). 150 µL of hemin solution in DMF was drop coated onto the smooth side of the BP electrode and left to dry in air. An electrical wire was subsequently attached to the back of the electrode then sealed using carbon paste and silicone paste, respectively.

For preparation of bioelectrodes, BOx was immobilized by drop-casting 150 µL of 5 mg mL^{-1} BOx in PB solution onto the electrode surface and leaving the enzyme to adsorb overnight at 4 °C. The electrodes and bioelectrodes were rinsed in PB buffer prior to electrochemical testing.

References

1. Trifonov, A. *et al.* Enzyme-Capped Relay-Functionalized Mesoporous Carbon Nanoparticles: Effective Bioelectrocatalytic Matrices for Sensing and Biofuel Cell Applications. *ACS Nano* **7**, 11358–11368 (2013).
2. Tsujimura, S., Murata, K. & Akatsuka, W. Exceptionally High Glucose Current on a Hierarchically Structured Porous Carbon Electrode with 'Wired' Flavin Adenine Dinucleotide-Dependent Glucose Dehydrogenase. *J. Am. Chem. Soc.* **136**, 14432–14437 (2014).
3. Cosnier, S., J. Gross, A., Le Goff, A. & Holzinger, M. Recent advances on enzymatic glucose/oxygen and hydrogen/oxygen biofuel cells: Achievements and limitations. *Journal of Power Sources* **325**, 252–263 (2016).
4. Minteer, S. D., Atanassov, P., Luckarift, H. R. & Johnson, G. R. New materials for biological fuel cells. *Materials Today* **15**, 166–173 (2012).
5. Sugimoto, Y., Kitazumi, Y., Shirai, O. & Kano, K. Effects of Mesoporous Structures on Direct Electron Transfer-Type Bioelectrocatalysis: Facts and Simulation on a Three-Dimensional Model of Random Orientation of Enzymes. *Electrochemistry* **85**, 82–87 (2017).
6. Cosnier, S., Holzinger, M. & Le Goff, A. Recent Advances in Carbon Nanotube-Based Enzymatic Fuel Cells. *Front. Bioeng. Biotechnol.* **2**, (2014).
7. Xia, H. *et al.* Factors affecting the interaction between carbon nanotubes and redox enzymes in direct electron transfer-type bioelectrocatalysis. *Bioelectrochemistry* **118**, 70–74 (2017).
8. Lalaoui, N., Holzinger, M., Le Goff, A. & Cosnier, S. Diazonium Functionalisation of Carbon Nanotubes for Specific Orientation of Multicopper Oxidases: Controlling Electron Entry Points and Oxygen Diffusion to the Enzyme. *Chemistry - A European Journal* **22**, 10494–10500 (2016).
9. Meredith, M. T. *et al.* Anthracene-Modified Multi-Walled Carbon Nanotubes as Direct Electron Transfer Scaffolds for Enzymatic Oxygen Reduction. *ACS Catal.* **1**, 1683–1690 (2011).
10. Jönsson-Niedziolka, M., Kaminska, A. & Opallo, M. Pyrene-functionalised single-walled carbon nanotubes for mediatorless dioxygen bioelectrocatalysis. *Electrochimica Acta* **55**, 8744–8750 (2010).
11. Giroud, F., Sawada, K., Taya, M. & Cosnier, S. 5,5-Dithiobis(2-nitrobenzoic acid) pyrene derivative-carbon nanotube electrodes for NADH electrooxidation and oriented immobilization of multicopper oxidases for the development of glucose/O2 biofuel cells. *Biosensors and Bioelectronics* **87**, 957–963 (2017).
12. Gross, A. J. *et al.* Robust bifunctional buckypapers from carbon nanotubes and polynorbornene copolymers for flexible engineering of enzymatic bioelectrodes. *Carbon* **107**, 542–547 (2016).
13. Bourourou, M. *et al.* Freestanding redox buckypaper electrodes from multi-wall carbon nanotubes for bioelectrocatalytic oxygen reduction via mediated electron transfer. *Chemical Science* **5**, 2885 (2014).
14. Scherbahn, V. *et al.* Biofuel cells based on direct enzyme–electrode contacts using PQQ-dependent glucose dehydrogenase/bilirubin oxidase and modified carbon nanotube materials. *Biosensors and Bioelectronics* **61**, 631–638 (2014).
15. Gross, Andrew. J. *et al.* A High Power Buckypaper Biofuel Cell: Exploiting

1,10-Phenanthroline-5,6-dione with FAD-Dependent Dehydrogenase for Catalytically-Powerful Glucose Oxidation. *ACS Catal.* 4408–4416 (2017) doi:10.1021/acscatal.7b00738.

16. MacVittie, K. *et al.* From "cyborg" lobsters to a pacemaker powered by implantable biofuel cells. *Energy & Environmental Science* **6**, 81–86 (2013).
17. Hou, C. & Liu, A. An integrated device of enzymatic biofuel cells and supercapacitor for both efficient electric energy conversion and storage. *Electrochimica Acta* **245**, 303–308 (2017).
18. Halámková, L. *et al.* Implanted Biofuel Cell Operating in a Living Snail. *J. Am. Chem. Soc.* **134**, 5040–5043 (2012).
19. Reid, R. C., Minteer, S. D. & Gale, B. K. Contact lens biofuel cell tested in a synthetic tear solution. *Biosensors and Bioelectronics* **68**, 142–148 (2015).
20. Szczupak, A. *et al.* Living battery – biofuel cells operating in vivo in clams. *Energy & Environmental Science* **5**, 8891–8895 (2012).
21. Katz, E. & MacVittie, K. Implanted biofuel cells operating in vivo – methods, applications and perspectives – feature article. *Energy & Environmental Science* **6**, 2791–2803 (2013).
22. Rinzler, A. G. *et al.* Large-scale purification of single-wall carbon nanotubes: process, product, and characterization. *Appl Phys A* **67**, 29–37 (1998).
23. Hussein, L., Urban, G. & Krüger, M. Fabrication and characterization of buckypaper-based nanostructured electrodes as a novel material for biofuel cell applications. *Physical Chemistry Chemical Physics* **13**, 5831 (2011).
24. Villarrubia, C. W. N., Artyushkova, K., Garcia, S. O. & Atanassov, P. NAD+/NADH Tethering on MWNTs-Bucky Papers for Glucose Dehydrogenase-Based Anodes. *J. Electrochem. Soc.* **161**, H3020–H3028 (2014).
25. Stines-Chaumeil, C., Roussarie, E. & Mano, N. The nature of the rate-limiting step of blue multicopper oxidases: Homogeneous studies versus heterogeneous. *Biochimie Open* **4**, 36–40 (2017).
26. Cracknell, J. A., McNamara, T. P., Lowe, E. D. & Blanford, C. F. Bilirubin oxidase from Myrothecium verrucaria: X-ray determination of the complete crystal structure and a rational surface modification for enhanced electrocatalytic O2 reduction. *Dalton Transactions* **40**, 6668 (2011).
27. Hussein, L., Feng, Y. J., Alonso-Vante, N., Urban, G. & Krüger, M. Functionalized-carbon nanotube supported electrocatalysts and buckypaper-based biocathodes for glucose fuel cell applications. *Electrochimica Acta* **56**, 7659–7665 (2011).
28. Ciniciato, G. P. M. K. *et al.* Development of paper based electrodes: From air-breathing to paintable enzymatic cathodes. *Electrochimica Acta* **82**, 208–213 (2012).
29. Pankratov, D. V. *et al.* A Comparative Study of Biocathodes Based on Multiwall Carbon Nanotube Buckypapers Modified with Three Different Multicopper Oxidases. *Electroanalysis* **25**, 1143–1149 (2013).
30. Hussein, L. *et al.* A highly efficient buckypaper-based electrode material for mediatorless laccase-catalyzed dioxygen reduction. *Biosensors and Bioelectronics* **26**, 4133–4138 (2011).
31. Sing, K. The use of nitrogen adsorption for the characterisation of porous materials. *Colloids and Surfaces A: Physicochemical and Engineering Aspects* **187–188**, 3–9 (2001).

32. Gonçalves, A. G., Figueiredo, J. L., Órfão, J. J. M. & Pereira, M. F. R. Influence of the surface chemistry of multi-walled carbon nanotubes on their activity as ozonation catalysts. *Carbon* **48**, 4369–4381 (2010).
33. Zebda, A. *et al.* Mediatorless high-power glucose biofuel cells based on compressed carbon nanotube-enzyme electrodes. *Nature Communications* **2**, 370 (2011).
34. Edwards, E. R., Antunes, E. F., Botelho, E. C., Baldan, M. R. & Corat, E. J. Evaluation of residual iron in carbon nanotubes purified by acid treatments. *Applied Surface Science* **258**, 641–648 (2011).
35. Wenzel, R. N. Surface Roughness and Contact Angle. *J. Phys. Chem.* **53**, 1466–1467 (1949).
36. Zhang, J., Jiang, D., Peng, H.-X. & Qin, F. Enhanced mechanical and electrical properties of carbon nanotube buckypaper by in situ cross-linking. *Carbon* **63**, 125–132 (2013).
37. McCreery, R. L. Advanced Carbon Electrode Materials for Molecular Electrochemistry. *Chemical Reviews* **108**, 2646–2687 (2008).
38. NICHOLSON, R. S. Theory and Application of Cyclic Voltammetry f m Measurement of Electrode Reaction Kinetics. 7.
39. Chen, P. & McCreery, R. L. Control of Electron Transfer Kinetics at Glassy Carbon Electrodes by Specific Surface Modification. *Anal. Chem.* **68**, 3958–3965 (1996).
40. Maddar, F. M., Lazenby, R. A., Patel, A. N. & Unwin, P. R. Electrochemical oxidation of dihydronicotinamide adenine dinucleotide (NADH): comparison of highly oriented pyrolytic graphite (HOPG) and polycrystalline boron-doped diamond (pBDD) electrodes. *Phys. Chem. Chem. Phys.* **18**, 26404–26411 (2016).
41. Banks, C. E., Davies, T. J., Wildgoose, G. G. & Compton, R. G. Electrocatalysis at graphite and carbon nanotube modified electrodes: edge-plane sites and tube ends are the reactive sites. *Chem. Commun.* **0**, 829–841 (2005).
42. Christenson, A., Shleev, S., Mano, N., Heller, A. & Gorton, L. Redox potentials of the blue copper sites of bilirubin oxidases. *Biochimica et Biophysica Acta (BBA) - Bioenergetics* **1757**, 1634–1641 (2006).
43. Xia, H., Kitazumi, Y., Shirai, O. & Kano, K. Enhanced direct electron transfer-type bioelectrocatalysis of bilirubin oxidase on negatively charged aromatic compound-modified carbon electrode. *Journal of Electroanalytical Chemistry* **763**, 104–109 (2016).
44. Lalaoui, N., Le Goff, A., Holzinger, M. & Cosnier, S. Fully Oriented Bilirubin Oxidase on Porphyrin-Functionalized Carbon Nanotube Electrodes for Electrocatalytic Oxygen Reduction. *Chemistry - A European Journal* **21**, 16868–16873 (2015).
45. Mazurenko, I. *et al.* How the Intricate Interactions between Carbon Nanotubes and Two Bilirubin Oxidases Control Direct and Mediated O_2 Reduction. *ACS Applied Materials & Interfaces* **8**, 23074–23085 (2016).
46. Muguruma, H., Iwasa, H., Hidaka, H., Hiratsuka, A. & Uzawa, H. Mediatorless Direct Electron Transfer between Flavin Adenine Dinucleotide-Dependent Glucose Dehydrogenase and Single-Walled Carbon Nanotubes. *ACS Catalysis* **7**, 725–734 (2017).
47. So, K. *et al.* Significance of the Length of Carbon Nanotubes on the Bioelectrocatalytic Activity of Bilirubin Oxidase for Dioxygen Reduction. *Electrochimica Acta* **192**, 133–138 (2016).

48. So, K., Kitazumi, Y., Shirai, O. & Kano, K. Analysis of factors governing direct electron transfer-type bioelectrocatalysis of bilirubin oxidase at modified electrodes. *Journal of Electroanalytical Chemistry* **783**, 316–323 (2016).
49. Gross, A. J. *et al.* Redox-Active Glyconanoparticles as Electron Shuttles for Mediated Electron Transfer with Bilirubin Oxidase in Solution. *Journal of the American Chemical Society* **139**, 16076–16079 (2017).

Chapter 3:

Use of alginate hydrogel coating to improve stability of carbon nanotube bioanode for glucose oxidation

Chapter 3 Use of alginate hydrogel coating to improve stability of carbon nanotube bioanode for glucose oxidation

Résumé

Dans le chapitre 1, l'étude comparative sur le buckypaper commercial et celui conçu au laboratoire montre que ce dernier est un matériau prometteur pour la construction de bioélectrodes pour les biopiles à combustible enzymatiques. C'est pourquoi nous avons choisi de poursuivre la conception de bioélectrodes avec le buckypaper « fait-maison » comme matériau conducteur dans ce chapitre. Précédement, un nouveau type de buckypaper incorporant directement des molécules redox a été développé.[1] Plus précisément, pour l'anode, le buckypaper a été fonctionnalisé avec de la 1, 10-phénanthronline-5, 6-quninone (PLQ) en utilisant la méthode de fonctionnalisation “one-pot”. La PLQ a été utilisée comme médiateur de la glucose déshydrogénase dépendante à FAD. Cette bioanode a produit le courant catalytique le plus élevé parmi les bioanodes sur papier carboné jusqu’ici rapporté. Cependant, dans ce travail, la bioanode présente une faible stabilité par rapport à la biocathode à transfert direct d'électrons. Dans ce chapitre, l'objectif est d'améliorer la stabilité de la bioanode par l'utilisation d'un revêtement d'hydrogel comme couche protectrice.

Depuis l'invention du premier stimulateur cardiaque implantable, les dispositifs médicaux implantables (IMDs) ont fait l'objet d'une attention considérable et sont maintenant devenus une grande famille d'implants comprenant le stimulateur cardiaque, les neurostimulateurs, l'implant cochléaire, *etc*.[2] Pour les IMDs actifs, qui nécessitent une alimentation électrique pour fonctionner, il est très important de pouvoir compter sur une alimentation sûre et fiable. Les biopiles à combustible enzymatiques (EFCs) qui captent l'énergie directement des fluides corporels en convertissant l'énergie chimique du glucose et de l’oxygène ont été considérées comme des candidates prometteuses pour remplacer les piles actuelles utilisées pour alimenter les IMDs. Des EFCs ont déjà été implantées dans différentes organismes vivants (plantes et animaux).[3,4] Néanmoins, les bioélectrodes enzymatiques dont la durée de vie est relativement courte restent un défi majeur dans ce domaine pour envisager leur utilisation dans le domaine médical.[5]

Jusqu'à présent, la plupart des bioélectrodes ont été fabriquées par immobilisation d'enzymes et de médiateurs sur la surface de l'électrode pour assembler une EFC sans

compartiment. La faible durée de vie de la bioanode basée sur le système de transfert d'électrons à médiation peut être attribuée non seulement à la désorption des enzymes, à leur désactivation, mais aussi celles des médiateurs. Une stratégie régulièrement rencontrée pour améliorer la stabilité des électrodes consiste à immobiliser les médiateurs et les enzymes sur la surface des électrodes par fixation covalente. Cependant, la modification covalente peut entraîner une baisse de l'activité enzymatique et, par conséquent, une diminution de la performance.[6] La plupart des hydrogels de polymères déclarés piègent les enzymes par encapsulation et impliquent souvent une réticulation de ces dernières avec la matrice du polymère.[7,8] Une autre approche consiste à concevoir l'interface entre les électrodes modifiées par une enzyme et le milieu environnant avec un hydrogel polymère comme solution pour améliorer la stabilité de bioélectrode.

Reuillard *et al.* ont électrodéposé une membrane de polypyrrole-polystyrène sur la bioanode préparée à partir de pastilles MWCNT pour empêcher la rupture de l'électrode.[9] Dans ce travail, on a observé une perte de 20% du médiateur, la naphthoquinone (NQ). L'effet du revêtement n'est pas clair car aucun résultat n'a été montré pour les électrodes non revêtues. Xiao *et al.* ont étudié l'effet de différents revêtements polymères déposés sur une bioanode à base d'hydrogel de polymère redox contenant de la lactate oxydase.[10] L'électrode revêtue de poly(acrylique acide) a montré une plage de réponse linéaire accrue pour la détection du lactate et une stabilité améliorée après 12 h de fonctionnement. Récemment, l'utilisation de polymères à base de biomatériaux pour améliorer la biocompatibilité de l'interface de l'électrode a suscité un intérêt croissant. L'amélioration de la stabilité des biocathodes basée sur des enzymes de type transfert direct d'électrons a été rapportée par revêtement avec un hydrogel biocompatible.[11,12]

Ici, l'alginate est exploré comme matériau pour former un revêtement d'hydrogel sur la surface de l'électrode. L'alginate est un copolymère linéaire de polysaccharide naturel que l'on trouve dans les algues brunes et qui consiste en $_{\beta\text{-D}}$-mannuronate (bloc M) et en $_{\alpha\text{-L}}$-guluronate (G-bloc) (**Figure 3.1**).[13] En présence de cations divalents (*i.e.* calcium ions), l'alginate est capable de former de l'hydrogel dans le modèle «boîte à œufs» par réticulation ionique.[13,14] L'hydrogel d'alginate de calcium a déjà montré diverses applications biomédicales (cicatrisation des plaies,[15] ingénierie tissulaire,[16] *etc*.) en raison de ses propriétés toxiques.

Dans ce chapitre, l'utilisation d'un hydrogel d'alginate polymère biocompatible

comme couche protectrice a été étudiée pour des bioélectrodes modifiées par des médiateurs ou/et des enzymes. La **figure 3.2A** représente l'électrode revêtue d'hydrogel dans une configuration couche par couche. Le film d'hydrogel a été caractérisé par voie électrochimique et l'effet du revêtement d'hydrogel sur la stabilité à long terme et opérationnelle des bioélectrodes a été étudié. Les différents paramètres de fabrication de l'hydrogel ont été étudiés et optimisés pour permettre les bioélectrodes revêtues d'hydrogel les plus performantes.

Chapter 3 Use of alginate hydrogel coating to improve stability of carbon nanotube bioanode for glucose oxidation

3.1 Abstract

In chapter 2, the comparison study on commercial and lab-made buckypaper shows that the latter is a promising material for the construction of bioelectrode for enzymatic biofuel cell. Therefore lab-made buckypaper is chosen as the material in this chapter. In the previous work, the development of a new type of buckypaper with embedded redox-molecules has been described.[1] Specifically, for the anode, the buckypaper was functionalized with 1, 10-phenanthroline-5, 6-quninone (PLQ) using the "one-pot" functionalization method. PLQ was used as the mediator for FAD-dependent glucose dehydrogenase (FAD-GDH). This bioanode produced the highest catalytic current among the reported paper-based bioanodes. However, in this work, the bioanode showed poor stability compared to the direct electron transfer-type biocathode. In this chapter, the aim is to improve the stability of the bioanode by the use of hydrogel coating as a protective layer.

3.2 Introduction

Implantable medical devices (IMDs) have achieved tremendous attention since the invention of the first implantable pacemaker, and have now evolved into a large family of implants including pacemakers, neurostimulators, cochlear implants, *etc*.[2] For active IMDs, which require power supply for device operation, a safe and reliable power source is of great importance. Enzymatic biofuel cells (EFCs) that harvest energy directly from body fluids by converting chemical energy in glucose have been regarded as a promising candidate to replace current batteries used for IMDs. Implantable EFCs operated in different plants and animals have been described.[3,4] Nevertheless, the short life time bioelectrodes remains a major challenge in this field.[5]

Most bioelectrodes to date have been fabricated by immobilization of enzymes and mediators onto electrode surface to assemble a compartment-less biofuel cell. The poor lifetime of the bioanode based on mediated electron transfer system can be attributed to not only the leakage and deactivation of enzymes, but the mediators as well. A common strategy to improve electrode stability is to immobilize mediators and enzymes onto electrode surface by covalent attachment. However, covalent modification can lead to lower enzyme activity and hence decreases performance.[6]

Most reported polymer hydrogels entrap enzymes through encapsulation and often involve cross-linking with the polymer matrix.[7,8] An alternative approach is to engineer the interface between enzyme-modified electrodes and the surrounding environment with polymeric hydrogel as a solution to improve bioelectrode stability.

Reuillard *et al.* electrodeposited a polypyrrole-polystyrene membrane on the bioanode prepared from MWCNT pellet to prevent electrode breaking.[9] In this work, 20% loss of the mediator, naphthoquinone (NQ) was observed. The effect of coating is unclear as no results were shown for uncoated electrode. Xiao *et al.* investigated the effect of different polymer coating deposited onto a redox polymer hydrogelbioanode containing lactate oxidase.[10] The poly(acrylic acid) coated electrode showed increased linear response range for lactate detection and improved stability after 12 h operation. Recently, there are more interests in using biomaterial-based polymer to improve biocompatibility of the electrode interface. Improvement of biocathode stability based on direct electron transfer-type enzymes has been reported by coating with biocompatible hydrogel.[11,12]

Here, alginate is explored as the material to form hydrogel coating on electrode surface. Alginate is a natural linear polysaccharide copolymers found in brown algae consisted of $_{\beta\text{-D}}$-mannuronate (M-block) and $_{\alpha\text{-L}}$-guluronate (G-block) (**Figure 3.1**).[13] In the presence of divalent cations (*i.e.* calcium ions), alginate is able to form hydrogel in "egg-box" model through ionic cross-linking.[13,14] Calcium alginate hydrogel has already been used for various biomedical applications (wound healing,[15] tissue engineering,[16] *etc.*) due to its non-toxic properties.

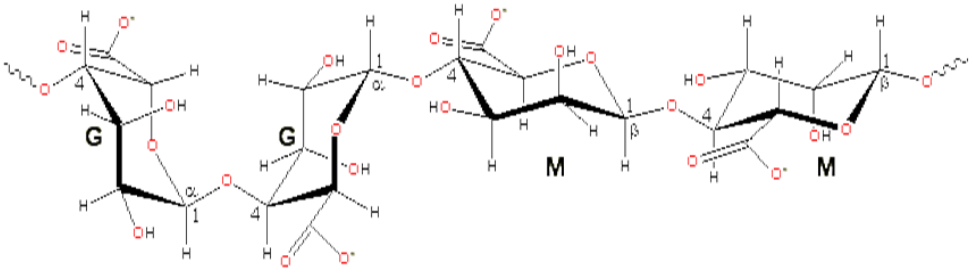

Figure 3.1 Alginate chain conformations.

In this chapter, the use of biocompatible polymer alginate hydrogel as a protective layer was investigated for bioelectrode modified with mediators and enzymes. **Figure 3.2A** depicts the hydrogel coated electrode in a layer-by-layer configuration. The hydrogel film was characterized electrochemically and the effect of hydrogel coating on the long-term and operational stability of bioelectrodes was investigated. The

different parameters of the hydrogel fabrication were investigated and optimized to allow the best performing hydrogel-coated bioelectrodes.

3.3 Results and discussion

3.3.1 Effect of hydrogel coating

3.3.1.1 Electrochemical characterization of the hydrogel-coated electrode

The 1, 10-phenanthronline-5, 6-quinone embedded buckypaper was fabricated based on previous published work from the laboratory,[1] followed by immobilization of FAD-GDH to obtain a glucose oxidizing bioanode (referred to as uncoated electrode in the following context). The alginate hydrogel is formed through ionic cross-linking in the presence of calcium ions. In order to form homogeneous hydrogel on the electrode surface, it is necessary to slow down the gelation process. Insoluble calcium carbonate ($CaCO_3$) and $_D$-glucono-δ-lactone (GDL) are used. The slow hydrolysis process of GDL can decrease the local pH, which then releases the calcium ions to cross-link with the alginate.[16] The reaction scheme is described below:

$$\text{D-glucono-δ-lactone} + H_2O \rightarrow \text{D-gluconic acid} + H^+$$

$$CaCO_3 + 2H^+ \rightarrow Ca^{2+} + H_2O + CO_2 \qquad (3.1)$$

In this work, a mixture of 40 μL consisted of alginate and $CaCO_3$ were deposited onto the buckypaper electrode surface (Ø = 6 mm). When the surface is dry, 40 μL of gluconolactone solution is drop-casted to allow slow formation of hydrogel.

The electrocatalytic performance of the uncoated and hydrogel-coated bioanode were evaluated by performing cyclic voltammetry at slow scan rates (1 mV s^{-1}) (**Figure 3.2B**). In the absence of glucose, a well-defined pair of peaks at $E_{1/2}$ = -0.11 V (*vs.* Ag/AgCl, pH 7.0) corresponding to the PLQ reversible redox couple is observed for the hydrogel-coated electrode, while two overlapping anodic peaks appear for the uncoated electrode. The difference in the redox systems may indicate the different microenvironments for the entrapped PLQ in the buckypaper in the presence or absence of alginate. As expected, based on the overlapping peak signal of the reduction peak, it can be claimed that the surface coverage for both configurations is similar. In the presence of 50 mmol L^{-1} glucose, electrocatalytic currents of both electrodes start to flow at low potential around -0.18 V while the cathodic wave intensity decrease. This confirms the role of PLQ in mediated bioelectrocatalytic oxidation of glucose. In terms of catalytic current density (J_{cat}), the uncoated

bioanodes reach 1490 ± 240 μA cm^{-2} at 0.2 V while the hydrogel-coated electrodes display lower values (750 ± 60 μA cm^{-2}) due to more severe mass transfer limitation.

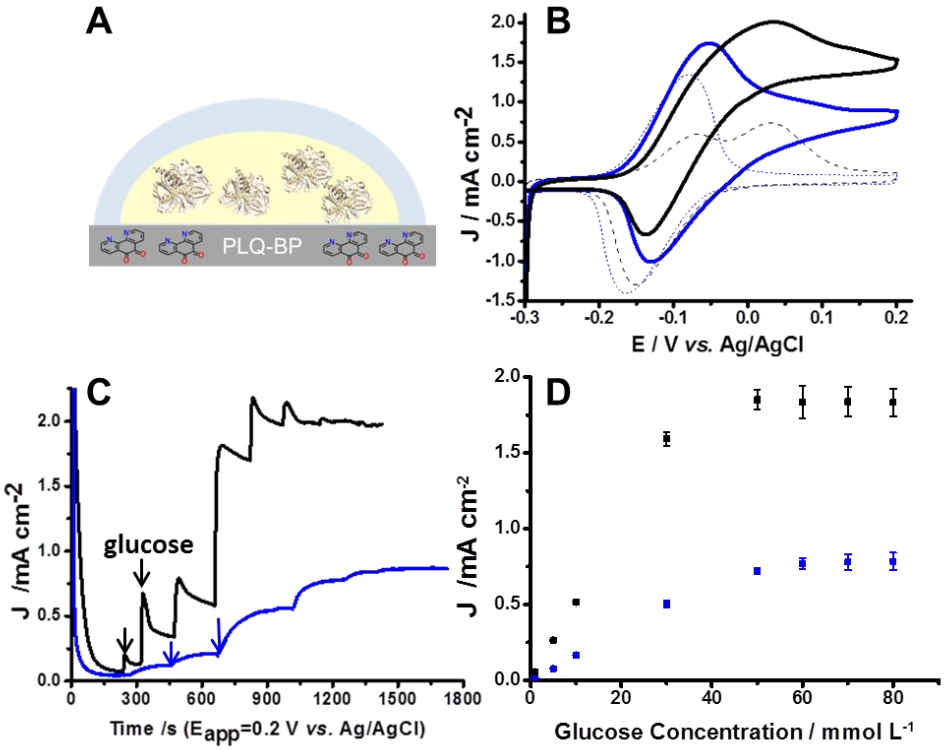

Figure 3.2 (A) Schematic representation of the hydrogel-coated bioanode(yellow layer: enzyme solution, blue layer: hydrogel coating); (B) representative cyclic voltammograms (CVs) of (black) uncoated and (blue) hydrogel-coated bianodes in 0.2 mol L^{-1} pH 7.0 HEPES in the (dash) absence and the (solid) presence of 50 mmol L^{-1} glucose (scan rate: 1 mV s^{-1}); (C) chronoamperograms (CAs) recorded at (black) uncoated and (blue) hydrogel-coated bianodes at E_{app}= 0.2 V *vs.* Ag/AgCl at different glucose concentrations in Ar saturated HEPES buffer pH 7.0 at 150 rpm; (D) plots of average current density obtained from (C) for different glucose concentrations recorded at (black) uncoated and (blue) hydrogel-coated bianodes.

To further verify the presence of the hydrogel coating, chronoamperometry was performed to probe the bioelectrocatalytic current at increasing glucose concentrations. As shown in **Figure 3.2C** and **Figure 3.2D**, for the hydrogel-coated electrode, much longer response time is required to reach steady-state current after each glucose injection and a lower current density is observed. Estimated apparent Michaelis constants K_m were derived from these experiments, which are 35.2 and 50.8 mmol L^{-1} for the uncoated and hydrogel-coated electrode, respectively. These results clearly confirm the presence of the hydrogel coating and show the significant effect of hydrogel diffusion barrier on the substrate diffusion efficiency from the bulk solution

to the electrode surface.

3.3.1.2 Storage stability of hydrogel coated electrode

To study the effect of an extra protective layer on the stability of the bioelectrode, cyclic voltammetry were performed daily in the absence and presence of glucose solution for electrodes with and without hydrogel coating. When electrodes are not tested, they are stored in HEPES buffer (with 2.5 mmol L^{-1} Ca^{2+}) in the absence of substrate at 4 °C. CVs obtained on day 0 and day 5 for both electrodes are shown in **Figure 3.3**. After 5 days of storage, the uncoated electrode only delivers 190 ± 230 μA cm^{-2} of catalytic current density, which accounts for only 15% of its initial value measured on day 0. The well-defined redox peaks have evolved into several overlapping undistinguishable peaks, which explain the loss of catalytic activity (**Figure 3.3A**). While for the hydrogel-coated electrode, the electrode is still active with 47% of the amount of PLQ and 45% of the catalytic current density remain on day 5 compared to the coated one (**Figure 3.3B**). The storage solution of both electrodes was also examined with Bradford reagent and enzymes were detected for both storage solutions, which indicate enzyme leakage from electrode surface to the solution. Nevertheless, the stability data, as summarized in **Table 3.1** demonstrates that the hydrogel coating layer allows for improved stability by better retention of mediator on electrode surface and possibly slows down the enzyme leakage process.

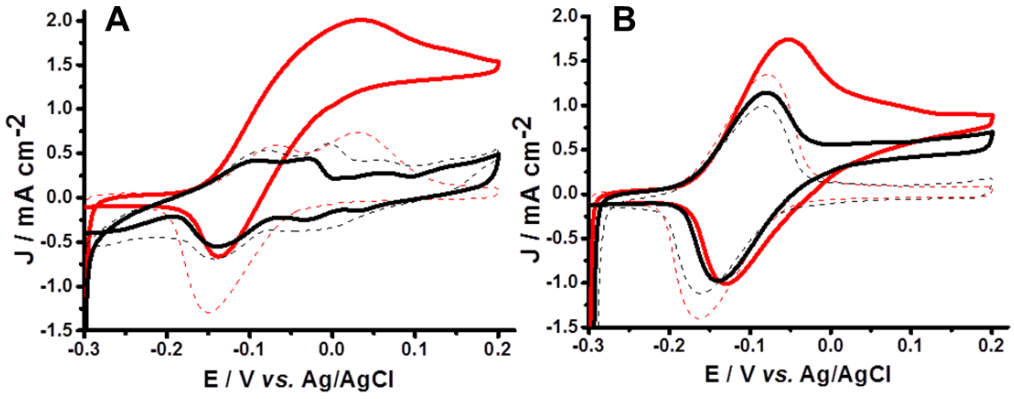

Figure 3.3 CVs recorded on (red) day 0 and (black) day 5 for (A) uncoated and (B) hydrogel-coated bianodes in 0.2 mol L^{-1} pH 7.0 HEPES in the (dash) absence and the (solid) presence of 50 mmol L^{-1} glucose (scan rate: 1 mV s^{-1}).

Table 3.1 Electrochemical and catalytic parameters for uncoated and hydrogel-coated BP_{PLQ} electrodes and BP_{PLQ}-GDH electrodes recorded on day 0 and day 5.

Electrode	Day	Γ_{PLQ} / 10^{-7} mol cm^{-2}	Relative stability	J_{cat} [a] / μA cm^{-2}	Relative stability	
BP_{PLQ}	0	2.7 ± 0.3	100%	/	/	(4)
	5	1.7 ± 0.5	65%			
BP_{PLQ}-gel	0	4.4 ± 0.3	100%	/	/	(4)
	5	3.3 ± 0.9	74%			
BP_{PLQ}-GDH	0	5.4 ± 1.3	100%	1490 ± 240	100%	(3)
	5	1.0 ± 0.9	17%	190 ± 230	15%	
BP_{PLQ}-GDH-gel	0	5.0 ± 0.8	100%	750 ± 60	100%	(5)
	5	2.3 ± 1.3	47%	340 ± 120	45%	

[a] J_{cat} background subtracted at 0.2V; calculated using the geometric surface area of BP electrodes (Ø = 6 mm). The number in brackets corresponds to the number of samples tested

Effect of hydrogel coating was also evaluated on bare electrodes without enzyme modification. As shown in **Figure 3.4A**, a higher PLQ surface coverage was observed for the hydrogel-coated electrodes. Previous study showed that the PLQ-embedded buckypaper surface is hydrophobic.[1] The increased surface coverage may be ascribed to the hydrophilic nature of the hydrogel, which improves the accessibility of the PLQ molecule entrapped in the electrode structure. The PLQ stability of bare electrodes was evaluated for one week. For both uncoated and hydrogel coated electrodes, the PLQ stability is much superior compared to their enzyme-modified counterparts (**Figure 3.4B**). On day 5, 65% and 74% of the amount of the PLQ initially observed on BP_{PLQ} and BP_{PLQ}-gel remained on the electrodes, in contrast to 17% and 47% for BP_{PLQ}-GDH and BP_{PLQ}-GDH-gel, respectively. This indicates the important impact of enzymes on the stability of the mediator entrapped in the electrode structure.. On one hand, the immobilization of protein increased hydrophilicity of the BP matrix and therefore displayed higher PLQ surface coverage (**Figure 3.4C**), leading to more PLQ being washed away by the buffer solution. On the other hand, although the exact mechanism is unclear, this could result from the progressive disconnection of the PLQ molecule within the buckypaper matrix in the process of electron shuttling between enzymes and the electrode. It should be noted that for both bare and enzyme-modified electrodes, the presence of hydrogel coating improves the stability of the mediator.

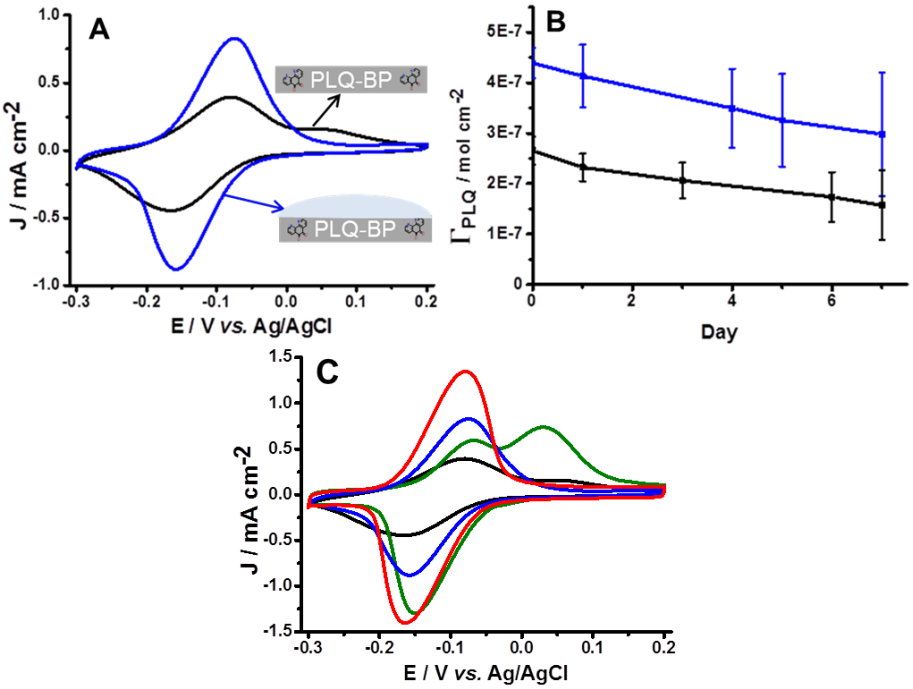

Figure 3.4 (A) CVs recorded on day 0 and for (black) uncoated and (blue) hydrogel-coated BP_{PLQ} in 0.2 mol L^{-1} pH 7.0 HEPES (scan rate: 1 mV s^{-1}); (B) evolution of PLQ surface coverage for (black) uncoated and (blue) hydrogel-coated BP_{PLQ} as a function of storage time; (C) overlay of CV scans recorded on day 0 in the absence of glucose in HEPES buffer for (black) uncoated BP_{PLQ}, (blue) hydrogel-coated BP_{PLQ}-gel, (green) uncoated bioanode BP_{PLQ}-FADGDH and (red) hydrogel-coated bioanode BP_{PLQ}-FADGDH-gel electrodes.

3.3.2 Optimization of hydrogel fabrication parameters

3.3.2.1 Comparison of hydrogels with different parameters

The different fabrication parameters can give rise to different hydrogel structure, which can lead to different effects on bioanode stability. For example, pore size of the hydrogel is an important parameter. The pore size of the hydrogel should be smaller than the size of the enzyme to prevent leaching from the surface. This is related to the concentration of the cross-linker, types of cross-linking method (in-situ gelation using $CaCO_3$ or diffusion gelation using $CaCl_2$, respectively).[17] Another factor to consider is the mass transfer efficiency. This is directly related to the thickness of the hydrogel layer, which can be modified by the volume of the drop-casting solution. It is evident that thicker hydrogel can cause slower substrate diffusion, but may be beneficial for retaining mediators and enzymes. The stability of the hydrogel itself is also important. The degradation of the hydrogel coating can happen as Ca^{2+} ions slowly diffuse out of

the matrix and result in change of the hydrogel structure.

Here, the effect of the thickness of hydrogel was investigated by using different drop-casting volumes of alginate mixture. Carbon nanotube is also exploited to improve conductivity and mechanical strength of the hydrogel.

Important remark:

In the following part of experiments, a different type of multi-walled CNT (MWCNT) with 90% carbon purity instead of MWCNT with 95% carbon purity obtained from Nanocyl was used to fabricate buckypaper. The supplier changed the production protocol for making the 95 % MWCNTs. The new formulation of the 95 % carbon purity MWCNTs samples was not suitable for making BP anymore. Consequently, a different type of MWCNTs had to be used to maintain the same fabrication procedures in this chapter.

For uncoated electrode, smaller PLQ surface coverage and lower catalytic current were observed for electrode prepared using CNTs with 90% carbon purity compared to CNT with 95% carbon purity. This may indicate the negative impact of impurities on the enzyme activity. Previously, impurities including metallic and carbonaceous of CNTs have been shown to have strong influence on the electrochemical properties.[18] On day 5, the uncoated electrode completely loses activity with negligible PLQ surface coverage and catalytic current (**Figure 3.5A**).

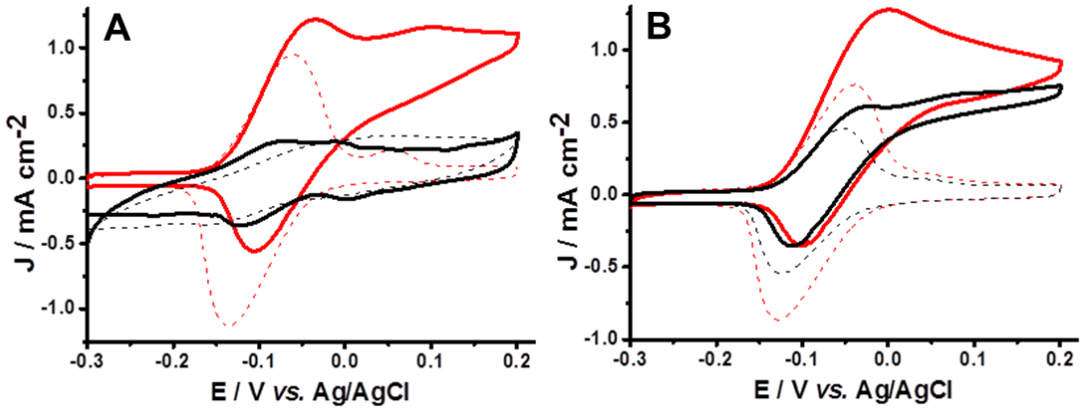

Figure 3.5 CVs recorded on (red) day 0 and (black) day 5 for (A) uncoated and (B) CNT incorporated hydrogel-coated bianodes in 0.2 mol L^{-1} pH 7.0 HEPES in the (dash) absence and the (solid) presence of 50 mmol L^{-1} glucose (scan rate: 1 mV s^{-1}).

Next, enzyme-modified BP_{PLQ} electrodes coated with different hydrogels were prepared by drop-casting 40 µL, 10 µL of alginate mixtures or 10 µL of CNT/alginate mixture onto electrode surface. The stability of these electrodes was evaluated and the

stability data obtained from CVs are summarized in **Table 3.2**. All three types of hydrogel coating lead to smaller catalytic currents due to diffusion barrier. Among them, the electrode coated with 10 μL of alginate mixtures presents the highest catalytic current on day 1, which is expected as diffusion is faster for thinner hydrogel. After 5 days of storage, for electrodes coated with 40 μL or 10 μL of alginate mixtures, less than 30% of the initial catalytic currents remain. The low stability may indicate that the hydrogel is not effective in preventing enzyme leakage from electrode surface.

The best performing bioelectrode on day 5 is the one coated with 10 μL of CNT/alginate mixture (**Figure 3.5B**). CNTs have been widely used to fabricate CNT/polymer composite electrodes in various research fields due to their excellent electronic and mechanical properties.[19–21] As shown in **Table 3.2**, similar PLQ surface coverage was achieved on day 5 for the three hydrogel-coated electrodes while higher catalytic current was obtained for the electrode coated with CNT/alginate mixture (67 % of residual activity). This could be explained by the improved conductivity and mechanical strength of the hydrogel. More detailed physicochemical studies are shown in the following section.

Table 3.2 Electrochemical and catalytic parameters for uncoated BP_{PLQ}-GDH electrodes and BP_{PLQ}-GDH coated with different hydrogel configurations recorded on day 0 and day 5 (MWCNTs with 90 % carbon purity are used here).

Electrode[a]	**Day**	Γ_{PLQ} **/ 10^{-7} mol cm^{-2}**	**Relative stability**	J_{cat} **[b] / μA cm^{-2}**	**Relative stability**	
BP_{PLQ}-GDH	0	3.0 ± 1.1	100%	1120 ± 250	100%	(7)
	5	0.2 ± 0.2	6%	60 ± 90	6%	
40uL gel	0	3.0 ± 0.9	100%	660 ± 180	100%	(3)
	5	1.1 ± 0.6	35%	180 ± 90	27%	
10uL gel	0	3.9 ± 0.2	100%	940 ± 70	100%	(2)
	5	1.1 ± 0.2	28%	210 ± 50	23%	
10uL gel with CNT	0	3.1 ± 0.7	100%	650 ± 210	100%	(6)
	5	1.2 ± 0.6	38%	430 ± 170	67%	

[a] Electrode fabricated using CNTs with 90% carbon purity; [b] J_{cat} background subtracted at 0.2 V; calculated using the geometric surface area of BP electrodes (Ø = 6 mm). The number in brackets corresponds to the number of samples tested

3.3.2.2 Characterization of the bioelectrode with optimized hydrogel coating

Figure 3.6 shows the optical images for the CNT incorporated hydrogel-coated electrode in wet and dry conditions. Optical microscopy is chosen as a simple method to probe the presence of the hydrogel on the electrode surface. A hydrophilic porous network of hydrogel is formed when fully hydrated.

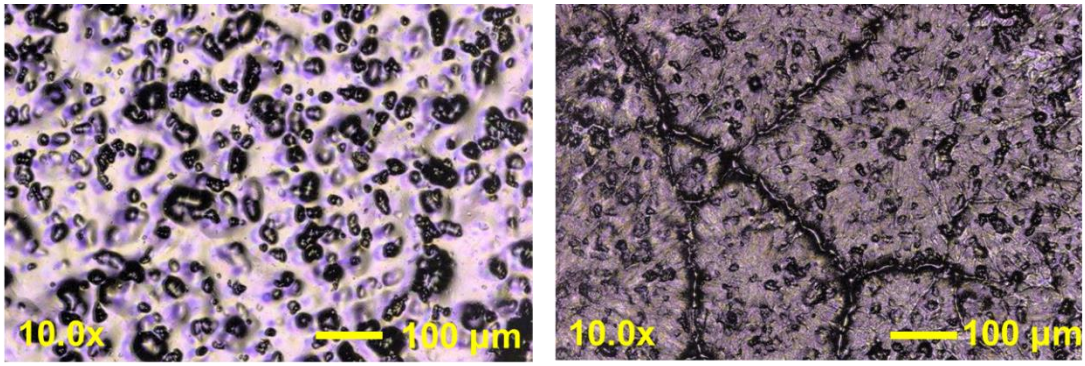

Figure 3.6 Optical images of the CNT incorporated hydrogel-coated bioanode in (left) wet and (right) dry conditions.

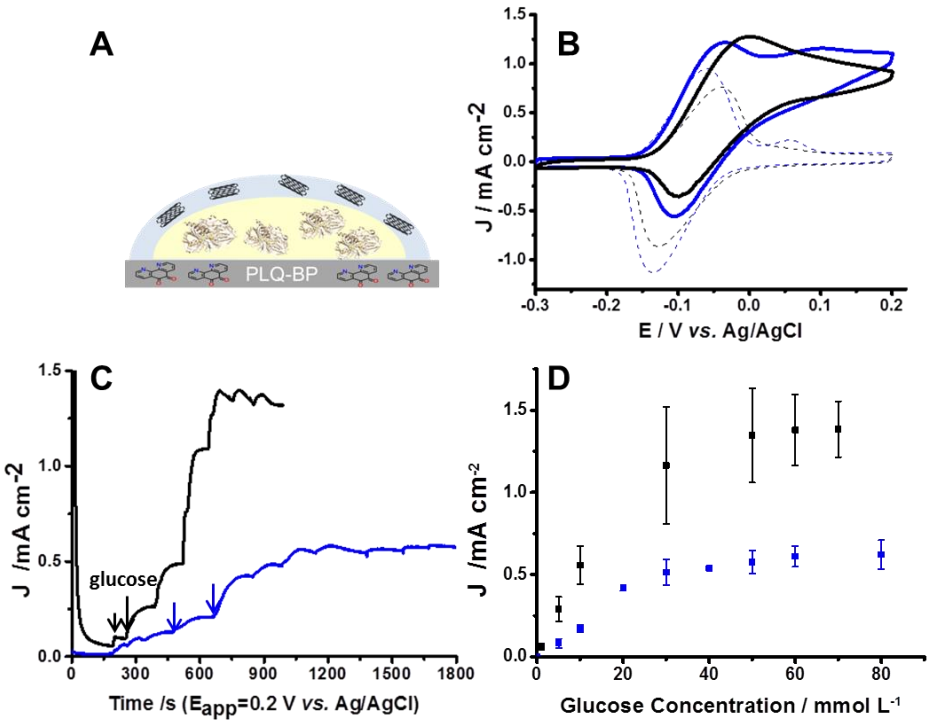

Figure 3.7 (A) Schematic representation of the CNT incorporated hydrogel-coated bioanode (yellow layer: enzyme solution, blue layer: CNT/hydrogel coating); (B) representative CVs of (black) uncoated and (blue) CNT incorporated hydrogel-coated bianodes in 0.2 mol L^{-1} pH 7.0 HEPES in the (dash) absence and the (solid) presence of 50 mmol L^{-1} glucose (scan rate: 1 mV s^{-1}); (C) chronoamperograms recorded at (black) uncoated and (blue) CNT incorporated hydrogel-coated bianodes at E_{app}= 0.2 V *vs.*

Ag/AgCl at different glucose concentrations in Ar saturated HEPES buffer pH 7.0 at 150 rpm; (D) plots of average current density obtained for different glucose concentrations recorded at (black) uncoated and (blue) CNT incorporated hydrogel-coated bianodes.

The same cyclic voltammetry and chronoamperometry procedures were used to characterize the catalytic performance of the uncoated and hydrogel-coated bioanode (**Figure 3.7**). Longer response time in CAs shows the presence of diffusion barrier. In terms of catalytic current density, the uncoated bioanodes reached 1120 ± 250 μA cm^{-2} at 0.2 V while the hydrogel-coated electrodes delivered 650 ± 210 μA cm^{-2}. The similar trend in electrochemical behavior confirms the versatility of this approach to prepare hydrogel-coated bioelectrodes.

Continuous operation stability of bioelectrodes was investigated by performing chronoamperometry measurement at 0.2 V for 16 h in glucose solution. The catalytic current of uncoated electrode decreased to 30% of its initial value in 3 h and continued to decrease to 10% in the following 13 h (**Figure 3.8A**) In contrast, the hydrogel-coated electrode still delivered current density of 490 μA cm^{-2} after 16 h (~63% of its initial value). The evolution of PLQ surface coverage and catalytic current before and after 16 h of operation were recorded using cyclic voltammetry (**Figure 3.8B** and **3.8C**). These results indicate that the presence of a CNT incorporated hydrogel allows for a better storage and operational stability of bioelectrode.

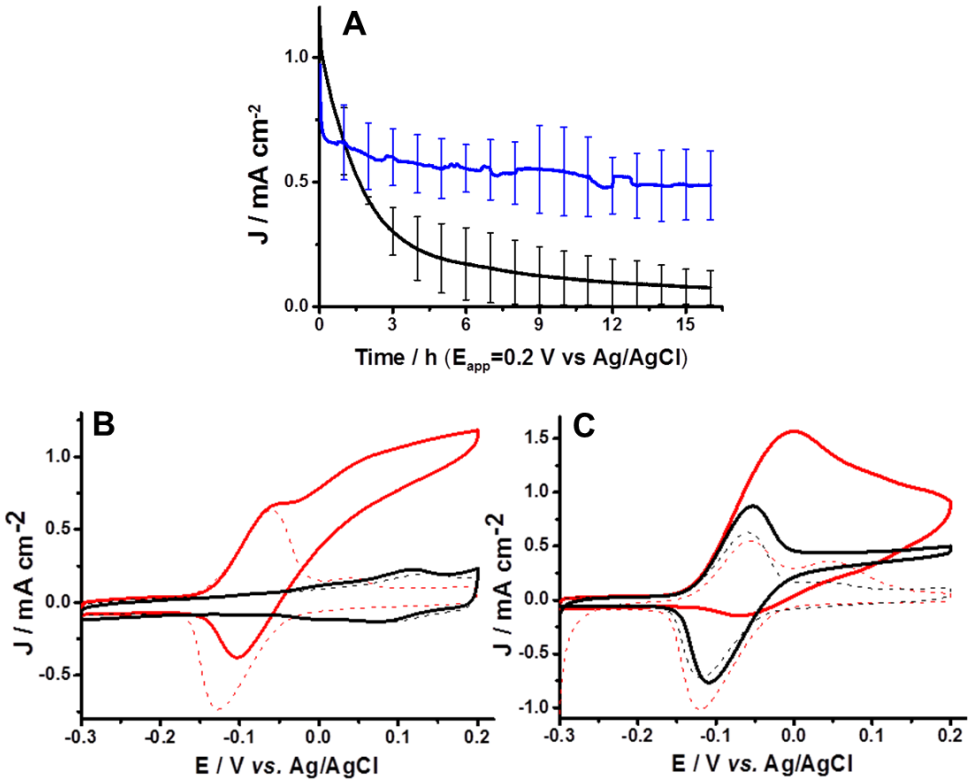

Figure 3.8 (A) CAs recorded at (black) uncoated and (blue) CNT incorporated hydrogel-coated bianodes at E_{app}= 0.2 V *vs.* Ag/AgCl for 16 h with 50 mmol L^{-1} glucose in Ar saturated HEPES buffer pH 7.0 at 150 rpm; CVs recorded (red) before and (black) after 16 h continuously operation for (B) uncoated and (C) CNT incorporated hydrogel-coated bianodes in 0.2 mol L^{-1} pH 7.0 HEPES in the (dash) absence and the (solid) presence of 50 mmol L^{-1} glucose (scan rate: 1 mV s^{-1}).

3.4 Conclusion

In conclusion, this work demonstrates the fabrication of hydrogel-coated electrode in a layer-by-layer configuration using alginate and assessed the effect on bioanode stability. Buckypaper electrodes prepared from two different types of CNTs were constructed and tested. The impurity level in CNTs has an influence on the ability to form buckypaper and on the electrochemical performance, as higher catalytic currents were observed for CNTs with higher carbon purity. The effect of the presence of the hydrogel coating was assessed by adapting different fabrication parameters. First, the presence of hydrogel layer decreased the catalytic current due to slower mass transfer efficiency of the substrate within the hydrogel film as revealed by cyclic voltammetry and choronoamperometry studies. Second, both storage and operational stability were improved when compared to uncoated electrode. Finally, the best performing electrode was identified as the one coated with hydrogel prepared from CNT/alginate

mixture, retaining 67% of its catalytic current after 5 days of storage or 63% after 16 h of continuous operation at 0.2 V. In the future work, instead of commercial alginate used in work, it can be envisioned to use chemically modified alginate with specific molecule to provide suitable anchor point (*i.e.* pyrene) to improve stability of the hydrogel film on electrode surface.

3.5 Experimental Section

3.5.1 Materials and reagents

N,*N*-dimethylformamide (DMF, 99.9%), 1,10-phenanthroline-5,6-dione (PLQ, 97%), $_{D}$-(+)-glucose (≥99.5%), sodium chloride (NaCl, 99.8%), calcium carbonate ($CaCO_3$, 99.0%), calcium chloride dihydrate ($CaCl_2 \cdot 2H_2O$, 99.9%), $_{D}$-glucono-δ-lactone (GDL), HEPES, sodium hydroxide (NaOH, pellet) were purchased from Sigma-Aldrich. Alginic acid sodium salt was obtained from Fluka. Flavin adenine dinucleotide-dependent glucose dehydrogenase (FAD-GDH, 1150 U mg^{-1} solid) from *Aspergillus sp.* was purchased from Sekisui Diagnostics (UK). Two different types of multi-walled carbon nanotubes MWCNTs (Ø = 9.5 nm, 1.5 μm length, ≥95% purity and Ø = 9.5 nm, 1.5 μm length, ≥90% purity) were obtained from Nanocyl. HEPES buffer used for electrochemical measurements contained 0.2 mol L^{-1} HEPES and 0.1 mol L^{-1} NaCl and was adjusted to pH 7.0 using NaOH pellets. Ca/HEPES Buffer solution for electrode storage was supplemented with 2.5 mmol L^{-1} $CaCl_2 \cdot 2H_2O$. Deionized (dI) water (18 MΩ) was obtained from a Millipore Ultrapure system and used to prepare solutions.

3.5.2 Preparation of FAD-GDH modified buckypaper bioanodes

The buckypaper bioélectrodes were prepared according to the procedure reported in our previous work.[1] In brief, 1 mg mL^{-1} of MWCNT (95% or 90% carbon purity) suspension was prepared in DMF and sonicated for 30 min. PLQ was dissolved in a minimum volume of DMF and added to MWCNT suspension to give a 2 mmol L^{-1} final concentration, followed by 30 min of sonication. 66 mL of the homogenous suspension was then filtrated through a PTFE membrane using a diaphragm pump. The following rinsing and drying procedures were the same as those described in chapter 2 (section 2.5.3.1).

For enzyme modification, BP was first cut into individual disk electrodes (Ø = 6

mm). FAD-GDH was immobilized by drop-casting 54 µL of 3 mg mL^{-1} FAD-GDH in HEPES buffer onto the electrode surface and leaving the enzyme to adsorb overnight at 4 °C.

3.5.3 Preparation of alginate hydrogel-coated bioanodes

Alginate (Alg) mixture was prepared by adding sodium alginate and calcium carbonate in dI water to give a final concentration of 20 mg mL^{-1} and 80 mmol L^{-1}, respectively. For CNT incorporated hydrogel, MWCNTs were also added to give a concentration of 2 mg mL^{-1}. The mixture was left to stir overnight to obtain a homogeneous dispersion.

To prepare hydrogel-coated electrode in "layer-by-layer" configuration, various volumes (10 and 40 µL) of Alg/$CaCO_3$ mixture were drop-casted onto the enzyme-modified electrode. The electrode was allowed to dry in air, and then the same volume of 160 mmol L^{-1} of GDL solution was added to the electrode surface. The electrode was then left overnight at 4 °C to allow hydrogel formation. Electrical connection was realized by attaching an electrical wire to the back side using carbon paste and then sealed with silicone paste.

3.5.4 Optical microscopy

Optical images of the electrodes were taken in wet and dry conditions. The electrode was hydrated with dI water and left in air until fully dried for the wet condition and dry condition, respectively. Optical images were obtained using a Keyence VK-X200 microscope at 10x magnification.

3.5.5 Electrochemical characterization

Electrochemical studies were performed at room temperature on an Eco Chemie Autolab PGSTAT 100 potentiostat with Nova 2.0 software. The three-electrode system consisted of a BP electrode as the working electrode, a Ag/AgCl (KCl_{sat}) as the reference electrode, and a platinum wire as the auxiliary electrode. All potentials in this chapter are referred to Ag/AgCl unless otherwise stated. Cyclic voltammetry was performed at a scan rate of 1 mV s^{-1}. For the evaluation of the bioanode stability, cyclic voltammetry was performed periodically. Before electrochemical measurements, the electrode is incubated in dI water for 1h to fully hydrate the

electrode and remove loosely bound enzymes. After measurements, electrode was stored in Ca/HEPES buffer at 4 °C.

PLQ surface coverage was calculated by integration of the cathodic peaks of CVs recorded in the absence of glucose, according to **Equation 2.2**. The current density values at 0.2 V were obtained by subtracting the background current obtained in the absence of glucose and reported based on the geometric surface area of the electrode.

References

1. Gross, Andrew. J. *et al.* A High Power Buckypaper Biofuel Cell: Exploiting 1,10-Phenanthroline-5,6-dione with FAD-Dependent Dehydrogenase for Catalytically-Powerful Glucose Oxidation. *ACS Catal.* 4408–4416 (2017) doi:10.1021/acscatal.7b00738.
2. Joung, Y.-H. Development of Implantable Medical Devices: From an Engineering Perspective. *Int Neurourol J* **17**, 98–106 (2013).
3. Mano, N., Mao, F. & Heller, A. Characteristics of a Miniature Compartment-less Glucose−O2 Biofuel Cell and Its Operation in a Living Plant. *J. Am. Chem. Soc.* **125**, 6588–6594 (2003).
4. Cinquin, P. *et al.* A Glucose BioFuel Cell Implanted in Rats. *PLOS ONE* **5**, e10476 (2010).
5. J. Moehlenbrock, M. & D. Minteer, S. Extended lifetime biofuel cells. *Chemical Society Reviews* **37**, 1188–1196 (2008).
6. Kowalewska, B. & Jakubow, K. The impact of immobilization process on the electrochemical performance, bioactivity and conformation of glucose oxidase enzyme. *Sensors and Actuators B: Chemical* **238**, 852–861 (2017).
7. Tsujimura, S., Murata, K. & Akatsuka, W. Exceptionally High Glucose Current on a Hierarchically Structured Porous Carbon Electrode with 'Wired' Flavin Adenine Dinucleotide-Dependent Glucose Dehydrogenase. *J. Am. Chem. Soc.* **136**, 14432–14437 (2014).
8. Rengaraj, S., Kavanagh, P. & Leech, D. A comparison of redox polymer and enzyme co-immobilization on carbon electrodes to provide membrane-less glucose/O2 enzymatic fuel cells with improved power output and stability. *Biosensors and Bioelectronics* **30**, 294–299 (2011).
9. Reuillard, B. *et al.* High power enzymatic biofuel cell based on naphthoquinone-mediated oxidation of glucose by glucose oxidase in a carbon nanotube 3D matrix. *Physical Chemistry Chemical Physics* **15**, 4892 (2013).
10. Xiao, X., Ó Conghaile, P., Leech, D. & Magner, E. Use of polymer coatings to enhance the response of redox-polymer-mediated electrodes. *ChemElectroChem* (2018) doi:10.1002/celc.201800983.
11. El Ichi-Ribault, S. *et al.* Laccase-based biocathodes: Comparison of chitosan and Nafion. *Analytica Chimica Acta* **937**, 43–52 (2016).
12. Jain, D. *et al.* Low-Molecular-Weight Hydrogels as New Supramolecular Materials for Bioelectrochemical Interfaces. *ACS Appl. Mater. Interfaces* **9**, 1093–1098 (2017).
13. Aslani, P. & Kennedy, R. A. Studies on diffusion in alginate gels. I. Effect of cross-linking with calcium or zinc ions on diffusion of acetaminophen. *Journal of Controlled Release* **42**, 75–82 (1996).
14. Draget, K. I., Skjåk-Bræk, G. & Smidsrød, O. Alginate based new materials. *International Journal of Biological Macromolecules* **21**, 47–55 (1997).
15. Pereira, R. *et al.* Development of novel alginate based hydrogel films for wound healing applications. *International Journal of Biological Macromolecules* **52**, 221–230 (2013).
16. Kuo, C. K. & Ma, P. X. Ionically crosslinked alginate hydrogels as sca!olds for tissue engineering: Part 1. Structure, gelation rate and mechanical properties. 11 (2001).

17. Esser, E. & Tessmar, J. K. V. Preparation of well-defined calcium cross-linked alginate films for the prevention of surgical adhesions. *J. Biomed. Mater. Res.* **101B**, 826–839 (2013).
18. Pumera, M., Ambrosi, A. & Chng, E. L. K. Impurities in graphenes and carbon nanotubes and their influence on the redox properties. *Chemical Science* **3**, 3347 (2012).
19. Wang, J., Dai, J. & Yarlagadda, T. Carbon Nanotube−Conducting-Polymer Composite Nanowires. *Langmuir* **21**, 9–12 (2005).
20. Sivakkumar, S. R., Ko, J. M., Kim, D. Y., Kim, B. C. & Wallace, G. G. Performance evaluation of CNT/polypyrrole/MnO2 composite electrodes for electrochemical capacitors. *Electrochimica Acta* **52**, 7377–7385 (2007).
21. He, L., Lin, D., Wang, Y., Xiao, Y. & Che, J. Electroactive SWNT/PEGDA hybrid hydrogel coating for bio-electrode interface. *Colloids and Surfaces B: Biointerfaces* **87**, 273–279 (2011).

Chapter 4:

Stretchable and flexible buckypaper-based lactate biofuel for wearable electronics

Chapter 4 Stretchable and flexible buckypaper-based lactate biofuel cell for wearable electronics

Résumé

Comme indiqué dans le premier chapitre (section 1.4.2), les biopiles enzymatiques sont très prometteuses en tant que source d'alimentation pour les dispositifs électroniques portables non invasifs dans le domaine médical en raison du niveau raisonnable de lactate présent dans la sueur. Pour répondre à l'exigence d'un dispositif portable, la biopile doit être flexible et étirable afin de résister à la tension causée par les mouvements du corps. Les biopiles à carburants enzymatiques à base de papier de carbone sont idéales pour les applications portables. Les propriétés exceptionnelles des bioélectrodes à base de buckypaper pour l'oxydation du glucose et la réduction de l'oxygène ont été démontrées dans les chapitres précédents. Dans ce chapitre, la flexibilité du papier a été utilisée pour fabriquer une biopile à combustible au lactate extensible et flexible.

Il existe un intérêt croissant pour les dispositifs électroniques portables, en particulier ceux destinés aux applications de contrôle de la condition physique et de la santé, telles que la surveillance du mouvement,[1] la détection de signaux physicochimiques[2,3] et la cicatrisation des plaies.[4] Le développement rapide de dispositifs portables nécessite le développement de sources d'énergie pouvant être facilement intégrées au corps humain. Malgré les énormes progrès récents des dispositifs portables, la plupart de ces dispositifs sont toujours alimentés par des batteries rigides et volumineuses qui posent des problèmes environnementaux. Les biocarburants enzymatiques (EFC), qui reposent sur les oxydoréductases pour convertir bioélectrocatalytiquement les biocarburants présents dans les fluides corporels humains, ont été considérés comme des candidats prometteurs pour l'alimentation des appareils électroniques portables de prochaine génération.[5,6] Les substrats ont été largement étudiés en raison de la facilité d'accès au lactate dans la sueur humaine et de leur intégration facile dans l'électronique portable.[7–9] La puissance des EFC et leur flexibilité sont deux défis majeurs dans ce domaine, compte tenu de la concentration limitée de lactate dans la sueur et de la contrainte externe imposée par les mouvements du corps. Pour surmonter ces problèmes, il est essentiel de développer des matériaux d'électrode capables d'améliorer l'efficacité du transfert d'électron enzymatique et d'offrir flexibilité et conformité lorsque le dispositif est

placé à même la peau.

Les nanotubes de carbone (CNTs) ont été largement utilisés pour fabriquer des bioélectrodes en raison de leurs propriétés électroniques exceptionnelles, de leur inertie électrochimique et de leur grande surface spécifique.[10] Pour fabriquer des électrodes destinées à des applications pratiques sur des cellules biocarburant, les CNTs sont souvent formés en encres,[11] pastilles,[8,12] papiers,[13,14] et fibres.[15] Les électrodes CNT sérigraphiées ont été populaires pour les EFCs portables; cependant, ce type d'électrode nécessite un mélange avec un liant élastomère, qui bloque inévitablement la surface active des CNTs et compromet le courant électrocatalytique (d'où les performances de puissance moindres).[11,16-18] Les pastilles CNTs, utilisées dans la première génération d'électrodes pour EFCs implantables, ont plusieurs millimètres d'épaisseur et sont donc volumineuses, ont un faible transfert de masse et ont tendance à être fragiles.[19,20]

Dans la présente étude, on a choisi du papier-buckypaper (BP) comme matériau d'électrode. Le BP est un matériau autosupporté et conducteur semblable à du papier, comprenant un réseau de CNTs enchevêtrés.[21] Plus tôt, une biopile lactate/O_2 avec des électrodes en BP a été explorée dans les larmes synthétiques.[22] Très récemment, une bioanode à base buckypaper pour l'oxydation du lactate a été couplée à une photocathode a également été rapportée.[23] Toutefois, la densité de puissance des deux dispositifs était plutôt faible et aucune extensibilité n'a été démontrée. Dans les deux systèmes, des BPs fabriqués à base de nanotubes de carbone à parois multiples (MWCNTs) de source commerciale ont été utilisés comme matériau d'électrode. Inversement, dans ce chapitre, les MWCNTs BP fabriqués en laboratoire ont été fabriqués à l'aide d'une méthode de filtration sous vide destinée à être utilisée comme matériau d'électrode. Le résultat précédent décrit au chapitre 2 montre que le BP fabriqué en laboratoire est supérieur au BP commercial en tant que matrice d'immobilisation de la bilirubine oxydase (BOx), qui montre un courant catalytique plus élevé pour la réaction de réduction d'oxygène (ORR). Une nouvelle classe de BP flexibles fabriqués en laboratoire a été développée dans notre groupe sur la base de la réticulation des CNTs avec des polymères linéaires de polynorbornène comprenant des groupes pyrènes. Le BP polynorbornène-pyrène est une excellente matrice pour le médiateur redox et l'immobilisation enzymatique.[14,24,25] Cependant, le manque d'extensibilité intrinsèque a entravé l'application des BP dans les EFC cutanées.

Dans ce chapitre, une EFC offrant de bonnes performance, possédant des propriétés

extensible, flexible et portable est présentée. Grâce à une combinaison unique d'électrodes de BP hautement conductrices et catalytiques et d'un support d'électrode à structure extensible, il a été possible de récupérer l'énergie directement de la transpiration d'un individu. Pour répondre à l'exigence des dispositifs portables de supporter des mouvements rigoureux et des déformations pendant l'exercice physique, une extensibilité "2 degrés" (c'est-à-dire une extensibilité structurelle et une extensibilité intrinsèque du matériau) a été réalisée en combinant une formule d'encre extensible avec une architecture "island-bridge".[11] Les électrodes de l'appareil ont été séparées en "îlots" solidaires du substrat et en "ponts" d'interconnexion en forme de serpentin, souples et extensibles, qui peuvent se dérouler sous contrainte.[11,26] Lorsqu'une contrainte externe est appliquée, la contrainte est répartie sur les "ponts" flexibles autour des "îlots" durs non extensibles, maintenant ainsi une résistance électrique stable. C'est pourquoi nous avons opté pour une interconnexion autoportante à boucles, adoptée dans le cadre de nos travaux précédents, afin d'accroître encore davantage sa souplesse et sa conductivité.[26]

Chapter 4 Stretchable and flexible buckypaper-based lactate biofuel cell for wearable electronics

This chapter is based on the following manuscript-

Xiaohong Chen, Lu Yin, Jian Lv, Andrew J. Gross, Minh Le, Nathaniel Georg Gutierrez, Yang Li, Itthipon Jeerapan, Fabien Giroud, Anastasiia Berezovska, Rachel K. O'Reilly, Sheng Xu, Serge Cosnier, Joseph Wang

Adv. Funct. Mater. **2019**, 1905785

4.1 Abstract

As discussed in the first chapter (section 1.4.2), enzymatic biofuel cell is a promising candidate as power source for wearable electronic devices due to the reasonable level of lactate present in sweat. To meet the requirement of wearable device, the biofuel cell needs to be flexible and stretchable in order to withstand the strain caused by body movement. Enzymatic biofuel cells based on buckypaper are ideal for wearable applications. The exceptional properties of buckypaper based bioelectrodes for glucose oxidation and oxygen reduction have been demonstrated in previous chapters. In this chapter, the flexibility of buckypaper was exploited to fabricate a stretchable and flexible lactate biofuel cell.

4.2 Introduction

There is a continuously growing interest for wearable electronic devices, particularly, devices for fitness and health monitoring applications such as motion monitoring,[1] physicochemical signal sensing,[2,3] and wound healing.[4] The rapid development of wearable devices demands the development of efficient reliable and conformal power sources that can be easily integrated onto the human body. Despite the tremendous recent progress of wearable devices, most of these devices are still powered by rigid and bulky batteries which pose environmental concerns. Enzymatic biofuel cells (EFCs), which rely on oxidoreductases to bioelectrocatalytically convert biofuels present in human body fluids, have been considered as promising candidates for powering next generation wearable electronic devices.[5,6] Specifically, epidermal skin-worn EFCs that use lactate as the substrate have been widely studied given the easy access to lactate in human sweat and their facile integration with wearable electronics.[7–9] The power output of EFCs and their flexibility are two major

challenges in this field considering the limited concentration of lactate in sweat and the external strain imposed from body movements. To overcome these issues, it is essential to develop electrode materials that can enhance enzyme electron transfer efficiency and provide flexibility and conformity when the device is mounted on the skin.

Carbon nanotubes (CNTs) have been widely used to construct bioelectrodes given their exceptional electronic properties, electrochemical inertness and high surface area.[10] To construct electrodes for practical biofuel cell applications, CNTs are often shaped into inks,[11] pellets,[8,12] papers,[13,14] and fibers.[15] Screen-printed CNT electrodes have been popular for wearable biofuel cells; however, this type of electrode requires mixing with an elastomeric binder, which inevitably blocks the active surface of CNTs and compromises electrocatalytic current (hence power performance).[11,16–18] CNT pellets, used in the first generation of implantable biofuel cells, are several millimeters thick and are therefore bulky, have slow mass transfer efficiency, and tend to be fragile.[19,20]

In the present study, buckypaper (BP) was chosen as the electrode material. BP is a self-supported and conductive paper-like material comprising a network of entangled CNTs.[21] Previously, a buckypaper-based lactate/O_2 EFC was explored in synthetic tears.[22] Very recently, a buckypaper-based lactate bioanode coupled with a photocathode was also reported.[23] However, the power density of both devices was rather low and no stretchability was demonstrated. In both systems, multi-walled carbon nanotubes (MWCNTs) BP from a commercial source were utilized as the electrode material. In contrast, in this chapter, lab-made MWCNTs BP using a vacuum filtration method was fabricated for use as the electrode material. The previous result described in chapter 2 shows that lab-made MWCNTs BP is superior to commercial MWCNTs BP as an immobilization matrix for bilirubin oxidase (BOx), which shows a higher catalytic current for the oxygen reduction reaction (ORR). A new class of lab-made flexible BPs has been developed in our group based on the cross-linking of CNTs with polynorbornene linear polymers comprising pyrene groups. The polynorbornene-pyrene BP is an excellent matrix for redox mediator and enzyme immobilization.[14,24,25] However, the lack of intrinsic stretchability has impeded the application of BPs in epidermal EFCs.

In this chapter, a high power, stretchable, flexible and wearable EFC is presented. Through a unique combination of highly conductive and catalytic BP electrodes with

a structurally stretchable substrate, it is possible to harvest energy directly from perspiration. To meet the requirement of wearable devices to endure rigorous movements and deformation during human exercise, a "2-degree" stretchability (*i.e.* structural stretchability and material intrinsic stretchability) was realized by combining a stretchable ink formula with an "island-bridge" architecture.[11] The electrodes of the device were separated into "islands", which are firmly bonded to the substrate, along with serpentine-shaped interconnecting "bridges", which are soft and stretchable and can unwind under stress.[11,26] When external strain is applied, the stress is distributed to the flexible "bridges" around the hard non-stretchable "islands", therefore maintaining electrical resistance stability. Herein, a free-standing, buckling-enabled interconnect design, adopted from our previous work, was chosen to further enhance its flexibility and conductivity.[26]

4.3 Results and discussion

4.3.1 Design of the EFC

As illustrated in **Figure 4.1**, the stretchable and flexible wearable EFCs are fabricated by integrating buckypaper-based electrodes and stretchable current collectors. The stretchable substrate is fabricated *via* a high-throughput and low-cost screen-printing method. The carbon-based electrode "islands" are interconnected by high-conductivity silver composite "bridges" in a serpentine shape. A "skeleton" layer composed of polystyrene (PS) and styrene ethylene butylene styrene (SEBS) is added below the carbon islands to enhance their mechanical stability, and a water-soluble sacrificial layer is added below the serpentine interconnects to allow their separation from the substrate. A flexible polymer is printed on both sides of the silver interconnects to avoid the direct contact of silver and the electrolyte. The printed sacrificial layer is dissolved in water to enable buckling of the serpentine structures during deformation. To complete the assembly of the skin patch illustrated in **Figure 4.1A**, pre-cut anodic and cathodic BP electrodes were thereafter attached to the carbon islands. A thin sheet of phosphate buffer solution-polyvinyl alcohol (PB-PVA) hydrogel was added as electrolyte and a sweat reservoir was applied onto the electrodes. The fabrication process is illustrated in detail in **Figure 4.2**.

The printed patch can be attached to the human epidermis in a wide range of locations where perspiration is usually observed (e.g. arm, neck, chest, back) while

maintaining high conformity (**Figure 4.1**). The system has been designed to endure mechanical strains caused by bodily movements. Endowed by the advantageous "island-bridge" structure, the EFC patch is highly flexible and stretchable (**Figure 4.1B**) and can endure severe bending (**Figure 4.1C**). The serpentine structures accommodate most of the stress. The patch is activated once perspiration takes place a few minutes after exercise, when the lactate (originating from the sweat) is absorbed into the hydrogel electrolyte and permeates to the bioelectrodes. The reaction mechanism is illustrated in **Figure 4.1D**. The bioanodes consist of a pyrene-polynorbornene functionalized BP with immobilized lactate oxidase (LOx) from microorganisms and 1,4-naphthoquinone (1,4-NQ) as the electron transfer mediator for mediated bioelectrocatalytic oxidation of lactate into pyruvate. The biocathodes consist of BPs with immobilized bilirubin oxidase (BOx) from *Myrothecium sp.* to catalyze the reduction of oxygen. For the cathode, BP is modified with protoporphyrin IX (PPIX) molecules which can orientate the enzyme preferentially through "lock-key" interaction between the substrate pocket near the T1 center of BOx and PPIX to facilitate direct electron transfer with the CNTs.[14,27] The current and voltage generated from the anodic and cathodic reactions can thereafter be exploited to power various electronics in a biofuel cell configuration.

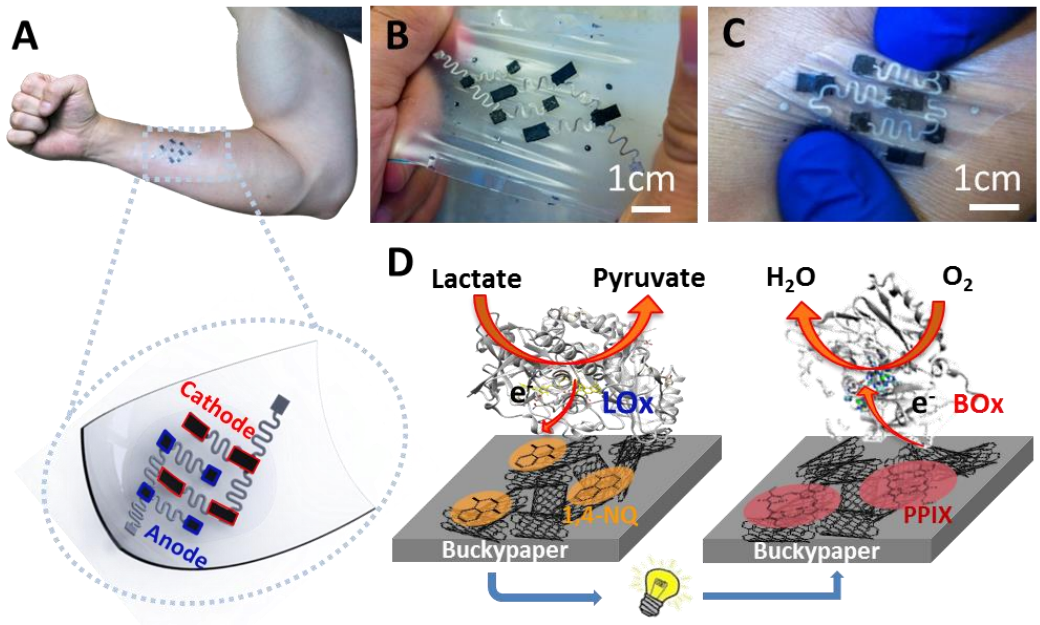

Figure 4.1 (A) Photograph of the stretchable EFC device on a human arm, (zoom) schematic illustration of the skin-mountable wearable EFC device; (B, C) Photographs of the EFC under stretching and bending, respectively; (D) Schematics of the redox energy generation from sweat lactate oxidation at the anode and O_2 reduction at the cathode by EFC.

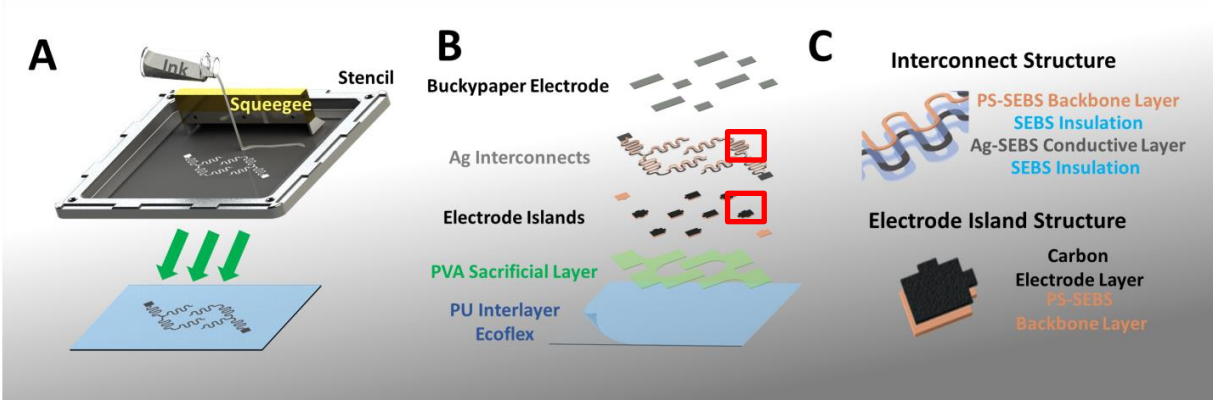

Figure 4.2 Schematic illustration of (A) the screen-printing process; (B) designed patterns for different screen-printing layer; (C) Zoom of the interconnect "bridge" and electrode "island" structure (red squares in (B)).

4.3.2 Performance of the EFC

The morphology of BP functionalized with the pyrene-polynorbornene homopolymer was characterized using scanning electrode microscopy (SEM) and revealed a homogenous mesoporous structure of entangled CNT bundles (**Figure 4.3A**). The electrochemical performance of the biocathodes and bioanodes were evaluated individually using a three-electrode set-up with a platinum counter electrode and an Ag/AgCl (3M KCl) reference electrode. **Figure 4.3B** shows overlaid linear sweep voltammograms (LSVs) recorded for the bioanode in the presence of 0 and 15 mmol L^{-1} lactate in 0.5 mol L^{-1} phosphate buffered solution (PB, pH 7.4), respectively. In the absence of lactate, the faradaic current corresponds to oxidation of the 1.4-naphthohydroquinone. Upon addition of lactate, the mediated bioelectrocatalytic current of lactate oxidation starts to flow and results in a current density of 1.3 mA cm^{-2} at 0.2 V. The current did not further improve when lactate concentration was increased to 20 mmol L^{-1} (data not shown), which indicates that the catalytic current is limited by the amount of enzymes immobilized on electrode surface. **Figure 4.3C** shows LSVs for the biocathode tested in buffer with air-saturated O_2. The oxygen reduction current starts to increase dramatically at a potential close to 0.5 V, reaching a maximum current density of -1.5 mA cm^{-2} at 0 V. The presence of lactate did not affect the performance of the BOx bioelectrode as the onset potential for ORR and the limiting current were unchanged. The high onset potential and steep oxygen reduction reaction slope indicate a more efficient direct electron transfer between the T1 center of BOx and the CNTs. The excellent performance is in agreement with other reported protoporphyrin-modified biocathodes.[14,27]

The power performance of the EFC was investigated using a unit cell device comprising a single biocathode and a single bioanode, as depicted in **Figure 4.1D**. As low oxygen concentration can limit the power of the EFC, the area of the biocathode was designed to be two times larger than the bioanode to ensure that the EFC performance was not limited by the cathode. LSVs were recorded from the open circuit voltage (OCV) to 0.01 V (near short circuit) in different lactate concentrations. The power-voltage curves are shown in **Figure 4.3D**. Both the OCV and peak power density increased with increasing lactate concentrations, reaching saturation at 10 mmol L^{-1} lactate with a OCV value of 0.74 V. A maximum power density of 0.5 mW cm^{-2} was recorded at 0.55 V in 10 mmol L^{-1} lactate. However, for subsequent characterization experiments, 15 mmol L^{-1} lactate was used to match the average lactate concentration in sweat.[28] Although the power density herein is lower than the maximum value of *ca* 1.2 mW cm^{-2} reported in the literature, where a battery type silver oxide cathode was used.[8] This work presents the use of a fully enzymatic fuel cell with an enzymatic biocathode for oxygen reduction. The power performance was compared with other reported work in the literatures and is summarized in **Table 4.1**. The power performance stability of the EFC was investigated periodically by performing linear sweep voltammetry in 15 mmol L^{-1} lactate over an extended period of 48 hours (**Figure 4.3E**). As shown in **Figure 4.3F**, the power density at 0.55 V decreases only by 16 % after 48 hours. Controlled experiments were conducted on EFCs fabricated by immobilizing enzymes on screen-printed current collectors and CNT ink[9] electrodes, respectively. The power performance of the controlled groups compared to the BP-based EFC was shown in **Figure 4.4**. For these two alternative systems, the power performance in 15 mmol L^{-1} lactate are negligible compared to the BP-based EFC, highlighting that the excellent performance of EFC originates from the BPs used in this work.

Table 4.1 Performance of wearable lactate-based EFCs reported in the literatures

Year	Anode	Cathode	OCV/ V	Power density/ μW cm^{-2}	Electrode Material	Reference
2014	LOx	Pt	0.7	100	CNT ink	Jia *et al.*[17]
2015	NADLDH	BOx	0.41	8	Buckypaper	Reid *et al.*[22]
2017	LOx	Ag_2O	0.5	1000	CNT pellet	Bandodkar *et al.*[8]
2019	LOx	BOx	0.55	20	Toray carbon	Escalone-Villalpando

					paper	*et al.*[29]
2019	LOx	BOx	0.74	520	Buckypaper	This work

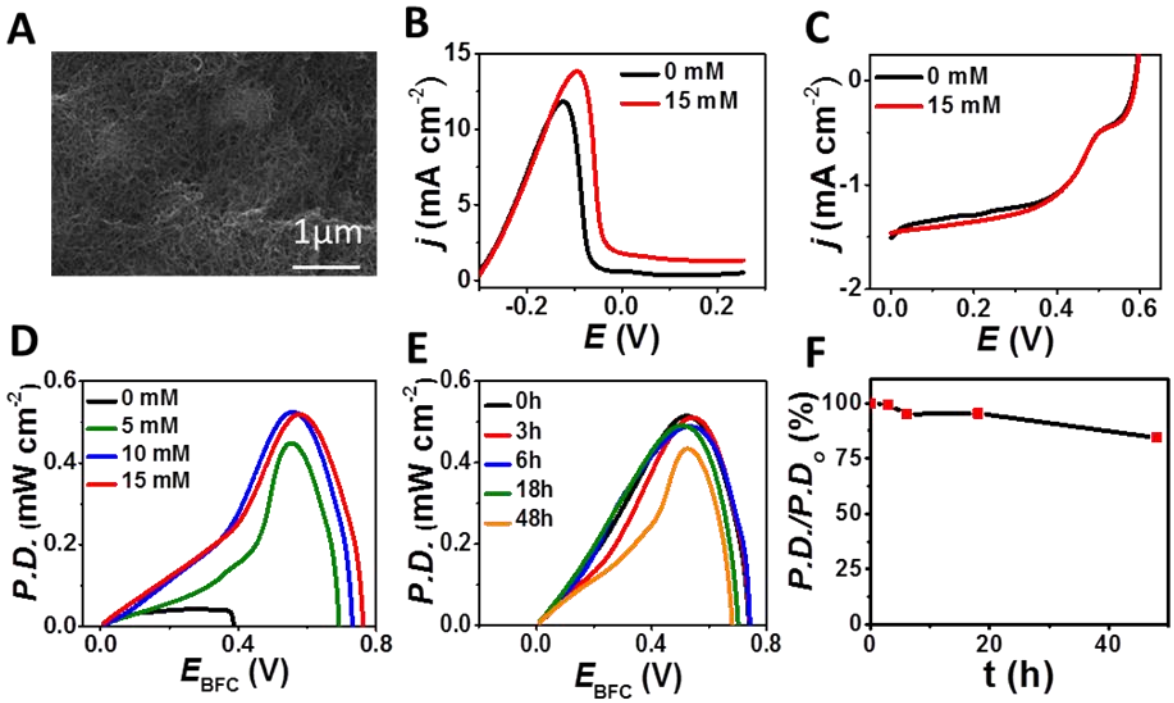

Figure 4.3 (A) SEM image of buckypaper functionalized with pyrene-polynorbornene. (B) LSV of the BP bioanode in the presence of (**black**) 0 mmol L^{-1} and (**red**) 15 mmol L^{-1} lactate in 0.5 mol L^{-1} PB (pH 7.4) at 5 mV s^{-1}. (C) LSV of the BP biocathode in air-equilibrated buffer with (**black**) 0 mmol L^{-1} and (**red**) 15 mmol L^{-1} lactate at 5 mV s^{-1}. (D) The power density versus voltage plots for the stretchable lactate EFC under different lactate concentrations (0, 5, 10 and 15 mmol L^{-1}) in 0.5 M PB (pH 7.4). (E) Plots showing the stability of the stretchable EFC in the presence of 15 mmol L^{-1} lactate at different times up to 48 hours. (F) The calculated relative change of power density at 0.55 V over 48 hours, based on the data in (E).

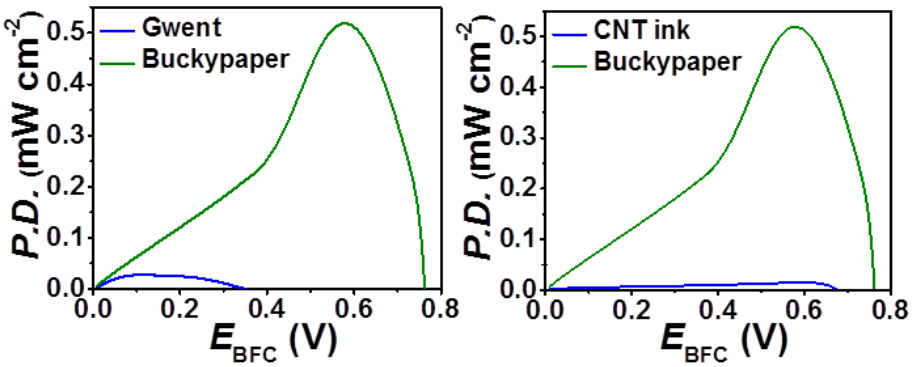

Figure 4.4 Plots of power density versus voltage of (green) stretchable buckypaper EFC and (left)(blue) screen-printed EFC based on current collector modified with enzymes and (right)(blue) screen-printed EFC based on CNT ink (formula from reported literature) modified with enzymes.

4.3.3 Self-charging behavior of the EFC

The ability of the EFC to function also as a self-powered supercapacitor was investigated. **Figure 4.5A** shows cyclic voltammograms (CVs) recorded for the EFC in the presence of 0 mmol L^{-1} and 15 mmol L^{-1} lactate in PB solution. In the absence of lactate, a quasi-symmetric rectangular shape of the CV curves indicates highly capacitive behavior, which is expected for high surface area nanostructured carbon electrodes.[12,30] Upon addition of 15 mmol L^{-1} lactate, the capacitive current increased, which can be explained by the additional electronic charge loading on the CNT matrix *via* the enzymatic oxidation of lactate. The capacitance of the device was further investigated by performing galvanostatic charge-discharge (GCD) at different constant current densities between 0 V and 0.8 V. This technique is a more accurate method to probe the device capability to function as real-world capacitors. GCD curves and the calculated areal capacitance at different current densities are shown in **Figure 4.6**. A high capacitance of 40 mF cm^{-2} was observed at 0.1 mA cm^{-2}, which is comparable to other reported self-charging biosupercapacitors.[31,32] It should be noted that no extra modification of the bioelectrodes was needed, such as manganese oxide to obtain this capacitive performance.

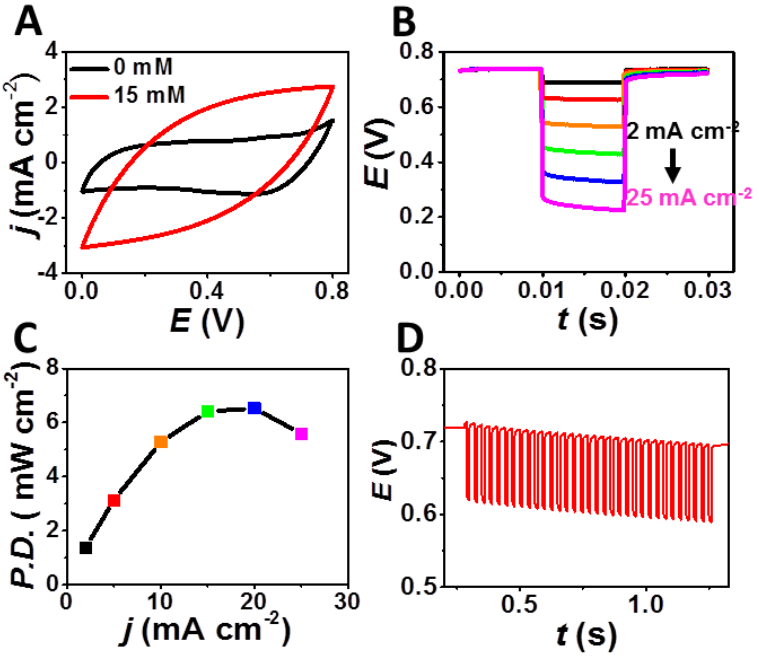

Figure 4.5 (A) CV of EFC in the presence of (**black**) 0 mmol L^{-1} and (**red**) 15 mmol L^{-1} lactate in 0.5 mol L^{-1} PB (pH 7.4) at 50 mV s^{-1}. (B) Overlay of potential profiles obtained from EFC discharge at 2, 5, 10, 15, 20 and 25 mA cm^{-2} over 10 ms. (C) Plot of the calculated pulse power density as a function of the discharge current density. (D) Potential profile of the EFC during a discharge at 5 mA cm^{-2} at 33 Hz frequency.

Current pulse chronopotentiometry was performed to evaluate the EFC power performance in pulse operation mode. **Figure 4.5B** shows the overlay of potential profiles of the EFC discharged from 2 to 25 mA cm^{-2} over a 10 ms pulse period. The potential profile at all discharge current densities showed the same feature, with an initial IR drop followed by a capacitive discharge and then the self-recharge back to its original voltage after the pulse. The calculated pulse power delivered by the EFC is shown in **Figure 4.5C**, reaching a maximum power of 6.5 mW cm^{-2} at 20 mA cm^{-2}. This value is around 13 times higher than the power delivered in convention mode when the current is continuously driven from the fuel cell. The EFC also shows good stability at high frequency discharge. As shown in **Figure 4.5D**, the EFC is discharged at 5 mA cm^{-2} at 33 Hz frequency (10 ms discharge and 20 ms rest) for 1 second and the OCV only decreases slightly. Although high frequency discharge of EFC is an interesting perspective, more experiments are needed to fully evaluate the device stability for long period of use at high frequency. Discharge current and discharge/resting period for each pulse should also be adjusted to allow high pulse power output and substrate diffusion back to BP.

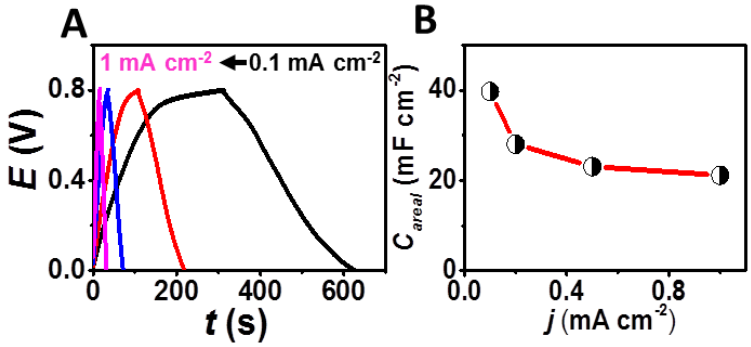

Figure 4.6 (A) GCD curves of the EFC at different charge-discharge current density (0.1, 0.2, 0.5, 1.0 mA cm^{-2}). (B) The calculated corresponding areal capacitance.

4.3.4 Mechanical resilience of the EFC

To highlight the resiliency of the BP-based "island-bridge" EFC, careful examination of its performance was carried out under severe mechanical distortions (**Figure 4.7**). The elastic and highly conductive silver composite ink is chosen as the "bridges" to minimize the power loss due to high interconnection resistance, and the serpentine structure is implemented to avoid increased strain-induced resistance during deformation by enabling buckling.[9,11,26,33] The mechanical stability of the

buckypaper EFC was evaluated using a stepping-motor controlled biaxial stretching stage. The printed EFC was stretched repeatedly to 120% of its original size in both x and y directions (**Figure 4.7B**). The ohmic resistance of the circuit between the silver contact on the end of the patch and the central printed carbon electrode was measured during a 100-cycle stretching test, as shown in **Figure 4.7C**. The resistance of the circuit varies less than 1 Ω in each stretching cycle (**Figure 4.7C** inset), with no trend of increasing resistance after all of the stretching cycles. The mechanical stability was further validated by monitoring the discharge current of the EFC under a constant load. One pair of electrodes was covered in PB-PVA gel electrolyte with 15 mmol L^{-1} lactate and connected to a 33 kΩ resistor, as shown in **Figure 4.7A**. The discharge current exhibited no significant change during 20 cycles of stretching, which further validates the mechanical stability of the patch as a practical wearable energy-harvesting device. The durability of the generated power performance was examined in connection to numerous stretching cycles. LSV scan was performed every 20 cycles of 20% biaxial stretching. The power density remained highly stable after 100 cycles of stretching (**Figure 4.7E and 4.7F**).

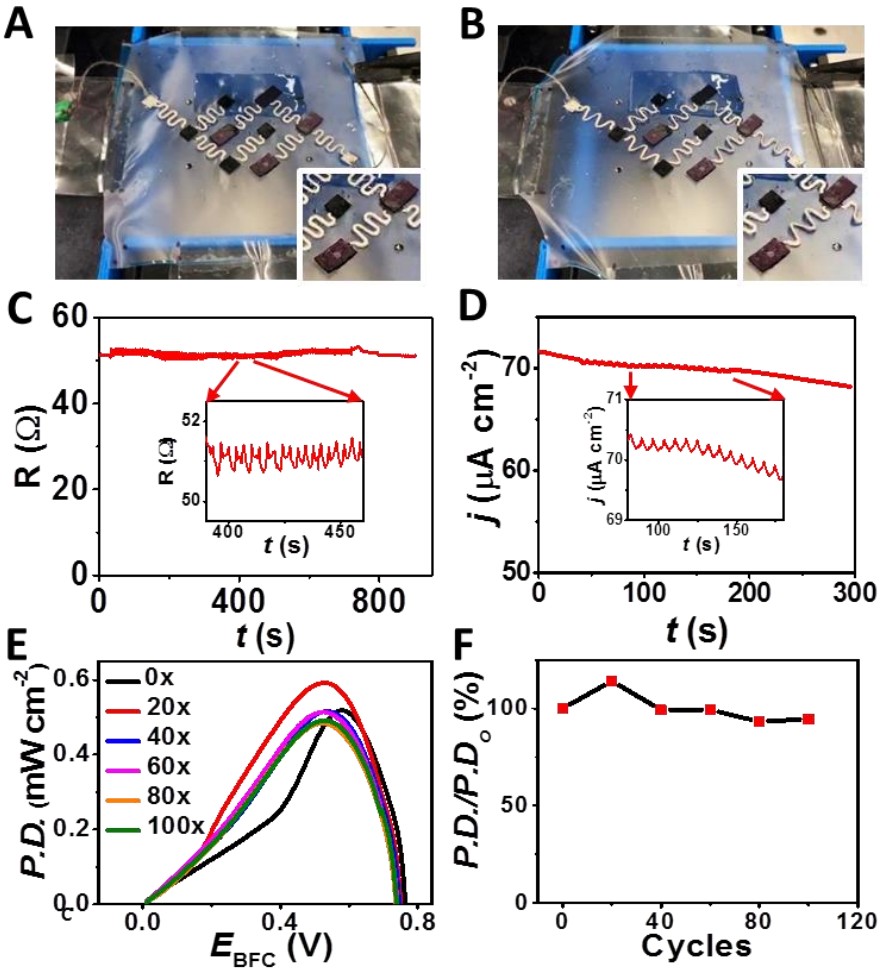

Figure 4.7 Mechanical resilience studies: Image of the wearable EFC (A) before and (B) after 20% stretching. (C) Resistance profile obtained during 20% stretching, (inset) zoom of resistance fluctuations. (D) Current density output profile of the EFC under a 33 kΩ load in PVA gel immersed in 15 mmol L^{-1} lactate, (inset) zoom of current density fluctuations. (E) Plots of EFC power density versus voltage under 20% stretching for 0, 20, 40, 60, 80 and 100 cycles in 15 mmol L^{-1} lactate. (F) The calculated relative change of power density at 0.55 V over 100 stretching cycles.

4.3.5 On-body power generation

The real-time power output of the wearable buckypaper EFC was tested by monitoring the current of the circuit (with 510 Ω load) when the volunteer was doing constant stationary cycling exercise. The power change of the EFC during the whole process is shown is **Figure 4.8A**. The power is very low before the volunteer started to sweat due to the absence of the fuel. After 10 minutes of exercise, perspiration is formed and visually observed on the subject, which is corroborated by a rapid increase in the power density of the EFC indicating lactate molecules from the sweat was transferred to the interface of the LOx bioanode. The highest power density obtained is around 450 μW after 30 minutes of perspiration, which is an output that is sufficient to power various wearable devices considering their low power requirements.[34] When the volunteer stopped cycling, a constant drop of power is observed, probably caused by the insufficient supply of lactate and oxygen dissolved in the sweat.[16] It has to be mentioned that the fuel cell was still able to deliver energy in absence of exercise as the power was near 100 μW after 15 minutes without new supply of substrate. The capability of the flexible buckypaper EFC to serve as the power source for wearable electronic devices was demonstrated by powering a LED during stationary cycling exercise. The voltage of the EFC was boosted using a flexible DC-DC converter, as shown in **Figure 4.8C, Figure 4.10** and **Video S1 and S2** (see supporting information of DOI: 10.1002/adfm.201905785). **Figure 4.8B** illustrates the circuit connection of the patch, the voltage booster, the LED and a switch which was used to control the "on" and "off" function of the LED. When connected with the sweat-based EFC, the LED lit up (**Figure 4.8E**) and its voltage can reach over 1.4 V both in pulse mode and continuous discharging modes (**Figure 4.9**), illustrating the feasibility of the voltage boosted buckypaper EFCs to supply energy for wearable electronics.

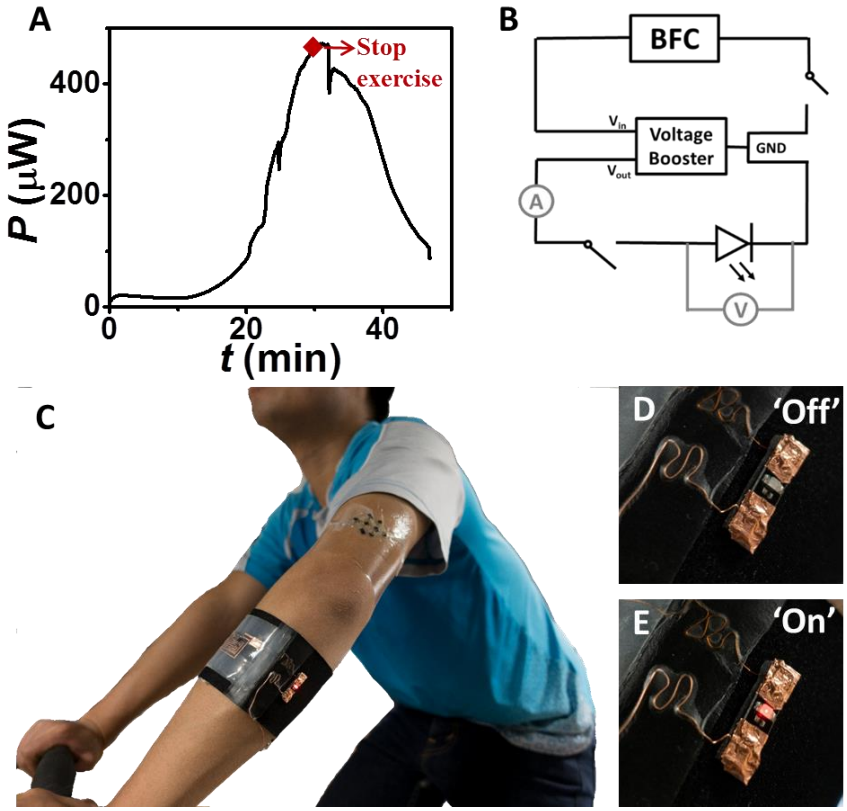

Figure 4.8 (A) Power output profile under 510 Ω load during an on-body experiment. (B) The circuit schematics for using the flexible and stretchable epidermal EFC patch to power an LED *via* a flexible DC-DC convertor. (C) Image of on-body experiment set up with a EFC mounted on the arm of the volunteer. (D) and (E) Imagesof the LED switched on and off, respectively.

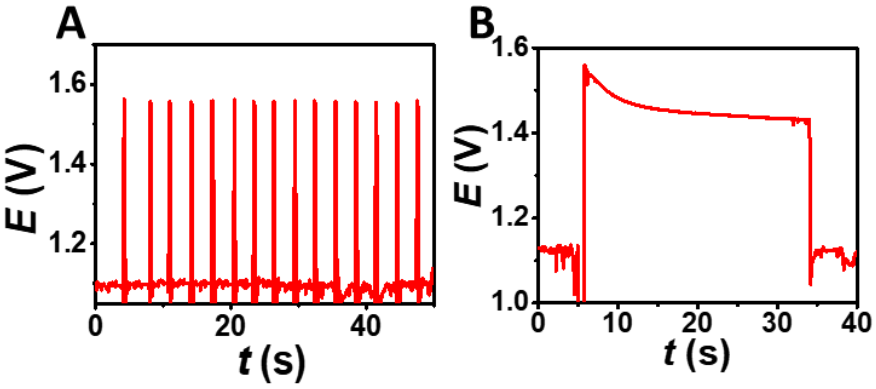

Figure 4.9 (A) and (B) Voltage output profile under 0.2s pulsed discharge and continuous discharge during exercise, respectively.

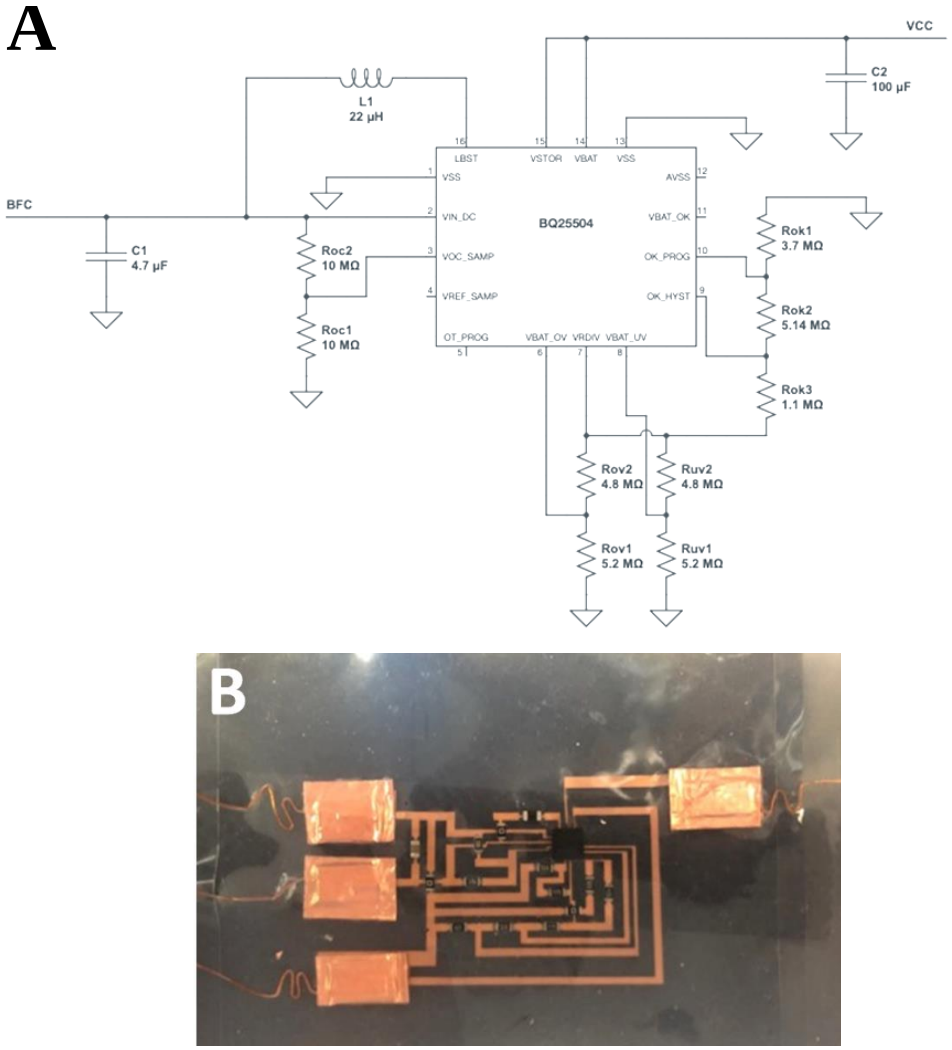

Figure 4.10 (A) The circuit diagram and (B) the photo of the prepared flexible voltage boosting circuit.

4.4 Conclusion

In conclusion, a stretchable and wearable enzymatic EFC that harvests energy from sweat has been created through the combination of a screen-printed current collector substrate and flexible enzyme-modified polynorbornene-based BPs. During *in vitro* experiments, the assembled EFC had a high OCV of 0.74 V and a maximum power density of 520 µW cm^{-2}. The stretchability of the device was realized through the coupling of "island-bridge" architecture and strain-enduring inks. The device was able to remain its performance stability under multiple stretching cycles. After coupling with a voltage booster, the BP-based EFC was able to power a commercial LED both in pulse mode and in continuous mode. We have demonstrated the promising potential of using BP as high-performance carbon electrode material for epidermal EFC with a stretchable supporting substrate. Such stretchable skin-worn devices are expected to contribute to the development of epidermal energy harvesting systems and wearable

electronics, in general. The reported BFC device still relies on exercises for sweat generation, which limits its usages for athletic purposes. The lactate (fuel) sweat concentration, and the hence the generated power, may depend on the specific individual and its activity. Challenges, such as the availability of biofuels or oxygen, can be addressed *via* different strategies such as the use of sweat-inducing chemicals or replacing the cathode with an air-breathing electrode. Future studies will aim at improving the biocompatibility, the catalytic performance of each individual bioelectrode, and further electronics integration along with extensive on-body operations.

4.5 Experimental section

4.5.1 Materials and reagents

1,4-naphthoquinone (1,4-NQ), protoporphyrin IX (PPIX, ≥95%), bovine serum albumin (BSA), glutaraldehyde, chitosan, toluene, L(+)-lactic acid, potassium phosphate dibasic (K_2HPO_4), potassium phosphate monobasic (KH_2PO_4), polyvinyl alcohol (PVA, MW 146 000–186 000 and MW 89 000-98 000), potassium hydroxide (KOH), ethanol, acetone, acetic acid, *N*,*N*-dimethylformamide (DMF, 99.9%) and Ag flakes (10 μm) were purchased from Sigma-Aldrich. Tetrahydrofuran (THF) was purchased from EMD Millipore. Hydroxyl-functionalized multi-walled carbon nanotubes (MWCNT-OHs, Ø = 10–20 nm, 10–30 μm length, >95% purity) were purchased from Cheap Tubes Inc. Commercial grade multi-walled carbon nanotubes (MWCNTs, Ø = 9.5 nm, 1.5 μm length, ≥90% purity) for buckypaper fabrication were purchased from Nanocyl. L-Lactate oxidase (LOx) from *Microorganism* was purchased from Toyobo. Bilirubin oxidase (BOx) from *Myrothecium sp.* was a gift from Amano Enzyme. Polyurethane (PU, Tecoflex SG-80A) was purchased from Lubrizol LifeSciences. Polystyene (PS) was obtained from polystyrene foam packaging material. Styrene Ethylene Butylene Styrene copolymer (SEBS) was purchased from Kraton. Ecoflex® 00-30 (Smooth-On, Inc. PA.) was prepared by mixing equal volumes of pre-polymers A and B, provided by the supplier. Perme-roll® Lite (L34R10) was purchased from Nitto Denko. Carbon paste (C2030519P4) was purchased from Gwent Group. 0.5 mol L^{-1} pH 7.4 Potassium phosphate buffer solution (PB) was prepared from potassium phosphate dibasic and potassium phosphate monobasic. Ultra-pure deionized water (DI, 18.2 MΩ) was used for all of

the aqueous solutions.

4.5.2 Formulations

4.5.2.1 Formulation of the interlayer PU ink

A PU interlayer was used to enhance the adhesion between the EFC and the substrate. A 12% PU ink was prepared by dissolving the Tecoflex PU beads in THF and mixed using a vortex machine overnight at room temperature.

4.5.2.2 Formulation of the PS-SEBS backbone polymer ink

3.6 g of polystyrene from packing foam and 0.4 g of SEBS beads were dissolved in 10 mL toluene. The mixture was then mixed using a vortex machine overnight at room temperature.

4.5.2.3 Formulation of the PVA sacrificial ink.

A water-soluble sacrificial layer ink was prepared by dissolving 1 g of PVA (MW 146 000–186 000) in 5 g of DI water in an 80 ºC water bath.

4.5.2.4 Synthesis of the PB-PVA hydrogel

A 20 wt% PVA (MW 89 000-98 000) solution is prepared by dissolving the PVA in water in an 80 ºC water bath. A 10 wt% KOH aqueous solution is also prepared and added to the PVA solution at 1:1 ratio by weight to form the hydrogel precursor. The hydrogel precursor is left in desiccator under vacuum for 1 day until cross-linked, and then taken out to then be washed in DI water to remove excess KOH. The washed hydrogel is soaked in 0.5 mol L^{-1} (pH 7.4) PB for later use.

4.5.2.5 Formulation of the SEBS insulation ink and Ag-SEBS conductive ink.

The SEBS insulation ink was prepared by dissolving the SEBS beads in toluene (0.6 g mL^{-1}). The stretchable conductive ink was prepared by mixing the silver flakes with the SEBS resin. A 0.4 g mL^{-1} of SEBS was prepared by dissolving the SEBS beads in toluene, then the silver flakes was mixed with the SEBS resin with the weight ratio of 2:1 ratio in a dual asymmetric centrifugal mixer (Flacktek Speedmixer, DAC 150.1 KV-K, FlackTek, SC, USA) under a speed of 1800 rpm for 5 min. To enhance the mixing of the ink, Zirconia (YSZ) beads (3 mm, Inframat Advanced Materials, CT, USA) were also added.

4.5.3 Procedures

4.5.3.1 “Island-bridge” electrode fabrication

A thin layer of Ecoflex was printed on the adhesive side of a Perme-Roll® Lite film and cured at 65 ^{o}C for 10 min to form the low elastic modulus substrate. Each layer depicted in **Figure 4.2** was screen printed on the non-adhesive side of the elastic substrate using an MPM-SPM semi-automatic screen printer (Speedline Technologies, Franklin, MA, USA). A 100 μm-thick stainless-steel printing stencil was designed in AutoCAD (Autodesk, USA) and laser-cut (Metal Etch Services, San Marcos, CA, USA). The printing steps are as follow: first, to enhance the adhesion, a PU interlayer was printed on top of the substrate and cured at 60 $^{\circ}$C for 15 min. Thereafter, a rigid “island-like” structure layer was printed using the PS-SEBS ink onto the modified stretchable film and cured at 65 $^{\circ}$C for 15 min. Then, the sacrificial layer was printed using PVA and cured at 80 $^{\circ}$C for 10 min. A stretchable insulating serpentine “bridge-like” structure layer was then printed using the SEBS ink and cured at 65 $^{\circ}$C for 15 min. A stretchable conductive serpentine “bridge-like” structure layer was subsequently printed using the Ag-SEBS ink and cured at 65 $^{\circ}$C for 15 min. Then another insulating layer was printed on top of the silver pattern using the SEBS ink and cured at 65 $^{\circ}$C for 15 min. Then a rigid conductive “island-like” layer was printed on top of the PS-SEBS using commercial carbon paste and left to dry at room temperature and then cured at 60 $^{\circ}$C for 15 min. Then, a backbone serpentine layer was printed using the PS-SEBS ink and cured at 65 $^{\circ}$C for 15 min. Finally, the sacrificial layer was removed by dissolving in DI water. Conductive stainless steel thin conductive threads (Adafruit, New York, USA) were attached to the contact points of the device using Ag-SEBS inks. The contact points were then insulated using PS-SEBS ink.

4.5.3.2 Fabrication of the polynorbornene-pyrene buckypaper

The polynorbornene homopolymer with pyrene groups ((Py_{50}), M_n, SEC = 10.2 kg mol^{-1}, $Đ_{SEC}$ = 1.22) was synthesized as previously reported *via* ring opening metathesis polymerization.[35] 66 mg of MWCNTs was dispersed in 66 mL of DMF, followed by sonication for 30 min. 6.6 mg of the polymer was added to the suspension. The suspension was then sonicated for a further 30 min. The as-prepared suspension was filtrated using a diaphragm pump (MZ 2C NT model, Vaccubrand) on

a Millipore PTFE filter (JHWP, 0.45 μm pore size). The resulting BP was rinsed with water, left under vacuum for 1 h, then left to dry in air overnight.

4.5.3.3 Assembly of the buckypaper biofuel cell

For anode preparation, the BP was first cut into square electrode (3 × 3 mm). 5 μL of 5 mg mL^{-1} MWCNT-OHs dispersed in 0.2 mol L^{-1} 1,4-NQ in 9:1 vol/vol ethanol/acetone solution was drop-casted onto the cut BP electrode surface. For the cathode, the BP was cut into rectangular electrodes (3 × 6 mm). 10 μL of 40 mmol L^{-1} PPIX in 9:1 vol/vol ethanol/acetone solution was drop-casted onto the cut BP electrode surface. The modified BP was then left to dry in air. Carbon paste was subsequently used to glue individual BPs onto screen-printed carbon "islands" and left to dry in an oven at 50 °C for 30 min. Thereafter, the cathodic BP was functionalized by drop-casting 10 μL of 40 mg mL^{-1} BOx in PB. The anodic BP was first rinsed with PB to remove loosely bound 1,4-NQ, and then followed by drop-casting 5 μL of a mixture of 40 mg mL^{-1} LOx and 10 mg mL^{-1} BSA. 3 uL of 1% glutaraldehyde solution was then drop-casted onto the surface followed by drop-casting 3 uL of 1 wt % chitosan in 0.1 mol L^{-1} acetic acid. The EFC device was then left to dry overnight at 4 °C.

4.5.3.4 Fabrication of the DC voltage booster circuit

A layer of poly(methyl methacrylate) (PMMA) (495K, A6) was coated onto a glass slide at a speed of 1500 rpm for 20 s, then cured by baking for 150 °C on a hotplate for 1 min. Afterwards, an Ecoflex (Smooth-On, 1:1) layer of 100-μm thickness was coated on top of the PMMA and cured at room temperature for two hours. On a separate glass slide, a layer of polydimethylsiloxane (PDMS, Sylgard 184 silicone elastomer, 20:1) was coated at 3000 rpm for 30 s, followed by curing in an oven at 150 °C for 30 min. A Cu sheet (20-μm-thick, Oak-Mitsui Inc.) was coated with PI (from poly(pyromellitic dianhydride-co-4,40-oxydianiline) amic acid solution, PI2545 precursor; HD MicroSystems) at 4000 rpm for 60 s, soft baked on a hotplate at 110 °C for 3 min, 150 °C for 1 min and finally cured in a nitrogen oven at 300 °C for 1 h. This Cu sheet was transferred on top of the PDMS/glass substrate. The interconnect layout, designed in AutoCAD, is patterned onto the Cu sheet *via* laser ablation. A laser (wavelength 1064 nm, pulse energy 0.42 mJ, pulse width 1 μs, frequency 35 KHz and mark speed 500 mm s^{-1}) ablated the Cu sheet into the designed pattern, and residual

Cu material was removed. The Cu pattern was picked off from the substrate with water soluble tape (3M Inc.) and transferred onto the prepared PMMA/Ecoflex/glass substrate. The water soluble tape was removed by room-temperature tap water. The Cu interconnections were cleaned by flux (WOR331928, Worthington Inc.) for removal of surface oxides. Sn42Bi57.6Ag0.4 alloy paste (Chip Quick Inc., SMDLTLFP-ND, low melting point 138 °C) was used to solder the chip components (including the BQ25504 Ultra Low-Power Boost Converter for Energy Harvesting, Texas Instruments) onto the Cu interconnects, followed by baking on a hotplate at ~150 °C for 4 min, and then cooling to room temperature. Finally, the entire surface of the circuit was encapsulated by Ecoflex with 1-mm thickness and cured at room temperature for 4 hours. The combined Ecoflex/Cu interconnect/circuit device was then removed from the glass/PMMA substrate using a razor blade.

4.5.4 Characterization methods

4.5.4.1 Morphology

The morphology of the BP was characterized using scanning electron microscope (Phillips XL30 ESEM) with an accelerating voltage of 20 kV.

4.5.4.2 Electrochemical measurements

The electrochemical performances of the half cells and EFC were conducted using a μAutolab Type II commanded by Nova software (Version 2.1). *In vitro* table-top electrochemical characterization was performed in 0.5 mol L^{-1} pH 7.4 PB. The enzyme-catalyzed lactate oxidation and oxygen reduction reactions at the bioanode and biocathodes were characterized by linear sweep voltammetry in a three-electrode system with a scan rate of 5 mV s^{-1}. The three-electrode system consisted of a BP electrode as the working electrode, a Platinum (Pt) wire as the counter electrode and an Ag/AgCl (3M KCl) as the reference electrode. The assembled EFC device was characterized in a two-electrode system with the bioanode as the counter and reference electrode and the biocathode as the working electrode. Linear sweep polarization curves of the EFC in different lactate concentrations were obtained by scanning from OCV to 0.01 V at 5 mV s^{-1}. The calculation of the power density of a single EFC was based on the geometrical area of the cathode (0.18 cm^2).

CV and galvanostatic charge/discharge (GCD) techniques were used to characterize

the capacitive behavior of the EFC. CVs were performed from 0 V to 0.8 V with a scan rate of 50 mV s^{-1}, while the GCD tests were carried out at current densities of 0.1, 0.2, 0.5 and 1 mA cm^{-2}. The capability of the EFC to serve as the pulse generator was characterized by chronopotentiometry. The minimum voltage at the end of each 10 ms pulse discharge was used to calculate the power density.

4.5.4.3 Mechanical resilience studies

The mechanical resiliency studies were conducted on a motorized linear stage connected to a controller (A-LST0250A-E01 Stepper Motor and Controller, Zaber Technologies, Vancouver, Canada). Four linear motors with the same speed were used to conduct 20% biaxial stretching. The stability of the EFC during the mechanical deformations was studied by measuring the resistance of the screen-printed current collector and the current output of the EFC with a 33 kΩ loading during 20% biaxial stretching.

4.5.4.4 On-body power generation

The flexible buckypaper-based EFC was mounted on the arm of one volunteer with the assistance of a piece of adhesive film (Perme-Rroll). The stainless conductive steel yarn was used to connect the EFC and a 510 Ω resistor to reach the maximal power density, with stretchable Ag ink as the joint bonding resin. The current of the circuit was record every 5 s by a potentiostat during which the volunteer was doing stationary cycling. The capability of the EFC to power one LED was demonstrated by using the flexible DC-DC converter to boost the voltage and a switch to control the “on” and “off” status. The voltage of the LED was tested in both pulse and continuous working mode. All on-body experiments were approved by the Human Research Protections Program at University of California, San Diego, and followed the guidelines of institutional Review Boards (IRB).

References

1. Lv, J. *et al.* Wearable, stable, highly sensitive hydrogel–graphene strain sensors. *Beilstein Journal of Nanotechnology* **10**, 475–480 (2019).
2. Bandodkar, A. J., Jeerapan, I. & Wang, J. Wearable Chemical Sensors: Present Challenges and Future Prospects. *ACS Sens.* **1**, 464–482 (2016).
3. Kim, J. *et al.* Wearable Bioelectronics: Enzyme-Based Body-Worn Electronic Devices. *Acc. Chem. Res.* **51**, 2820–2828 (2018).
4. Banerjee, J. *et al.* Improvement of Human Keratinocyte Migration by a Redox Active Bioelectric Dressing. *PLoS ONE* **9**, e89239 (2014).
5. Bandodkar, A. J. & Wang, J. Wearable Biofuel Cells: A Review. *Electroanalysis* **28**, 1188–1200 (2016).
6. Rasmussen, M., Abdellaoui, S. & Minteer, S. D. Enzymatic biofuel cells: 30 years of critical advancements. *Biosensors and Bioelectronics* **76**, 91–102 (2016).
7. Koushanpour, A., Gamella, M. & Katz, E. A Biofuel Cell Based on Biocatalytic Reactions of Lactate on Both Anode and Cathode Electrodes – Extracting Electrical Power from Human Sweat. *Electroanalysis* **29**, 1602–1611 (2017).
8. Bandodkar, A. J. *et al.* Soft, stretchable, high power density electronic skin-based biofuel cells for scavenging energy from human sweat. *Energy & Environmental Science* **10**, 1581–1589 (2017).
9. Lv, J. *et al.* Sweat-based wearable energy harvesting-storage hybrid textile devices. *Energy Environ. Sci.* **11**, 3431–3442 (2018).
10. Gooding, J. J. Nanostructuring electrodes with carbon nanotubes: A review on electrochemistry and applications for sensing. *Electrochimica Acta* **50**, 3049–3060 (2005).
11. Bandodkar, A. J., Jeerapan, I., You, J.-M., Nuñez-Flores, R. & Wang, J. Highly Stretchable Fully-Printed CNT-Based Electrochemical Sensors and Biofuel Cells: Combining Intrinsic and Design-Induced Stretchability. *Nano Letters* **16**, 721–727 (2016).
12. Agnès, C. *et al.* Supercapacitor/biofuel cell hybrids based on wired enzymes on carbon nanotube matrices: autonomous reloading after high power pulses in neutral buffered glucose solutions. *Energy & Environmental Science* **7**, 1884 (2014).
13. Hussein, L., Urban, G. & Krüger, M. Fabrication and characterization of buckypaper-based nanostructured electrodes as a novel material for biofuel cell applications. *Physical Chemistry Chemical Physics* **13**, 5831 (2011).
14. Gross, Andrew. J. *et al.* A High Power Buckypaper Biofuel Cell: Exploiting 1,10-Phenanthroline-5,6-dione with FAD-Dependent Dehydrogenase for Catalytically-Powerful Glucose Oxidation. *ACS Catal.* 4408–4416 (2017). doi:10.1021/acscatal.7b00738
15. Kwon, C. H. *et al.* High-power biofuel cell textiles from woven biscrolled carbon nanotube yarns. *Nature Communications* **5**, (2014).
16. Jia, W., Valdés-Ramírez, G., Bandodkar, A. J., Windmiller, J. R. & Wang, J. Epidermal Biofuel Cells: Energy Harvesting from Human Perspiration. *Angewandte Chemie International Edition* **52**, 7233–7236 (2013).
17. Jia, W. *et al.* Wearable textile biofuel cells for powering electronics. *Journal of Materials*

Chemistry A **2**, 18184–18189 (2014).

18. Jeerapan, I., R. Sempionatto, J., Pavinatto, A., You, J.-M. & Wang, J. Stretchable biofuel cells as wearable textile-based self-powered sensors. *Journal of Materials Chemistry A* **4**, 18342–18353 (2016).
19. Zebda, A. *et al.* Mediatorless high-power glucose biofuel cells based on compressed carbon nanotube-enzyme electrodes. *Nature Communications* **2**, 370 (2011).
20. Zebda, A. *et al.* Single Glucose Biofuel Cells Implanted in Rats Power Electronic Devices. *Scientific Reports* **3**, (2013).
21. Gross, A. J., Holzinger, M. & Cosnier, S. Buckypaper bioelectrodes: Emerging materials for implantable and wearable biofuel cells. *Energy Environ. Sci.* (2018). doi:10.1039/C8EE00330K
22. Reid, R. C., Minteer, S. D. & Gale, B. K. Contact lens biofuel cell tested in a synthetic tear solution. *Biosensors and Bioelectronics* **68**, 142–148 (2015).
23. Yu, Y., Zhai, J., Xia, Y. & Dong, S. Single wearable sensing energy device based on photoelectric biofuel cells for simultaneous analysis of perspiration and illuminance. *Nanoscale* **9**, 11846–11850 (2017).
24. Gross, A. J. *et al.* Robust bifunctional buckypapers from carbon nanotubes and polynorbornene copolymers for flexible engineering of enzymatic bioelectrodes. *Carbon* **107**, 542–547 (2016).
25. Fritea, L. *et al.* A bifunctional triblock polynorbornene/carbon nanotube buckypaper bioelectrode for low-potential/high-current thionine-mediated glucose oxidation by FAD-GDH. *Journal of Materials Chemistry A* **7**, 1447–1450 (2019).
26. Yin, L. *et al.* Highly Stable Battery Pack *via* Insulated, Reinforced, Buckling-Enabled Interconnect Array. *Small* **14**, 1800938 (2018).
27. Lalaoui, N., Le Goff, A., Holzinger, M. & Cosnier, S. Fully Oriented Bilirubin Oxidase on Porphyrin-Functionalized Carbon Nanotube Electrodes for Electrocatalytic Oxygen Reduction. *Chemistry - A European Journal* **21**, 16868–16873 (2015).
28. Harvey, C. J., LeBouf, R. F. & Stefaniak, A. B. Formulation and stability of a novel artificial human sweat under conditions of storage and use. *Toxicology in Vitro* **24**, 1790–1796 (2010).
29. Escalona-Villalpando, R. A. *et al.* Clean energy from human sweat using an enzymatic patch. *Journal of Power Sources* **412**, 496–504 (2019).
30. Pankratov, D., Falkman, P., Blum, Z. & Shleev, S. A hybrid electric power device for simultaneous generation and storage of electric energy. *Energy Environ. Sci.* **7**, 989–993 (2014).
31. Pankratov, D., Blum, Z., Suyatin, D. B., Popov, V. O. & Shleev, S. Self-Charging Electrochemical Biocapacitor. *ChemElectroChem* **1**, 343–346 (2014).
32. Pankratov, D. *et al.* A Nernstian Biosupercapacitor. *Angewandte Chemie International Edition* **55**, 15434–15438 (2016).
33. Yin, L. *et al.* From All-Printed 2D Patterns to Free-Standing 3D Structures: Controlled Buckling and Selective Bonding. *Advanced Materials Technologies* **3**, 1800013 (2018).
34. Gong, S. & Cheng, W. Toward Soft Skin-Like Wearable and Implantable Energy Devices. *Advanced Energy Materials* **7**, 1700648 (2017).
35. Cosnier, S., Haddad, R., Moatsou, D. & O'Reilly, R. K. Biofunctionalizable flexible bucky paper by combination of multi-walled carbon nanotubes and polynorbornene-pyrene – Application to

the bioelectrocatalytic reduction of oxygen. *Carbon* **93**, 713–718 (2015).

Chapter 5:

Redox-active glyconanoparticles as electron shuttles for mediated electron transfer with bilirubin oxidase in solution

Chapter 5 Redox-active glyconanoparticles as electron shuttles for mediated electron transfer with bilirubin oxidase oxidase in solution

Résumé

La consommation croissante des combustibles fossiles et leur épuisement programmé ont conduit au développement de méthodes de production d'électricité propres. Ces dernières ont favorisé l'émergence de nouvelles sources d'énergie durables et renouvelables sans émissions de gaz à effet de serre ni pollution de l'environnement. Parmi tous les systèmes de production d'énergie, les piles à combustible représentent une nouvelle stratégie de production d'énergie propre. Une sous-catégorie de piles à combustible, les biopiles qui convertissent l'énergie chimique en énergie électrique par des réactions électro-enzymatiques, a suscité une attention considérable au cours des vingt dernières années. Cependant, il convient de noter que les biopiles ne sont pas destinées à surmonter l'épuisement des combustibles fossiles et à entrer en compétition avec les sources d'énergie renouvelables comme les énergies hydroélectrique, solaire et éolienne. Le champ d'application des biopiles enzymatiques est limité, du moins pour le moment, à la production d'électricité pour alimenter des systèmes microélectroniques tels que des actionneurs et des capteurs.

L'attractivité des biopiles à combustibles réside dans les propriétés de la catalyse enzymatique comme l'activité à température ambiante et leur bio-spécificité. En particulier, la haute spécificité des biopiles envers le «carburant» (sucres, alcools ou hydrogène) à l'anode et la réduction des oxydants (O_2, H_2O_2) à la cathode dans des conditions douces (20-40°C) permet leur utilisation dans des milieux complexes comme les organismes vivants ou les végétaux sans aucune séparation entre les bioanodes et les biocathodes.

Outre leur très grande spécificité vis-à-vis de leurs substrats, l'utilisation d'enzymes offre plusieurs avantages par rapport aux catalyseurs classiques à base de métaux nobles. En particulier, les enzymes sont biocompatibles et sans danger pour l'environnement, bien qu'elles soient intrinsèquement complexes et fragiles. Toutefois, les enzymes présentent des inconvénients majeurs: leur stabilité opérationnelle, leur fragilité aux températures élevées, en général au-dessus de 60 °C à l'exception d'enzymes issues d'organismes thermophiles qui présentent des enzymes thermorésistantes actives à 75-80 °C, la perte d'activité catalytique aux basses

températures et enfin la stabilité mécanique de l'enzyme à l'interface enzyme-électrode. Il s'avère actuellement urgent d'élaborer des stratégies innovantes pour préserver, optimiser et améliorer la stabilité et l'activité des électrodes enzymatiques pour la bioélectrocatalyse dans conditions variées.

Une grande majorité des biopiles enzymatiques génère de l'énergie électrique à partir de la dégradation enzymatique du glucose et de l'oxygène, deux substrats présents dans les fluides physiologiques. Ainsi, parallèlement à l'alimentation d'appareils électroniques portables (téléphone portable, baladeur numérique, GPS, capteurs, etc.), une application fascinante concerne l'implantation de biopiles dans le corps humain en tant que source autonome d'énergie théoriquement illimitée comparativement aux piles scellées style piles bouton. De telles biopiles pourraient ainsi constituer une alternative prometteuse pour alimenter des dispositifs médicaux implantés. Eu égard à leur performance, il faut toutefois ne pas étendre leur application à l'alimentation des pacemakers qui actuellement utilisent des piles leur conférant une durée de vie allant jusqu'à 8 ans chez le patient. Par contre, la génération in situ d'énergie par les biopiles leur ouvre la possibilité d'accumuler une énergie assez importante pour périodiquement transmettre par radiofréquence des informations par exemple directement sur un téléphone portable.

Cependant, le développement de biopiles implantées est confronté à trois verrous technologiques majeurs qui entravent actuellement leur application réelle in vivo, à savoir la stérilisation de la biopile, leur courte durée de vie et, dans une moindre mesure, leur faible rendement énergétique due à la faible concentration dans l'organisme du glucose et de l'oxygène. La stérilisation du système est obligatoire pour éviter les problèmes inflammatoires qui induisent la formation d'une gangue autour de la biopile rendant la diffusion des substrats très difficile. Cependant, la stérilisation de la biopile complète induit forcément une désactivation chimique (avec, par exemple, l'hypochlorite de sodium, le formaldéhyde ou l'ozone) ou physique (irradiation gamma ou par rayons X ou exposition à des températures extrêmes supérieures à 140 ° C) des enzymes qui sont préalablement fixées sur les électrodes.

Il faut souligner qu'en raison du petit nombre de biopiles enzymatiques implantées chez les animaux, l'impact de la stérilisation a rarement été examinée, bien qu'elle soit un facteur décisif pour l'avenir de ces technologies. En fait, la plupart des biopiles implantées ou partiellement insérées décrites à ce jour dans la litérature, n'ont pas été stérilisés et ont été placés chez dans des insectes, gastéropodes ou mammifères sans

conditions stériles.

Par ailleurs, la faible stabilité des biopiles enzymatiques est également liée à la perte d'activité ou/et de connexion électrique des enzymes immobilisées. En effet, les bioanodes et biocathodes sont basées sur l'immobilisation de différentes enzymes rédox sur la surface des électrodes pour leur connexion électrique. Cette fixation peut être obtenue par piégeage physique, par greffage chimique ou par des interactions affines. La première procédure conduit à une dénaturation liée au concept de piégeage lui-même qui génère un environnement généralement peu biocompatible. De plus, l'activité de l'enzyme piégée peut être affectée par la perméabilité et l'hydrophilie de la matrice inorganique ou organique hôte, ainsi que par des contraintes stériques qui bloquent sa flexibilité conformationnelle. Concernant le processus de greffage chimique et les liaisons affines, il en résulte une meilleure accessibilité du substrat à l'enzyme immobilisée mais la quantité de biocatalyseur est limitée à une quasi-monocouche à l'interface électrode modifiée -solution.

Concernant plus spécifiquement le processus de connexion électrique, il existe quelques exemples de transfert d'électrons direct entre les enzymes immobilisées et la surface de l'électrode. Cependant, le site prosthétique de nombreuses enzymes oxydoréductases est en général profondément enfoui dans une matrice protéique isolante empêchant ce type de transfert direct d'électrons. Dans ce contexte, de nombreuses configurations de biopiles utilisent des petites molécules électroactives pour établir une communication électrique entre les enzymes et la surface des électrodes. Ces médiateurs redox doivent également être immobilisés sur le matériau enzyme-électrode. Toutefois, le greffage covalent de ces médiateurs rédox réduit considérablement leur degré de mobilité et pénalise leur potentialité vis-à-vis de l'interaction avec le site actif de l'enzyme, diminuant ainsi l'efficacité du transfert d'électrons. Quant à l'immobilisation non-covalente, elle entraine une diminution inéluctable de l'activité électrocatalytique via la perte en solution de ces molécules rédox. De plus, un autre facteur déterminant pour la durée de vie d'une biopile, est la stabilité chimique des médiateurs rédox immobilisés qui doivent subir un nombre très important de cycles d'oxydation et de réduction successifs. Enfin, il faut souligner que l'immobilisation d'enzymes peut également fixer les enzymes susceptibles d'engendrer un transfert direct d'électron dans des orientations totalement inefficaces.

Dans ce contexte, en rupture avec les concepts développés jusqu'ici dans le domaine des biopiles enzymatiques qui consistent à immobiliser tous les composants

bioélectrocatalytiques (enzymes, médiateur rédox) sur les électrodes. Nous nous proposons de concevoir une approche totalement innovante basée, pour la première fois, sur une configuration de biopile comprenant des enzymes et des médiateurs redox en solution au sein de compartiments poreux voire avec comme objectif des compartiments poreux et conducteurs jouant le rôle d'électrodes.

Les enzymes en solution peuvent tourner librement et ainsi présenter une configuration idéale pour l'interaction avec le médiateur rédox conduisant à un transfert indirect d'électron bien plus efficace qu'en configuration immobilisée. Il est également possible d'utiliser des concentrations élevées d'enzyme. De plus, la possibilité de renouveler périodiquement la solution d'enzymes et de médiateurs rédox permet de prolonger la durée de vie de la biopile. Enfin, cette stratégie originale permettrait de stériliser les compartiments d'électrodes puis à injecter une solution aqueuse stérile d'enzymes et de médiateurs redox supprimant ainsi les inconvénients de désactivation de l'enzyme immobilisée lors du processus de stérilisation de l'ensemble.

Le verrou technologique majeur de ce concept est relatif aux tailles similaires des molécules rédox et du substrat de l'enzyme de l'anode, à savoir le glucose. Or, le compartiment poreux contenant la solution d'enzymes et de médiateur rédox doit présenter une perméabilité permettant une bonne diffusion du glucose tout en retenant le médiateur rédox.

Pour remédier à cet inconvénient, nous avons donc envisagé de développer une version supramoléculaire de ces médiateurs redox en concevant des nanoparticules redox.

Les nanoparticules / micro-particules, en particulier métalliques, sont largement utilisées dans divers domaines. Parmi les différentes particules décrites dans la littérature, les particules d'argent sont une des plus importantes catégories en raison de leurs caractéristiques physiques, chimiques et biologiques favorables. Ainsi, de nombreuses études ont été menées pour évaluer leurs propriétés et les utiliser dans diverses applications, telles que les diagnostics, les thérapies antibactériennes et anticancéreuses et l'optoélectronique. Les nano/microparticules sont devenues des composants importants dans les dispositifs de biodétection. Par exemple, les particules de métaux nobles comme l'argent et l'or sont largement employées pour la résonance des plasmons de surface qui améliore considérablement les signaux SPR ou Raman. Ces matériaux, ainsi que d'autres matériaux tels que les nanoparticules de platine ou les nanoparticules d'oxydes métalliques, sont également utiliser pour augmenter les

propriétés catalytiques ou conductrices dans les biocapteurs électrochimiques. Ces particules peuvent être fonctionnalisées en surface par des traitements incluant la carboxylation, l'amidation, l'amination, l'hydroxylation et même la magnétisation pour faciliter la fixation d'une molécule d'intérêt spécifique. Toutefois, ces procédures s'avèrent complexes et couteuses.

Eu égard à ces inconvénients, nous nous sommes intéressés à l'élaboration et la caractérisation de glyconanoparticules (vésicules, agrégats de micelles) obtenues à partir de l'auto-assemblage de copolymères composés d'une queue hydrophobe (polystyrène) et d'une tête en oligosaccharides comme partie hydrophile. Ces glyconanoparticules qui sont stables en suspension en milieu aqueux, présentent une couche externe composée de β-cyclodextrine. Ce groupement permet une post-fonctionnalisation de la nanoparticule par des molécules hydrophobes via des interactions hôte-invité avec l'intérieur de la cavité hydrophobe de la cyclodextrine. Outre la possibilité jusqu'à présent impossible de connecter des enzymes en solution par des médiateurs rédox insolubles en milieu aqueux, ces nanoparticules offrent également l'avantage de constituer une plateforme polyvalente permettant de fixer un large éventail de médiateurs rédox sans avoir à effectuer de modification chimique particulière de ces médiateurs.

Chapter 5 Redox-active glyconanoparticles as electron shuttles for mediated electron transfer with bilirubin oxidase in solution

This chapter is based on the following manuscript-

Andrew J. Gross, Xiaohong Chen, Fabien Giroud, Christophe Travelet, Redouane Borsali, Serge Cosnier

J. Am. Chem. Soc. **2017**, 139, 16076-16079

5.1 Abstract

In previous chapters, all bioelectrodes have been fabricated by immobilizing redox mediators and enzymes on electrode surface, which has been the classic way to construct high-power biofuel cell. However, the life time of these devices are still not up to the standard for commercial applications. The instability is generally attributed to the fragile nature of enzymes. Once the immobilized enzymes lose their activity, it is difficult to recover the activity of the enzyme-modified electrodes. In this chapter, a different configuration of bioelectrode is envisioned by using solution phase mediators and enzymes. This can open up a possible new strategy to fabricate solubilized enzymatic biofuel cell to overcome the short lifetime issue.

5.2 Introduction

Electron transfer (ET) reactions are vital in biological systems including metabolic pathways and photosynthesis.[1] In nature, many ET processes involve redox proteins that rely on intramolecular electron transfer and long range electron transport between enzymes. The high efficiency and specificity of nature's biocatalysts has driven the development of biomimetic enzyme-electrode interfaces for applications such as energy conversion and biosensing.[2] Biofuel cells are emerging devices capable of converting chemical energy into electrical energy which ideally exploit fast and efficient ET between electrodes and enzymes.[3] In most cases, such electron transfer reactions are hampered due to the insulating globular structure of the protein matrix surrounding the enzyme's active site. Improvements in the electrical wiring of enzymes and the stability of enzyme-electrode interfaces are required to address limitations of biofuel cells including limited operational stability and low power output.

Direct electron transfer (DET) over short distances (≤ 1.5 nm) between the redox center(s) of enzymes and electrodes has been achieved for a limited number of enzymes including multi-copper oxidases (MCOs). MCOs are of great interest for the reduction of O_2 at the cathode in biofuel cells.[4,5] Mediated electron transfer (MET) is an alternative to DET which enables ET with a wide range of enzymes. For MET, redox polymers or redox molecules are employed to shuttle electrons to and from the enzyme's active site, for reduction and oxidation reactions respectively.[6,7] This can reduce the kinetic hindrance of interfacial ET but commonly at the expense of a high overpotential. Use of a mediator is attractive but complex synthesis, chemical stability and leaching of the mediator *in vivo* and *ex vivo* are major concerns. An approach to address these limitations has been to use carbon or metallic nanoparticles (NPs).

Early works have described the use of gold NPs functionalized with enzyme cofactor for high catalytic turnover of glucose *via* modified apo-glucose oxidase (GOx)[8] and apo-glucose dehydrogenase (GDH).[9] More recently, gold NPs have been elegantly bonded to GOx and MCO enzymes to facilitate enzyme wiring with the electrode.[10,11] Whilst these examples highlight improved enzyme wiring *via* electronic bridging, multi-step synthesis and protein engineering are necessary. Alternatively, carbon and metallic NPs directly immobilized on electrode surfaces create high area meso- and nano-structured interfaces for DET *via* oriented immobilization and enzyme trapping.[12,13] Surface immobilization of catalytic components is the classic approach for biofuel cell construction. Immobilization is considered effective for electrode stabilization. Nevertheless, desorption, limiting surface coverage and enzyme activity loss (for example, due to conformational changes) are constraining factors.[14,15]

Here, we further extend the use of MET between electrodes and enzymes to a strategy which uses mediator-containing sugar-coated nanoparticles in solution. To the best of our knowledge, no polymeric nanoparticle system has been explored either for ET with enzymes or for bioelectrocatalytic applications. In addition, we move away from the mainstream use of immobilized biocatalytic components and instead explore their use in solution. This unconventional approach in particular opens up the possibility for (i) higher amounts of enzyme and mediator, (ii) improved enzymatic activity, and (iii) the possibility to refuel electrode compartments for prolonged fuel cell performance. The cyclodextrin-based NPs are envisaged here for solution-based biofuel cells and flow-through biosensors but could also be harnessed for applications

including light harvesting.[16]

5.3 Results and discussion

5.3.1 Characterization of NPs

The encapsulated nanoparticles were prepared by self-assembly of an amphiphilic β-cyclodextrin modified polystyrene polymer (PSCD) (**Figure 5.1A**). The PSCD polymer was synthesized according to a convenient protocol *via* click chemistry of functionalized cyclodextrin and polystyrene blocks in high yield.[17] Self-assembly of PSCD was explored in the absence and presence of bis-pyrene-ABTS (2,2'-Azino-bis(3-ethylbenzothiazoline-6-sulfonic acid)) *via* nanoprecipitation in a large excess of water (see Experimental section 5.5.2).

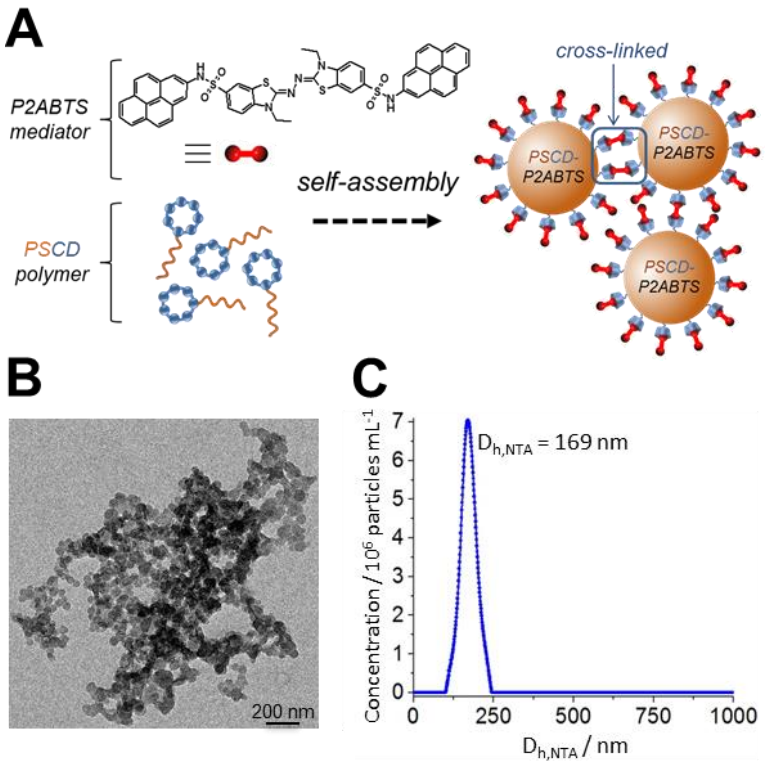

Figure 5.1 (A) Schematic representation of the self-assembly of bis-pyrene-ABTS encapsulated glyconanoparticles. (B) TEM imaging and (C) hydrodynamic diameter distribution by NTA of PSCD-P2ABTSNP.

The possibility to spontaneously self-assemble nanoparticles from β-cyclodextrin modified polystyrene solutions was first confirmed by transmission electron microscopy (TEM) and nanoparticle tracking analysis (NTA). TEM imaging of the bis-pyrene-ABTS nanoparticles (PSCD-P2ABTS$_{NP}$) revealed aggregated clusters

composed of individual nanoparticles with an average diameter of 51 ± 18 nm (**Figure 5.1B**). NTA analysis revealed direct evidence for NPs undergoing Brownian motion with $D_{h,NTA}$ = 169 and 74 nm for the PSCD-P2ABTS$_{NP}$ nanoparticles and unmodified nanoparticles (PSCD$_{NP}$), respectively (**Figure 5.1C** and **Figure 5.2**). The difference between self-assembly performed in the absence and presence of bis-pyrene-ABTS is consistent with the incorporation of guest molecules. The clusters can form in solution with bis-pyrene-ABTS molecules functioning as molecular bridges where each pyrene functionality forms a 1:1 inclusion complex with a β-cyclodextrin cavity present in the outer layer of individual nanoparticles.[18] Non-specific aggregation must also be considered and likely contributes to the self-assembly of the clusters.

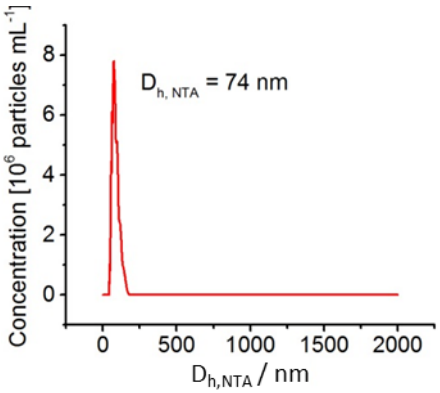

Figure 5.2 Number-weighted hydrodynamic diameter distribution by nanoparticle tracking analysis of PSCD$_{NP}$. It is noted that the PSCD-P2ABTS$_{NP}$ assemblies are *ca.* twice the size of the PSCD$_{NP}$ assemblies suggesting that *ca.* 2^3 = 8 individual nanoparticles come together in solution to form the PSCD-P2ABTS$_{NP}$ clusters.

Dynamic light scattering (DLS) experiments were performed to examine the PSCD-P2ABTS$_{NP}$ nanoparticles in more detail (**Figure 5.3A**). Hydrodynamic diameters ($D_{h,\,DLS}$) were calculated using the Stokes-Einstein equation (**Equation 5.1**) where K_B = Boltzmann constant, T = temperature, η = pure solvent viscosity, and D = diffusion coefficient:

$$D_{h,\,DLS} = \frac{K_B T}{3\pi\eta D} \qquad (5.1)$$

The relaxation time distribution plot, corresponding to a mass-weighted distribution, reveals the presence of two particle sizes with $D_{h,DLS}$ = 195 and 1800 nm. The percentage of small nanoparticles was calculated using **Equation 5.2**, assuming that the nanoparticles behave like hard spheres in water and have the same density. N_{Small}

refers to the number of small nanoparticles, τ_{Small} is the relaxation time corresponding to the small nanoparticles (fast relaxation mode), and S_{Small} is the surface area under the peak related to the small nanoparticles: [19]

$$\frac{N_{Small}}{N_{Big}} = \left(\frac{\tau_{Big}}{\tau_{Small}}\right)^3 \left(\frac{S_{Small}}{S_{Big}}\right) \qquad (5.2)$$

The smaller population is complimentary to that obtained by NTA. The larger population confirms the presence of large agglomerations in the suspension but their presence is very small in number terms. Hence, the estimated number of the smaller objects with $D_{h,DLS}$ = 195 nm is 97.5%.

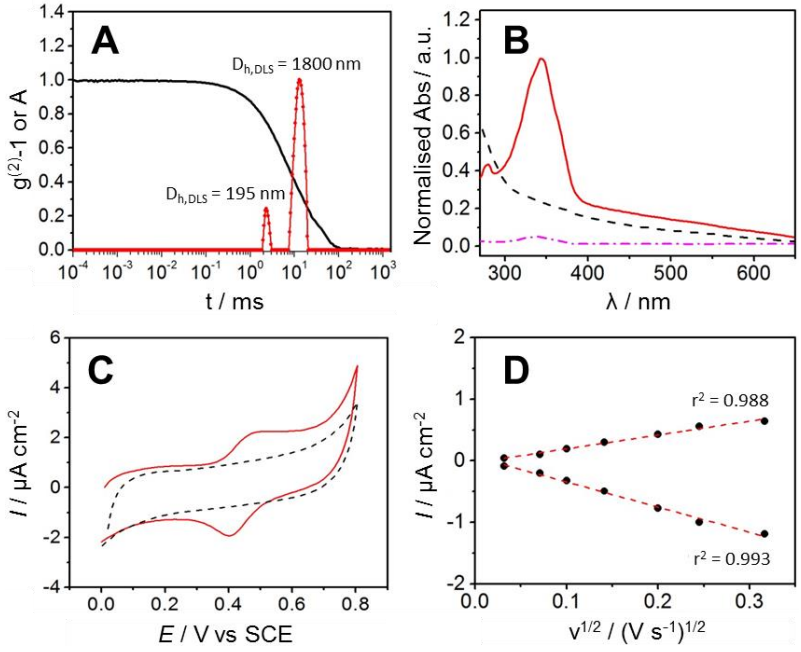

Figure 5.3 (A) DLS autocorrelation function ($g^{(2)}$ – 1) measured at 90° and relaxation time distribution of PSCD-P2ABTS$_{NP}$. (B) UV-visible spectra for (red-) PSCD-P2ABTS$_{NP}$, (black--) PSCD$_{NP}$ and (pink-·-) H_2O-P2ABTS. (C) CVs at glassy carbon of as-prepared (red-) PSCD-P2ABTS$_{NP}$ and (black--) PSCD$_{NP}$ at 100 mV s^{-1}. (D) Corresponding plots of peak current *vs.* the square root of the scan rate for PSCD-P2ABTS$_{NP}$.

The feasibility to encapsulate bis-pyrene-ABTS during nanoparticle self-assembly was established by UV-visible spectroscopy (**Figure 5.3B**). Three suspensions were investigated: as-prepared PSCD$_{NP}$ and PSCD-P2ABTS$_{NP}$, and saturated bis-pyrene-ABTS (H_2O-P2ABTS) in 0.1 mol L^{-1} phosphate buffer (PB). The absorption spectrum for PSCD$_{NP}$ shows background absorbance due to the polymer and no well-defined peaks. In contrast, PSCD-P2ABTS$_{NP}$ and H_2O-P2ABTS exhibit a single well-defined absorption peak at λ_{max} = 344 and 340 nm, respectively, confirming the presence of the ABTS functionality in its reduced state. The absorption

is markedly enhanced for PSCD-P2ABTS$_{NP}$ compared to the saturated H_2O-P2ABTS solution, consistent with a dramatic improvement in solubility for bis-pyrene-ABTS *via* the polymeric architecture.

The concentration of the bis-pyrene-ABTS in aqueous PSCD-P2ABTS$_{NP}$ solution was estimated according to classical calibration plots recorded for dissolved $ABTS^{2-}$ and $ABTS^{\bullet-}$ (**Figure 5.4**). A series of $ABTS^{2-}$ solutions in the concentration range of 2 to 9 µmol L^{-1} were prepared in 0.1 mol L^{-1} phosphate buffer (pH 5.6). The absorbance spectra of the $ABTS^{2-}$ solutions were measured at wavelengths in the range of 220 to 700 nm. After each measurement, 15 µL of 50 µg mL^{-1} bilirubin oxidase (BOx) solution was added to the solution and left for 5 min to react, followed by a second measurement of absorbance in the same range (**Figure 5.4B**). The peak absorbance at 340 and 414 nm, representing $ABTS^{2-}$ and $ABTS^{\bullet-}$, respectively, were subsequently measured and plotted *vs.* $ABTS^{2-}$ concentration (**Figure 5.4C**). Linear fitting results give molar extinction coefficients of 35840 and 33070 L mol^{-1} cm^{-1} for $ABTS^{2-}$ and $ABTS^{\bullet-}$, respectively. Based on the linear calibration curves obtained for both $ABTS^{2-}$ and $ABTS^{\bullet-}$ solutions, the concentration of bis-pyrene-ABTS was estimated to be 6.5 µmol L^{-1}.

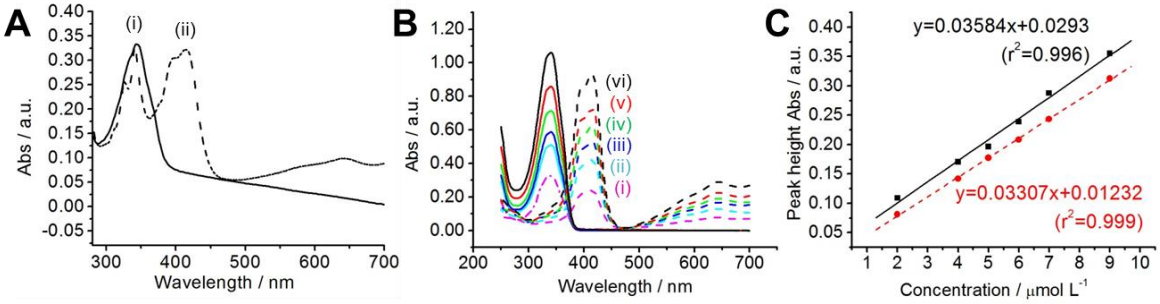

Figure 5.4 (A) UV-visible absorption spectra of (i) PSCD-P2ABTS$_{NP}$ and (ii) PSCD-P2ABTS$_{NP}$ with 11 nmol L^{-1} BOx. (B) UV-visible absorption spectra of (i) 2, (ii) 4, (iii) 5, (iv) 6, (v) 7 and (vi) 9 µmol L^{-1} of (solid line) $ABTS^{2-}$ and (dashed line) $ABTS^{\bullet-}$ with 11 nmol L^{-1} BOx. (C) Linear calibration curves determined from the spectra in (B) according to Beer-Lambert Law. The calibration plot performed with $ABTS^{\bullet-}$ at λ_{max} = 414 nm was used to eliminate the possible interference of pyrene and served as a second method to estimate the concentration.

The electrochemical activity of as-prepared PSCD-P2ABTS$_{NP}$ and PSCD$_{NP}$ nanoparticles in aqueous solutions was investigated at a glassy carbon electrode (GCE) without additional supporting electrolyte. **Figure 5.3C** shows cyclic voltammograms (CVs) recorded at 100 mV s^{-1} of the redox encapsulated and control nanoparticles. The CV clearly shows an electrochemically reversible redox couple at $E_{1/2}$ = 0.46 V

corresponding to the one electron oxidation of $ABTS^{2-}$ to $ABTS^{\bullet-}$ for $PSCD\text{-}P2ABTS_{NP}$. No redox signal is observed for $PSCD_{NP}$ in the absence of bis-pyrene-ABTS. The redox functionalities are therefore clearly present and accessible. The plots in **Figure 5.3D** and **Figure 5.5** show that the peak currents for the oxidation and reduction processes are proportional to the square root of the scan rate, as expected for diffusion-controlled behavior. Poor fitting was observed for the peak current *vs.* scan rate over a wide scan rate range, discounting the presence of adsorbed electroactive species. Furthermore, after recording several CV cycles in $PSCD\text{-}P2ABTS_{NP}$ solution, no evidence for adsorbed electroactive NPs was observed at a GCE in PB (**Figure 5.6**). Although this data does not reveal evidence for NP adsorption, the possibility of dynamic adsorption/desorption during potential cycling cannot be entirely ruled out. Repeated potential cycling of $PSCD\text{-}P2ABTS_{NP}$ showed good stability with little change in the electrochemical redox activity after 10 cycles (**Figure 5.7**). The electrochemical stability provides further evidence for the stable entrapment of bis-pyrene-ABTS as well as the oxidized radical form in the nanoparticles.

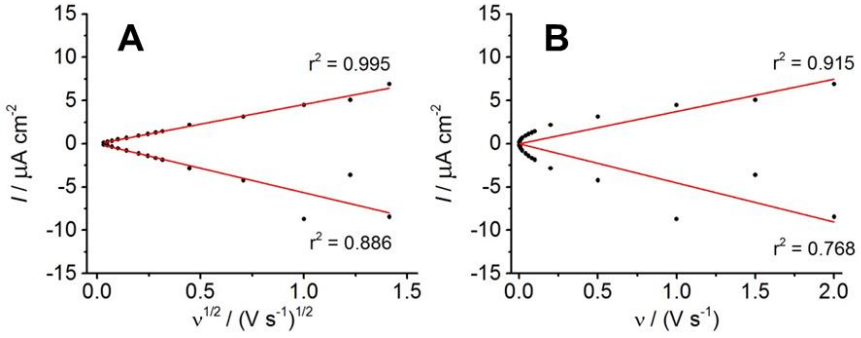

Figure 5.5 Plots of peak current recorded at glass carbon electrode vs. (A) square root of the scan rate and (B) scan rate for as-prepared $PSCD\text{-}P2ABTS_{NP}$ solution for scan rates between 1 mV s^{-1} and 2 V s^{-1}.

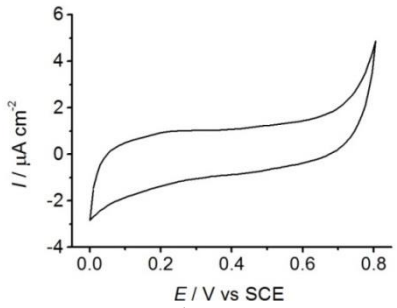

Figure 5.6 CV recorded at a GCE in 0.1 mol L^{-1} PB pH 7 at 100 mV s^{-1} to test for the presence of adsorbed species after performing a scan rate study in as-prepared aqueous PSCD-P2ABTS$_{NP}$ solution (ca. 15 potential cycles from 0 V to 0.8 V) then rinsing the electrode with 0.1 mol L^{-1} PB pH 7.

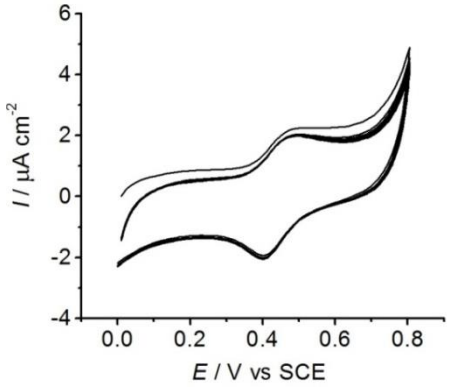

Figure 5.7 Ten consecutive CVs recorded of as-prepared aqueous PSCD-P2ABTS$_{NP}$ solution at GCE (pH = 5.6) at 100 mV s^{-1}.

5.3.2 Oxygen reduction performance

Next the catalytic activity of the PSCD-P2ABTS$_{NP}$ nanoparticles for the 4-electron 4-proton reduction of O_2 to water with BOx from *Myrothecium verrucaria* (*Mv*BOx, 68 kDa) was investigated. This enzyme offers high enzymatic activity, stability at neutral pH, and a relatively good stability towards chloride ions.[20] **Figure 5.8** shows CVs which demonstrate bioelectrocatalytic O_2 reduction at GCE with 3.5 µmol L^{-1} BOx in quiescent oxygen saturated solution ([O_2] ~ 1.1 mmol L^{-1}). A summary of the catalytic parameters are displayed in **Table 5.1**. For all cases, the limiting catalytic currents were obtained from CV scans at 0.1 V *vs.* SCE. The biocathodes prepared with the dissolved mediators, bis-pyrene-ABTS and $ABTS^{2-}$, exhibited maximum current densities for O_2 reduction of -0.67 ± 0.15 µA cm^{-2} (**Figure 5.8A**) and -1.20 ± 0.03 µA cm^{-2} (**Figure 5.8E**), respectively. The smaller current observed with bis-pyrene-ABTS is consistent with its very poor solubility. For the biocathode without NPs or dissolved mediator, a limiting current of 1.39 ± 0.46 µA cm^{-2} was obtained (**Figure 5.8D**). For this case, effective DET is clearly observed between

GCE and BOx in solution. Quasi-steady-state (sigmoidal) voltammograms are obtained for the PSCD-P2ABTS$_{NP}$ biocathode which exhibits a comparably remarkable current density of -3.97 ± 0.86 µA cm^{-2} (**Figure 5.8C**). For control experiments utilizing PSCD$_{NP}$ nanoparticles, very low current densities were observed due to the insulating polymeric structure blocking ET between the enzyme and the electrode (**Figure 5.8B**). PSCD-P2ABTS$_{NP}$ solutions prepared at different concentrations (with $D_{h,DLS}$ between 190 and 390 nm) demonstrated a linear dependence of catalytic current on mediator concentration and also revealed a catalytic improvement with the NPs compared to dissolved ABTS^{2-} (**Figure 5.9** and **5.10**)

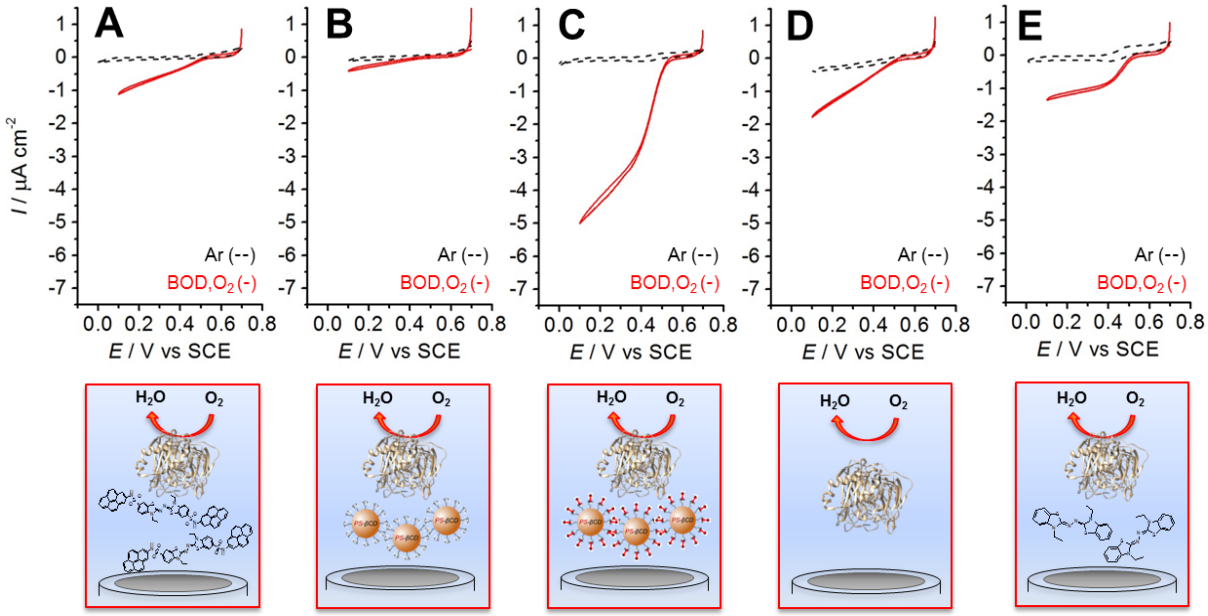

Figure 5.8 CVs recorded at GCE at 5 mV s^{-1} (pH = 5.6) with (black--) argon saturation and (red-) O_2 saturation with BOx for (A) saturated bis-pyrene-ABTS in PB, (B) as-prepared PSCD$_{NP}$ (pH = 5.9), (C) as-prepared PSCD-P2ABTS$_{NP}$, (D) BOx only, and (E) ABTS in PB. [BOx] = 3.5 µmol L^{-1} and [mediator] = 6.5 µmol L^{-1} (< 6.5 µmol L^{-1} for saturated bis-pyrene-ABTS).

Table 5.1 Catalytic parameters from cyclic voltammetry at glassy carbon cathodes with 3.5 µmol L^{-1} BOx and mediator in solution under oxygen saturated conditions

Electrode interface	**$E_{1/2}$ mediator (V *vs* SCE)**	**Electron transfer**	**Onset potential (V *vs.* SCE)**	**Maximum J_{cat} (µA cm^{-2})[e]**
GCE-P2ABTS-BOx[a,d]	-	MET	0.547 ± 0.002	-0.67 ± 0.15
GCE-PSCD$_{NP}$-BOx[c]	-	DET	0.478 ± 0.008	-0.30 ± 0.02
GCE-P2ABTS$_{NP}$-BOx[b,c]	0.46	MET	0.532 ± 0.020	-3.97 ± 0.86
GCE-BOx[d]	-	DET	0.543 ± 0.003	-1.39 ± 0.46

GCE-ABTS-BOx[b,d]	0.46	MET	0.543 ± 0.005	-1.20 ± 0.03

[a] [med] < 6.5 µmol L^{-1}, [b] [med] = 6.5 µmol L^{-1}, [c] as-prepared solution, [d] 0.1 mol L^{-1} phosphate buffer (pH = 5.6), [e] current measured at 0.1 V *vs.* SCE from CVs.

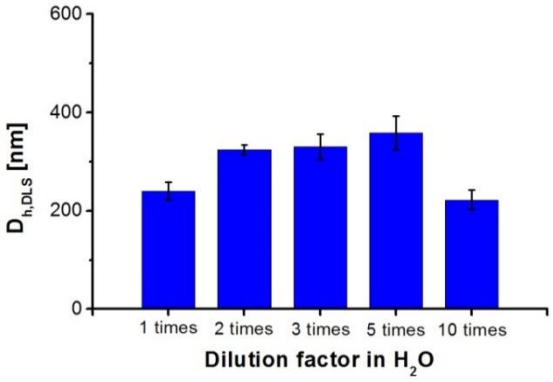

Figure 5.9 DLS analysis of as-prepared PSCD-P2ABTS$_{NP}$ and diluted PSCD-P2ABTS$_{NP}$ solutions used to investigate catalytic as a function of mediator concentration. Dilutions with estimated bis-pyrene-ABTS concentrations were prepared in purified water: 3.25 µmol L^{-1} (2 times), 2.17 µmol L^{-1} (3 times), 1.3 µmol L^{-1} (5 times) and 0.65 µmol L^{-1} (10 times). At least 3 DLS measurements were performed per solution type.

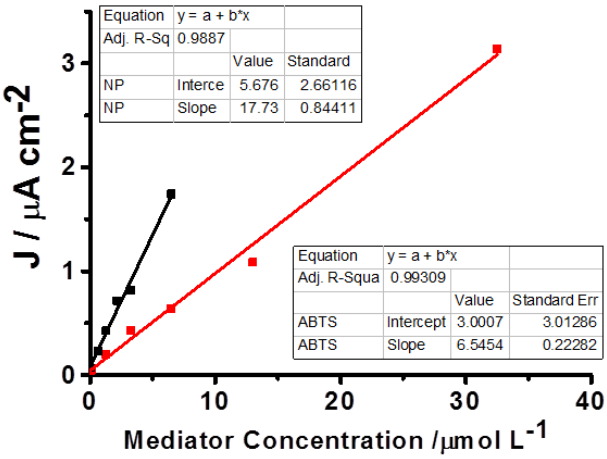

Figure 5.10 Plots of catalytic current versus mediator concentration for as-prepared and diluted PSCD-P2ABTS$_{NP}$ solutions (black) and $ABTS^{2-}$ in phosphate buffer (pH = 5.6) (red) *vs.* mediator concentration. [BOx] = 0.5 µmol L^{-1}. Current measured from amperograms recorded at 0.2 V *vs.* SCE after 600 seconds with O_2 saturation and stirring at 100 rpm.

The enhancement in catalytic current observed for PSCD-P2ABTS$_{NP}$ is consistent with an efficient intra-electron transfer chain between neighboring ABTS redox units of clustered particles and the mono- and tri-nuclear Cu sites of enzymes in solution, as represented in **Figure 5.11A**. The redox conduction observed for bis-pyrene-ABTS nanoparticles at GCE is explained by the phenomena of electron hopping widely reported for redox polymers,[21] where electron transfer proceeds by sequential

self-exchange steps between adjacent redox groups within, between and at the periphery of individual NPs. Mediated electron transfer was also observed for visibly aggregated PSCD-P2ABTS$_{NP}$ in solution, confirming the ability of the redox particles to accept and transfer electrons over substantial distances (**Figure 5.12**). The source of catalytic enhancement for the NPs is in part attributed to free rotation of the particles on the timescale of the experiment which allows many redox sites at the NPs surface to access enzymatic active sites close to the electrode, enabling many catalytic events. Similar rotation enhancement effects are known with redox dendrimers.[22] Effective redox hopping across and around the redox NPs also allows many "active" mediators, therefore facilitating many enzymes to be connected.

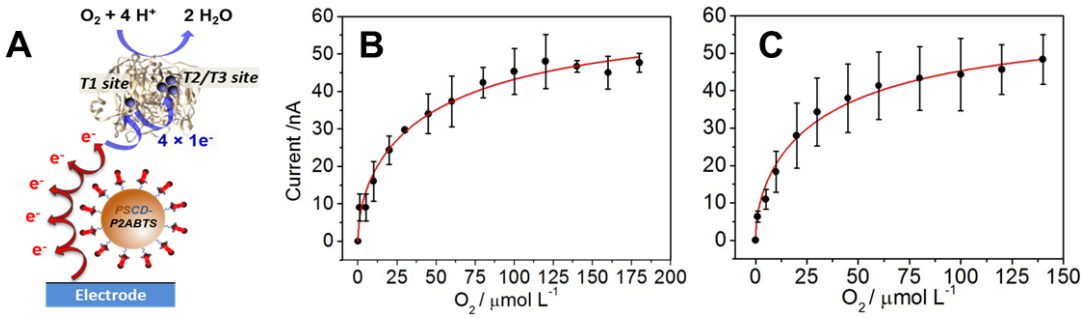

Figure 5.11 (A) Schematic representation of the intra-electron transfer chain between redox nanoparticles and BOx. (B, C) Plots of limiting current as a function of substrate concentration with lines of best fit to **Equation 5.3** for (B) $ABTS^{2-}$ and (C) P2ABTS$_{NP}$ solutions. [BOx] = 10 nmol L^{-1} and [med] = 6.5 µmol L^{-1}. Current measured from amperograms at 0.2 V *vs.* SCE.

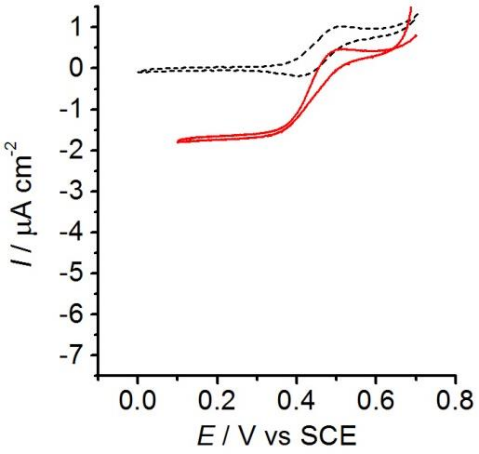

Figure 5.12 CVs recorded at GCE at 5 mV s^{-1} (pH = 5.6) with (black--) argon saturation and (red-) O_2 saturation with BOx for visibly aggregated PSCD-P2ABTS$_{NP}$ after leaving the sample at room temperature in air for ≥ 6 months.

The mediated BOx-catalyzed bioelectrocatalytic reduction of O_2 is considered to follow a ping-pong bi-bi mechanism with a two substrate reaction[4]. Next, kinetic

parameters for PSCD-P2ABTS$_{NP}$ and ABTS were determined from the catalytic current as a function of the substrate (O_2) concentration. This approach permits extraction of the Michaelis constant (K_M) and k_{cat}, according to **Equation 5.3,** as described by Bartlett and coworkers for mediated homogeneous bioelectrocatalysis *via* ping-pong enzyme kinetics.[23] The kinetic parameters were determined by non-linear fitting using **Equation 5.3** (where the current is half order in mediator and enzyme) where I_{lim} = limiting current, n = number of electrons transferred in the redox event, F = Faraday constant, A = geometric electrode area, D_m = mediator diffusion coefficient, [med] = mediator concentration, k_{cat} = catalytic rate constant, [e] = enzyme concentration, [s] = substrate concentration, and K_M = Michaelis constant:[24]

$$I_{lim} = nFA\left(\frac{2D_m[med]k_{cat}[e][s]}{K_M + [s]}\right)^{1/2} \qquad (5.3)$$

Figure 5.11B and **5.11C** shows the calibration plots and non-linear best fit for the BOx-oxygen reaction with the ABTS^{2-} and P2ABTS$_{NP}$ mediator solutions containing 10 nmol L^{-1} BOx, respectively. From chronoamperograms recorded at 0.2 V *vs.* SCE in triplicate, the estimated k_{cat} and K_M values are 142 ± 15 s^{-1} and 77 ± 15 µmol L^{-1} for the PSCD-P2ABTS$_{NP}$ mediator and 200 ± 25 s^{-1} and 107 ± 25 µmol L^{-1} for the ABTS^{2-} mediator. The different kinetic values suggest that the BOx has a higher affinity for oxygen in the presence of the NPs compared to the dissolved ABTS^{2-} mediator, although with a slower turnover rate. The values obtained are of the same order reported for MCO enzymes for O_2 reduction in solution including 118 ± 10 s^{-1} for *Trametes versicolor* laccase (*Tv*laccase)/ABTS^{2-},[25] and 57 s^{-1} and 230 s^{-1} for *Mv*BOx /ABTS^{2-}.[26,5] The K_M values fall in the general range of 10 to 500 µmol L^{-1} found in the literature. Crucially, these results confirm that the NPs serve as effective electron relays.

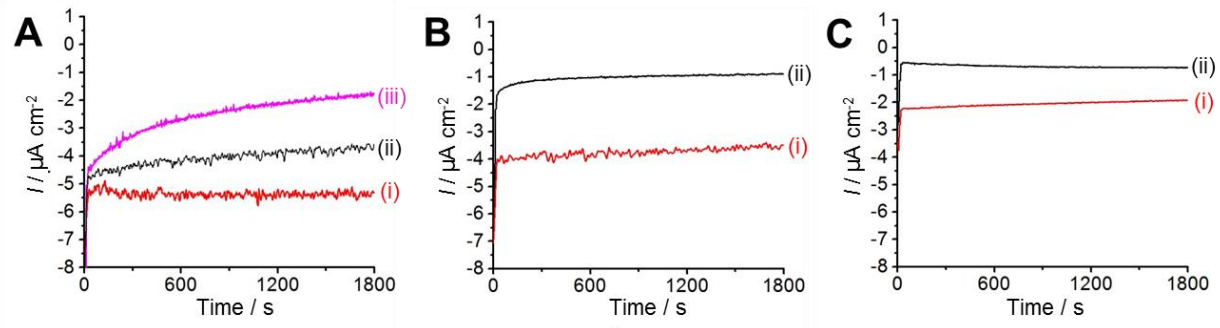

Figure 5.13 Chronoamperograms recorded for 1800 s at E_{app} = 0.2 V *vs.* SCE at GCE in oxygen-saturated solution of (A) PSCD-P2ABTS$_{NP}$ as-prepared pH = 5.6 with BOx, (B) ABTS^{2-} in

phosphate buffer (pH = 5.6) with BOx, and (C) BOx only in phosphate buffer (pH = 5.6) on (i) day 0, (ii) day 1, (iii) day 2. [BOx] = 3.5 μmol L^{-1}.

A preliminary assessment of short term biocathode stability was performed. Electrocatalytic currents were monitored by chronoamperometry in oxygen-saturated solution at 0.2 V *vs.* SCE for periods of 1800 s on two days **(Figure 5.13** and **Table 5.2**). The catalytic currents were stable during 1800 s for PSCD-P2ABTS$_{NP}$, $ABTS^{2-}$, and BOx solutions with 3.5 μmol L^{-1} BOx. After storage at room temperature overnight, the operational stability during a further 1800s, after 15 min oxygen purging, remained relatively stable (current fluctuation below 10%). However, the current densities were drastically lower in all three cases. The percentage of current remaining after 3600 s (2 × 1800 s) operation and 24 h storage is 60%, 33% and 10% for the PSCD-P2ABTS$_{NP}$, $ABTS^{2-}$, and BOx only biocathodes, respectively. After a further 24 h and a total operation time of 5400 s, 18% of the initial current remained for the PSCD-P2ABTS$_{NP}$ biocathode. The current density was therefore still higher for the nanoparticle biocathode after 2 days than for the $ABTS^{2-}$ and BOx after only 1 day. The homogeneous ABTS/BOx solution with MET is therefore extremely unstable. The BOx solution with DET is slightly better but still very poor. Remarkably, a major improvement in biocathode stability was observed using the redox NPs. The improved stability is, at least in part, attributed to the NP architecture stabilizing reactive $ABTS^{\bullet-}$ radicals. The apparent improvement in enzyme stability is tentatively attributed to the NPs which help prevent enzymes from interacting with each other without significantly impeding enzyme diffusion. And probably offer a slightly better environment that impedes enzyme denaturation in buffer.

Table 5.2 Stability data obtained during 1800 s on two days from single-potential amperometry at E_{app} = 0.2 V *vs.* SCE at glassy carbon cathodes with 3.5 μmol L^{-1} BOx and mediator in solution under oxygen purging conditions

–	Day 0		Day 1	
GCE interface	**J_{cat} / μA cm^{-2} [d]**	**Residual J_{cat} / %**	**J_{cat} / μA cm^{-2} [d]**	**Residual J_{cat} / %**
P2ABTS$_{NP}$/BOx[a,b]	-5.4	100%	-3.6	67%
$ABTS^{2-}$/BOx[a,c]	-3.6	100%	-0.9	25%
BOx[c]	-1.9	100%	-0.7	37%

[a] [med] = 6.5 μmol L^{-1}, [b] as-prepared solution (pH = 5.6), [c] 0.1 mol L^{-1} PB (pH = 5.6), [d] current measured at 1800 s.

5.4 Conclusion

In conclusion, this work demonstrates the ability of polymeric glyconanoparticles containing redox-active bis-pyrene-ABTS molecules to function as electron shuttles in solution for the electrical wiring of BOx. Thanks to an intimate MET exchange between nanoparticles containing a high density of electron acceptors, enhanced catalytic currents have been observed compared to homogeneous mediators. In addition to enhanced catalytic performance and low overpotentials, the biocathode with redox nanoparticles showed dramatically improved stability after 60 min operation and 24 h storage, suggesting that the polymer architecture stabilizes both the enzyme and mediator. Furthermore, the large size of the nanoparticles should permit their containment in permselective membranes. In future work, the nanoparticle system will be exploited to solubilize new hydrophobic mediators at high concentrations for bioelectrocatalysis towards a refuelable all-in-solution biofuel cell for powering electronics devices. Biofuel cell designs are envisaged in which enzymes and nanoparticles are periodically introduced to prolong biofuel cell lifetime.

5.5 Experimental Section

5.5.1 Materials and reagents

Mono-sodium phosphate monohydrate (NaH_2PO_4, ≥ 98%), di-sodium hydrogen phosphate heptahydrate (Na_2HPO_4, ≥ 98%), 2,2'-azino-bis(3-ethylbenzothiazoline-6-sulphonic acid) (ABTS) diammonium salt (> 98%), propargylamine, sodium hydroxide (NaOH), potassium tert-butoxide, pyrenemethylammonium hydrochloride, benzotriazol-1-yloxytris(dimethylamino)phosphoniumhexafluorophosphate, tetrahydrofuran (THF) and sodium azide (NaN_3) were purchased from Sigma Aldrich and used as received. The ω-hydroxy-polystyrene (M_n = 3800 g mol^{-1}) was purchased from Polymer Source. β-Cyclodextrin and Cu/CuO nanopowder were purchased from Alfa Aesar, tosyl chloride (TsCl) was obtained from Fluka, pyridine was purchased at SDS, N-methyl-2-pyrrolidone (NMP, > 99%) was purchased from Acros Organics, and methanol (MeOH) and dichloromethane (CH_2Cl_2) were purchased from Biosolve. Bilirubin oxidase (BOx, EC 1.3.3.5, with determined activity of 8.362 U mg^{-1} solid / 9.098 U mL^{-1}) from *Myrothecium sp.* was purchased from Amano (Japan), stored at -20 °C, and used as received. Purified water was obtained by water purification to a

resistivity of 18.2 MΩ cm using a Millipore Ultrapure system. High purity oxygen and argon were obtained from Messer.

5.5.2 Synthesis protocols

5.5.2.1 Synthesis of polystyrene-*b*-β-cyclodextrin (PSCD)

The amphiphilic β-cyclodextrin-modified polystyrene polymer (PSCD) (M_n = 4900 g mol^{-1}) was obtained by click chemistry of functionalized polystyrene and β-cyclodextrin blocks using a Cu nanopowder catalyst according to our previous work with a yield of 8 g (90%) according to the reported procedure (see **Scheme 5.1**).[17]

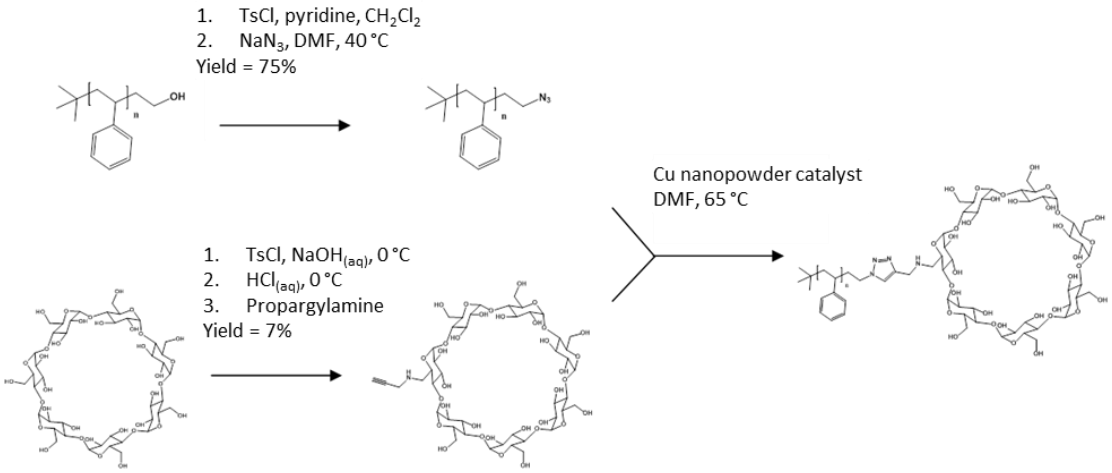

Scheme 5.1 Synthetic pathway for preparation of polystyrene-*b*-β-cyclodextrin (PSCD).

5.5.2.2 Synthesis of bis-pyrene-2,2'-azino-bis(3-ethylbenzothiazoline-6-sulfonic acid) (bis-pyrene-ABTS; P2ABTS)

The bis-pyrene-ABTS compound was synthesized by reaction of 1-pyrenemethylamine, 2,2'-azino-bis(3-ethylbenzothiazoline-6-sulphonic acid) (ABTS) potassium salt and benzotriazol-1-yloxytris(dimethylamino)phosphoniumhexafluorophosphate, with a yield of 65% according to the reported procedure.[27]

5.5.2.3 Self-assembly of $PSCD_{NP}$ and $PSCD\text{-}P2ABTS_{NP}$ *via* nanoprecipitation

Polymer solutions were prepared by dissolving either 10.3 mg of PSCD, or 10.3 mg of PSCD together with 5 mg of bis-pyrene-ABTS (*i.e.* 1:3 moles polymer to bis-pyrene-ABTS), in 4 mL of NMP. The mixtures were subsequently mechanically agitated at 500 rpm overnight then sonicated at room temperature for 10-15 min. For

nanoprecipitation, 1 g of the polymer solution was slowly added dropwise to 40 g of purified water under stirring at 500 rpm. The resulting suspension was subsequently stirred at room temperature at 500 rpm for 1.5 h. The suspension was then dialyzed against purified water (cut-off = 3500 Da; one night; 3 × 2 L purified water replacements). The nanoparticle suspensions were stored at room temperature.

5.5.3 Characterization protocols

5.5.3.1 Nanoparticle tracking analysis (NTA)

NTA was performed to obtain number-weighted hydrodynamic distributions using a Nanosight LM10HS optical microscope equipped with a blue-purple laser (λ_{ex} = 405 nm), a camera and a chamber mounted on a modified microscope stage (Nanosight, Amesbury, UK). The original aqueous suspensions of nanoparticles were diluted with purified water and introduced into the chamber by a syringe. Video clips of the nanoparticles subjected to their natural Brownian motion were captured over 60 s at 25.0 °C and analyzed using the analytical software version 2.1, giving access to number-weighted size distributions.

5.5.3.2 Transmission electron microscopy (TEM)

5 μL of nanoparticle suspension was dropped onto a glow discharged carbon-coated copper grid. 5 μL of 2 w/v % aqueous uranyl acetate stain solution was added and the sample dried in a desiccator overnight. Imaging was performed at 200 kV using a Philips CM200 microscope with a TEM-CAM 216 (TVIPS) camera.

5.5.3.3 Dynamic light scattering (DLS)

Dynamic light scattering measurements were performed using an ALV/CGS-8FS/N069 goniometer with an ALV/LSE-5004 multiple τ digital corrector with a 125 ns initial sampling time and a 35 mW red HeNe linearly polarized laser operating at λ = 632.8 nm. Nanoparticle suspensions were loaded into 10 mm diameter quartz cells thermostatted at 25 ± 0.1 °C. Data were collected using the digital ALV correlator control software at an observation angle relative to the transmitted beam of 90° (scattering vector modulus 1.87×10^{-2} nm^{-1}) for a counting time of typically 180 s. Relaxation time distributions were determined using Contin analysis of the autocorrelation functions.

5.5.3.4 UV-visible spectroscopy

UV-visible absorption spectra were recorded in quartz cuvettes using a Perkin Elmer UV-Lambda 650 spectrophotometer at room temperature with a 1 cm optical path length. The enzymatic activity of bilirubin oxidase was determined from the absorbance of the oxidized ABTS radical (ABTS•-) formed by reaction in the presence of oxygen and BOx in 0.1 mol L^{-1} phosphate buffer (pH = 5.6) (**Equation 5.4** and **Figure 5.14**). The evolution of the absorbance of ABTS•- was measured at a fixed wavelength of 414 nm for 5 min. The background absorbance was obtained from a phosphate buffer solution containing only $ABTS^{2-}$ and no enzyme. Specifically, 1.088 mg of BOx was dissolved in 1 mL of 0.1 mol L^{-1} phosphate buffer (pH = 5.6). The solution was then diluted by a factor of 10 to 0.1088 mg mL^{-1}. The enzymatic reaction experiment was initiated immediately after addition and mixing of 4.6 µL enzyme solution to 50 µmol L^{-1} $ABTS^{2-}$ solution at a final volume of 1 mL. The enzymatic activity was calculated using **Equation 5.5** where dA/dt = absorbance change per time unit, L = optical path length, ε = millimolar extinction coefficient of ABTS•- (ε = 33.07 L $mmol^{-1}$ cm^{-1}), V_{total} = final volume of the reaction mixture in the cuvette, df = dilution factor of enzyme solution, and V_{enzyme} = volume of enzyme solution added to the cuvette.

$$4\,ABTS^{2-} + O_2 + 4H^+ \rightarrow 4\,ABTS^{\bullet-} + 2H_2O \qquad (5.4)$$

$$\text{Enzyme activity (U mg}^{-1}\text{ solid)} = \frac{dA}{dt} \times \frac{L}{\varepsilon} \times V_{total} \times \frac{df}{V_{enzyme}} \qquad (5.5)$$

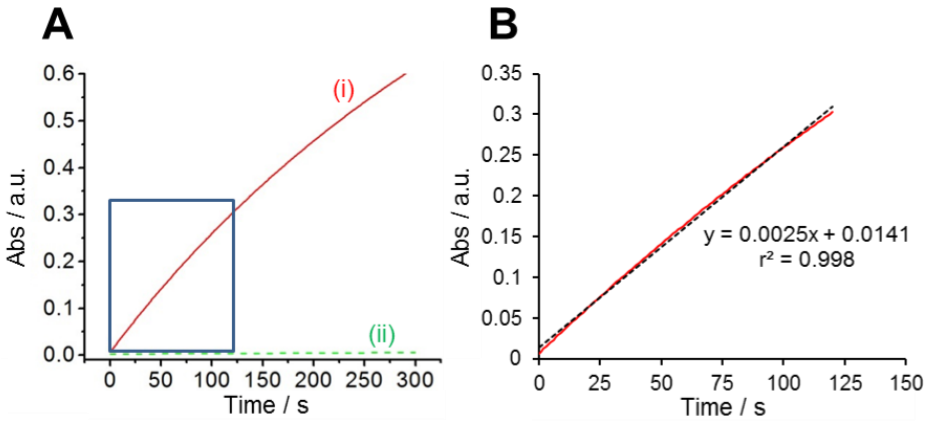

Figure 5.14 (A) Spectrophotometric enzyme assay recorded at λ = 414 nm for 300 s in 50 µmol L^{-1} $ABTS^{2-}$ in phosphate buffer (pH = 5.6) with (i) 7.3 nmol L^{-1} BOx and (ii) without BOx. (B) Fitting of the linear region of the curve (i) shown in (A) for a minimum of 2 min.

5.5.3.5 Electrochemistry

Electrochemical measurements were performed at room temperature using an Eco Chemie Autolab PGSTAT 100 potentiostat running Nova 2.1 software. A conventional three-electrode cell setup was used for all electrochemical experiments comprising a glassy carbon working electrode (GCE, 3 mm diameter), a saturated calomel reference electrode (SCE) and a Pt wire counter electrode. Diffusion coefficients were estimated according to the Randles-Sevcik equation (**Equation 5.6**) at room temperature (25 °C) where I_p = peak current, n = number of electrons transferred in the redox event, A = geometric electrode area, D = diffusion coefficient, C = concentration of electroactive species, and v = scan rate: [28]

$$I_p = (2.69 \times 10^5)\, n^{3/2} A D^{1/2} C v^{1/2} \qquad (5.6)$$

The enzyme-substrate kinetic parameters, k_{cat} and K_M, were determined from a plot of the catalytic current at varying oxygen concentrations (1 to 300 μmol L^{-1}). For these experiments, the steady state current response was determined from single-potential amperometry performed at 0.2 V *vs.* SCE in 0.1 mol L^{-1} potassium phosphate buffer (pH = 5.6) containing 10 nmol L^{-1} BOx. Experiments were performed at room temperature with stirring at 150 rpm to avoid diffusion limitation. The oxygen concentration was monitored using an Ocean Optics NeoFox-GT oxygen sensor probe and NeoFox viewer software.

References

1. Moser, C. C., Keske, J. M., Warncke, K., Farid, R. S. & Dutton, P. L. Nature of biological electron transfer. *Nature* **355**, 796–802 (1992).
2. Saboe, P. O., Conte, E., Farell, M., Bazan, G. C. & Kumar, M. Biomimetic and bioinspired approaches for wiring enzymes to electrode interfaces. *Energy Environ. Sci.* **10**, 14–42 (2017).
3. Cosnier, S., J. Gross, A., Le Goff, A. & Holzinger, M. Recent advances on enzymatic glucose/oxygen and hydrogen/oxygen biofuel cells: Achievements and limitations. *Journal of Power Sources* **325**, 252–263 (2016).
4. Stines-Chaumeil, C., Roussarie, E. & Mano, N. The nature of the rate-limiting step of blue multicopper oxidases: Homogeneous studies versus heterogeneous. *Biochimie Open* **4**, 36–40 (2017).
5. Tsujimura, S. *et al.* Bioelectrocatalytic reduction of dioxygen to water at neutral pH using bilirubin oxidase as an enzyme and 2,2′-azinobis (3-ethylbenzothiazolin-6-sulfonate) as an electron transfer mediator. *Journal of Electroanalytical Chemistry* **496**, 69–75 (2001).
6. Kano, K. & Ikeda, T. Fundamentals and Practices of Mediated Bioelectrocatalysis. *Analytical Sciences* **16**, 1013–1021 (2000).
7. Ruff, A. Redox polymers in bioelectrochemistry: Common playgrounds and novel concepts. *Current Opinion in Electrochemistry* **just accepted**, (2017).
8. Xiao, Y., Patolsky, F., Katz, E., Hainfeld, J. F. & Willner, I. 'Plugging into Enzymes': Nanowiring of Redox Enzymes by a Gold Nanoparticle. *Science* **299**, 1877–1881 (2003).
9. Zayats, M., Katz, E., Baron, R. & Willner, I. Reconstitution of Apo-Glucose Dehydrogenase on Pyrroloquinoline Quinone-Functionalized Au Nanoparticles Yields an Electrically Contacted Biocatalyst. *J. Am. Chem. Soc.* **127**, 12400–12406 (2005).
10. Lalaoui, N. *et al.* Direct Electron Transfer between a Site-Specific Pyrene-Modified Laccase and Carbon Nanotube/Gold Nanoparticle Supramolecular Assemblies for Bioelectrocatalytic Dioxygen Reduction. *ACS Catal.* **6**, 1894–1900 (2016).
11. Holland, J. T., Lau, C., Brozik, S., Atanassov, P. & Banta, S. Engineering of Glucose Oxidase for Direct Electron Transfer via Site-Specific Gold Nanoparticle Conjugation. *J. Am. Chem. Soc.* **133**, 19262–19265 (2011).
12. Gutiérrez-Sánchez, C., Pita, M., Vaz-Domínguez, C., Shleev, S. & De Lacey, A. L. Gold Nanoparticles as Electronic Bridges for Laccase-Based Biocathodes. *J. Am. Chem. Soc.* **134**, 17212–17220 (2012).
13. Trifonov, A., Tel-Vered, R., Fadeev, M. & Willner, I. Electrically Contacted Bienzyme-Functionalized Mesoporous Carbon Nanoparticle Electrodes: Applications for the Development of Dual Amperometric Biosensors and Multifuel-Driven Biofuel Cells. *Adv. Energy Mater.* **5**, 1401853 (2015).
14. Aquino Neto, S., Forti, J. C., Zucolotto, V., Ciancaglini, P. & De Andrade, A. R. The kinetic behavior of dehydrogenase enzymes in solution and immobilized onto nanostructured carbon platforms. *Process Biochemistry* **46**, 2347–2352 (2011).
15. A. Sheldon, R. & Pelt, S. van. Enzyme immobilisation in biocatalysis: why, what and how.

Chemical Society Reviews **42**, 6223–6235 (2013).

16. Li, J.-J., Chen, Y., Yu, J., Cheng, N. & Liu, Y. A Supramolecular Artificial Light-Harvesting System with an Ultrahigh Antenna Effect. *Adv. Mater.* **29**, 1701905 (2017).
17. Gross, A. J. *et al.* Redox-Active Carbohydrate-Coated Nanoparticles: Self-Assembly of a Cyclodextrin–Polystyrene Glycopolymer with Tetrazine–Naphthalimide. *Langmuir* **32**, 11939–11945 (2016).
18. Liu, P. *et al.* Competitive Host–Guest Interaction between β-Cyclodextrin Polymer and Pyrene-Labeled Probes for Fluorescence Analyses. *Anal. Chem.* **87**, 2665–2671 (2015).
19. Korchia, L. *et al.* Photodimerization as an alternative to photocrosslinking of nanoparticles: proof of concept with amphiphilic linear polyoxazoline bearing coumarin unit. *Polym. Chem.* **6**, 6029–6039 (2015).
20. Mano, N. & Edembe, L. Bilirubin oxidases in bioelectrochemistry: Features and recent findings. *Biosensors and Bioelectronics* **50**, 478–485 (2013).
21. Heller, A. Miniature biofuel cells. *Phys. Chem. Chem. Phys.* **6**, 209–216 (2004).
22. Goldsmith, J. I., Takada, K. & Abruña, H. D. Probing Diffusional Transport in Redox-Active Dendrimers. *J. Phys. Chem. B* **106**, 8504–8513 (2002).
23. Flexer, V., Ielmini, M. V., Calvo, E. J. & Bartlett, P. N. Extracting kinetic parameters for homogeneous [Os(bpy)2ClPyCOOH]+ mediated enzyme reactions from cyclic voltammetry and simulations. *Bioelectrochemistry* **74**, 201–209 (2008).
24. Bartlett, P. N. & Pratt, K. F. E. A study of the kinetics of the reaction between ferrocene monocarboxylic acid and glucose oxidase using the rotating-disc electrode. *Journal of Electroanalytical Chemistry* **397**, 53–60 (1995).
25. Farneth, W. E., Diner, B. A., Gierke, T. D. & D'Amore, M. B. Current densities from electrocatalytic oxygen reduction in laccase/ABTS solutions. *Journal of Electroanalytical Chemistry* **581**, 190–196 (2005).
26. Pankratov, D. *et al.* The influence of nanoparticles on enzymatic bioelectrocatalysis. *RSC Advances* **4**, 38164 (2014).
27. Bourourou, M. *et al.* Freestanding redox buckypaper electrodes from multi-wall carbon nanotubes for bioelectrocatalytic oxygen reduction via mediated electron transfer. *Chemical Science* **5**, 2885–2888 (2014).
28. Kissinger, P. T. & Heineman, W. R. Cyclic voltammetry. *J. Chem. Educ.* **60**, 702 (1983).

Chapter 6:

Conclusions and perspectives

Chapter 6 Conclusions and perspectives

6.1 Conclusions

L'objectif de cette thèse est d'explorer les formulations, les caractérisations et les applications pratiques des buckypapers dans les biopiles enzymatiques (EFCs).

Après un chapitre de revue de la littérature sur ces biopiles enzymatiques, le deuxième chapitre de la thèse commence par une étude comparative entre différents buckypapers (un commercial et un fabriqué au laboratoire) sur leurs propriétés physico-chimiques et leur comportement électrocatalytique. Le BP commercial (c-BP) possède une teneur plus élevée en oxygène mais une structure plus ordonnée et plus souple avec des nanotubes de diamètre nettement plus large par rapport au BP fabriqué au laboratoire (l-BP). Les mesures BET ont révélé une surface spécifique 9 fois plus petite pour le BP commercial, tandis que des résultats contradictoires ont été obtenus pour les mesures de surface électroactive, ce qui suggère que les espèces redox chargées ne diffusent pas efficacement dans la structure mésoporeuse plus dense du l-BP pendant la courte période de l'expérience en voltampérométrie cyclique.

Les électrodes de BP modifiées avec BOx ont été étudiées et la meilleure performance catalytique pour des électrodes non modifiées et modifiées par l'hémine a été obtenue pour 1-BP. Pour les électrodes non modifiées, un DET négligeable a été observé pour c-BP comparé à celui obtenu pour l-BP. Cela suggère que la structure de c-BP était moins bien adaptée à une adsorption et une orientation efficaces des enzymes. Lorsque les électrodes étaient modifiées par l'hémine, des courants électrocatalytiques plus importants ont été observés en raison de la fonctionnalisation des groupes de porphyrine promoteurs du DET. L'amélioration du DET à 1-BP était supérieure et donnait une densité de courant de -1,32 mA cm^{-2} et une pente très prononcée pour la vague bioélectrocatalytique de réduction de O_2. Les données indiquent qu'une surface hautement mésoporeuse mais également un taux de recouvrement élevé en hémine sont nécessaires pour une bioélectrocatalyse de type DET efficace avec la BOx à 1-BP.

Au chapitre 3, une bioanode pour l’oxydation du glucose revêtue d’un hydrogel d’alginate a été fabriquée couche par couche. Pour réticuler l'alginate afin de former un hydrogel, du $CaCO_3$ insoluble et du gluconolactone ont été utilisés. La lente hydrolyse du gluconolactone permet la libération progressive de l'agent de réticulation,

l'ion calcium, qui conduit ensuite à un film homogène. Des électrodes autosupportées (buckypaper) préparées à partir de deux types de CNTs différents ont été construites et testées. Un courant catalytique plus élevé a été observé pour les CNTs avec une pureté de carbone plus élevée. La présence d'une couche d'hydrogel diminue le courant catalytique en raison d'un transfert de masse du substrat plus lent à travers cette couche, comme le révèlent les études de voltampérométrie cyclique et de choronoampérométrie. Il est important de noter que la stabilité en stockage a été améliorée par rapport à une électrode non revêtue. Le revêtement d'hydrogel a été optimisé en modifiant le volume d'hydrogel et en ajoutant des CNTs à la matrice d'hydrogel. L'électrode la plus performante a été identifiée comme étant l'électrode revêtue d'hydrogel préparée à partir du mélange CNTs / alginate, retenant 67% de son courant électrocatalytique après 5 jours de stockage.

Au chapitre 4, une EFC lactate/O_2 extensible et portable qui récupère l'énergie de la sueur a été créé grâce à la combinaison d'un substrat collecteur de courant sérigraphié et de PA souples à base de polynorbornène modifié par des enzymes. Au cours d'expériences *in vitro*, l'EFC assemblée présentait une valeur d'OCV élevée (de l'ordre de 0,74 V) et une densité de puissance maximale de 520 µW cm^{-2}. L'extensibilité du dispositif a été réalisée grâce au couplage d'une architecture en "îlot" et d'encres résistantes aux contraintes mécaniques. Le dispositif a pu conserver ses performances après plusieurs cycles d'étirement. La biopile peut également fonctionner comme un supercondensateur autonome, pouvant délivrer une puissance maximale de 6,5 mW cm^{-2} à une densité de courant impulsionnelle de 20 mA cm^{-2}. Après couplage avec un élévateur de tension, le prototype de cette EFC basé sur des électrodes en BP était en mesure d'alimenter une LED commerciale en mode pulsé et en mode continu en convertissant l'énergie chimique du lactate présent dans la sueur (lui-même généré au cours d'un exercice physique).

Le chapitre 5 a mis en évidence l'auto-assemblage et la caractérisation de nanoparticules enrobées de cyclodextrine contenant des molécules ABTS-bis-pyrène possédant une activité redox, ainsi que leur capacité à fonctionner en tant que navettes électroniques en solution pour assurer le transfert électronique médié entre le matériau d'électrode et la BOx pour la réduction de O_2. Les glyconanoparticules encapsulées ont été préparées par auto-assemblage de polymère de polystyrène modifié par la β-cyclodextrine (PSCD) en présence de bis-pyrène-ABTS *via* la nanoprécipitation. Des nanoparticules encapsulées dans du bis-pyrène-ABTS ont été étudiées par voie

électrochimique et spectroscopique. Une densité de courant de -3,97 ± 0,86 µA cm^{-2} pour la réduction de O_2 est observée avec le système de nanoparticules redox, tandis que les bioélectrodes équivalentes avec l'ABTS seul dissout en tant que médiateurs n'affichaient que -1,20 ± 0,03 µA cm^{-2}. Outre des performances catalytiques améliorées et de faibles surtensions, la biocathode avec nanoparticules redox a montré une stabilité considérablement améliorée après 60 min de fonctionnement et 24 h de stockage, ce qui suggère que l'architecture polymère stabilise à la fois l'enzyme et le médiateur.

6.2 Perspectives

Dans ce travail, le potentiel considérable des papiers autosupportés en carbone a été démontré en tant que matériau d'électrode pour les biopiles enzymatiques. La grande surface spécifique et les propriétés électroniques exceptionnelles du buckypaper permettent un câblage électrique amélioré des enzymes sur la surface de l'électrode, permettant ainsi d'obtenir des biopiles offrant des performances intéressantes. Sur la base des conclusions présentées ci-dessus, certaines stratégies sont discutées ici pour faire face aux défis posés par les EFCs à base de buckypaper.

En ce qui concerne le chapitre 2, le buckypaper fabriqué en laboratoire a montré des performances nettement supérieures en termes de réaction de réduction de l'oxygène par rapport au buckypaper issu du commerce. Les travaux futurs sur l'intensification de la production de BP dans le processus de fabrication continu tout en maintenant les propriétés exceptionnelles des BP sont intéressants. Pour améliorer le courant bioélectrocatlytique au niveau de la bioélectrode, il est nécessaire de comprendre les facteurs limitants de la réaction enzymatique au sein de la matrice poreuse. De plus, l'activité enzymatique sur la surface de l'électrode et la distribution de l'enzyme dans le buckypaper en réseau poreux doivent également être étudiées.

Le chapitre 3 a montré que le revêtement d'hydrogel peut améliorer la stabilité de la bioanode par rapport à une électrode non revêtue. Néanmoins, la stabilité devrait encore être améliorée sur la base des résultats obtenus dans ce travail. Une stratégie consiste à immobiliser les médiateurs, les enzymes et l'hydrogel par une liaison covalente (ou non-covalente mais offrant un site d'ancrage par interaction π-π). La taille des pores de l'hydrogel doit être contrôlée pour être plus petite que les enzymes afin d'empêcher le relargage des enzymes.

Le résultat décrit au chapitre 4 a démontré le potentiel prometteur de l'utilisation de

BP comme matériau d'électrode à haute performance pour les EFCs cutanées avec un substrat de support extensible. De tels dispositifs portés à même la peau et étirables devraient contribuer au développement de systèmes de récupération d'énergie cutanée et de produits électroniques portables. Ce dispositif des EFCs repose toujours sur des exercices pour la production de sueur, ce qui limite encore ses utilisations à des fins sportives uniquement. Différentes stratégies, telles que l'utilisation de produits chimiques induisant la transpiration[1] ou le remplacement de la cathode par une électrode respirante, permettent de relever des défis, tels que la disponibilité de biocarburants ou d'oxygène. Les futures études devraient viser à améliorer la biocompatibilité, les performances catalytiques de chaque bioélectrode et une intégration électronique plus poussée ainsi que des essais étendus sur d'autres zones du corps.

Le chapitre 5 a présenté une autre configuration de biocathode avec des glyconanoparticules et des enzymes redox-actives en solution. Le projet a été développé plus avant par mon collègue, qui a préparé les glyconanoparticules contenant de la phénanthrénéquinone piégée en tant que médiateur de la glucose déshydrogénase dépendante du FAD. Une nouvelle EFC solubilisée a été construite en combinant les demi-cellules anodiques et cathodiques.[2] L'EFC peut être perfectionnée pour permettre un échange aisé des solutions avec des médiateurs et/ou d'enzymes actives, ce qui devrait conduire à prolonger la durée de vie du dispositif complet.

Chapter 6 Conclusions and perspectives

6.1 Conclusions

The objective of this thesis is to explore the formulations, characterizations and practical applications of buckypapers in enzymatic biofuel cells.

After a chapter of literature review on enzymatic biofuel cells, the second chapter of the thesis starts with a comparison study between commercial and lab-made buckypapers on their physico-chemical properties and catalytic behavior. Commercial BP possesses higher oxygen content but more ordered and looser structure with significantly wider diameter nanotubes compared to lab-made BP (l-BP). BET measurements revealed a 9-times smaller surface area for commercial BP while contradictory results were obtained for electroactive surface area measurements, which suggest that the charged redox species did not effectively diffuse into the denser mesoporous structure of l-BP during the time scale of the experiment.

BP electrodes modified with BOx were studied and the best catalytic performance at unmodified and hemin-modified electrodes was obtained at l-BP. At unmodified BP, negligible DET was observed at commercial BP compared to the lab-made counterpart. This suggests the structure of c-BP was less well suited to effective enzyme adsorption and orientation. At hemin-modified CNT electrodes, enhanced currents were observed due to the functionalization of DET promoting porphyrin groups. The DET enhancement at l-BP was superior and gave a current density of -1.32 mA cm^{-2} and a very pronounced slope for the bioelectrocatalytic wave. The data indicates that highly mesoporous surface but also a high coverage of hemin are required for effective DET-type bioelectrocatalysis with BOx at l-BP.

In chapter 3, alginate hydrogel-coated glucose oxidizing bioanode was fabricated in a layer-by-layer configuration. To cross-link alginate to form hydrogel, insoluble $CaCO_3$ and gluconolactone were used. The slow hydrolysis of gluconolactone enables the gradual release of cross-linker, calcium ion, which then leads to homogeneous film. Buckypaper electrodes prepared from two different types of CNTs were constructed and tested. Higher catalytic current was observed for CNTs with higher carbon purity. The presence of hydrogel layer decreases the catalytic current due to slower mass transfer efficiency as revealed by cyclic voltammetry and choronoamperometry studies. Importantly, both storage and operational stability improved compared to uncoated electrode. Hydrogel coating was optimized by

changing hydrogel volume and adding CNT into the hydrogel matrix. The best performing electrode was identified as the one coated with hydrogel prepared from CNT/alginate mixture, retaining 67% of its catalytic current after 5 days of storage.

In chapter 4, a stretchable and wearable enzymatic lactate/O_2 EFC that harvests energy from sweat has been created through the combination of a screen-printed current collector substrate and flexible enzyme-modified polynorbornene-based BPs. During in vitro experiments, the assembled EFC had a high OCV of 0.74 V and a maximum power density of 520 μW cm^{-2}. The stretchability of the device was realized through the coupling of "island-bridge" architecture and strain-enduring inks. The device was able to maintain its performance stability under multiple stretching cycles. The biofuel cell can also function as a self-power supercapacitor, which can deliver a maximum power of 6.5 mW cm^{-2} at a pulse current density of 20 mA cm^{-2}. After coupling with a voltage booster, the BP-based EFC was able to power a commercial LED both in pulse mode and in continuous mode by converting the chemical energy in sweat lactate generated during exercise.

Chapter 5 demonstrated the self-assembly, characterization of cyclodextrine-coated nanoparticles containing redox-active bis-pyrene-ABTS molecules and their ability to function as electron shuttles in solution for the electrical wiring of BOx. The encapsulated glyconanoparticles were prepared by self-assembly of β-cyclodextrin modified polystyrene (PSCD) polymer in the presence of bis-pyrene-ABTS *via* nanoprecipitation. Bis-pyrene-ABTS encapsulated nanoparticles were investigated electrochemically and spectroscopically. Enhanced current density of -3.97 ± 0.86 μA cm^{-2} for mediated O_2 reduction are observed with the redox nanoparticle system, in constrast to -1.20 ± 0.03 μA cm^{-2} for the equivalent bioelectrode cells with dissolved $ABTS^{2-}$ as mediators. In addition to enhanced catalytic performance and low overpotentials, the biocathode with redox nanoparticles showed dramatically improved stability after 60 min operation and 24 h storage, suggesting that the polymer architecture stabilizes both the enzyme and mediator.

6.2 Perspectives

In this work, the great potential of buckypaper as electrode material for enzymatic biofuel cells has been demonstrated. The large specific surface area and exceptional electronic properties of buckypaper allow the enhanced electrical wiring of enzymes on electrode surface, leading to high performance biofuel cell. Based on the

conclusions presented above, some strategies are discussed here to tackle the challenges of buckypaper based enzymatic biofuel cells.

In regard to chapter 2, lab-made buckypaper has shown superior performance in terms of oxygen reduction reaction compared to commercial buckypaper. Future work on the scale-up of producing buckypaper in continuous manufacturing process while maintaining the exceptional properties of BPs is of interest. To improve the bioelectrocatlytic current at bioelectrode, understanding of the limiting factors of the enzymatic reaction within the porous matrix is necessary. In addition, enzyme activity on electrode surface and enzyme distribution in the porous network buckypaper should also be investigated.

Chapter 3 showed that the hydrogel coating can improve the bioanode stability compared to uncoated electrode. Nevertheless, stability should be further improved on the basis of the results obtained in this work. One strategy is to immobilize mediators, enzymes and hydrogel through covalent attachment. The pore size of the hydrogel should be controlled to be smaller than enzymes to prevent enzyme leaching.

The result described in chapter 4 demonstrated the promising potential of using BP as high-performance electrode material for epidermal EFC with a stretchable supporting substrate. Such stretchable skin-worn devices are expected to contribute to the development of epidermal energy harvesting systems and wearable electronics. The reported BFC device still relies on exercises for sweat generation, which limits its usages for athletic purposes. Challenges, such as the availability of biofuels or oxygen, can be addressed *via* different strategies such as the use of sweat-inducing chemicals[1] or replacing the cathode with an air-breathing electrode. Future studies should aim at improving the biocompatibility, the catalytic performance of each individual bioelectrode, and further electronics integration along with extensive on-body operations.

Chapter 5 demonstrated an alternative configuration of biocathode with redox-active glyconanoparticles and enzymes in solution. The project was further developed by my colleague, who has prepared glyconanoparticles with entrapped phenanthrenequinone as mediators for FAD-dependent glucose dehydrogenase. A novel solubilized EFC has been constructed by the combination of anodic and cathodic half-cells.[2] The EFC should be further developed to enable the easy exchange of solutions with fresh mediators and enzymes, leading to extended lifetime of the device.

References

1. Kim, J. *et al.* Simultaneous Monitoring of Sweat and Interstitial Fluid Using a Single Wearable Biosensor Platform. *Advanced Science* **5**, 1800880 (2018).
2. Hammond, J. L. *et al.* Solubilized Enzymatic Fuel Cell (SEFC) for Quasi-Continuous Operation Exploiting Carbohydrate Block Copolymer Glyconanoparticle Mediators. *ACS Energy Lett.* 142–148 (2018) doi:10.1021/acsenergylett.8b01972.

Publications and presentations

Publications

A High Power Buckypaper Biofuel Cell: Exploiting 1,10-Phenanthroline-5,6-dione with FAD-Dependent Dehydrogenase for Catalytically-Powerful Glucose Oxidation

Andrew. J. Gross, Xiaohong Chen, Fabien Giroud, Caroline Abreu, Alan Le Goff, Michael Holzinger, Serge Cosnier- *ACS catalysis* **2017**, 7, 4408−4416
DOI: 10.1021/acscatal.7b00738

Redox-Active Glyconanoparticles as Electron Shuttles for Mediated Electron Transfer with Bilirubin Oxidase in Solution

Andrew. J. Gross, Xiaohong Chen, Fabien Giroud, Christophe Travelet, Redouane Borsali, Serge Cosnier- *J. Am. Chem. Soc* **2017**, 139, 16076-16079
DOI: 10.1021/jacs.7b09442

Comparison of Commercial and Lab-made MWCNT Buckypaper: Physicochemical Properties and Bioelectrocatalytic O_2 Reduction

Xiaohong Chen, Andrew. J. Gross, Fabien Giroud, Michael Holzinger, Serge Cosnier- *Electroanalysis* **2018**, 30, 1511−1520
DOI: 10.1002/elan.201800136

Stretchable and flexible buckypaper-based lactate biofuel cell for wearable electronics

Xiaohong Chen, Lu Yin, Jian Lv, Andrew J. Gross, Minh Le, Nathaniel Georg Gutierrez, Yang Li, Itthipon Jeerapan, Fabien Giroud, Anastasiia Berezovska, Rachel K. O'Reilly, Sheng Xu, Serge Cosnier, Joseph Wang- *Adv. Funct. Mater.* **2019**, 1905785

DOI: 10.1002/adfm.201905785

Use of alginate hydrogel coating to improve stability of carbon nanotube bioanode for glucose oxidation

Manuscript under preparation

Poster presentations

XXIV International Symposium on Bioelectrochemistry and Bioenergetics, High Power Glucose/O_2 Biofuel Cell Constructed from Redox-Embedded Carbon Nanotube Buckypapers. Xiaohong Chen, Andrew J. Gross, Fabien Giroud, Caroline Abreu, Alan Le Goff, Michael Holzinger, Serge Cosnier. *Lyon, July 2017* (won the best poster award)

Oral communications

Journée de Printemps de la section Rhône-Alpes de la Société Chimique de France, Preparation of Calcium Alginate Hydrogel Coated Nanostructured Carbon Electrodes for Improved Bioanode Stability. Xiaohong Chen, Fabien Giroud, Andrew J. Gross, Serge Cosnier. *Lyon, June 2018*

Annual Meeting of the doctoral School of Chemistry and Life Sciences, Bioelectrocatalytic oxidation of different substrates by immobilizing oxidoreductases onto functionalized buckypapers. Xiaohong Chen, Fabien Giroud, Andrew J. Gross, Serge Cosnier. *Grenoble, June 2018* (flash communication)

XVIème colloque du Groupe Français de Bioélectrochimie, Free-standing Commercial and Lab-Made Carbon Nanostructured Electrodes for Enzymatic Biofuel Cells Applications. Xiaohong Chen, Andrew J. Gross, Fabien Giroud, Michael Holzinger, Serge Cosnier. *Sète, September 2018*

235th ECS meeting, Redox Active Metallic and Glyco-Based Nanoparticles for Enzymatic Bioelectrocatalysis. Xiaohong Chen, Jules L Hammond, Andrew J. Gross, Fabien Giroud, Redouane Borsali, Serge Cosnier. *Dallas, TX, May 2019*

Research visit during the doctoral program (Dec 2018 – May 2019)

Visiting graduate student in Department of Nanoengineering at University of California, San Diego (USA) under the supervision of Prof. Joseph Wang.

Acknowlegements

My PhD study at BEA has officially come to an end. Whilst the past few years in France have been very challenging for me, they have become an extraordinary experience that I will always remember with gratitude. And I would like to take this opportunity to express my greatest appreciation to those who accompanied me during this journey.

My deepest gratitude goes first and foremost to my supervisor and co-supervisor: Dr. Serge Cosnier and Dr. Fabien Giroud for their greatest support on my PhD fellowship application and giving me the opportunity to conduct research in BEA. I am grateful for their mentoring, inspiration and full support throughout the past four years. Most importantly, Serge inspired me to do my best and offered me many opportunites to participate in conferences and exchange program. Fabien is the one who is always there for questions, discussions and offerering help in either professional or personal life. It is their constant support and encouragement that makes this dissertation possible.

I would like to extend my gratitude to the members of my jury: Dr. Sophie Tingry, Dr. Carole Chaix, Dr. Laurent Bouffier and Pr. Guy Royal. Thank you for taking the time and effort to read my dissertation and for the inspiring discussions and useful advice to improve my dissertation.

I would like to express my sincere appreciation to Dr. Andrew Gross, who guided me during master internship and continues to help me during my first year to get familiar with the research. I am also gratefuel for the useful discussion and your help on correcting my writings.

During my PhD, I was fortunate to be able to work with different collaborators. I am grateful for the opportunity to work with Dr. Radoune Borsali and Dr. Christophe Travelet at CERMAV on the glyconanoparticle project.

I am also grateful for the opportunity to work with Pr. Joseph Wang at University of California, San Diego during my visit. I benefit from the knowledge transfer and discussion with all the fellows. I thank IDEX for providing the travel grant for funding this exchange program.

I would like to thank staffs from the department and the doctoral school: Regine Rozand, Véronique Gineste and Magali Pourtier for their help on the complicated administrative procedure.

I would like to thank all memebers of the BEA group: Dr. Michael Holzinger, Dr. Karine Gorgy, Yannig Nedellec, Dr. Alan Le Goff, Dr. Chantal Gondran and Arielle Le Pellec. I am greatful for every colleague for always being nice to me and for your kind assistance.

I would like to also express sincere thanks to my office buddies: Anastasiia Berezovska, Dr. Deborah Brazzolotto, Dr. Ilaria Sorrentino, Marie Berthuel, Marie Carrière, Dr. Jules Hammond, Monica Brachi and Rosanna Puopolo. Thank you for the company and I will always cherish the laughters we share.

Many thanks to all the friends I met in the past four years: Dr. Hang Yu, Dr. Yang Si, Nur Istiqomah Khamidy, Zhejian Cao, Dr. Wanxin Tang, Dr. Itthipon Jeerapan, Dr. Jian Lv, Lu Yin, Songsong Tang, Zhihua Lin, Yuan Du, Dr. Zhanhong Li and Chochanon Moonla. I am deeply greatful for your company and support.

Finally, I want to express my greatest thanks to my family. Thank you for always being there.

Xiaohong Chen

Bioelectrocatalytic oxidation and reduction of different substrates using carbon nanostructured electrodes

The aim of this thesis is to explore the formulations, characterizations and practical applications of buckypapers (BPs) as electrode material for enzymatic biofuel cells (EFCs). The thesis starts with a general introduction about EFCs in chapter 1. Chapter 2 concerns the comparison of commercial and laboratory-made BP. Commercial BP is macroporous and possesses higher oxygen content but more ordered and looser structure with significantly wider diameter nanotubes. Lab-made BP is mesoporous and possesses 9-times higher specific surface area. The latter also shows superior performance for oxygen reduction when immobilized with bilirubin oxidase (BOx). The third chapter investigates the effect of alginate hydrogel coating on bioanode stability for glucose oxidation. The hydrogel coating was prepared by drop-casting alginate/$CaCO_3$ mixture, followed by addition of gluconolactone to form uniform hydrogel film by ionic cross-linking. Both operational and storage stability have been improved compared to the uncoated electrode. The fourth chapter describes a wearable lactate/O_2 EFC by the integration of flexible buckypaper bioelectrodes and a screen-printed stretchable substrate. The assembled EFC was able to maintain its performance stability under stretching conditions and could power a LED in both pulse and continuous discharge mode. The last chapter presented the self-assembly, characterization of redox-active nanoparticles entrapped with mediators. The cathode could deliver a current density of 4 $\mu A\ cm^{-2}$ with BOx and redox-active nanoparticles in solution.

Keywords: Enzymatic biofuel cell, bioelectrocatalysis, buckypaper, redox mediators, electrochemistry

Oxydation et réduction bioélectrocatalytique de différents substrats à l'aide d'électrodes en carbone nanostructurées

Le but de cette thèse est d'explorer les formulations, les caractérisations et les applications pratiques des buckypapers (BPs) en tant que matériau d'électrode pour les biopiles enzymatiques (EFCs). La thèse commence par une introduction générale sur les EFCs au chapitre 1. Le chapitre 2 concerne la comparaison des BPs commerciales et de BPs fabriquée en laboratoire. La BP commerciale est macroporeuse et possède une teneur plus élevée en oxygène mais une structure plus ordonnée et plus souple avec des nanotubes de diamètre nettement plus large. La BP fabriquée en laboratoire est mésoporeuse et possède une surface spécifique 9 fois supérieure. Ce dernier présente également des performances supérieures pour la réduction de l'oxygène lorsqu'il est immobilisé avec la bilirubine oxydase (BOx). Le troisième chapitre étudie l'effet du revêtement d'hydrogel d'alginate sur la stabilité de la bioanode pour l'oxydation du glucose. Le revêtement d'hydrogel a été préparé par un mélange d'alginate/$CaCO_3$ coulé par coulée, puis par addition de gluconolactone pour former un film d'hydrogel uniforme par réticulation ionique. La stabilité opérationnelle et la stabilité au stockage ont été améliorées par rapport à l'électrode non revêtue. Le quatrième chapitre décrit un lactate/O_2 EFC pour l'usure par l'intégration de bioélectrodes à godets souples et d'un substrat étirable sérigraphié. L'EFC assemblé était capable de maintenir sa stabilité de performance dans des conditions d'étirement et pouvait alimenter une LED en mode de décharge pulsée et continue. Le dernier chapitre a présenté l'autoassemblage, la caractérisation de nanoparticules rédox-actives piégées avec des médiateurs. La cathode pourrait délivrer une densité de courant de 4 $\mu A\ cm^{-2}$ avec BOx et des nanoparticules rédox-actives en solution.

Mots clés: Biopile enzymatique, bioélectrocatalyse, buckypaper, médiateurs rédox, électrochimie